

# Deformation-fluid multiphase interaction within the fractures of the Barcelona Plain and the Vallès Basin: influence on fault rocks and diagenesis

Interacció multifàsica entre deformació i fluids a les fractures del Pla de Barcelona i de la Conca del Vallès: influència en les roques de falla i en la diagènesi

Irene Cantarero Abad

**ADVERTIMENT.** La consulta d'aquesta tesi queda condicionada a l'acceptació de les següents condicions d'ús: La difusió d'aquesta tesi per mitjà del servei TDX ([www.tdx.cat](http://www.tdx.cat)) ha estat autoritzada pels titulars dels drets de propietat intel·lectual únicament per a usos privats emmarcats en activitats d'investigació i docència. No s'autoritza la seva reproducció amb finalitats de lucre ni la seva difusió i posada a disposició des d'un lloc aliè al servei TDX. No s'autoritza la presentació del seu contingut en una finestra o marc aliè a TDX (framing). Aquesta reserva de drets afecta tant al resum de presentació de la tesi com als seus continguts. En la utilització o cita de parts de la tesi és obligat indicar el nom de la persona autora.

**ADVERTENCIA.** La consulta de esta tesis queda condicionada a la aceptación de las siguientes condiciones de uso: La difusión de esta tesis por medio del servicio TDR ([www.tdx.cat](http://www.tdx.cat)) ha sido autorizada por los titulares de los derechos de propiedad intelectual únicamente para usos privados enmarcados en actividades de investigación y docencia. No se autoriza su reproducción con finalidades de lucro ni su difusión y puesta a disposición desde un sitio ajeno al servicio TDR. No se autoriza la presentación de su contenido en una ventana o marco ajeno a TDR (framing). Esta reserva de derechos afecta tanto al resumen de presentación de la tesis como a sus contenidos. En la utilización o cita de partes de la tesis es obligado indicar el nombre de la persona autora.

**WARNING.** On having consulted this thesis you're accepting the following use conditions: Spreading this thesis by the TDX ([www.tdx.cat](http://www.tdx.cat)) service has been authorized by the titular of the intellectual property rights only for private uses placed in investigation and teaching activities. Reproduction with lucrative aims is not authorized neither its spreading and availability from a site foreign to the TDX service. Introducing its content in a window or frame foreign to the TDX service is not authorized (framing). This rights affect to the presentation summary of the thesis as well as to its contents. In the using or citation of parts of the thesis it's obliged to indicate the name of the author.

Facultat de Geologia  
Departament de Geoquímica, Petrologia i Prospecció Geològica  
Programa de Doctorat “Ciències de la Terra”  
Universitat de Barcelona

**Deformation-fluid multiphase interaction within the fractures  
of the Barcelona Plain and the Vallès Basin: influence on fault  
rocks and diagenesis**

**Interacció multifàsica entre deformació i fluids a les fractures del Pla  
de Barcelona i de la Conca del Vallès: influència en les roques de falla i  
en la diagènesi**

by

**Irene Cantarero Abad**

PhD thesis supervised by:

**Dr. Anna Travé Herrero**  
Departament de Geoquímica,  
Petrologia i Prospecció Geològica  
Facultat de Geologia  
Universitat de Barcelona

**Dr. Gemma Alías López**  
Departament de Geoquímica,  
Petrologia i Prospecció Geològica  
Facultat de Geologia  
Universitat de Barcelona

**2013**



Facultat de Geologia  
Departament de Geoquímica, Petrologia i Prospecció Geològica  
Programa de Doctorat “Ciències de la Terra”  
Universitat de Barcelona

**Deformation-fluid multiphase interaction within the fractures  
of the Barcelona Plain and the Vallès Basin: influence on fault  
rocks and diagenesis**

**Interacció multifàsica entre deformació i fluids a les fractures del Pla  
de Barcelona i de la Conca del Vallès: influència en les roques de falla i  
en la diagènesi**

Memòria de tesi doctoral presentada per Irene Cantarero Abad per optar al grau de Doctora en Geologia. La tesi doctoral ha estat desenvolupada en el marc del Programa de Doctorat de Ciències de la Terra sota la direcció de la Dra. Anna Travé Herrero i la Dra. Gemma Alías López.

Irene Cantarero Abad

PhD supervisors

Dr. Anna Travé Herrero

Dr. Gemma Alías López

**2013**





*A mis padres,*

*Caminante, son tus huellas  
el camino y nada más;  
caminante, no hay camino,  
se hace camino al andar.*

*Al andar se hace camino  
y al volver la vista atrás  
se ve la senda que nunca  
se ha de volver a pisar.*

*Caminante no hay camino  
sino estelas en la mar...*

*“Caminante no hay camino” Antonio Machado*



## Agradecimientos

Parece mentira pero aquí estoy, frente al ordenador, escribiendo al fin los agradecimientos de mi tesis. Y me siento tremendamente afortunada de tener tanto que agradecer a tanta gente que de una manera u otra ha ayudado a que este proyecto tirara adelante.

En primer lloc, vull agrair a les meves directores de tesi, l'Anna Travé i la Gemma Alías per haver confiat en mi per a dur a terme aquest projecte.

Anna, qui ens anava a dir que preguntar-te a quart de carrera “què és això de les beques de col·laboració?” ens portaria fins aquí, oi? Moltes gràcies per aquest confiança cega que tan sovint m'has concedit i que ha fet que aprenguéssim a valorar-me i créixer com a investigadora i com a persona.

Gemma, ha estat un privilegi treballar i aprendre al teu costat. Les teves correccions meticuloses i la teva curiositat per les coses han fet que aquest treball anés millorant dia a dia. I, sobretot, gràcies per fer-me costat sempre que ho he necessitat.

Aquest treball ha estat finançat pels projectes de recerca dirigits per l'Anna Travé CGL2006-04860 i CGL2010-18260, el Grup Consolidat de Recerca “Geologia Sedimentària” (2009 SGR-1458) i per la beca 2010FI\_B2 00179 finançada pel Comissionat per a Universitats i Recerca del Departament d'Innovació, Universitats i Empresa de la Generalitat de Catalunya i el Fons Social Europeu.

També vull fer un agraïment especial a la Vinyet Baqués, companya inseparable de despatxos, congressos i viatges emocionants. Gràcies pel teu suport, la teva paciència, els teus consells i en definitiva per la teva amistat. Per mi has estat un exemple a seguir en molts sentits.

Gràcies a l'Eduard Roca, per les seves crítiques constructives i revisions al llarg de la tesi sobre la tectònica de les zones d'estudi i la revisió dels talls.

Al David Gómez-Gras, per obrir-me sempre les portes del seu despatx, per acompanyar-me a mostrejar sondatges, per ensenyar-me la geologia de Montjuïc, per estar sempre disposat a discutir el que necessités i pels riures que hem fet.

Al David Parcerisa, per la informació i discussions sobre el turó de l'Hospital, per ensenyar-me la geologia de Montjuïc i per estar sempre disposat a ajudar.

A en Pere Anadón per les discussions sobre el Microcodium.

A en Juandi Martín i la Montserrat Inglés per l'assessorament en la preparació de mostres d'agregats orientats i la seva posterior interpretació.

Vull aprofitar aquestes línies per recordar a en Ramón Vaquer, que em va ajudar en tants moments, des dels campaments d'ígnia a segon de carrera fins a l'estudi de les argiles del meu primer article. Encara em sembla olorar els teus cigarrets quan passo per davant del teu despatx...

Je veux remercier Olivier Vidal pour son accueil et son hospitalité à Grenoble, ainsi que pour les révisions sur l'article des modèles thermodynamiques. Je remercie également Pierre Lanari pour sa patience, son aide dans cette technique, pour sa grande implication sur cet article, mais surtout pour son amitié. Merci à mes collègues et amis d'ISTerre pour avoir fait de mon stage un séjour des plus agréable, surtout à Hélène Delavault la meilleure co-bureau française qui puisse exister.

També vull agrair a en Jordi Jubany i Daniel Meroño de GISA, Estibalitz Allende de Payma, l'Albert Ventayol de Bosch i Ventayol i les empreses Geotec-262 i Eurogeotecnica per facilitar informació i accés als sondatges realitzats per les línies de metro L-1, L-2 i L-9.

Aquesta tesis no s'hagués dut a terme sense el treball d'un gran nombre de tècnics als que vull expressar el meu agraïment:

Al Jordi Illa, per la preparació de les mostres, tot sovint laboriosa.

Al Vicenç, la Dolors, la Fadoua i la Montse del Servei de Làmina Prima per la realització de les làmines primes i la seva ajuda sempre que l'he necessitada.

Al Joaquim Perona per les anàlisis dels isòtops estables i la seva bona disponibilitat en tot moment.

Al Xavier Llobet del Servei de Microsonda Electrònica, al Xavier Alcobé del Servei de Difracció, a l'Eva Prats, l'Anna Maria Dominguez, el Javier García Veigas i l'Aranzazu Villuendas del Servei de Microscòpia Electrònica i l'Elisenda Seguí del Servei de

Fluorescència dels Centres Científics i Tecnològics de la Universitat de Barcelona pel seu assessorament durant les sessions de treball de les diferents tècniques.

Gràcies al Jordi Bàguena i la Montse Errea, secretaris del departament, per resoldre totes les gestions burocràtiques.

Gracias a Carmen, Guillem, Ander, Ramón, Emili, Sergio, Mar, Àlex, Agustín, Flavia, Sara, Hasdrúbal, Sedo y Adrià (espero no haberme dejado a nadie!), compañeros del Departament de Geoquímica, Petrologia i Prospecció Geològica por soportarme en los malos momentos y por compartir las alegrías, haciendo de esto del doctorado algo más divertido.

Carmen, siempre cerca con las palabras adecuadas para animarme. Como me dices tan a menudo, tú sí que eres una “máquina”!

Guillem, quantes estones bones hem compartit! Espero que continuem “discutint” molts més anys.

Adri, gracias por un sinfín de cosas, por acompañarme al campo, por los CD's de Frank Sinatra y de coplilla para los trayectos y por los momentos de desahogo compartidos.

També em sento molt agraïda amb la resta de professors del departament de GPPG, per l'ajuda científica que he rebut sempre que l'he demanada però sobretot per les seves mostres d'estima.

Finalmente mi agradecimiento de todo corazón a la gente que quiero y que me ha animado a seguir siempre adelante.

A l'Eloi i la resta de la família Carola Molas. Eloi, com posar en paraules tot el que has fet per mi, necessitaria centenars de pàgines. T'estimo.

A mis tíos, Salva y Olga. Gracias por vuestro apoyo desde la distancia.

A mi hermana. Lara, gracias por estar ahí. Te quiero murcileja!

Por último, y lo más importante, a mis padres. Papá, gracias por inculcarme desde pequeña la curiosidad por las cosas. Mamá, sin ti no habría llegado hasta aquí. Gracias por tu apoyo incondicional y por enseñarme que siempre hay que intentar superarse. Os quiero.



# Table of contents

<b>Agradecimientos</b>	i
<b>Table of contents</b>	v
<b>Summary</b>	vii
<b>List of figures</b>	ix
<b>List of tables</b>	xvii
<b>1. Introduction</b>	1
1.1. Thesis structure	1
1.2. Objectives	1
1.3. State of the art	2
1.3.1. Geofluids and fractures	2
1.3.2. Shear zones, fault rocks and microstructures	3
1.3.3. Fault reactivation	9
1.3.4. Pressure-temperature-age estimates in fault zones	12
<b>2. Geological setting</b>	15
2.1. Tectonic phases affecting the Catalan Coastal Ranges	16
2.1.1. The Hercynian deformation	16
2.1.2. The Mesozoic deformation	17
2.1.3. The Paleogene deformation	17
2.1.4. The Neogene deformation and current configuration	17
2.2. Stratigraphy in the Catalan Coastal Ranges	19
2.3. Hydrothermalism	21
2.4. Tectonothermal evolution	22
<b>3. Methodology</b>	23
3.1. Field work	23
3.2. Laboratory work	23
3.3. Office work	26
3.3.1. Chlorite-quartz-water thermometer	28
3.3.2. Mica-quartz-water thermobarometer	29
3.3.3. Chlorite-mica-quartz-water multi-equilibrium approach	29
<b>4. Results</b>	31
4.1. Studied domains	31
4.1.1. The Barcelona Plain	31
4.1.2. The Vallès Half-graben	34
4.2. Deformation phases	35
4.3. Outcrop description	39



4.3.1. Hospital outcrop.....	39
4.3.2. Enric outcrop.....	39
4.3.3. Sariol outcrop.....	41
4.3.4. Siurana outcrop.....	43
4.3.5. Sastre outcrop.....	46
4.3.6. Caritg outcrop.....	47
4.3.7. Guixeres outcrop.....	47
4.3.8. Torrent del Corró outcrop.....	48
4.3.9. Camí d'en Cisa outcrop.....	51
4.4. Petrology and geochemistry.....	51
4.4.1. Host rocks.....	51
4.4.2. Fault rocks.....	55
4.5. Pressure and temperature estimates.....	71
4.5.1. Chemical variations and thermobarometry.....	72
4.5.2. P-T estimates.....	76
<b>5. Discussion.....</b>	<b>79</b>
5.1. Evolution and origin of fluids.....	79
5.1.1. Diagenesis of the Triassic dolostones.....	79
5.1.2. Diagenesis of the Miocene fault rocks.....	80
5.1.3. Relationships among fluids, deformation phases and tectonic events.....	86
5.2. Controls in the migration paths for fluids.....	95
5.2.1. The Barcelona Plain.....	95
5.2.2. The Vallès fault.....	99
5.3. Controls on fault reactivation.....	99
5.3.1. The role of the Hercynian structures during the Mesozoic extension.....	99
5.3.2. Reactivation during the Paleogene.....	102
5.3.3. Reactivation during the Neogene.....	102
<b>6. Conclusions.....</b>	<b>105</b>
<b>7. References.....</b>	<b>109</b>
<b>Appendix 1: Geochemical data.....</b>	<b>127</b>
<b>Appendix 2: Publications of this thesis.....</b>	<b>155</b>

## Summary

The faults limiting the Barcelona Plain and the Vallès Half-graben (Catalan Coastal Ranges, NE Spain) have allowed the study of a complex and multiphase tectonic/fluid history from the Hercynian to recent times. Furthermore, this study has allowed to define the factors that control the fluid regime and the fluid flow pathways through faults.

A multidisciplinary methodology involving field and petrological observations and microstructural analyses combined with geochemical data has been used to characterize host rocks, fault rocks and fracture-related cements.

Four tectonic events that encompass seven deformation phases have been established: Hercynian compression, Mesozoic extension ( $D_1$ - $D_2$ ), Paleogene compression ( $D_3$ ) and Neogene extension ( $D_4$ - $D_7$ ).

Faults affect crystalline Hercynian basement, Triassic dolostones and Miocene detritic rocks. The fault rocks formed in the area include gouges, cataclasites, breccias and pseudotachylytes. Veins are formed by different mineral assemblages that involve calcite, quartz, laumontite, K-white mica, chlorite and iron oxides, depending on the P-T conditions and thus, on the age.

During the exhumation of the late-Hercynian granodiorite, after the Hercynian compression, M1 and M2 muscovite and microcline crystallized as result of deuteric alteration in joints, at temperatures between 330°C and 370°C.

During the first Mesozoic rifting (Late Permian-Middle Jurassic), faults controlled the thickness and distribution of the Triassic sediments. Fracture-related dolomite cements precipitated from the Triassic seawater during increasing burial in a relatively closed hydrological regime. The second Mesozoic rifting (Late Jurassic-Late Cretaceous) is characterized by precipitation of M3 and M4 phengite together with chlorite and calcite C1 at temperatures between 190 and 310°C.

During the Paleogene compression, low-temperature meteoric fluids, favored by tectonic uplift, produced calcitization of the Triassic dolomite cements and dolostones.

In the Vallès fault, by means of a shortcut, Mesozoic structures were uplifted and a gouge and subvertical stylolites were generated.

During the Neogene syn-rift, hydrothermal fluids up to 190°C ascended through the faults. In the Hospital fault these fluids upflowed within the relay area during fault growth by tip propagation due to a seismic pumping effect.

The Neogene post-rift in the Barcelona Plain developed at shallow conditions under low-temperature meteoric regime. At the same period, the Vallès fault was dominated by hydrothermal conditions, which remain active until nowadays.

Faults acted as conduits for hot fluids during both Mesozoic and Neogene extensional events. Topographically-driven meteoric fluids warmed at depth and suffered a strong interaction with the host rocks. During the Mesozoic, ascending warm fluids mixed with marine waters in both main faults whereas, during the Neogene, the ascending fluids mixed with marine waters in the Hospital fault and with meteoric waters in the Vallès fault.

Pedogenic products precipitated along Neogene faults control cross-fault fluid flow by reducing fault core permeability.

This work highlights the presence of fault reactivation from Hercynian to Recent times. Hercynian structures have demonstrated to play an important role on the localization of later structures. The main factors that control this process are: fault orientation, fabric softening, fluid pressure and cementation hardening.

## List of figures

<b>Figure 1.1.</b> Schematic model of fault rock distribution in a normal fault and relation of fault regimes to likely metamorphic environments (synthesized from Sibson 1977, 1986 and 2000).	4
<b>Figure 1.2.</b> Schematic blocks showing fault zone architecture at different magnifications. A) At regional scale, fault zones are represented by a fault trace. Sometimes a fault scarp is also recognized. B) At outcrop scale, protolith, damage zone and fault core are identified. C) Fault rocks and related structures (veins, slip surfaces, stylolites) constitute the fault core (Mercier et al. 2011).	5
<b>Figure 1.3.</b> Sketch of the geometries of the most common kinematic indicators used within brittle fault rocks, Riedel shears (R-, R'-, Y- and P-shears), foliation (S) and tension gashes (Passchier & Trouw 1996).	9
<b>Figure 1.4.</b> Mohr circles showing both the Coulomb failure envelope (law for intact rock) and the frictional sliding envelope (law for reactivation of pre-existing faults). Circles represent the progressive raising of the main principal stress ( $\sigma_1$ ). A) The circle represents a stress field in which any pre-existing fault forming $25^\circ$ with $\sigma_1$ will slip. B) The circle has two points of contact within the frictional sliding envelope indicating that any pre-existing fault whose orientation lies in the shaded area (between $10$ and $39^\circ$ respect $\sigma_1$ ) will slip. C) When the differential stress achieves a level that intercepts the Coulomb failure envelope, new faults at $30^\circ$ with $\sigma_1$ will form and pre-existing faults with orientations in the shaded area will slip (between $7.5$ and $42^\circ$ ) (Davis & Reynolds 1996).	10
<b>Figure 1.5.</b> Mohr circles illustrating the effects of a reduction in: A) cohesion and B) the coefficient of friction	11
<b>Figure 1.6.</b> The increase in fluid pressure ( $P_f$ ) produces a decrease in $\sigma_1$ and $\sigma_3$ and, in consequence, in the effective normal stress. This fact can produce the reactivation of pre-existing faults	13
<b>Figure 2.1.</b> Schematic map of the northwestern Mediterranean showing the main tectonic features (tertiary basins, orogens and types of crust) (synthesized from Vergés & Sàbat 1999 and Lewis et al. 2000). The box indicates the location of the Catalan Coastal Ranges, which is enlarged in figure 2.2.	15
<b>Figure 2.2.</b> Onshore and offshore Neogene basins of the Catalan Coastal Ranges (Bartrina et al. 1992 and Cabrera et al. 2004). The cross-section is shown in figure 2.3.	18
<b>Figure 2.3.</b> Cross-section of the Catalan Coastal Ranges and the Valencia Trough marked in figure 2.2. FPT: Frontal Paleogene Thrust (Santanach et al. 2011)	19
<b>Figure 3.1.</b> Method to obtain an oriented sample from an outcrop (green area) and an oriented thin section from a sample (orange area) (modified from Passchier & Trouw 1996). Observe that sample is sawn parallel to striations. If a sample is oriented it is possible to extrapolate the sense of shear identified in the thin section to the outcrop scale. In this figure it is also shown how to re-orientate a sample in the office in order to measure minor structures that later will be plotted together with field data	24

<b>Figure 3.2.</b> Estimation of P-T conditions of chlorite formation (red point) from equilibria convergence of reactions (1) to (4) .....	28
<b>Figure 3.3.</b> Construction of the P-T line (dashed line) by varying the H <sub>2</sub> O content of vacancies in reactions (5) to (7). V: vacancy.....	29
<b>Figure 3.4.</b> Convergence of 159 equilibria to obtain the P-T equilibrium conditions of a mica-chlorite pair. Red circle marks the convergence area.....	30
<b>Figure 4.1.</b> Simplified geological map of the central Catalan Coastal Ranges (modified from Santanach et al. 2011). Squares indicate the location of the study areas. T: Tagamanent; MT: Martorell; BT: Berta Mine; CM: Caldes de Montbui; LG: La Garriga; CE: Caldes d'Estrac.....	31
<b>Figure 4.2.</b> Schematic geological map of the northeastern sector of the Barcelona Plain with outcrops location. Cross-sections are shown in figure 4.3.....	32
<b>Figure 4.3.</b> Schematic cross-sections of the Barcelona Plain marked in figure 4.2. ....	33
<b>Figure 4.4.</b> Schematic map of the southern area of the Miocene hangingwall where main outcrops are located. ....	34
<b>Figure 4.5.</b> Schematic geological map of the studied area in the Vallès Half-graben. A) Location of the two studied outcrops, the Torrent del Corró in the granodioritic footwall and the Camí d'en Cisa outcrop in the contact between the granodiorite and the Miocene. A1) Sketch with sample location of the Torrent del Corró outcrop. ....	35
<b>Figure 4.6.</b> Stereoplots of the structural data of all the studied outcrops. Horizontal divisions will be explained in the discussion section. DF: deformation phase; Type are the families of fractures .....	37
<b>Figure 4.7.</b> Hospital outcrop. A) General view of the Hospital outcrop and interpretation of the main features. The black square is enlarged in B. B) Tectonic contact between the granodiorite and the Miocene where Triassic, Ordovician and Silurian rocks are sliced inbetween. The three main fault families are plotted in the stereogram. C) Green cataclastic fault core generated in the type 1B fault. D) Foliated gouge with S-C structure formed also in the type 1B fault .....	40
<b>Figure 4.8.</b> Schematic map of the Enric hill, where the Hospital fault places the Middle Triassic clays and sandstones (M2 facies) on the late Hercynian granodiorite. Within the Middle Triassic dolostones (M3 facies), a system of minor faults (type 1A) with a tail geometry is shown. ....	41
<b>Figure 4.9.</b> Enric outcrop. A) View of the poorly outcropping Hospital fault and hand samples of the main fault rocks. B) Synthetic cross-section of the Hospital fault at this point with the main fault rocks and the identified sets of fractures, which are also plotted in a stereogram. Although separated, type 3A faults are minor structures linked with the displacement of the main fault plane. ....	42
<b>Figure 4.10.</b> Enric outcrop. A) Type 1A listric normal faults affecting the M3 dolostones. B) View of the drag developed in the hangingwall in contact with the fault plane. ....	42

**Figure 4.11.** Sariol outcrop. A) View of the Hospital fault from the Sariol outcrop to the southwest. B) Synthetic sketch of the fault zone at the Sariol outcrop and stereoplot of the sets of fractures. Red faults are type 2B faults reactivated during development of type 3D faults (in black). C) Thin section of fault rocks developed within the granodiorite. D) Thin section of fault rocks and cements developed within the dolostones. .... 43

**Figure 4.12.** A) Schematic geological map of the northeastern ending of the Barcelona Plain (enlarged from figure 4.2). The square marks the location of the Siurana outcrop and the star the Sastre outcrop. Darker patches indicate real outcrops. The detailed map of the hills at the SW of Montgat Nord is from Parcerisa (2002). B) Stereoplot of normal and inverse (dashed line) fault of the Siurana outcrop. .... 44

**Figure 4.13.** Siurana outcrop. A) Steep trench where the complex structure of the beginning of the splay crops out. B) Silurian rocks are sliced in a fault affecting the granodiorite. C) Silurian black shales in the fault that places the Buntsandstein on the granodiorite. .... 45

**Figure 4.14.** Sastre outcrop. A) Fault zone between the late Hercynian granodiorite and the Buntsandstein conglomerates, slicing metamorphic Paleozoic materials. B) Type 2B faults with a white calcite film affecting the Buntsandstein conglomerates. C) Unconformity between the Silurian phyllites and the Buntsandstein basal conglomerates. .... 46

**Figure 4.15.** Caritg outcrop. A-B) Outcrop views of type 3D faults affecting Miocene conglomerates. C) Projection of the fault data in a stereoplot. D) Hand sample of a cataclasite. Observe the variability in clast size. .... 48

**Figure 4.16.** Generations of fractures affecting Triassic dolostones of M1 facies. A) Outcrop view affected by faults 1A, 3A, 3D and 3E. B) Cataclasite formed in the footwall of type 1A faults. C) Microfault of type 2B within M1 facies. This thin section is cut parallel to the strike of the fault, showing the sinistral component of displacement. D) Type 3A normal fault in M1 facies characterized by its undulating plane. Observe the detail of the karstic breccias on the fault plane. E) Type 3E open joint in M1 facies filled by clays of the M2 and detail of the speleothem covering the walls. .... 49

**Figure 4.17.** Torrent del Corró outcrop. A) Lateral view of the outcrop where the step-like geometry can be observed and synthetic outcrop map indicating view location. B) Schematic cross-section of the outcrop shown in A, highlighting the step-like geometry and localization of foliation and cataclasis. C) Reactivated fault zone between the granodiorite and the phyllites and enlarged area showing the crosscutting relationship between the thrust fault and the later normal fault. Photograph location is shown in A. D) Detail of the S-C structure developed in the phyllites that indicates the normal displacement of the fault. .... 50

**Figure 4.18.** Camí d'En Cisa outcrop and interpretation of the main normal faults affecting the granodioritic footwall of the Vallès fault. .... 52

**Figure 4.19.** A) Microphotograph of the granodiorite under cross-polarized light. B) Poikilitic orthose crystals (cross-polarized light). C) K-white mica resulting from alteration at the vicinity of the Vallès fault. D) Microcline crystal with its characteristic tartan-like twin. .... 53

**Figure 4.20.** A-B) Microphotographs of dolostone HR1 (plane light and cathodoluminescence). HR1 in yellowish and replacive dolomite in red. C) Microphotograph of dolmicrite HR2 affected by a calcite fracture (plane light). D-E) Microphotographs of dolostone HR3 under plane light and cathodoluminescence, respectively. F) Microphotograph of dolostone HR4 (plane light). ..... 54

**Figure 4.21.** Microphotographs of Miocene conglomerates under plane light. A) Subangular quartzite clast and phyllite clast with a concavo-convex contact. Observe at the top the irregular void within the matrix. B) Fracture porosity bordering the rounded phyllite clasts. .... 55

**Figure 4.22.** Complete sequence of fracture-related cements for the different deformation phases and previous alteration and diagenetic products. .... 57

**Figure 4.23.** Dolomite cements related to the first deformation phase. A-B) Plane light and cathodoluminescence images of the cataclasite cemented by dolomite D1 in a HR1 dolostone. Within the clast, replacive dolomite RD1 is observed. C-D) Plane light and cathodoluminescence images of the cataclasite cemented by dolomite D1 in a HR2 dolmicrite. E-F) Plane light and cathodoluminescence images of the cataclasite cemented by dolomite D2 in a HR3 dolostone. G) Crosscutting relationships among the three cements in a HR1 dolostone. H-I) Plane light and cathodoluminescence images of a fracture cemented by dolomite D3 and a later generation of calcite CD4 affecting a HR1 dolostone. .... 58

**Figure 4.24.** Fault rocks and cements related to D2. A-B) Plane light and cathodoluminescence images of quartz crystals (qtz), calcite cements C1a,b,c and later C2a related to deformation phase D3. C) Cross-polarized image of the dilatant random breccia. D) Plane light image of the cataclasite. Observe the three neoformed minerals linked to this fault rock: chlorite, calcite C1f and iron oxides. E) Cathodoluminescence of calcite cements C1c and C1d. F) Image of cathodoluminescence of calcites C1d and C1e. G) Foliated gouge with phyllosilicates displaying an S-C structure. H) Random breccia affected by fractures filled with chlorite. I) Multiepisodic pull-apart cemented by calcite C1 (plane polarized light). J) Cross-polarized light of the cataclasites and microfractures formed by chlorite and K-white mica. K) Vein filled with chlorite and K-white mica. L) Cathodoluminescence image of calcite C1 filling voids. As in the Hospital fault, several generations of calcite C1 with oscillating cathodoluminescence are observed. .... 59

**Figure 4.25.** Pseudotachylyte microphotographs. A-B) Pseudotachylyte affected by later laumontite and calcite fractures (plane light and cross-polarized light, respectively). C) SEM image of the pseudotachylyte. Observe the fine-grained matrix where micrometric micacrystals have grown by later alteration and the corroded geometry of the quartz clast. .... 60

**Figure 4.26.** Cements related to the third deformation phase. A) Void within the dilatant breccia filled with the zoned orange and brown luminescent calcite C2a. B) Fracture within the Triassic sandstones in the hangingwall of the Hospital fault filled with calcite C2a. C) Calcite cements C2b and C2c cementing the random breccia developed in the granodiorite at the Sariol outcrop. D-E) Fracture filled with calcitized dolomite CD1 and later CD4 under plane light and cathodoluminescence, respectively. F) Cathodoluminescence image of calcitized dolomite CD3 cementing a fracture. Plane light photograph is shown in figure 4.20C. G-H) Plane light and cathodoluminescence

images of calcitized dolomite CD1 and CD2. Observe corrosion in the first cement. I) Patch of calcitized dolostone with luminescence similar to CD3..... 62

**Figure 4.27.** Fault rocks and cements of the Enric outcrop. A) Pseudotachylyte vein with banded structures crosscutting the previous random breccia. B) Plane light photograph of a pseudotachylyte vein. Observe the yellow color due to opaque inclusions. C) Under cross-polarized light, a micromosaic resulting of devitrification constituting the pseudotachylyte matrix is observed. D) SEM image of the pseudotachylyte. A clast of albite is embedded in the crystalline mosaic. Note the difference in size and morphology between the clast and the crystals of the mosaic. E) SEM image of the mosaic. It is formed by polygonal crystals (red arrow) that show triple points. F) Crack-seal veins of calcite C3a overprinting a pseudotachylyte vein and type 3B joint crosscutting both. G) Detail of the crack-seal structures and the internal shear planes (cross-polarized light). H) Cathodoluminescence image of calcite cements C3a and C3b showing their crosscutting relationship. I) Slightly foliated cataclasite coeval to crack-seal displacement. .... 64

**Figure 4.28.** Fault rocks and cements of the Vallès fault formed in D4. A-B) Cataclasite formed during D4 that crosscuts three previous cataclasites formed during D2. Plane and cross-polarized light, respectively. C) Ultracataclasite (cross-polarized light). D) Cataclasite developed in type 3A normal fault and chlorite vein parallel to the fault plane (plane light). E) Vein formed by laumontite L1 (plane light). F) Detail of the laumontite crystals of the first generation (cross-polarized light). G) Calcite C4 crosscutting a laumontite L1 vein (cross-polarized light). H) Calcite vein resulting from the opening of a previous stylolite (plane light). I) Zoned cathodoluminescence of calcite C4. J) Calcite C4 replaced by laumontite L2. K) Vein formed by laumontite L2. Crystal size grows towards the center. L) Breccia cemented by laumontite L2. .... 65

**Figure 4.29.** Wispy seam crosscutting a crack-seal vein (plane light). .... 66

**Figure 4.30.** A-B) Plane and cross-polarized images of fractures filled with calcite C5 affecting the gouge. C-D) Plane and cross-polarized images of the cataclasite developed on the previous granodiorite random breccia. E-F) Plane and cross-polarized images of the cataclasite developed in the calcitized dolostone of the hanging-wall. Observe vug porosity filled with cement PC1a. G-H) Palisade PC1 domain. I) Porosity filled with calcite PC1b in the granodiorite cataclasite..... 68

**Figure 4.31.** Diagenetic products developed in the cataclasites of the Caritg hill. A) Plane light image of a palisade aggregate formed by orange bladed calcite. B-C) Plane light and cathodoluminescence images of an orange bladed calcite palisade. Observe the luminescent nucleus and the non-luminescent borders. D-E) Plane light images of spherulites of orange bladed calcite. F-G) Plane and cross-polarized light images of the contact between the orange and white bladed calcites. H) Micrite strip and channel porosity. I) Vug porosity partially filled with bladed calcite alternating with clays (plane light). J-L) Plane light images of spherulites crosscut by microfractures. .... 69

**Figure 4.32.** Soil and karst products. A) Calcite nodule C7 embedded in an horizon formed by calcite C8 (plane light). B-C) Plane light images of calcite C8 with spherulitic (B) and corn-cob (C) arrangements. D) Cross-polarized image of speleothem formed by High-Mg calcite bladed crystals. E) Speleothem constituted of fibrous aragonite crystals and sparry dolomite and calcite crystals (cross-polarized light). F) Pearls and fragments of rafts (plane light)..... 71



- Figure 4.33.** Microphotographs of chlorite and mica from Hospital and Vallès faults. A) Chlorite resulting from biotite alteration. B) Neoformed chlorite between cataclasite clasts. C) Coarse white mica M1 rimmed by M2. D) Small white mica flakes overgrowing and crosscutting coarse detrital flakes of M1 and M2 mica. E-F) Plane and cross-polarized light photographs of chlorite and mica association in a type 1B fracture. .... 72
- Figure 4.34.** Ternary plot muscovite (mus)-celadonite (cel)- pyrophyllite (pyr) of mica in fault rocks of the Vallès fault. .... 73
- Figure 4.35.** P-T diagram showing the results of mica-quartz-water thermometer for the four groups of mica. .... 73
- Figure 4.36.** Ternary plot amesite (am)-clinochlore+daphnite (clin+daph)- sudoite (sud) of chlorite in fault rocks. A) Vallès fault. B) Hospital fault. .... 74
- Figure 4.37.** Histograms of chlorite temperatures. A) Vallès fault. B) Hospital fault... 75
- Figure 4.38.** Histogram of chlorite temperature for each group of chlorite calculated with the compositions from the Monte Carlo simulation. .... 76
- Figure 4.39.** P-T path of fault rocks in the Vallès fault. Squares represent chlorite in equilibrium with M3 mica and diamonds represents chlorite in equilibrium with M4 mica. The different colours represents the four chlorite generations. The blue area indicates the location of chlorites under 190°C, which are not in equilibrium with mica. .... 76
- Figure 5.1.**  $\delta^{18}\text{O}$ - $\delta^{13}\text{C}$  plot of the Triassic host rocks and the first fault-related dolomitic cements. Dolomitic cements (D1 and D2) are progressively more  $\delta^{18}\text{O}$ -depleted than the host rocks but mantain their  $\delta^{13}\text{C}$  values. .... 79
- Figure 5.2.** Comparison of Microcodium images of Košir (2004) (left column) with images of the pedogenic structures within the fault rocks of the Miocene conglomerates (right column, plane light). A-B) Equant calcite mosaic. Scale bar in A is 200  $\mu\text{m}$ . C-D) Bladed crystals forming palisades. Scale bar in C is 0.5 mm. E-F) Spherulites. Scale bar in E is 100  $\mu\text{m}$ . .... 81
- Figure 5.3.** Comparison of the diagenetic features of Rossi & Cañaveras (1999) (left column) with images of the pedogenic structures within the fault rocks of the Miocene conglomerates showing clear resemblances. .... 82
- Figure 5.4.** Difference between the pseudospherulites of Rossi & Cañaveras (1999) (left column) and spherulites of the fault rocks of the Miocene conglomerates. A) Spherulites are formed by an unique crystal (cross-polarized light). B) Spherulites are formed by different crystals showing independent extinction (cross-polarized light). .... 83
- Figure 5.5.** Stable isotope results of the main diagenetic products. For the orange bladed calcite, luminescence variations (from luminescent in the nucleus to non-luminescent in the borders) are related to an increase in the influence of soil-derived  $\text{CO}_2$  and a decrease of evaporation. .... 84
- Figure 5.6.** Factors controlling the precipitation of the pedogenic products. 1) Evaporation increases the Mg/Ca ratio but still low-Mg calcite precipitates. 2) Biota activity become more important and increases the rate of  $\text{CO}_2$  supply. This increase

causes the change from low-Mg bladed calcite to high-Mg bladed calcite and to acicular aragonite precipitation. This explains the morphology zonations of the orange calcite aggregates (modified from Tucker & Wright 1990). ..... 85

**Figure 5.7.** A) P-T path of fault rocks in the Vallès fault and interpretation of the age through fission-track constraints. Squares represent chlorite in equilibrium with M3 mica and diamonds represents chlorite in equilibrium with M4 mica. The different colours represents the four chlorite generations. The blue area indicates the location of chlorites under 190°C, which are not in equilibrium with mica. B) Temperature and age comparison with other mineralizations of the Catalan Coastal Ranges (Berta, Rigròs and Atrevida) and the Iberian Chain (Espadán Ranges). The asterisk marks the new data obtained in this thesis. 1) Cardellach et al. (2002); 2) Piqué et al. (2008); 3) Martín-Martín et al. (2006, 2008, 2009); 4) Canals et al. (1992). ..... 88

**Figure 5.8.** Evolution of the Vallès and Hospital faults from Mesozoic to Neogene. A) Mesozoic extensional event. Topographically driven meteoric fluids, percolating in emerged areas, are warmed at depth and upflow through faults. Due to the submarine conditions of the major part of the basin, these fluids are mixed with marine waters at shallower settings. B) Paleogene compressional event. In the Vallès fault a thrust system uplifts the previous normal fault. Deformation is localized in the thrust faults generating a blue gouge. In the Hospital fault, the previous Mesozoic fault is inverted and percolation of low-temperature meteoric waters occurs. C) Neogene extensional event. During this event, the Neogene normal Vallès fault is formed (CCO) and the reactivation of some of the Mesozoic structures occurs (TCO). Hydrothermal fluids are topographically driven meteoric fluids warmed at depth. In the Hospital fault, syn-rift and post-rift stages differ. During the syn-rift, meteoric hot fluids are mixed with marine waters, as occurred during the Mesozoic. On the opposite, the post-rift is dominated by low-temperature meteoric fluids. TCO, Torrent del Corró outcrop; CCO: Camí d'en Cisa outcrop; FPT, Frontal Paleogene thrust. .... 91

**Figure 5.9.** Stable isotope plot of the fault rock cements related to their deformation phase. Values of the cements studied by Parcerisa (2002) (sparry calcite and oncoliths) and Cardellach et al. (2002) (calcite I and calcite II) have been included and marked in the legend with an asterisk. .... 92

**Figure 5.10.** Structural evolution of the basin and distribution and evolution of fluids through time in the northern sector of the Barcelona Plain from Late Permian to recent. A) Deposition of the Triassic rocks and dolomitization during the first Mesozoic rifting event. B) Cretaceous rifting localized in the southern segment and circulation of ascending hot fluids. C) Basin inversion, folding, erosion and percolation of low-temperature meteoric fluids that produced the calcitization of previous dolomites. D) Segment connection through fault growth and upflow of hot fluids in the relay area during the Neogene syn-rift. E) Propagation of the Hospital fault to the surface and percolation of low-temperature meteoric fluids. F) Generation of the NW-SE set of fractures that segmented the Hospital fault and development of soil and speleothems. .. 96

**Figure 5.11.** Sketch of the mechanism of fault growth by tip propagation of the southern segment at kilometeric scale. PST: pseudotachylyte. .... 98

**Figure 5.12.** Effects of pedogenesis in cross-fault fluid flow within Miocene conglomerates. .... 98

<b>Figure 5.13.</b> Schematic model of fracture formation during evolution of the granodiorite and reactivation of these previous structures during later tectonic events in the Vallès half-graben (modified from Yoshida et al. 2012).....	101
<b>Figure 5.14.</b> A) Plane light image of a fracture filled by chlorite in the Vallès fault. B) Foliation plane formed by chlorites in the Hospital fault. Chlorites are disconnected and misoriented avoiding sliding (plane light).....	103

## List of tables

<b>Table 1.1.</b> Textural classification of fault rocks proposed by Sibson (1977) and completed by Scholz (2002).	6
<b>Table 1.2.</b> Fault rock classification according to Passchier & Trouw (1996).	7
<b>Table 1.3.</b> Fault rock classification proposed in this work integrating previous terminologies.	8
<b>Table 3.1.</b> Atom site distribution of chlorite.	27
<b>Table 3.2.</b> Atom site distribution of mica.	27
<b>Table 1.</b> Stable isotope data ( $\delta^{18}\text{O}$ - $\delta^{13}\text{C}$ ) of host rocks and cements of the studied area.	129
<b>Table 2.</b> Elemental composition of Triassic dolostones and calcite and dolomite cements.	131
<b>Table 3.</b> Elemental composition of diagenetic products within the faults rocks developed in the Miocene conglomerates.	143
<b>Table 4.</b> Composition and atom site distribution of the four mica groups of the Vallès fault.	147
<b>Table 5.</b> Composition (%wt), atom site distribution and estimated temperature of chlorites from the Hospital fault.	149
<b>Table 6.</b> Composition (%wt), atom site distribution and estimated temperature of chlorites from the Vallès fault.	151



# 1. INTRODUCTION

## 1.1. Thesis structure

This PhD thesis volume consist on the compilation of three papers submitted to international journals indexed in the science citation reports. One of the papers is published, one is accepted and the third one is under review:

- **Cantarero I.**, Travé A., Alías G., Baqués V. (2010) Pedogenic products sealing normal faults (Barcelona Plain, NE Spain). *Journal of Geochemical Exploration*, 106, 44-52. Impact factor: 2.125. Position 24/77 (2<sup>nd</sup> quartile) in Geochemistry & Geophysics.
- **Cantarero I.**, Travé A., Alías G., Baqués V. Polyphasic hydrothermal and meteoric fluid regimes during the growth of a segmented fault involving crystalline and carbonate rocks (Barcelona Plain, NE Spain). *Geofluids* (accepted). Impact factor: 1.533. Position 37/76 (2<sup>nd</sup> quartile) in Geology (2011).
- **Cantarero I.**, Lanari P., Vidal O., Alías G., Travé A., Baqués V. Long-term fluid circulation in extensional faults in the central Catalan Coastal Ranges: P-T constraints from neoformed chlorite and K-white mica. *International Journal of Earth Sciences* (under review). Impact factor: 2.342. Position: 32/170 (1st quartile) in Geosciences (2011).

The PhD thesis volume also includes the summary of all the results and a general discussion of all the data included in the three papers completed with some unpublished data.

## 1.2. Objectives

The **main goal** of this thesis is to decipher the different fluid-fault systems occurring during the evolution of two sedimentary basins: the Barcelona Plain and the Vallès half-graben. These basins are located in the central Catalan Coastal Ranges (NE Spain) which constitute the northwestern margin of the Valencia Trough. A lot of works focused on this topic have been performed in the Penedès half-graben, the continuation towards the south of the Vallès half-graben (e.g. Travé et al. 1998, 2001, 2009; Baqués

et al. 2010, 2012a, b). In the Penedès basin, Cretaceous and Jurassic rocks crop out in the horst and Miocene rocks fill the basin. On the opposite, the horsts of the Vallès basin and the Barcelona Plain are constituted by Paleozoic crystalline rocks and Triassic sedimentary rocks. Thus, this thesis provides new information about the relationships between fluids and faults at the basement-cover contact.

An important part of this thesis has been focused on the deformation processes and fracture-related cements affecting a late Hercynian granodiorite, as it constitutes the footwall of the studied faults. The study of fracture-fluid system evolutions within granitic rocks is of high interest in order to evaluate their suitability to host underground storage and waste disposal facilities (Iwatsuki et al. 2002; Drake & Tullborg 2009; Yoshida et al. 2012) and to evaluate their exploitability as Hot Fractured Rocks (HFR) geothermal reservoirs (Bando et al. 2003; Bartier et al. 2008).

Moreover, the Barcelona Plain is a highly urbanized area where in the last years important infrastructures, such as underground and high speed train tunnels, have been made and for that reason, in a good study of faults is required. The mentioned infrastructures have provided us with core samples to complete the study.

In order to reach the main goal, **specific objectives** have been proposed:

- To establish the different deformation phases that acted pervasively in the faults that limit the Barcelona Plain and the Vallès basin.
- To characterize petrographically and geochemically the fault rocks and cements of the faults.
- To link the different deformation phases to the main tectonic events described in the Catalan Coastal Ranges.
- To estimate the pressure-temperature conditions during fault evolution.
- To unravel the origin of the fluids and the hydrological regime associated with each tectonic event.
- To establish the factors that control the pathways for fluids.
- To discern the mechanisms responsible for hydrothermalism.

### 1.3. State of the art

#### 1.3.1. Geofluids and fractures

A **Geofluid** is any subsurface fluid which is involved in the dynamic processes that occur within the Earth from the surface to the core. In the crust, they are ubiquitous to depths of at least 10-15 km (Deming 1994). Sources for crustal fluids include meteoric, marine, connate and formation waters, hydrocarbon fluids, metamorphic waters derived from reactions during prograde metamorphism and magmatic fluids (Fyfe et al. 1978). Their circulation through the crust mobilizes and transports both heat and dissolved ions producing chemical reactions within the rocks of the crust, which alter their geological and geophysical properties, and creating concentrations of economic resources (Garven 1989; Duddy et al. 1994; Putnis 2002). Therefore, the continental crust can be defined as a solid framework that evolves through interaction with geological fluids (Deming 1994). Moreover a close relationship exists between fluids and deformation as fluids help to enable deformation, changing temperature and the effective stress, and deformation facilitates fluid migration, generating conduits for the fluids (Sibson 1977; Aydin 2000). Thus, the microstructural analysis of deformed rocks provides information on deformation mechanisms, fluid flow pathways, fluid chemistry and origin and the amount of fluid involved (Schulz & Evans 1998; Breesch et al. 2009).

Within the central Catalan Coastal Ranges, the works about geofluids have been centered on three aspects. The first one is the petrological and geochemical study of fault-related cements in order to establish the different fault-fluid systems through time. These studies have been mainly performed in two different regional domains: a) in the Penedès half-graben, where faults affect Cretaceous, Jurassic and Miocene rocks (Travé et al. 1998; Baqués et al. 2010, 2012a,b); and, b) in the transition zone between the Vallès and Penedès half-grabens in both Burdigalian rocks (Travé et al. 2001, 2009) and basement granodiorite (Cardellach et al. 2002). The second tackled aspect is the diagenetic study of the Burdigalian deposits of the transition zone (Parcerisa et al. 2002, 2005) and of the Miocene and Oligocene deposits of the Barcelona Plain (Gómez-Gras et al. 2000, 2001; Parcerisa 2002). Finally, the third aspect covers the modelization of fluid circulation at basin scale (Carmona et al. 2000; Bitzer et al. 2001).

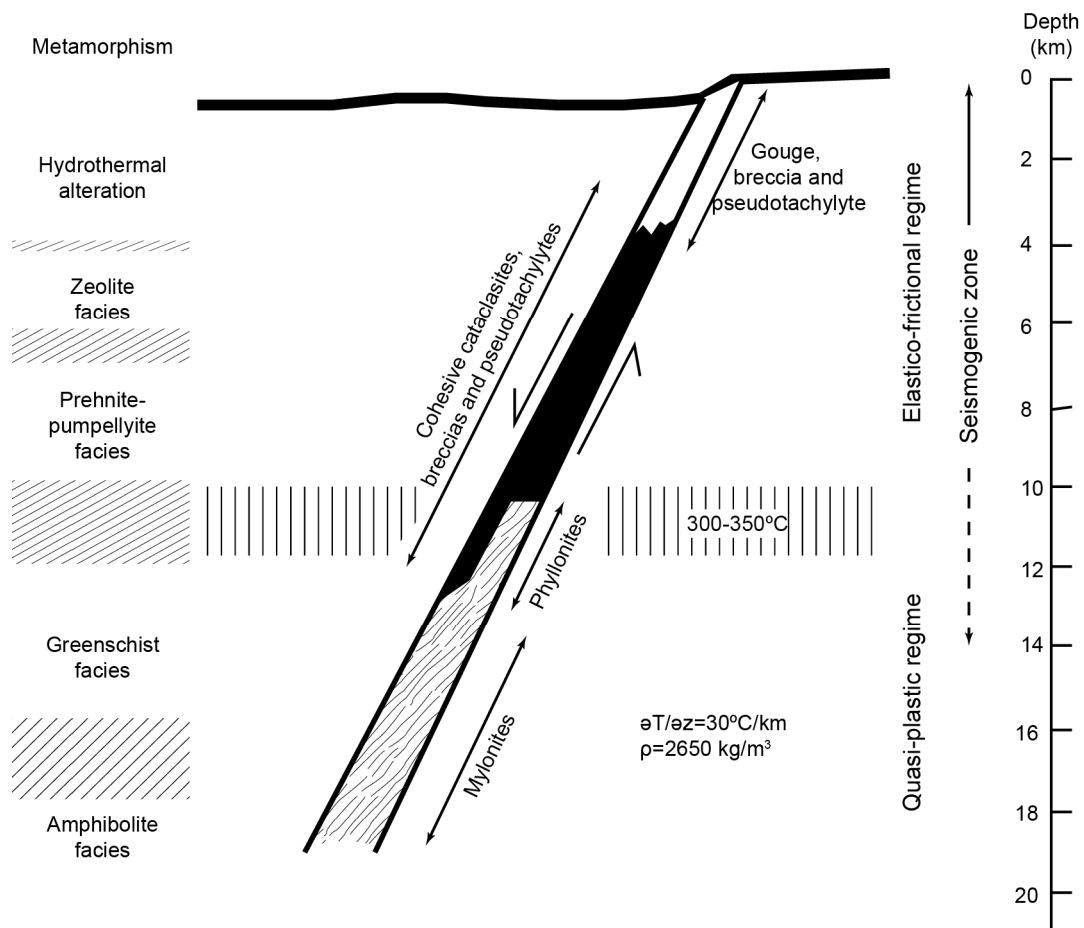
### **1.3.2. Shear zones, fault rocks and microstructures**

*Shear zones* or fault zones are high-strain zones caused by the concentration of deformation in planar zones due to the relative movement of two rigid wall-rock blocks (Passchier & Trouw 1996). I would added that a fault zone represents a volume of rock



modified mechanically and structurally by the formation of a fault from its origin until present, including all the deformations related to eventual reactivations.

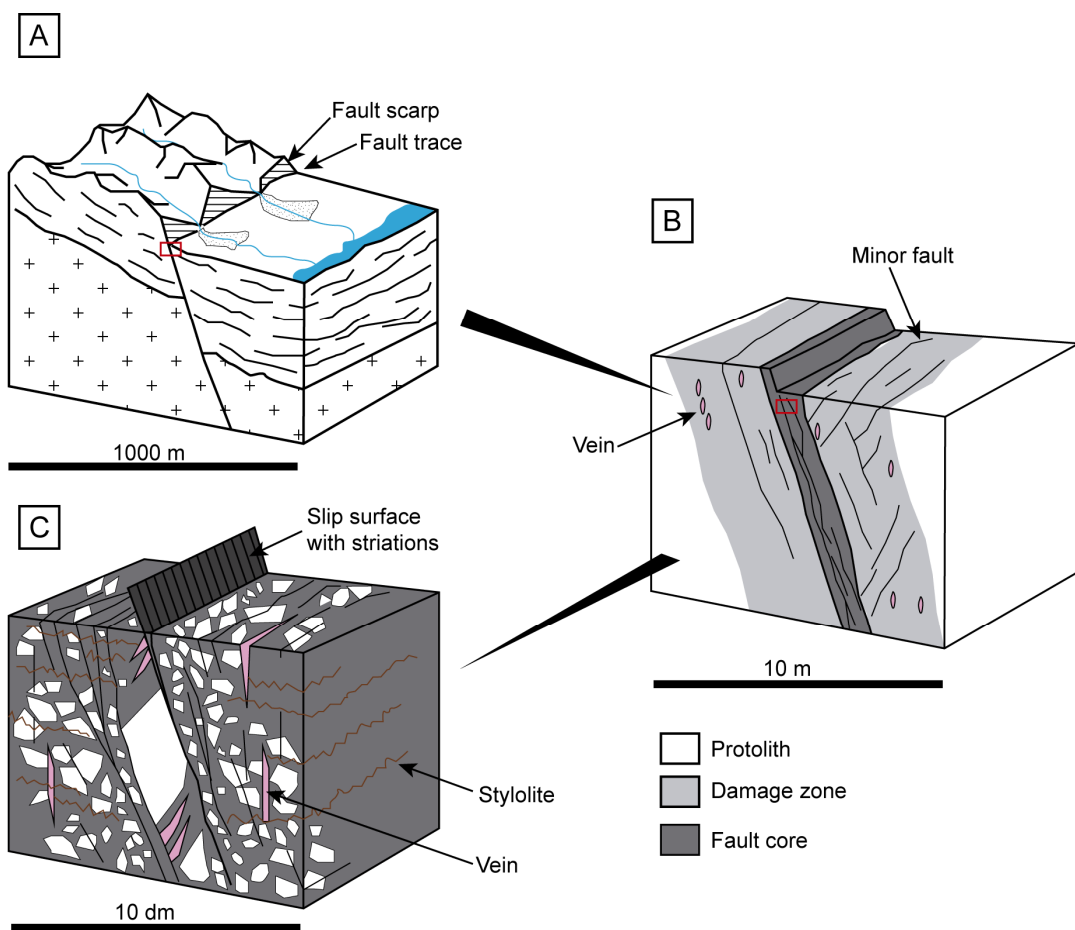
Shear zones can be divided into brittle and ductile zones. In brittle fault zones, deformation is generated by elasto-frictional mechanisms (fracturation, cataclasis and frictional sliding) whereas in the ductile zones, deformation is generated by quasi-plastic mechanisms (pressure-solution and intracrystalline deformation produced by twinning, kinking, dislocation and diffusion creep and grain boundary sliding). The transition depth between these two zones depends on several factors such as the geothermal gradient, the lithology and grain size, the fluid pressure, inherited fabrics or the stress field orientation. In normal conditions (geothermal gradient of 20-30°C/km), this limit is found between 10 and 15 km depth (Sibson 1977) (fig. 1.1).



**Figure 1.1.** Schematic model of fault rock distribution in a normal fault and relation of fault regimes to likely metamorphic environments (synthesized from Sibson 1977, 1986 and 2000).

Although at regional scale, fault zones are represented with a trace (fig. 1.2A), the **architecture** of upper-crustal fault zones is defined by three primary components (but

not all of the components are necessarily present): fault core, damage zone and protolith (Caine et al. 1996) (fig. 1.2B). The *fault core* is the zone where most of the displacement is accommodated and includes slip surfaces and fault rocks (fig. 1.2C). The *damage zone* is the network of subsidiary structures that bound the fault core. Some of these structures are small faults, veins, joints, cleavage and folds (fig. 1.2B). The *protolith* is the undeformed rock that surrounds the previous zones. The thickness, geometry and distribution of fault components and the magnitude of permeability contrasts between them control fluid flow within and near the fault zone (Caine et al. 1996; Rowland & Sibson 2004).



**Figure 1.2.** Schematic blocks showing fault zone architecture at different magnifications. A) At regional scale, fault zones are represented by a fault trace. Sometimes a fault scarp is also recognized. B) At outcrop scale, protolith, damage zone and fault core are identified. C) Fault rocks and related structures (veins, slip surfaces, stylolites) constitute the fault core (Mercier et al. 2011).

The rocks found in shear zones whose textures result, at least in part, from the shearing process, are named *fault rocks*. Fault rocks can be highly deformed and transformed in such way that one cannot even recognise their original structure.

## 1. Introduction

They are divided into brittle fault rocks (breccias, gouges, cataclasites and pseudotachylytes) and ductile fault rocks (mylonites) depending on the deformation regime they were formed. Fault rocks have been usually classified according to textural criteria (Sibson 1977; Scholz 2002), based on parameters such as fabric, cohesivity, clast size and matrix percentage in the rock (table 1.1).

**Table 1.1.** Textural classification of fault rocks proposed by Sibson (1977) and completed by Scholz (2002)

INCOHESIVE	RANDOM FABRIC			FOLIATED FABRIC					
	Fault breccia (visible fragments >30% of rock mass)			-					
	Fault gouge (visible fragments <30% of rock mass)			Foliated gouge (Scholz 2002)					
COHESIVE	Nature of matrix	Glass/ devitrified glass	Pseudotachylyte	-					
		Tectonic reduction in grain size dominates grain growth by recrystallisation and neomineralisation	Crush breccia Fine crush breccia Crush microbreccia			(fragments > 0.5 cm) (0.1cm<fragments<0.5cm) (fragments < 0.1cm)		0-10%	Proportion of matrix
								10-50%	
			Protocataclasite	Protomylonite		Mylonite series	50-90%		
			Cataclasite				Mylonite	>90%	
			Ultracataclasite				Ultramylonite		
		Cataclasite series	Phyllonite varieties	Blastomylonite					
						Significant grain growth			
						-			

Later classifications have modified this textural classification adding more subdivisions (i.e. incohesive cataclasite, foliated cataclasite) and including concepts such as the metamorphic degree or the lithology, especially in ductile rocks (Passchier & Trouw 1996) (table 1.2).

A new classification integrating both terminologies for a better classification of fault rocks is proposed (table 1.3). Brittle fault rocks are dominated by cataclasis and are

formed by fragments of the host rock, normally angular, embedded in a finer matrix.

**Table 1.2.** Fault rock classification according to Passchier & Trouw (1996)

BRITTLE FAULT ROCKS				
INCOHESIVE	Random fabric			Foliated fabric
	Fine grained matrix	Incohesive breccia	fragments>30%vol	
		Incohesive cataclasite	fragments<30%vol	
		Fault gouge	fragments isolated in the matrix	
COHESIVE	Cohesive breccia			
	Cohesive cataclasite			Foliated cataclasite (mica-rich host rock)
	Glassy matrix	Pseudotachylyte		
DUCTILE FAULT ROCKS				
COHESIVE	Foliated fabric			
	According to % of matrix in relation to porphyroclasts		According to metamorphic grade	According to lithology
	Protomylonite	10-50%	high-, medium-, low-grade	i.e. quartzite-mylonite granodiorite-mylonite quartz-feldspar mylonite quartz-mylonite calcite-mylonite
	(Meso-)mylonite	50-90%		
	Ultramylonite	>90%		
	Blastomylonite	Static recrystallization		
			Phyllonite (mica-rich)	

The cohesivity of some of these rocks is due to the precipitation of minerals such as calcite, quartz, chlorite, epidote, etc. The classification between breccia, cataclasite or gouge depends on the volume of fragments (table 1.3). Inside the brittle cohesive rocks, pseudotachylytes require a special mention. These fault rocks are formed by glass derived from a friction-induced melt. They are composed by a dark matrix with wall rock fragments, which are usually corroded. Commonly, they show a main fault plane with straight boundaries from which derive irregular injection veins towards the host rock.

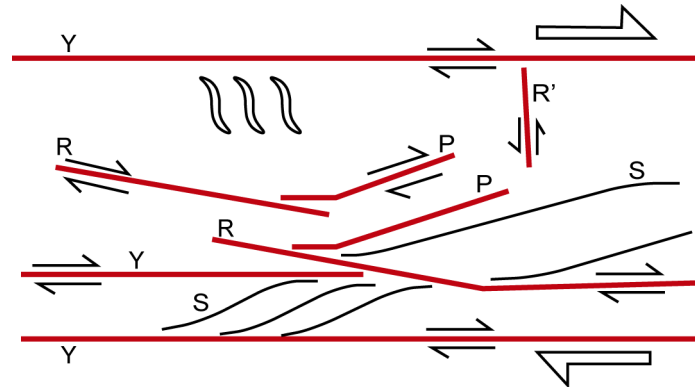
Ductile fault rocks or mylonites correspond to rocks of small grain size and strongly developed foliations and stretching lineations, which usually contain porphyroclasts.

**Table 1.3.** Fault rock classification proposed in this work integrating previous terminologies

BRITTLE FAULT ROCKS						
Random fabric						Foliated fabric
INCOHESIVE	Fine grained matrix	Incohesive breccia                      fragments>30%vol				
		Incohesive cataclasite                      fragments<30%vol				
		Fault gouge		fragments isolated in the matrix		Foliated gouge
COHESIVE	Crush breccia		fragments >0.5 cm		Proportion of matrix	
	Fine crush breccia		fragments <0.5 cm			
	Crush microbreccia		fragments <0.1 cm			
	Protocataclasite			0-10%		
	Cataclasite			10-50%		
Ultracataclasite			50-90%	Foliated cataclasite (mica-rich host rock)		
			>90%	Foliated ultracataclasite		
Glassy/ devitrified glassy matrix		Pseudotachylyte				Foliated pseudotachylyte
DUCTILE FAULT ROCKS						
Foliated fabric						
COHESIVE	According to % of matrix in relation to porphyroclasts			According to metamorphic grade		According to lithology
	Protomylonite                      10-50%		Phyllonite (mica-rich)	high-, medium-, low-grade	i.e. quartzite-mylonite granodiorite-mylonite quartz-feldspar mylonite quartz-mylonite calcite-mylonite	
	(Meso-)mylonite                      50-90%					
	Ultramylonite                      >90%					
	Blastomylonite                      Static recrystallization					

Fault rocks show **microstructures** that are characteristic of the deformation regime and some of them can also be used as kinematic indicators to provide the sense of shear. However, **kinematic indicators** in brittle fault rocks are not as clear and abundant as in ductile fault rocks (White et al. 1986). The most useful kinematic indicator in the brittle regime are Riedel shears, which are formed by a set of subsidiary shear fractures (Y-, R-, R' and P-shears) whose orientations and the produced deflection of the foliation (S) indicate the sense of shear (fig. 1.3). Another common indicator is the presence of en-echelon tension gashes and the geometry of the mineral fibers displayed within them. Striations or slickenfibres on slickensides also can be used to establish the movement

direction; however, care must be taken as they only record the last movement stage of the fault.

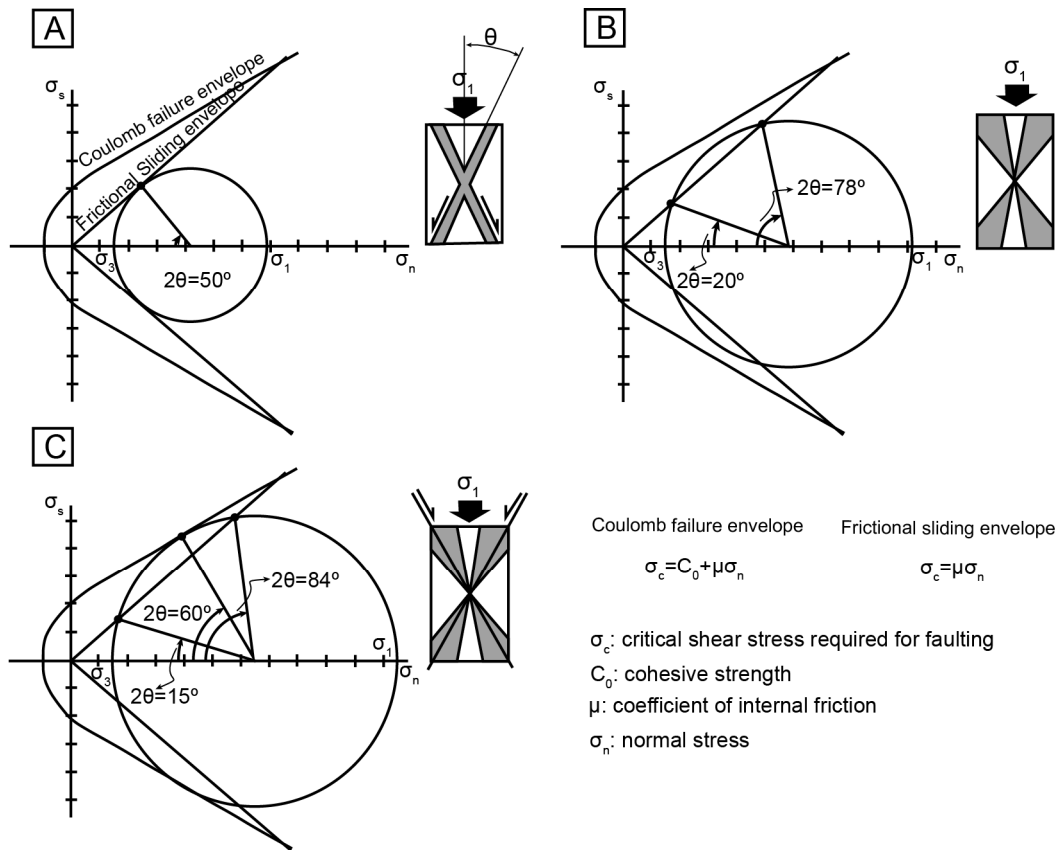


**Figure 1.3.** Sketch of the geometries of the most common kinematic indicators used within brittle fault rocks, Riedel shears (R-, R'-, Y- and P-shears), foliation (S) and tension gashes (Passchier & Trouw 1996).

The cross-cutting relationships between different fault rocks and their related microstructures, added to mineral composition, give information about the evolution of P-T conditions and the reactivation of fault zones. These overprinting relationships can be translated into terms of deformation phases. **Deformation phases** are periods of active deformation of rocks which are characterized by groups of structures that can be separated by overprinting criteria. These active periods are separated by intervals of little or no deformation during which P-T conditions and orientation of the stress field can change (Passchier & Trouw 1996). The term deformation phase refers to the relative age of the structures and is generally of local significance. In its turn, deformation phases can be encompassed within **tectonic events**, which involve a larger scale of deformation (i.e. plate motion).

### 1.3.3. Fault reactivation

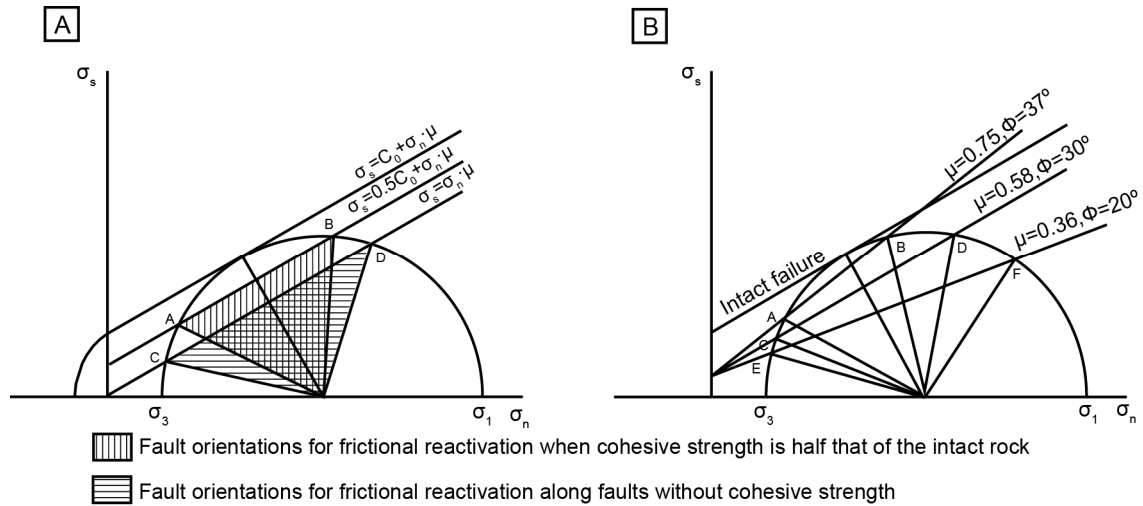
Pre-existing faults can be reactivated before the formation of a new fault because they are weaker than the surrounding intact rock according to the predicted Coulomb and Frictional envelope laws (Donath & Cranwell 1981) (fig. 1.4). The phenomenon of fault reactivation or fault rejuvenation has been described in numerous faults (Hills 1963; Sykes 1978; Plawman 1983; Powell 1987; Biddle & Rudolph 1988; Allen & Vincent 1997; Bellahsen et al. 2006; Lacroix et al. 2012). Fault reactivation is evidenced by stratigraphical and structural criteria but also by the observation of the crosscutting relationships among fault rocks, microstructures and kinematic indicators.



**Figure 1.4.** Mohr circles showing both the Coulomb failure envelope (law for intact rock) and the frictional sliding envelope (law for reactivation of pre-existing faults). Circles represent the progressive raising of the main principal stress ( $\sigma_1$ ). A) The circle represents a stress field in which any pre-existing fault forming  $25^\circ$  with  $\sigma_1$  will slip. B) The circle has two points of contact within the frictional sliding envelope indicating that any pre-existing fault whose orientation lies in the shaded area (between  $10^\circ$  and  $39^\circ$  respect  $\sigma_1$ ) will slip. C) When the differential stress achieves a level that intercepts the Coulomb failure envelope, new faults at  $30^\circ$  with  $\sigma_1$  will form and pre-existing faults with orientations in the shaded area will slip (between  $7.5^\circ$  and  $42^\circ$ ) (Davis & Reynolds 1996).

Reactivation is controlled by four main factors:

- Fault orientation: faults reactivate if they have a preferential orientation respect to the stress field. Fault orientations suitable for reactivation are controlled in turn by the cohesion and frictional behavior of faults and the pore fluid pressure.
- Fault cohesion: the cohesive strength controls the angles at which failure will occur. The decrease in cohesive strength increases the range of fault orientations that will reactivate (Etheridge 1986) (fig. 1.5A). Cementation produces hardening and prevents reactivation whereas the presence of water in intergranular boundaries reduces the cohesion (Griggs 1967).



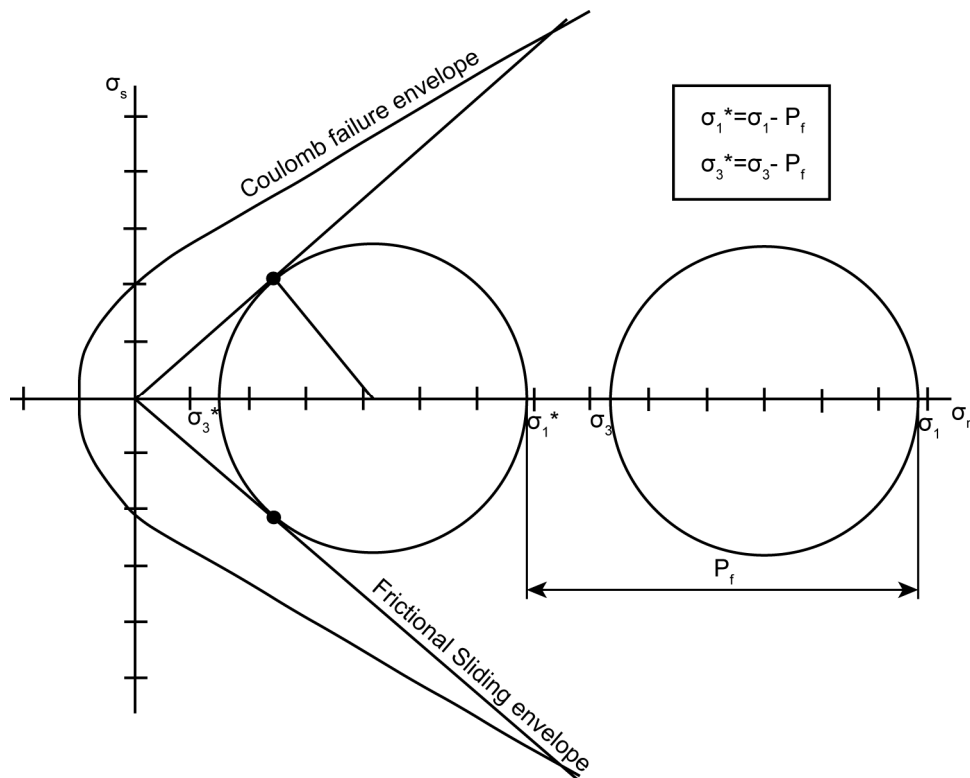
**Figure 1.5.** Mohr circles illustrating the effects of a reduction in: A) cohesion and B) the coefficient of friction.

- Coefficient of friction: the frictional behavior is controlled by the frictional characteristics of the rocks, the nature of the fault rocks, the pore-fluid conditions and the stress regime. The early part of friction behavior on faults, produced at low stress, is controlled by fault surface topography (asperity and roughness) but at high normal stress that effect is diminished and the friction is nearly independent on the rock type (Byerlee 1978). As wear continues and blocks are separated by fault rocks, then the frictional properties depend on the fault rocks and not in the fault surfaces (Sibson 1977). The decrease of the friction angle increases the range of fault orientations that can be reactivated (fig. 1.5B). Some processes can reduce the friction coefficient:

- Reaction softening: retrograding reactions are the responsible for reemplacing strong minerals, such as feldspar, by weaker minerals such as phyllosilicates. Phyllosilicates exhibit weak strength and low-frictional behavior, yielding to fault reactivation (Wintsch et al. 1995). This is the reason because clay-rich gouges are weaker than predicted (Byerlee 1978).
- Grain-boundary hydration: Platy phyllosilicates can form bonds with water molecules, causing the concentration of shear in these water layers, and thus, reducing the friction coefficient (Morrow et al. 2000). Chlorite and kaolinite are two of the phyllosilicates that demonstrate the greatest difference in dry and wet conditions (Behnsen & Faulkner 2012).



- Fabric softening: Although phyllosilicates are characterized by their low friction coefficient, their mechanical properties are very anisotropic. Therefore, the development of foliations underlined by phyllosilicates lower the strength of faults (Wintsch et al. 1995; Buatier et al. 2012).
- Pressure of fluids: an increase in fluid pressure can cause a great decrease in the effective normal stress, and thus reduce the frictional behavior, required for further shear failure (Sibson 1977) (fig. 1.6). For a given stress field, high pore-fluid pressure increases the range of fault orientations that can be reactivated, and therefore, can even induce the reactivation of misorientated faults (Sibson & Scott 1998). Pore fluids can also reduce the cohesion of the material by wetting mineral grains.



**Figure 1.6.** The increase in fluid pressure ( $P_f$ ) produces a decrease in  $\sigma_1$  and  $\sigma_3$  and, in consequence, in the effective normal stress. This fact can produce the reactivation of pre-existing faults.

### 1.3.4. Pressure-temperature-age estimates in fault zones

Quantification of parameters such as time, pressure and temperature is required for a complete study of fault evolution.

In ancient fault zones, **time** constraints are difficult to achieve because subsequent reactivations can lead to the replacement of previous minerals and to the resetting of their isotopic composition. Moreover to apply radiometric dating, suitable minerals have to be present, meaning synkinematic or hydrothermal minerals with the necessary geochemistry for the dating methods. Some of the most common methods are K-Ar, Rb-Sr and Ar-Ar dating in neoformed illites (Tritlla & Solé 1999; Siebel et al. 2009; Mutlu et al. 2010; Duvall et al. 2011), Sm-Nd dating in fluorite (Piqué et al. 2008) and (U-Th)/He dating in fluorites and apatites (Siebel et al. 2009). For calcites, absolute dating is challenging. U-Th dating is only suitable for Quaternary samples and it has been applied in speleothems for paleoclimatic purposes (Causse et al. 2004; Hoffmann et al. 2009). Some works have also used U-Pb dating. The main problem with these techniques is the U content of calcites. If the content is low (few ppb), the amount of sample required to obtain a good precision is too large.

**Temperature and pressure** conditions are commonly obtained from fluid inclusion data from minerals precipitated within fractures (Berwouts et al. 2008; Breesch et al. 2009; Onasch et al. 2009). This technique is valid if fluid inclusions have not suffered re-equilibration, factor that depends on the strength of the host mineral, the presence of twins and the size of the fluid inclusion. Calcite is a soft and twinned mineral, easy to deform during subsequent tectonic activity. This fact often generates problems when obtaining temperatures due to stretching (Bodnar 2003).

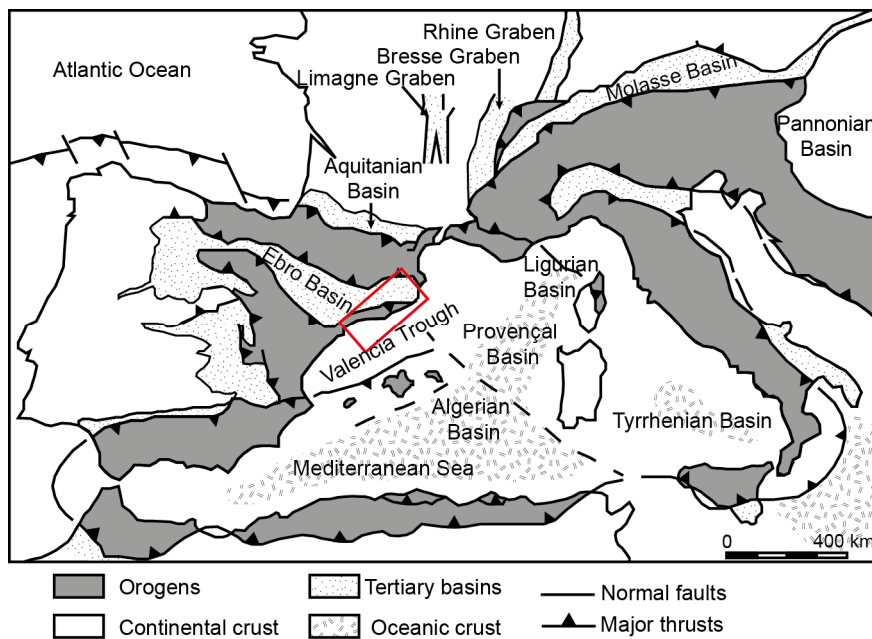
Another way to determine temperature and pressure conditions is by means of thermodynamic modeling. These methods require minerals with composition sensitive to pressure or temperature conditions (i.e. K-white mica and chlorite) (Cathelineau & Nieva 1985; Cathelineau 1988; Vidal et al. 2001, 2005, 2006; Dubacq et al. 2010).

In this work, main neoformed minerals are calcite and subordinated chlorite and K-white mica. Due to the small size of veins and crystals radiometric methods could not be applied. Neither fluid inclusions within calcites were found. However, thanks to the chlorite-K-white mica association thermodynamic modeling was applied to estimate P-T conditions during fault evolution.



## 2. GEOLOGICAL SETTING

The northwestern Mediterranean is composed by a system of Oligocene-early Miocene extensional basins, as the Valencia Trough and the Provençal and Ligurian basins. The opening of the Valencia Trough is related to the southwestward propagation of the Western European rift system (Rhine, Bresse and Limagne grabens) and the Burdigalian oceanic accretion associated with the counterclockwise rotation of the Corsica-Sardinia block from the European margin to its current position (Cherchi & Montadert 1982; Roca et al. 1999). This study is focused on the Catalan Coastal Ranges (CCR), in the NE of Spain, which constitute the northwestern margin of the Valencia Trough. The Catalan Coastal Ranges separate the thin continental crust of this trough from the thickened crust of the Iberian Peninsula (fig. 2.1). In the Ligurian and Provençal basins, among others, oceanic crust is even formed due to extension (Roca et al. 1999; Faccena et al. 2001).



**Figure 2.1.** Schematic map of the northwestern Mediterranean showing the main tectonic features (tertiary basins, orogens and types of crust) (synthesized from Vergés & Sàbat 1999 and Lewis et al. 2000). The box indicates the location of the Catalan Coastal Ranges, which is enlarged in figure 2.2.

The Catalan Coastal Ranges display a well-developed horst and graben structure limited by NE-SW and NNE-SSW striking normal faults segmented by later NW-SE to NNW-SSE faults, acquired during the opening of the Valencia Trough (Roca & Guimera 1992; Gaspar-Escribano et al. 2004). The Neogene extensional structure is

superimposed on a Paleogene contractional structure which in its turn was the result of the inversion of major Mesozoic normal faults (Guimerà 1984; Bartrina et al. 1992; Roca 1996; Vergés & García-Senz 2001). Moreover, previously to these tectonic events, Hercynian deformation and late-Hercynian processes also took place as recorded by the outcropping Paleozoic rocks studied in this thesis.

### **2.1. Tectonic phases affecting the Catalan Coastal Ranges**

#### **2.1.1. The Hercynian deformation**

The European Hercynian belt resulted from the oblique convergence and collision among two supercontinents, Gondwana to the south and Laurentia-Baltica to the north, and small microplates as Avalonia and Armorica at the end of the Paleozoic (Matte 2001). This belt is sinuous and spread from the Iberian Peninsula to northeastern Bohemia (Dias & Ribeiro 1995). It has a strong curvature at the SW of Europe known as the Ibero-Armorican Arc (Matte 2001). The Catalan Coastal Ranges belong to the northern limb of this arc (Julivert & Durán 1990a).

First order structures have an NW-SE trend. Two main deformation phases have been described during the Hercynian deformation of the Catalan Coastal Ranges (Julivert & Durán 1990a). The first phase is the most important and took place during the Upper Carboniferous. It is dominated by tight folds with a southwestern vergence and thrusts facing to the frontal part of the belt associated with a pervasive regional foliation that roughly trends NW-SE and dips to the NE. The second phase is characterised by open and upright folds and related crenulation cleavage. Most Paleozoic rocks are affected by regional metamorphism under low-grade conditions (greenschists facies), but high-grade metamorphism (amphibolites facies) also occur in small areas in the lowest stratigraphic levels.

After deformation, plutonic and hypabyssal rocks (named as late-Hercynian rocks), mainly acidic and intermediate in composition, intruded the previously described Paleozoic sequence and generated contact metamorphism (Enrique 1990). This emplacement was produced in a shallow brittle environment through the action of passive mechanisms such as stoping or cauldron subsidence (Serra & Enrique 1989).

### **2.1.2. The Mesozoic deformation**

The extensional process that took place during the Mesozoic is related to the opening of the western Tethys and of the North Atlantic (Salas & Casas 1993; Rossi et al. 2001). Two rift and two related post-rift stages have been described (Salas et al. 2001). The first rift stage (Late Permian-Early Jurassic) was related to the westward propagation of the Tethys and southward propagation of the Arctic-North Atlantic rift. This event was followed by an Early to Middle Jurassic post-rift stage characterised by thermal subsidence. The second rift stage (Late Jurassic-Early Cretaceous) was the result of the gradual opening of both the North Atlantic Basin and the Bay of Biscay. A later stage of thermal subsidence was produced during the Late Cretaceous post-rift (late Albian-Maastrichtian). The faults limiting the grabens formed during this period had a NE-SW and NW-SE orientation (Calvet et al. 1990) and generated a crustal thinning along the Valencia trough about 1.6-1.7 (35-40%) (Roca & Guimerà 1992; Roca 1996).

### **2.1.3. The Paleogene deformation**

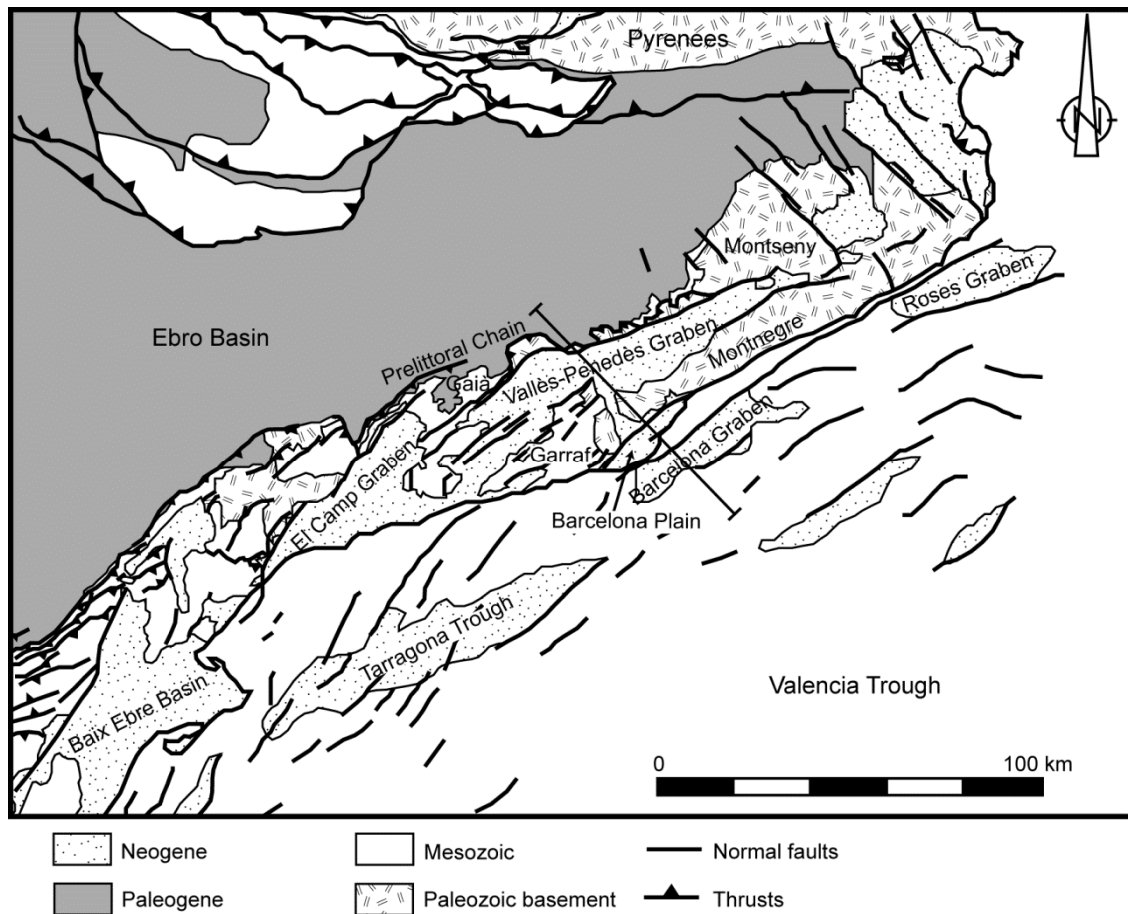
During the Late Cretaceous-early Oligocene, the N-S convergence between the Iberian and European plates produced the partial subduction of the Iberian plate underneath the European plate and the formation of the Pyrenees (Séguret 1972; ECORS team 1988; Muñoz 1992, 2002; Vergés 1993). In the Catalan Coastal Ranges, this compressional phase occurred between the middle Eocene and late Oligocene (Anadón et al. 1985) and generated the Catalan Intraplate Chain (Guimerà 1984; Bartrina et al. 1992). The Catalan Intraplate Chain was created by ENE-WSW to NE-SW thick-skinned thrusts, which had a certain left-lateral component (Ashauer & Teichmüller 1935; Anadón et al. 1985; Roca 1996). A maximum shortening of 4-6 km in a NW-SE direction occurred (Roca 1996; Lewis et al. 2000). These thrusts uplifted about 1500 m the hangingwalls and their erosion produced thick syntectonic successions in the Ebro foreland basin and the Barcelona piggy-back basin (Cabrera et al. 2004; Gaspar-Escribano et al. 2004).

### **2.1.4. The Neogene deformation and current configuration**

The normal faults that produced the Neogene horst and graben structure are listric faults striking NE-SW and NNE-SSW with a detachment level at 12-16 km (Roca & Guimerà 1992; Gaspar-Escribano et al. 2004). They generated a crustal thinning about 1.4-1.5 (30-35%), similar to the one produced during the Mesozoic (Roca & Guimerà 1992;

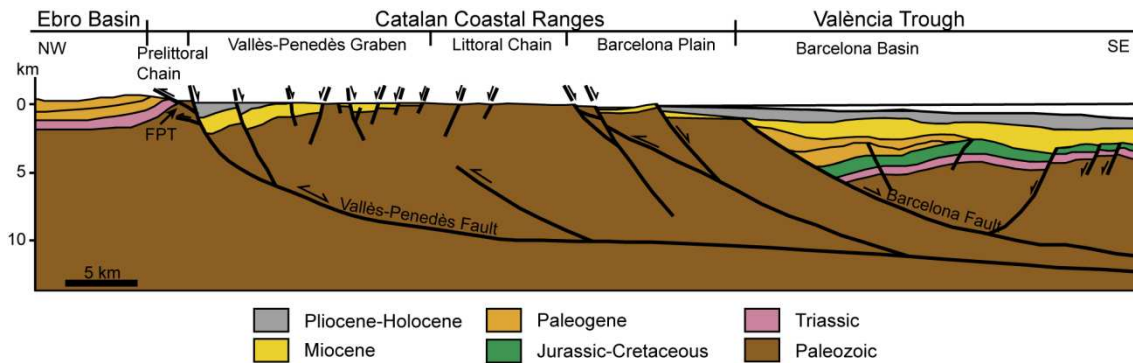
Roca 1996). This is related to a total minimum extension of 15.5 km produced by 10.8 km of extension in the Barcelona fault and 4.7 km in the Vallès-Penedès fault (Gaspar-Escribano et al. 2004). The tectonic evolution of the area during the Neogene extension is divided into a syn-rift stage (late Oligocene-late Burdigalian), an early post-rift stage (late Burdigalian-Langhian) and a late post-rift stage (Serravalian to Present) (Calvet et al. 1996). Two small compressional stages are recognised in the Neogene extension: one between the late Langhian-Serravalian (early post-rift) and the other during the Messinian (late post-rift) (Gaspar-Escribano et al. 2004).

The grabens of the central part of the Catalan Coastal Ranges are represented by the Vallès-Penedès graben, the Barcelona Plain and the Barcelona graben and the horsts are represented by the Littoral Chain (Garraf, Collserola and Montnegre Horsts) and the Prelittoral Chain (fig. 2.2 and 2.3).



**Figure 2.2.** Onshore and offshore Neogene basins of the Catalan Coastal Ranges (Bartrina et al. 1992 and Cabrera et al. 2004). The cross-section is shown in figure 2.3.

The two studied basins are the Barcelona Plain and the Vallès graben, both located in the central Catalan Coastal Ranges (fig. 2.2 and 2.3). The Barcelona Plain is a 40 km long and 2-10 km wide basin that is mainly filled by Miocene continental-transitional siliciclastic deposits and Quaternary fluvio-deltaic deposits. The Vallès graben is up to 65 km long and from 3 to 15 km wide and it is filled by more than 3000 m of sediment next to the fault (Cabrera 1981; Bartrina et al. 1992; Roca et al. 1999). The horsts are mainly formed by a Paleozoic basement and a Mesozoic cover.



**Figure 2.3.** Cross-section of the Catalan Coastal Ranges and the Valencia Trough marked in figure 2.2. FPT: Frontal Paleogene Thrust (Santanach et al. 2011).

## 2.2. Stratigraphy of the Catalan Coastal Ranges

The Paleozoic stratigraphic sequence is divided into a pre-Carboniferous sequence (pre-orogenic) and a Carboniferous sequence (syn-orogenic), which are separated by an unconformity (Julivert & Durán 1990b). The stratigraphic sequence from base to top is composed of (Julivert & Durán 1990b): 1) Pre-Cambrian and Ordovician rocks: pelites with interlayered fine-grained sandstones, acid tuffites, limestones, diabases and calcsilicate rocks. 2) Silurian rocks: black shales or slates with abundant graptolite fauna that have interlayered thin quartzite beds and sulphide layers. 3) Upper Silurian to Devonian rocks: massive nodular limestone with crinoids (La Creu Formation) and limestones, nodular marls and varicoloured marls and shales (Olorda Formation). 4) Carboniferous rocks: black chert with phosphate nodules, carbonate/shale horizon and a thick terrigenous sequence (Culm facies).

In the study areas, although Triassic, Jurassic and Cretaceous units were deposited, Jurassic and Cretaceous rocks have been eroded. Therefore only the Triassic units are described.



The Triassic units, from base to top, are: Buntsandstein, Muschelkalk, Keuper and Imón Formation. The Buntsandstein unit (Upper Permian? to lower Anisian) consists of red conglomerates, sandstones and lutites of fluvial origin, which have a thickness from 145 to 310 m. The sedimentation of this unit was controlled by fault activity (Calvet & Marzo 1994). The Muschelkalk is divided into three subunits. The Lower Muschelkalk (Anisian) is mainly composed of carbonatic facies and varies its thickness from 70 to 120 m from NE to SW. Its lower boundary is gradual with the lutites of the upper Buntsandstein whereas its upper boundary with the Middle Muschelkalk is abrupt. In its turn, the Lower Muschelkalk is divided into four units that from base to top are (Ramon & Calvet 1987): El Brull laminated limestones and dolostones, Olesa bioclastic limestones, Vilella Baixa bioturbated limestones and Colldejou white dolostones. The Middle Muschelkalk (upper Anisian to lower Nadinian) is constituted by red sandstones and lutites (Calvet & Marzo 1994). It ranges from 50 to 115 m in thickness and is subdivided into four units: Fontpineda lutites and gypsum, Bosc de Guanta sandstones and lutites, L'Arbolí lutites and gypsum and Riera de Sant Jaume lutites. Mostly these units represent supralittoral plains, playa-lake or terminal alluvial fan deposits. Finally, the Upper Muschelkalk (Ladinian) is formed by carbonatic facies deposited on a ramp-type platform that range from 100 m in the north to 140 m in the south (Tucker & Marshall 2004). It has been subdivided in several units that vary according to its location along the Catalan Coastal Ranges. In the central area (Gaià-Montseny domain), five units have been distinguished from base to top (Calvet et al. 1987): Rojals oolitic limestones and dolostones; Benifallet dolostones and bioturbated limestones, Collbató bioclastic limestones, Querol stromatolites, and Capafonts marly dolostones, marls and breccias. The Keuper (Carnian-Norian) is formed by alternations of lutites with carbonates and gypsum levels, with thickness oscillating between 100 and 150 m (Calvet & Marzo 1994). The Imón Formation (Rhaetian?) is constituted by well-stratified dolostones from 30 to 40 m (Arnal et al. 2002; Tucker & Marshall 2004).

The Oligocene rocks of the Barcelona basin crop out in the locality of Montgat and have been studied in detail by Parcerisa (2002). They consist of two lithostratigraphic units of Chattian age separated by a NW-SE thrust: the Pla de la Concòrdia Unit and the Turó de Montgat Unit. The first unit is formed by lacustrine sediments, calcretes, sandstones and conglomerates with carbonatic clasts and registers the transition from colluvial to distal alluvial environments. The latter unit is formed by massive siliciclastic conglomerates,

sandstones and clays and records a colluvial sedimentation followed by middle-distal alluvial deposits.

The grabens formed during the Neogene extension are filled with rocks from late Oligocene to Present. In the central Catalan Coastal Ranges, three depositional complexes have been identified (Cabrera & Calvet 1996). The Lower Continental Complexes (Aquitanian-late Burdigalian) consist of alluvial fans deposited at the foot of the active faults bounding the grabens in the NW and in the SE. In the distal areas lacustrine facies were deposited. The Transitional-Marine Complexes (late Burdigalian to late Langhian) are made of terrigenous shallow bay successions, evaporitic coastal sabkha sequences, fan delta deposits and carbonate and mixed terrigenous-carbonate platforms. These complexes were produced by the transgressions of marine waters through the south of the basins and during highstand sea levels. The Upper Continental Complexes (Langhian to Tortonian) are constituted by alluvial fan deposits only fed from the northern boundary of the basins. The Messinian is represented by a regional erosive surface produced by a sea level drop that affected the underlying deposits.

### **2.3. Hydrothermalism**

The Catalan Coastal Ranges are characterised by the presence of abundant hot water springs that can reach up to 70°C. The water origin of these springs are meteoric fluids that have been topographically-driven through the fractured rocks (Carmona et al. 2000; Bitzer et al. 2001). They usually occur at the intersection between the NW-SE to NNW-SSE faults and the main fault system bounding the grabens (Fernández & Banda 1989). Most of these springs are preferably located in the igneous basement, which constitutes the footwall of the main fault system, as occurs in Caldes de Montbui, La Garriga and Caldes d'Estrac (Albert et al. 1979).

Hydrothermalism has occurred at different periods during the evolution of the Catalan Coastal Ranges. At least, two hydrothermal events have been proposed from the study of fault-controlled barite-fluorite-sulphur veins (Canals et al. 1997): one during the Mesozoic (at least Jurassic) and the other during the Neogene (lower Miocene) (Cardellach et al. 2002).

### 2.4. Tectonothermal evolution

The tectonothermal evolution of the Catalan Coastal Ranges has been studied from fission-track and (U-Th)/He analyses in zircons and apatites of the basement granodiorite (Juez-Larré 2003). These plutons suffered exhumation during the Permian as it is marked by the unconformity with the overlying Buntsandstein facies. During the Mesozoic, zircon fission-tracks (ZFT) and apatite fission-tracks (AFT) ages reveal peak temperatures up to the apatite and zircon partial annealing zone (PAZ) (60-110°C and 175-300°C, respectively), contemporaneous to the two rift Mesozoic phases. These temperatures have been mainly related to sedimentary burial and magmatic and hydrothermal activity. Regional geothermal gradient has been settled around 27-35°C/km (Juez-Larré 2003). During the Paleogene, exhumation and erosion up to 800 m took place, producing cooling. At that time, the Catalan Intraplate Chain was formed, achieving heights between 1200 and 1700 m. The calculated geothermal gradient is 15°C/km (Juez-Larré 2003). The current configuration in horsts and grabens is the result of tectonic subsidence, flexural uplift, erosion and sedimentation processes. Flexural uplift and erosion have been estimated in 700-1200 m and 1900-2500 m, respectively, yielding to elevations about 300-800 m (Gaspar-Escribano et al. 2004). Although this exhumation and erosion produced basement cooling, some samples, mostly next to the graben boundary, show temperatures up to the apatite PAZ, probably due to fluid convection (ter Voorde et al. 2007). The regional geothermal gradient was about  $24\pm3^\circ\text{C}/\text{km}$  during this period (Juez-Larré 2003).

Taking into account the values estimated for subsidence, uplift and erosion, samples cropping out nowadays in the Catalan Coastal Ranges were buried at 3.6 and 2.5 km depths in the Prelittoral and Littoral Chains, respectively, previous to the Paleogene compression and 2.2 km previous to the Neogene extension (Juez-Larré 2003; ter Voorde et al. 2007).

### **3. METHODOLOGY**

In this chapter is explained the methodology and the techniques used to accomplish the proposed objectives. The work has included field work, laboratory work and office work.

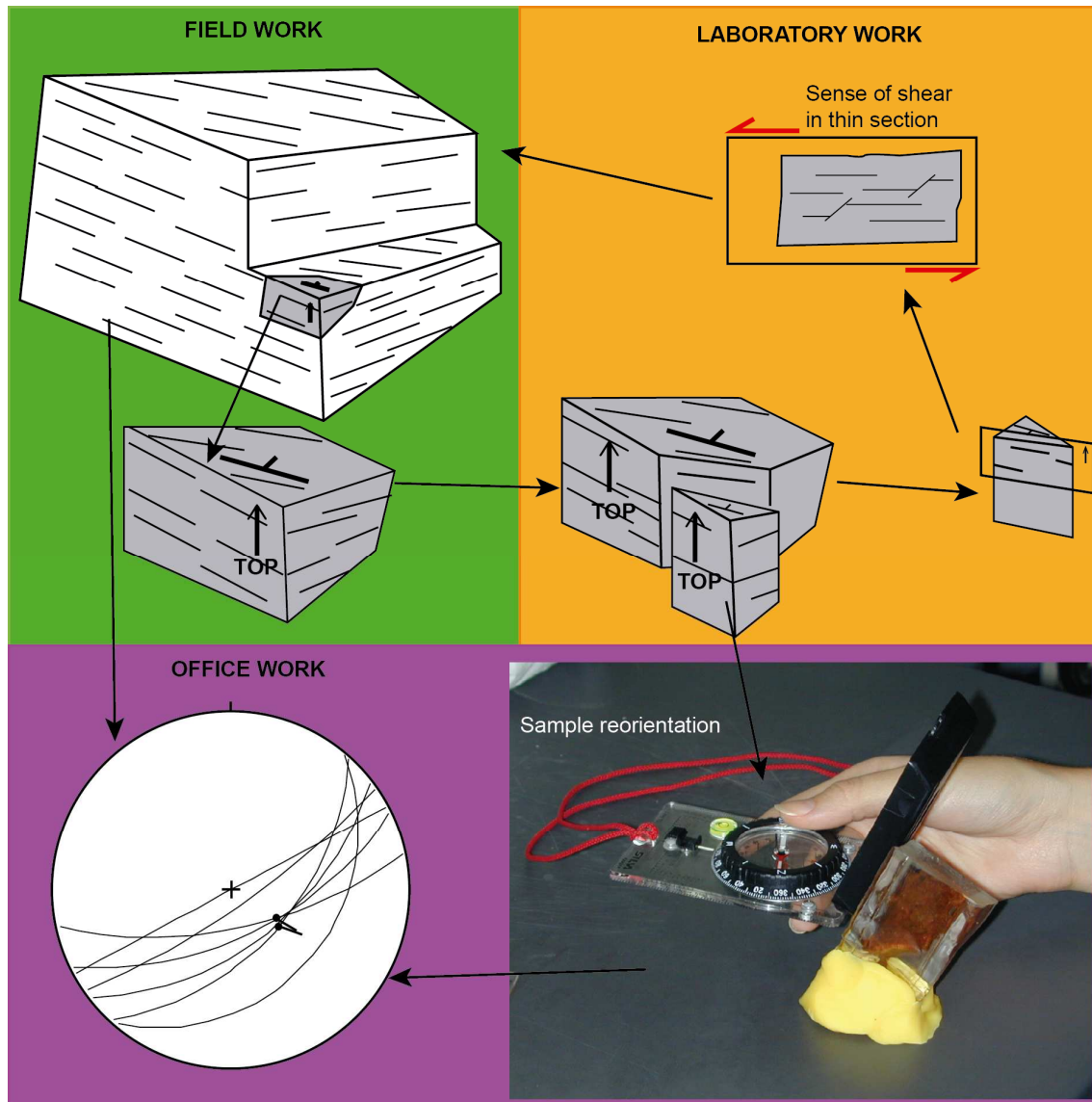
#### **3.1. Field work**

Nine outcrops were chosen because of their structural location and the outcropping rocks. In the north of the Barcelona Plain (in the area between Santa Coloma de Gramanet, Badalona and Montgat), the Hospital fault can be followed for about 6 km leading to the selection of five outcrops. Two more outcrops were selected in the fault hangingwall. On the opposite, the Vallès fault rarely crops out as it is covered by farm fields and do not generate a fault scarp. This fact has caused the study of two outcrops located between Setmenat and Caldes de Montbui. In each outcrop, schematic cartographies and cross-sections have been done in order to provide a geological framework for this study. Structural data of fractures, slickenlines and bedding were measured. After that, representative veins, fault rocks and host rocks were sampled. Before sampling, samples were carefully oriented in the field marking dip and strike of a planar surface of the specimen on that surface (fig. 3.1).

#### **3.2. Laboratory work**

To perform the petrologic and geochemical study, 128 thin sections were prepared. Due to the incohesive character and fragility of most of the samples, previously to their sawing, samples were impregnated in a non-saturated polyester resin to consolidate them. After that, samples were sawn parallel (p) and perpendicular (n) to fault slip to document variations in textures, microstructures and compositions of the fault rock. When carbonates were a component of the sample, thin sections were partially stained with alizarin and potassium ferricyanide to distinguish the different carbonatic minerals, as calcite gets red, ferroan calcite purple, dolomite remains unstained and ferroan dolomite gets blue (Dickson 1966).

The petrographic study was done under the optical microscope. A detailed mapping of the thin sections was done. This mapping gives information about the crosscutting relationships of the several fault rocks and fractures, kinematic indicators, preferential



**Figure 3.1.** Method to obtain an oriented sample from an outcrop (green area) and an oriented thin section from a sample (orange area) (modified from Passchier & Trouw 1996). Observe that sample is oriented parallel to striations. If a sample is oriented it is possible to extrapolate the sense of shear identified in the thin section to the outcrop scale. In this figure it is also shown how to re-orientate a sample in the office in order to measure minor structures that later will be plotted together with field data.

orientations and mineralogy. Calcite and dolomite cements and carbonate host rocks were further studied under a cathodoluminescence microscope. This technique has allowed to distinguish different generations of carbonate cements. A Technosyn Cold Cathodoluminescence Model 8200 MkII operating at 16-19 kV and 350  $\mu$ A gun current was used.

To complement the petrologic observations, especially in micron-sized materials, some carbon-coated thin sections and gold-coated chips were examined under ESEM Quanta 200 FEI, XTE 325/D8395 scanning electronic microscope. Scanning electronic

microscope coupled with cathodoluminescence was applied in the study of cataclasites in granodiorites and pseudotachylytes.

To obtain the qualitative characterization of the minerals in fault and host rocks, X-ray diffraction was done. Analyses were done in a diffractometer of geometry Bragg-Brentano PAnalytical X'Pert PRO MPD alpha 1, which uses a radiation  $K_{\alpha 1}\text{Cu}$  of 1.5406 Å operating at 45 kV and 40 mA. Whole-rock powders were scanned from 4 to  $100^{\circ}2\theta$  with a  $0.017^{\circ}2\theta$  step size and a count time of 50 s per step. Also oriented aggregates were used for clay fraction determination. The separation of this fraction was done through suspension methods. From each sample three diffractograms were obtained: a normal one, a diffractogram after a thermal treatment (2 hours at 550°C) and another one after the saturation of the sample in an atmosphere of ethylene glycol during 24 hours at 50°C. Oriented aggregates were scanned from 2 to  $62^{\circ}2\theta$  (normal sample) and 2 to  $30^{\circ}2\theta$  (ethylene glycol and thermal treatment samples) with a  $0.033^{\circ}2\theta$  step size and a count time of 50 s per step. Identification of mineral phases was done with the X'pert HighScore Plus software.

The elemental composition of carbonate cements and host rocks, chlorite, mica and feldspars was obtained from carbon-coated thin sections with a CAMECA model SX-50 electron microprobe. It operated at 15 nA of current intensity and 20 kV of excitation potential and a beam diameter of 10 µm. The detection limits for carbonates are 99 ppm for Na, 312 ppm for Ca, 436 ppm for Mg, 149 ppm for Fe, 107 ppm for Mn and 124 ppm for Sr whereas for silicates are 428 ppm for Na, 275 ppm for Mg, 272 ppm for Al, 288 ppm for Si, 263 ppm for K, 260 ppm for Ca, 290 ppm for Ti, 672 ppm for Mn, 647 ppm for Fe. The precision of major elements is about 0.64% (at  $2\sigma$  level).

Samples for carbon and oxygen stable isotopes analyses of carbonate host rocks and cements were powered with a microdrill. The  $\text{CO}_2$  extraction was done in a Carbonate Kiel Device III attached to a Thermal Ionization Mass Spectrometer Thermo Electron (Finnigan) MAT-252 following the method of McCrea (1950). Samples ( $60 \pm 10 \mu\text{g}$ ) were reacted with 100% phosphoric acid at  $70^{\circ}\text{C}$  during 3 minutes for calcite and 15 minutes for dolomite. The International Standard NBS-19 was used as reference. The results are expressed in ‰ PDB standard (VPDB). Standard deviation is  $\pm 0.02\text{‰}$  for  $\delta^{13}\text{C}$  and  $\pm 0.05\text{‰}$  for  $\delta^{18}\text{O}$ .

Finally, 16 samples of a black shale material in fault zones, Ordovician phyllites and shales and granodiorite have been analyzed by X-Ray Fluorescence (FRX) in order to discern the origin of the black shale material. Major elements were measured in fused samples with a Panalytical PW 2400 spectrophotometer, using a Rh anode. Fused samples were prepared with 0.3 g of molten and dry sample mixed with 5.7 g of lithium tetraborate and 5 mg of lithium iodide. The mixture was homogenized and fused at 1125°C obtaining pearls of 30 mm of diameter. Minor elements were measured in pressed pellets using a Philips PW 2400 spectrophotometer with an excitation source of Rh. Pellets were prepared in an agate mortar with 5 g of molten and dry sample and 2 ml of 20% solution of Elvacite 2044 dissolved with acetone. Pellets have a diameter of 40 mm and are made with an aluminum capsule, in which the treated sample and boric acid are added. The capsule is compacted with a Herzog press that applies 200 kN during 60 s.

All these analyses have been performed in the Serveis Científic-Tècnics of the Universitat de Barcelona.

### **3.3 Office work**

At the office, samples were again reoriented according to the measure taken in the field to check and obtain the orientation of minor fractures not seen in the field (fig. 3.1). This step leads to relate micro and macro structures or to define new ones. Structural data has been plotted in lower hemisphere Schmidt stereoplots to represent the different identified fracture families (fig. 3.1).

The petrological and geochemical analyses allowed to identify the different fault-related cement generations. The integration between cements and the crosscutting relationships between them and other microstructures allowed to characterize the successive fluid-fault systems.

To estimate the P-T conditions during fault evolution, thermobarometric methods from the analyses of the elemental composition of the chlorite and K-white mica have been applied. Their temperature and pressure of formation have been calculated applying thermodynamic models based on the equilibrium between these minerals, quartz and water. Chlorite and K-white mica minerals are good candidates as thermobarometers because they present many chemical substitutions (simple and coupled) controlled by

the equilibrium conditions (P, T, pH,  $fO_2$ ...) that can be modelled using a set of different end-members (Vidal et al. 2001, 2005, 2006; Parra et al. 2002; Dubacq et al. 2010). Three main substitutions occur in chlorite (FeMg<sub>-1</sub>, Tschermak and di/trioctahedral substitutions) that can be modelled using the following set of five end-members (e.g. Vidal et al. 2005) (table 3.1): Mg-amesite (Si<sub>2</sub>Al<sub>4</sub>Mg<sub>4</sub>O<sub>10</sub>(OH)<sub>8</sub>), Fe-amesite (Si<sub>2</sub>Al<sub>4</sub>Fe<sub>4</sub>O<sub>10</sub>(OH)<sub>8</sub>), daphnite (Si<sub>3</sub>Al<sub>2</sub>Fe<sub>5</sub>O<sub>10</sub>(OH)<sub>8</sub>), clinochlore (Si<sub>3</sub>Al<sub>2</sub>Mg<sub>5</sub>O<sub>10</sub>(OH)<sub>8</sub>), and sudoite (Si<sub>3</sub>Al<sub>4</sub>Mg<sub>2</sub>□<sub>1</sub>O<sub>10</sub>(OH)<sub>8</sub>), where □ represents vacancies. In K-white mica, three additional substitutions occur (NaK<sub>-1</sub>, V(H<sub>2</sub>O)<sub>-1</sub> and pyrophyllitic substitutions) and can be modelled using the following set of seven end-members (table 3.2): muscovite (Si<sub>3</sub>Al<sub>3</sub>□<sub>1</sub>K<sub>1</sub>O<sub>10</sub>(OH)<sub>2</sub>), Fe-celadonite (Si<sub>4</sub>Al<sub>1</sub>Fe<sub>1</sub>□<sub>1</sub>K<sub>1</sub>O<sub>10</sub>(OH)<sub>2</sub>), Mg-celadonite (Si<sub>4</sub>Al<sub>1</sub>Mg<sub>1</sub>□<sub>1</sub>K<sub>1</sub>O<sub>10</sub>(OH)<sub>2</sub>), phlogopite (Si<sub>3</sub>Al<sub>1</sub>Mg<sub>3</sub>K<sub>1</sub>O<sub>10</sub>(OH)<sub>2</sub>), pyrophyllite (Si<sub>4</sub>Al<sub>2</sub>□<sub>2</sub>O<sub>10</sub>(OH)<sub>2</sub>), pyrophyllite·1H<sub>2</sub>O (Si<sub>4</sub>Al<sub>2</sub>□<sub>1</sub>(H<sub>2</sub>O)<sub>1</sub>O<sub>10</sub>(OH)<sub>2</sub>), and paragonite (Si<sub>3</sub>Al<sub>3</sub>□<sub>1</sub>Na<sub>1</sub>O<sub>10</sub>(OH)<sub>2</sub>).

**Table 3.1.** Atom site distribution of chlorite

	T1	T2	M1	M23	M4
Mg-amesite	Si <sub>2</sub>	Al <sub>2</sub>	Al	Mg <sub>4</sub>	Al
Fe-amesite	Si <sub>2</sub>	Al <sub>2</sub>	Al	Fe <sub>4</sub>	Al
Clinochlore	Si <sub>2</sub>	Si, Al	Mg	Mg <sub>4</sub>	Al
Daphnite	Si <sub>2</sub>	Si, Al	Fe	Fe <sub>4</sub>	Al
Sudoite	Si <sub>2</sub>	Si, Al	V	Mg <sub>2</sub> , Al <sub>2</sub>	Al

T: tetrahedral position  
M: octahedral position  
V: vacancies

**Table 3.2.** Atom site distribution of mica

	T1	T2	M1	M23	A
Pyrophyllite	Si <sub>2</sub>	Si <sub>2</sub>	V	Al <sub>2</sub>	V
Muscovite	Si <sub>2</sub>	Si, Al	V	Al <sub>2</sub>	K
Celadonite	Si <sub>2</sub>	Si <sub>2</sub>	V	Al, Mg	K
Paragonite	Si <sub>2</sub>	Si, Al	V	Al <sub>2</sub>	Na

T: tetrahedral position  
M: octahedral position  
A: interlayer position

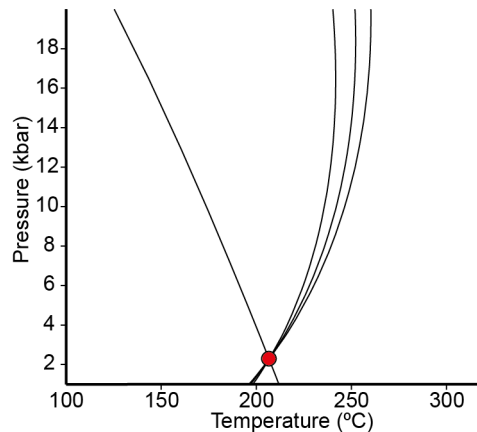


Three thermometers have been used. This study was performed in the Institut des Sciences de la Terre of the Université Joseph Fourier in Grenoble.

#### 3.3.1. Chlorite-quartz-water thermometer

Chlorite shows an increase in  $\text{Al}^{\text{IV}}$  and a decrease in vacancy contents with increasing temperature (e.g. Cathalineaue & Nieva 1985 and Vidal et al. 2001). The multi-equilibrium approach of Vidal et al. (2005, 2006) proposes a simultaneous estimate of  $\text{Fe}^{3+}$  content in chlorite and equilibrium temperature by the convergence of the following equilibria at a given pressure (fig.3.2):

- (1) 5 Mg-amesite + 4 daphnite  $\leftrightarrow$  4 clinochlore + 5 Fe-amesite
- (2) 2 clinochlore + 3 sudoite  $\leftrightarrow$  4 Mg-amesite + 7 quartz +  $4\text{H}_2\text{O}$
- (3) 16 daphnite + 15 sudoite  $\leftrightarrow$  6 clinochlore + 20 Fe-amesite + 35 quartz +  $20\text{H}_2\text{O}$
- (4) 4 daphnite + 6 sudoite  $\leftrightarrow$  3 Mg-amesite + 5 Fe-amesite + 14 quartz +  $8\text{H}_2\text{O}$



**Figure 3.2.** Estimation of P-T conditions of chlorite formation (red point) from equilibria convergence of reactions (1) to (4).

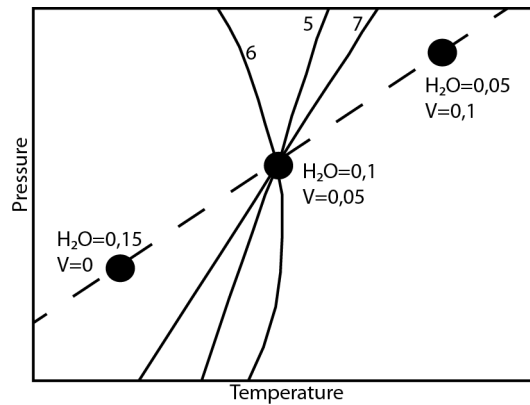
The positions of these equilibria, (1) to (4), depend on the thermodynamic standard state property for the different phases and thus the activities of the chlorite end-members, quartz and water. In this work, the temperature and  $\text{XFe}^{3+}$  of chlorite were estimated at 1 kbar, which is the maximum pressure according to the regional geology, and with water activity equal to 1. Following the Vidal et al. (2005, 2006) approach, the convergence is always produced with the minimum  $\text{Fe}^{3+}$  proportion and it was considered to be achieved when the temperature difference between the four equilibria was less than  $30^\circ\text{C}$ .

### 3.3.2. Mica-quartz-water thermobarometer

K-white mica increases its Si content, by Tschermak substitution, with an increase of pressure (Massone & Schreyer 1989). At low temperature, the pyrophyllitic substitution also controls the Si and interlayer contents (e.g. Agard et al. 2001). The mica-quartz-water thermobarometer used in this study models the variation of composition with respect to temperature and pressure, taking into account mica hydration of vacancies (Dubacq et al. 2010). For a mica in chemical equilibrium with quartz and water, these three equilibria can be written:

- (5)  $3 \text{ celadonite} + 2 \text{ pyrophyllite} \leftrightarrow 2 \text{ muscovite} + \text{biotite} + 11 \text{ quartz} + 2\text{H}_2\text{O}$
- (6)  $3 \text{ celadonite} + 2 \text{ pyrophyllite} \cdot 1\text{H}_2\text{O} \leftrightarrow 2 \text{ muscovite} + \text{biotite} + 11 \text{ quartz} + 3\text{H}_2\text{O}$
- (7)  $\text{pyrophyllite} \cdot 1\text{H}_2\text{O} \leftrightarrow \text{pyrophyllite} + \text{H}_2\text{O}$

The convergence of these equilibria at various P-T conditions is achieved by varying the  $\text{XH}_2\text{O}_{\text{interlayer}}$  content (i.e. pyrophyllite·1H<sub>2</sub>O proportion). A mica-quartz-H<sub>2</sub>O equilibrium line is then drawn, along which the hydration state varies (Dubacq et al. 2010) (fig. 3.3). The pressure conditions were then estimated at the temperature estimated from the chlorite-quartz-water equilibria (Lanari et al. 2012).

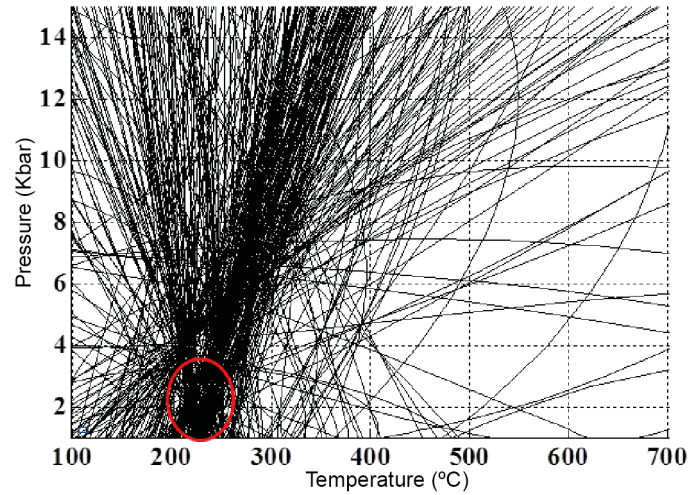


**Figure 3.3.** Construction of the P-T line (dashed line) by varying the H<sub>2</sub>O content of vacancies in reactions (5) to (7). V: vacancy.

### 3.3.3. Chlorite-mica-quartz-water multi-equilibrium approach

After the application of the previous thermometer and barometer, the equilibrium of chlorite and K-white mica was checked through a full chlorite-mica multi-equilibrium approach involving  $\text{XFe}^{3+}$  in both chlorite and mica and  $\text{XH}_2\text{O}_{\text{interlayer}}$  in mica. P-T equilibrium conditions of chlorite-mica-quartz-water assemblage were calculated from the convergence of 159 equilibria written from the previous mentioned chlorite and

mica end-members (fig. 3.4). Only those equilibria showing a good convergence were selected, for which the sum of the Gibbs free energy of a selected set of reactions ( $\Delta rG$ ) of the calculated P and T was less than 7000 J.



**Figure 3.4.** Convergence of 159 equilibria to obtain the P-T equilibrium conditions of a mica-chlorite pair. Red circle marks the convergence area.

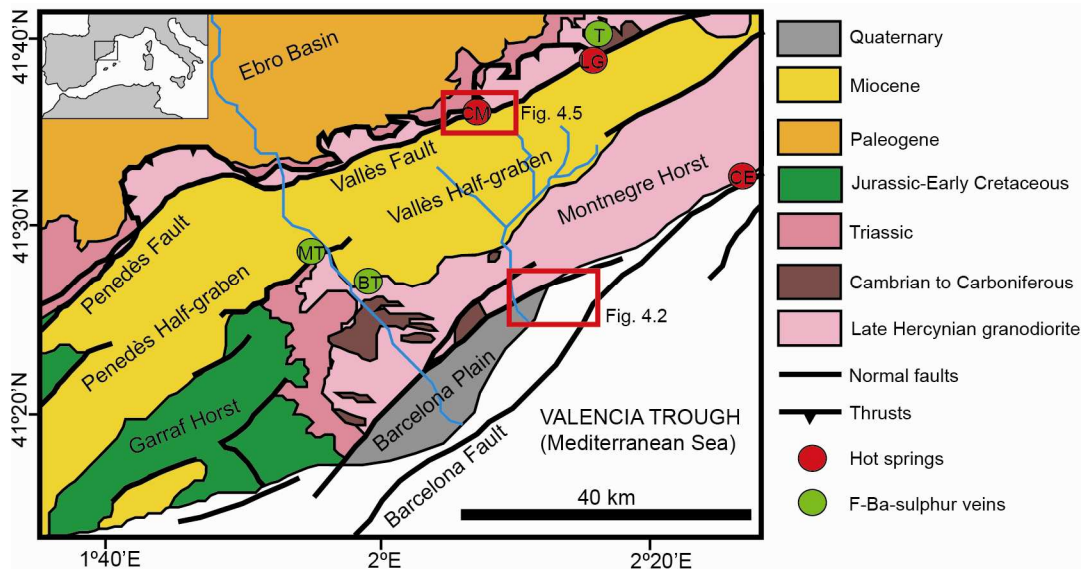
In order to give an age for each fluid-fault system, we have compared our data (elemental composition, isotopes, formation temperatures and pressures) with other works performed in the central Catalan Coastal Ranges (Travé et al. 2001, 2009; Cardellach et al. 2002; Parcerisa 2002; Juez-Larré 2003; Baqués et al. 2010, 2012a,b).

The integration of all the results has lead to the writing of this memory and the papers within it.

## 4. RESULTS

### 4.1. Studied domains

The faults bounding the Barcelona Plain and the Vallès Half-graben (fig. 4.1) have been studied from a petrological, geochemical and structural point of view in order to establish the successive deformation phases, fluid origin, fluid regimes, fluid pathways and P-T conditions during fault evolution.



**Figure 4.1.** Simplified geological map of the central Catalan Coastal Ranges (modified from Santanach et al. 2011). Squares indicate the location of the study areas. T: Tagamanent; MT: Martorell; BT: Berta Mine; CM: Caldes de Montbui; LG: La Garriga; CE: Caldes d'Estrac.

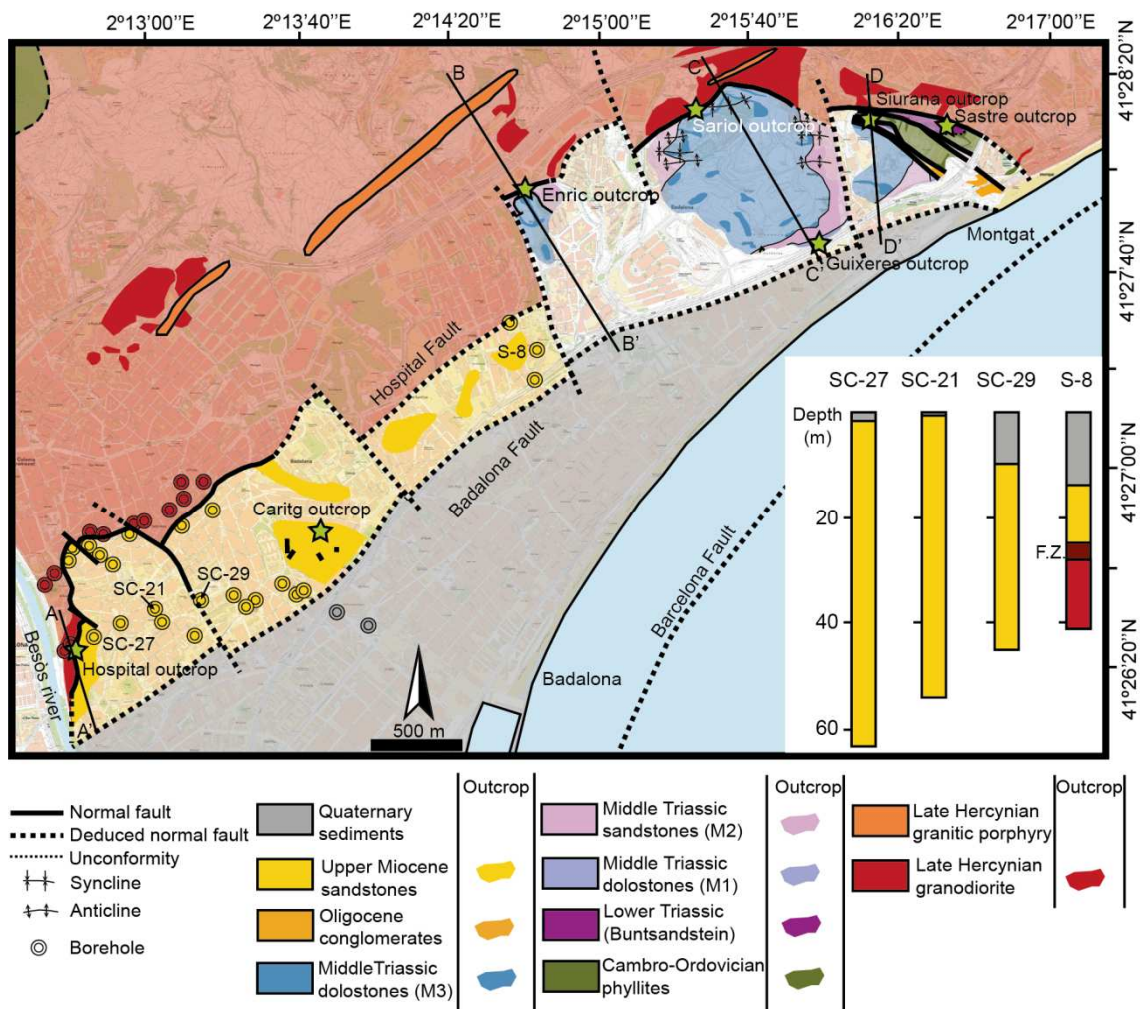
#### 4.1.1. The Barcelona Plain

The Barcelona Plain is a highly urbanised area, and therefore, with a lack of good and extense outcrops. However, the study of the relationship between deformation and fluid flow through faults is important in these highly populated areas specially when underground tunnels have to be done. We have focused the study of the Barcelona Plain on its northeastern sector, between the cities of Sta. Coloma de Gramanet, Badalona and Montgat. In this area, different outcrops formed by different lithologies and with a broad range of ages (from Ordovician to recent) affected by faults have been chosen. The Barcelona Plain is bounded in the northwest by the Hospital fault.

The **Hospital fault** is a NE-SW fault zone with increasing dip towards the northeast from 29 to 63°SE that separates the late Hercynian granodiorite (footwall) from the

#### 4. Results

Miocene rocks in the south and from the Triassic rocks in the north (hangingwall) (fig. 4.2 and 4.3), and shows in its northern ending a splay pattern. It had a minimum normal displacement of 1-2 km, estimated from the fault dip (30-50°SE) and the thickness of the absent rocks from the contact aureole (about 800 m). The Hospital fault is cut and displaced in segments, from 200-1500 m long, by NW-SE faults. Five outcrops have been studied along the Hospital fault. The Hospital, Enric and Sariol outcrops have been studied from a structural, petrological and geochemical point of view whereas the Siurana and Sastre outcrops, located in the splay area have been analysed from a structural point of view.



**Figure 4.2.** Schematic geological map of the northeastern sector of the Barcelona Plain with outcrops location. Cross-sections are shown in figure 4.3.

The **Miocene hangingwall** is constituted by conglomerates of the Upper Continental Complexes which are affected by minor faults (fig. 4.4). The thickness of the Miocene units, controlled by borehole correlation, decreases towards the northeast (fig. 4.2). Due to the high urbanization of the area and the low topographic relief, these rocks are



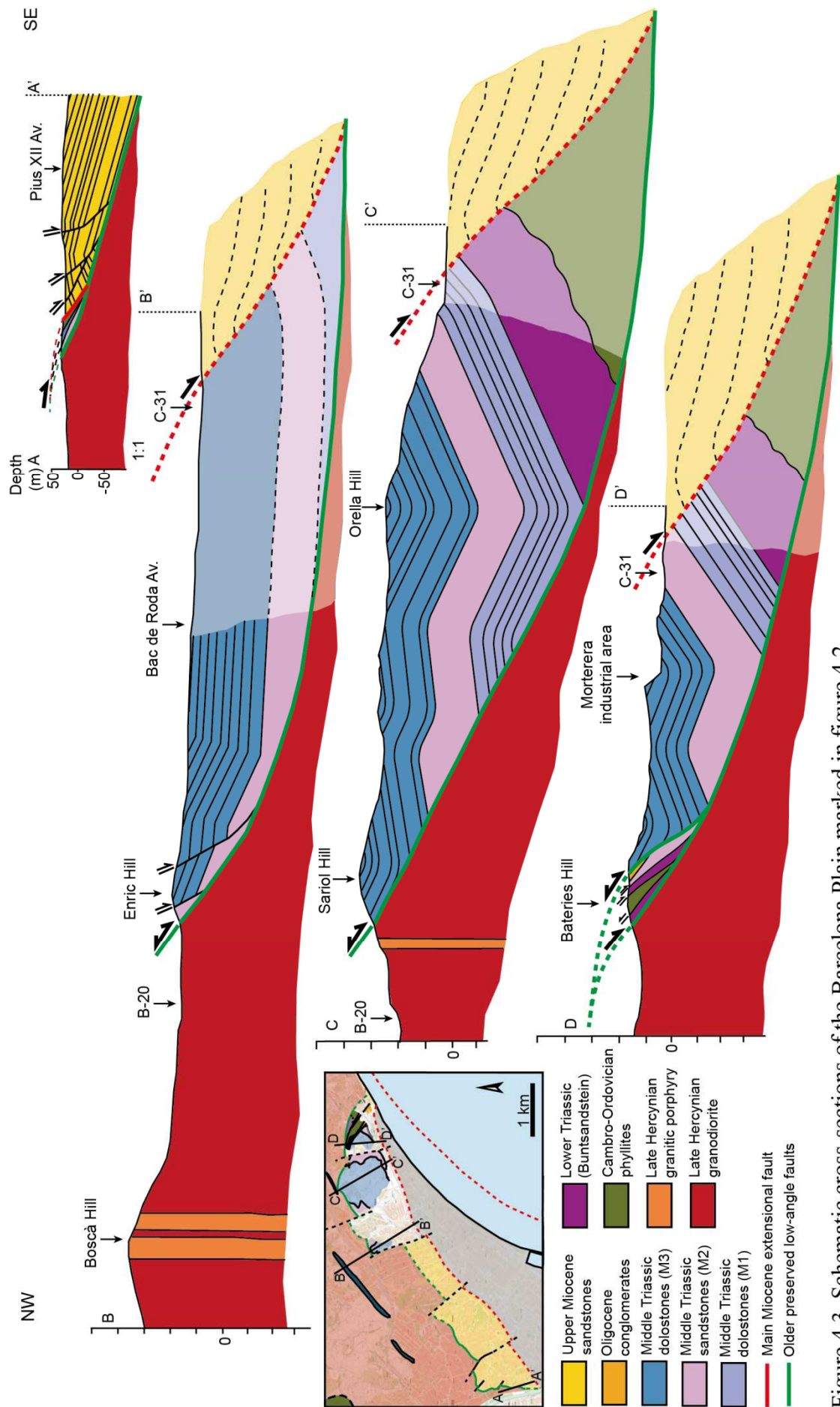
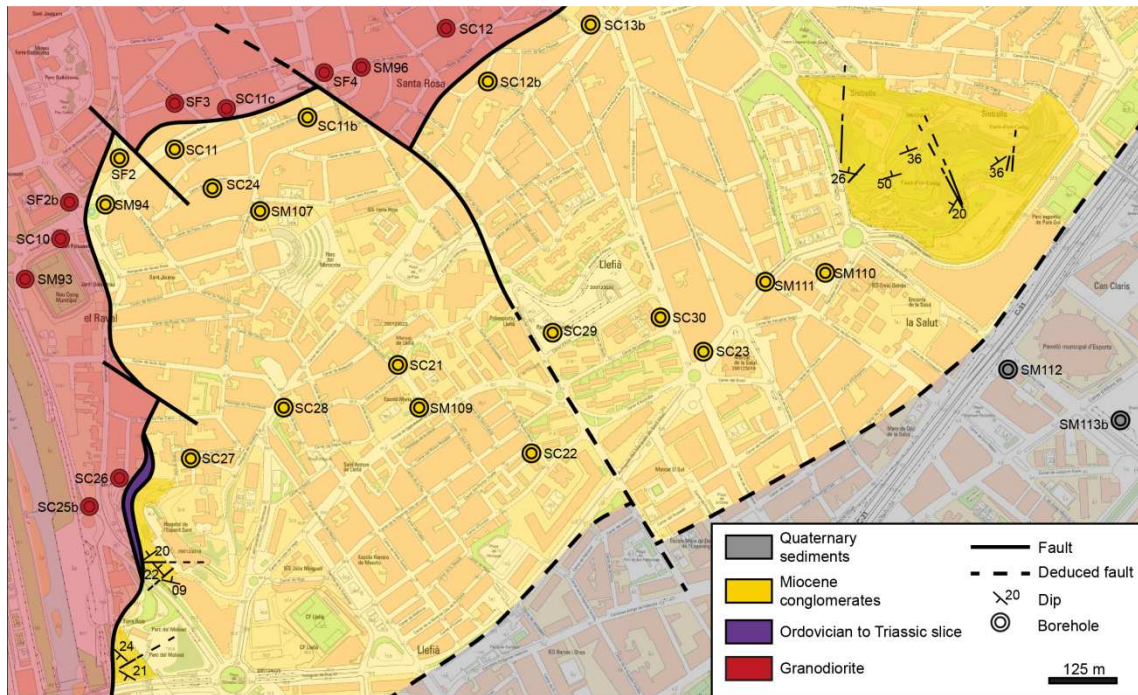


Figure 4.3. Schematic cross-sections of the Barcelona Plain marked in figure 4.2.



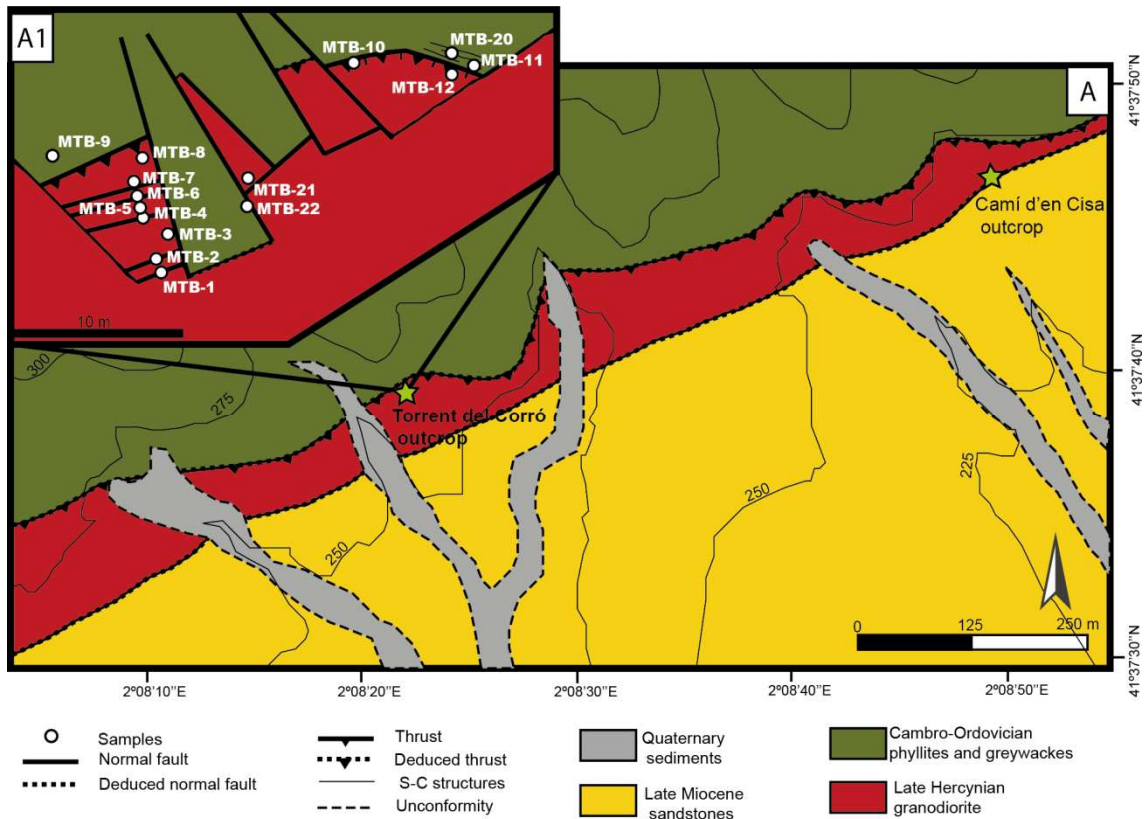
**Figure 4.4.** Schematic map of the southern area of the Miocene hangingwall where main outcrops are located.

barely exposed (fig. 4.4). Two outcrops have been studied, the Caritg and the Hospital outcrops.

The **Triassic hanginwall** is mainly constituted by Muschelkalk facies M1, M2 and M3. Locally, Buntsandstein facies also crop out. Faults affecting M1 facies have been studied in the Guixeres outcrop, M3 facies in the Enric outcrop and Buntsandstein facies in the Sastre outcrop.

### 4.1.2. The Vallès Half-graben

Tha Vallès Half-graben is bounded to the north by the Vallès-Penedès fault, a major NE-SW normal fault that juxtaposes the late Hercynian granodiorite against the Miocene deposits that fill the basin. This basement fault had a normal displacement up to 4 km during the Neogene extension (Roca et al. 1999). The study is centred on the neighbouring of Caldes de Montbui. Two outcrops have been studied (fig. 4.5). The Torrent del Corró outcrop (TCO) is located in the granodioritic footwall at 50 m from the Neogene main fault plane. The Camí d'en Cisa outcrop (CCO), 600 m to the northeast from the previous outcrop, is the contact between the granodiorite and the Miocene rocks.




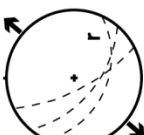
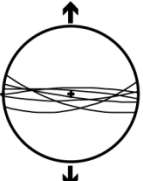

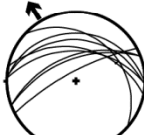

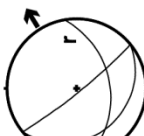

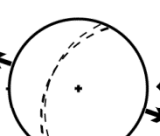
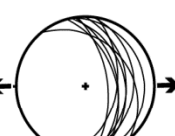
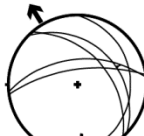


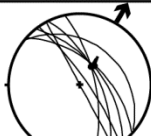
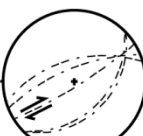

**Figure 4.5.** Schematic geological map of the studied area in the Vallès Half-graben. A) Location of the two studied outcrops, the Torrent del Corró in the granodioritic footwall and the Camí d'en Cisa outcrop in the contact between the granodiorite and the Miocene. A1) Sketch with sample location of the Torrent del Corró outcrop.

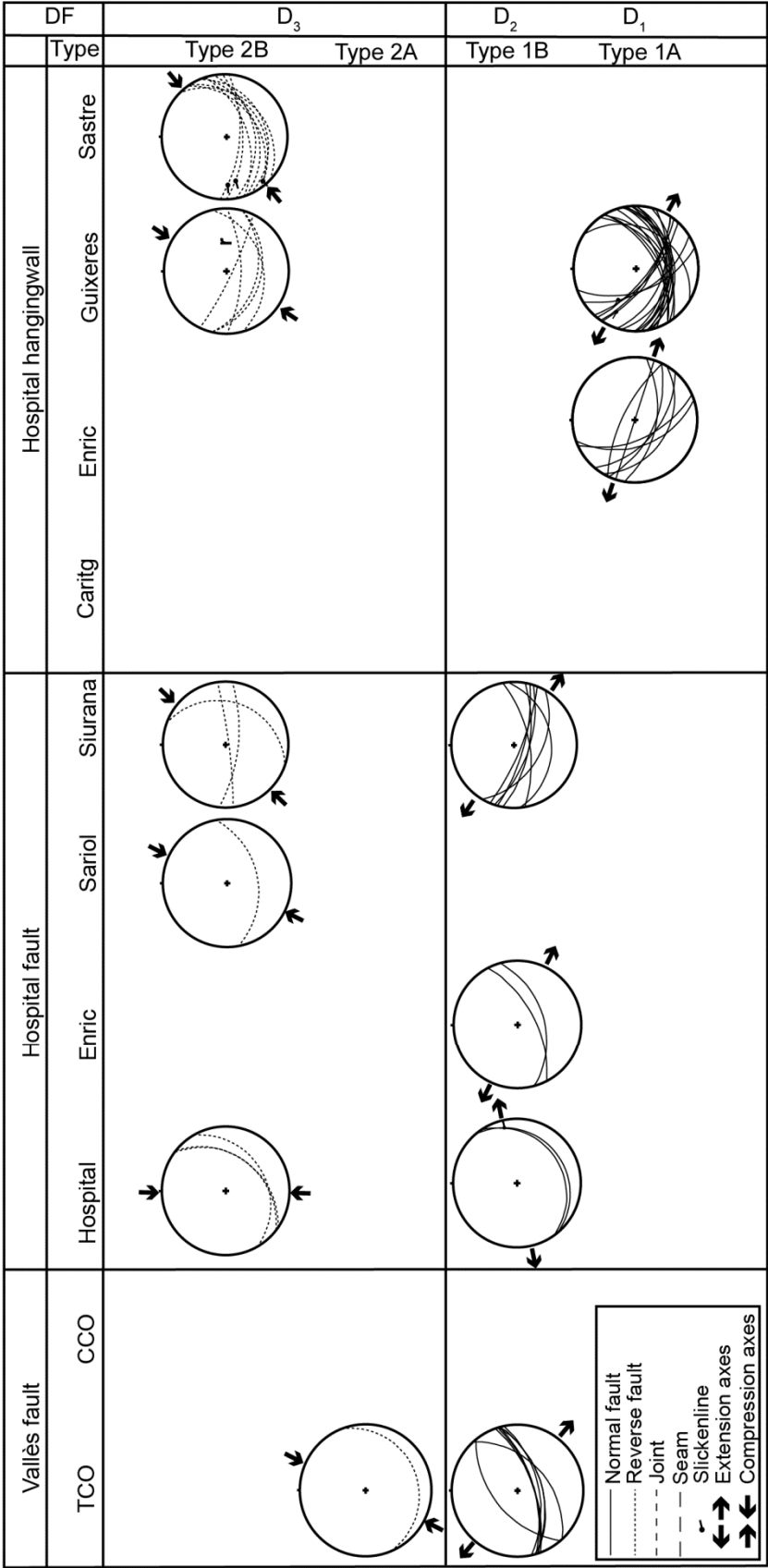
## 4.2. Deformation phases

Ten fracture families (or types) have been recognized from structural data acquired in the field and from reoriented hand samples and thin sections. The criteria to differentiate families has been the crosscutting relationships between fractures but the presence of conjugated systems and minor structures related to a main fault were also taken into account. In some cases, the geochemistry of cements was used in a later stage to separate phases. In turn, the ten families have been encompassed within seven deformation phases in function of the stress conditions (fig. 4.6).

The **first deformation phase (D<sub>1</sub>)** is characterized by type 1A faults resulting from extensional axes with a WNW-ESE direction. These faults are NE-SW normal faults with dip around 49°SE and NW-SE normal faults with a certain right-lateral component with dip from 60 to 90° to the SW and NE. This kind of faults has been uniquely recognized in the Triassic hangingwall.



DF	Type	D <sub>7</sub>	D <sub>6</sub>		D <sub>5</sub>	D <sub>4</sub>	
		Type 3F	Type 3E	Type 3D	Type 3C	Type 3B	Type 3A
Hospital hangingwall	Sastre						
	Guixeres						
	Enric						
	Caritg						
Hospital fault	Siurana						
	Sariol						
	Enric						
	Hospital						
Vallès fault	CCO						
	TCO						



**Figure 4.6.** Stereoplots of the structural data of all the studied outcrops. Horizontal divisions will be explained in the discussion section. DF: deformation phase; Type are the families of fractures.

The **second deformation phase (D<sub>2</sub>)** is characterized by extensional axes with orientation from WSW-ENE to NW-SE. It is represented by type 1B faults, which are normal faults with NE-SW trending and dip between 24 and 67° to the SE. In the Hospital outcrop, slickenlines with 14/076 orientation indicate a certain left-lateral motion during normal faulting. Although 1B faults have the same orientation than type 1A faults, the petrologic and geochemical study of their fault rocks and cements has demonstrated their different timing.

The **third deformation phase (D<sub>3</sub>)** is characterized by N-S to NE-SW compressional axes. Two types of fractures have been identified: type 2A faults in the Vallès half-graben and type 2B faults in the Barcelona Plain. Both types are NE-SW reverse faults with a certain left-lateral motion and dip from 22 to 44°SE. This faulting episode was the responsible of the formation of the NE-SW oriented folds in the Muschelkalk units outcropping in the Barcelona Plain. Minor faults of this group affecting Triassic rocks of the horst reactivate previous 1A faults.

The **fourth deformation phase (D<sub>4</sub>)** is characterized by NNW-SSE to NNE-SSW extensional axes. Two fracture families are encompassed within this deformation phase, type 3A and 3B. Type 3A normal faults show a NE-SW to E-W trend that mostly dip towards the southeast. This fracture family has been identified in all the domains. Some planes are the reactivation of type 1 and type 2 faults. Type 3B fractures are NW-SE joints with dip of 55°NE that have only been recognized within the Enric outcrop.

The **fifth deformation phase (D<sub>5</sub>)** is defined by NNW-SSE compressional axes that produce type 3C seams, which have NNE-SSW orientation and low dip to the NW. These seams have only been identified in the Hospital fault.

The **sixth deformation phase (D<sub>6</sub>)** is defined by NE-SW extensional axes and has been recognized in the Barcelona Plain. Type 3D and 3E fractures are englobed within this phase. Type 3D fractures are normal faults of mainly N-S direction dipping from 30 to 80°E and barely to the SW and NE-SW normal faults that are the reactivation of previous 3A and 2B faults. Type 3E fractures are open joints, up to 50 cm, of NW-SE trend and dip to the SW. They are the reactivation of type 1A faults.

The **seventh deformation phase (D<sub>7</sub>)** is represented by type 3F dextral strike-slip faults of NW-SE and dip between 50 to 65 ° to the northeast and southwest. In the Barcelona Plain, type 3F faults have been deduced by cartographical criteria.

### 4.3. Outcrop description

#### 4.3.1. Hospital outcrop

The Hospital fault in this segment acquires a N-S trace because of the topographic relief. It juxtaposes the Miocene conglomerates against the late Hercynian granodiorite, but in the tectonic contact, Triassic and Silurian rocks are sliced in between (fig. 4.7A-B). Deformation phases D<sub>2</sub>, D<sub>3</sub> and D<sub>6</sub> have been identified.

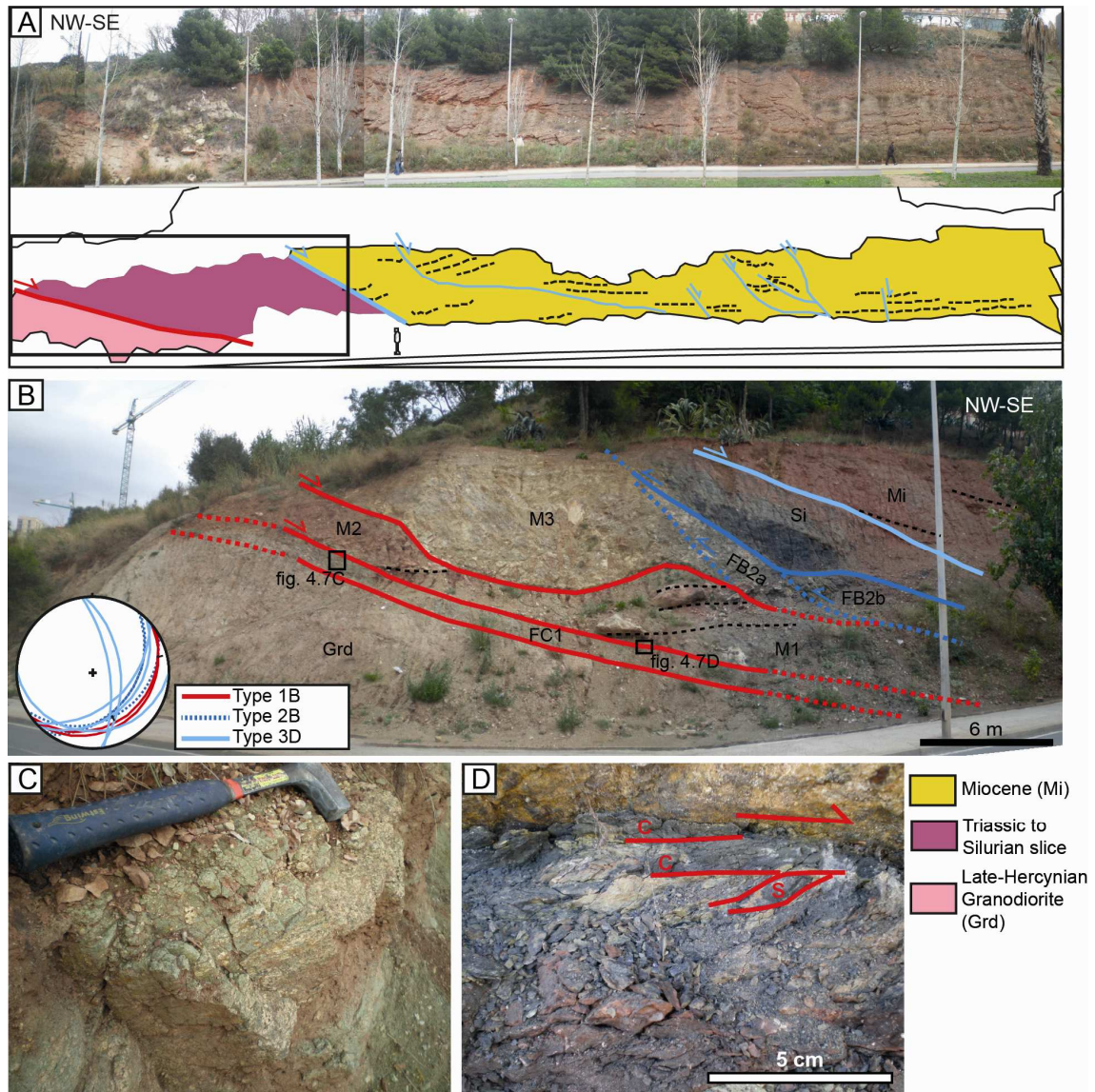
Deformation phase D<sub>2</sub> is represented by a type 1B normal fault that juxtaposes the Middle Triassic clays and sandstones against the late Hercynian granodiorite. This major normal fault has low dip (about 30°SE) and generates a core zone about 70 cm width (FC1) with well-defined sharp boundaries. The core is formed by 60 cm of a cataclastic green material and by 10 cm of a discontinuous foliated red and black clay gouge (fig. 4.7C-D).

Deformation phase D<sub>3</sub> is defined by type 2B reverse faults, which develop two decimetric-scale duplexes in the hangingwall that locates the Ordovician phyllites and Silurian black shales on top of the Middle Triassic dolostones (fig. 4.7B). Each duplex is constituted by different breccias. Breccia FB2a is constituted by dolomitic clasts from the Triassic unit M3 whereas breccia FB2b contains clasts of the Ordovician phyllites.

Finally, the deformation phase D<sub>6</sub> is shown by type 3D extensional faults. One major fault settles the Miocene in contact with the Silurian black shales. The Silurian acts as a detachment level and accommodates all the deformation. In the Miocene conglomerates minor type 3D normal faults produce decimetric displacements that tilt the bedding. These minor faults form discrete planes that do not develop fault cores and damage zones.

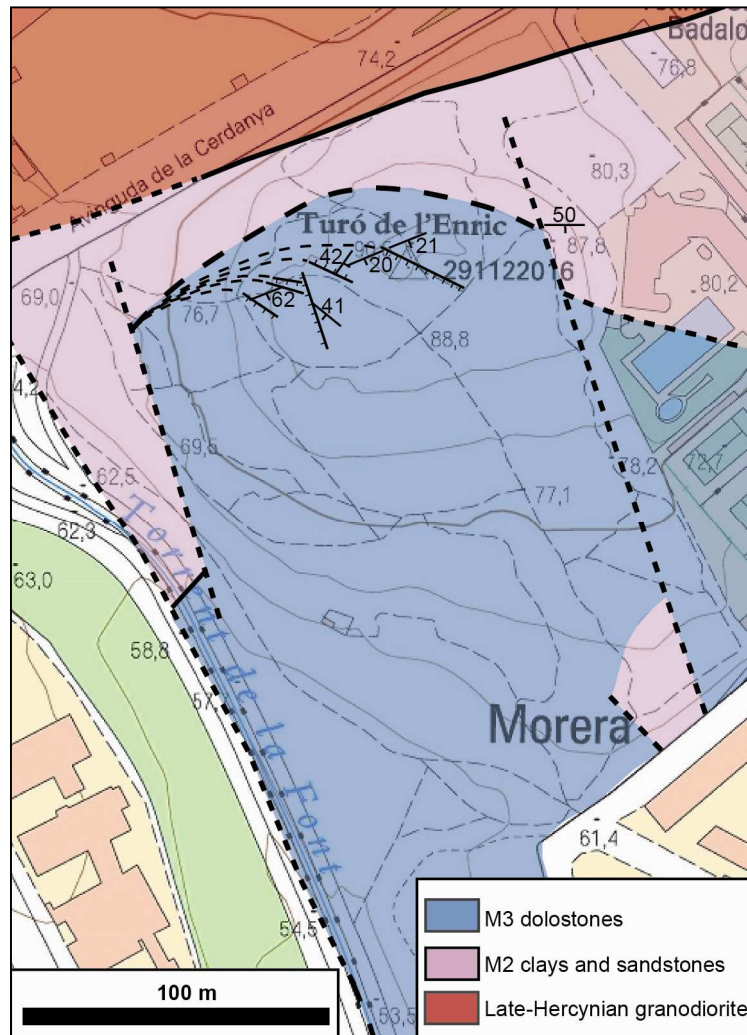
#### 4.3.2. Enric outcrop

The Enric outcrop have a very bad exposure due to the vegetation. The Hospital fault in this outcrop dips 55° towards the SE and places the Middle Triassic clays and sandstones (M2 facies) on the late Hercynian granodiorite (fig. 4.8). Fault zone



**Figure 4.7.** Hospital outcrop. A) General view of the Hospital outcrop and interpretation of the main features. The black square is enlarged in B. B) Tectonic contact between the granodiorite and the Miocene where Triassic, Ordovician and Silurian rocks are sliced inbetween. The three main fault families are plotted in the stereogram. C) Green cataclastic fault core generated in the type 1B fault. D) Foliated gouge with S-C structure formed also in the type 1B fault.

architecture is formed by a damage zone around 2 m thick with an irregular boundary with the granodiorite and a fault core 20 cm thick with sharp and well defined boundaries. The damage zone is formed by a dark green cohesive breccia resulting from deformation phases D<sub>2</sub>, D<sub>4</sub> and D<sub>5</sub>. The fault core is constituted by a greenish-yellow semicohesive gouge formed during D<sub>4</sub> (fig. 4.9). Both fault rocks resulted from the brittle deformation of the granodiorite.



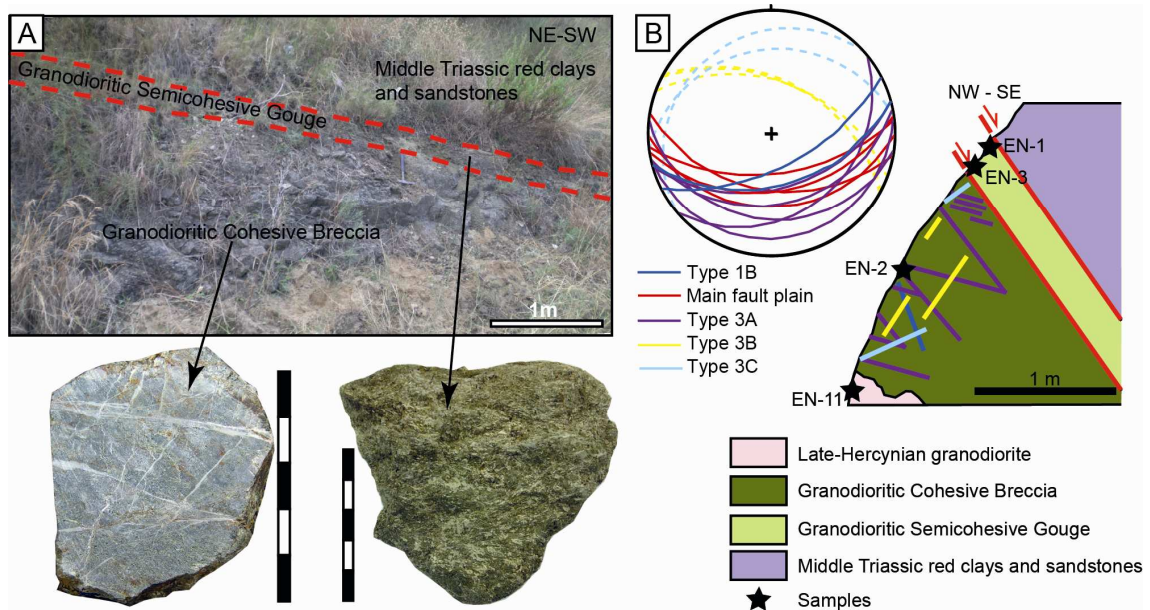
**Figure 4.8.** Schematic map of the Enric hill, where the Hospital fault places the Middle Triassic clays and sandstones (M2 facies) on the late Hercynian granodiorite. Within the Middle Triassic dolostones (M3 facies), a system of minor faults (type 1A) with a tail geometry is shown.

In the hangingwall, M3 dolostones are deformed during the first deformation phase D1. Type 1A normal faults with listric geometries have been recognized (fig. 4.10A). These faults generate fault cores from 1 to 30 cm wide filled by uncohesive breccias with an important percentage of a yellowish matrix (fig. 4.10B). The damage zone consists of joints and minor faults and is several meters wide. Cohesive breccias are also developed in the footwall. Some faults produce a drag in the bedding of their hangingwalls (fig. 4.10B).

#### 4.3.3. Sariol outcrop

The Hospital fault in this segment has a E-W strike, dips about 60°S and juxtaposes the Triassic dolostones of the M3 facies against the late Hercynian granodiorite. The fault





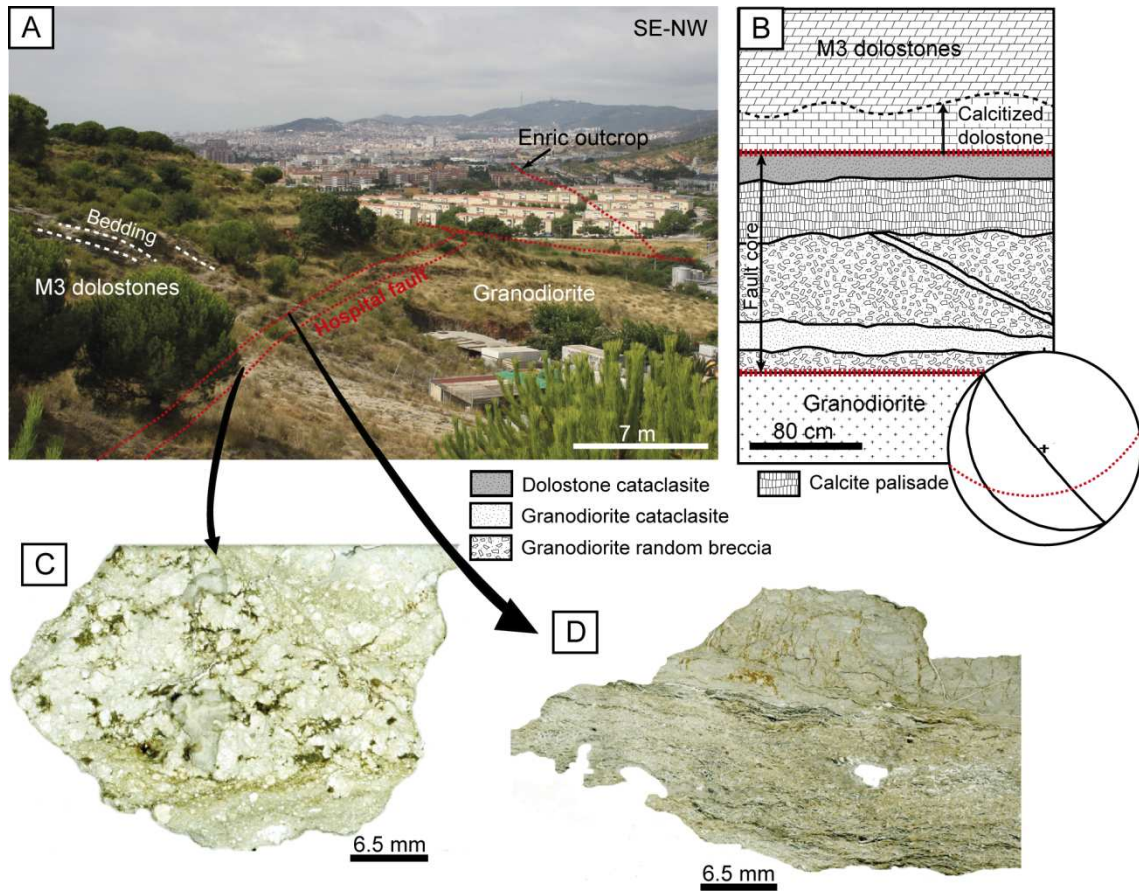
**Figure 4.9.** Enric outcrop. A) View of the poorly outcropping Hospital fault and hand samples of the main fault rocks. B) Synthetic cross-section of the Hospital fault at this point with the main fault rocks and the identified sets of fractures, which are also plotted in a stereogram. Although separated, type 3A faults are minor structures linked with the displacement of the main fault plane.



**Figure 4.10.** Enric outcrop. A) Type 1A listric normal faults affecting the M3 dolostones. B) View of the drag developed in the hangingwall in contact with the fault plane.

zone is not well exposed due to vegetation, antropic actions and the low slope of the hill. Apparently, damage zone is absent and, uniquely, a fault core, which thickness is around 1-3 m thick, is developed. This fault core is the result of fault activity during deformation phases D<sub>3</sub> and D<sub>6</sub>. The fault core is formed by white-greyey breccias and cataclasites resulting from the deformation of both the footwall and the hangingwall

(fig. 4.11). Also minor faults with NW-SE orientation and variable dip to the SW, which formed cataclasites during deformation phase D<sub>6</sub>, have been identified.



**Figure 4.11.** Sariol outcrop. A) View of the Hospital fault from the Sariol outcrop to the southwest. B) Synthetic sketch of the fault zone at the Sariol outcrop and stereonet of the sets of fractures. Red faults are type 2B faults reactivated during development of type 3D faults (in black). C) Thin section of fault rocks developed within the granodiorite. D) Thin section of fault rocks and cements developed within the dolostones.

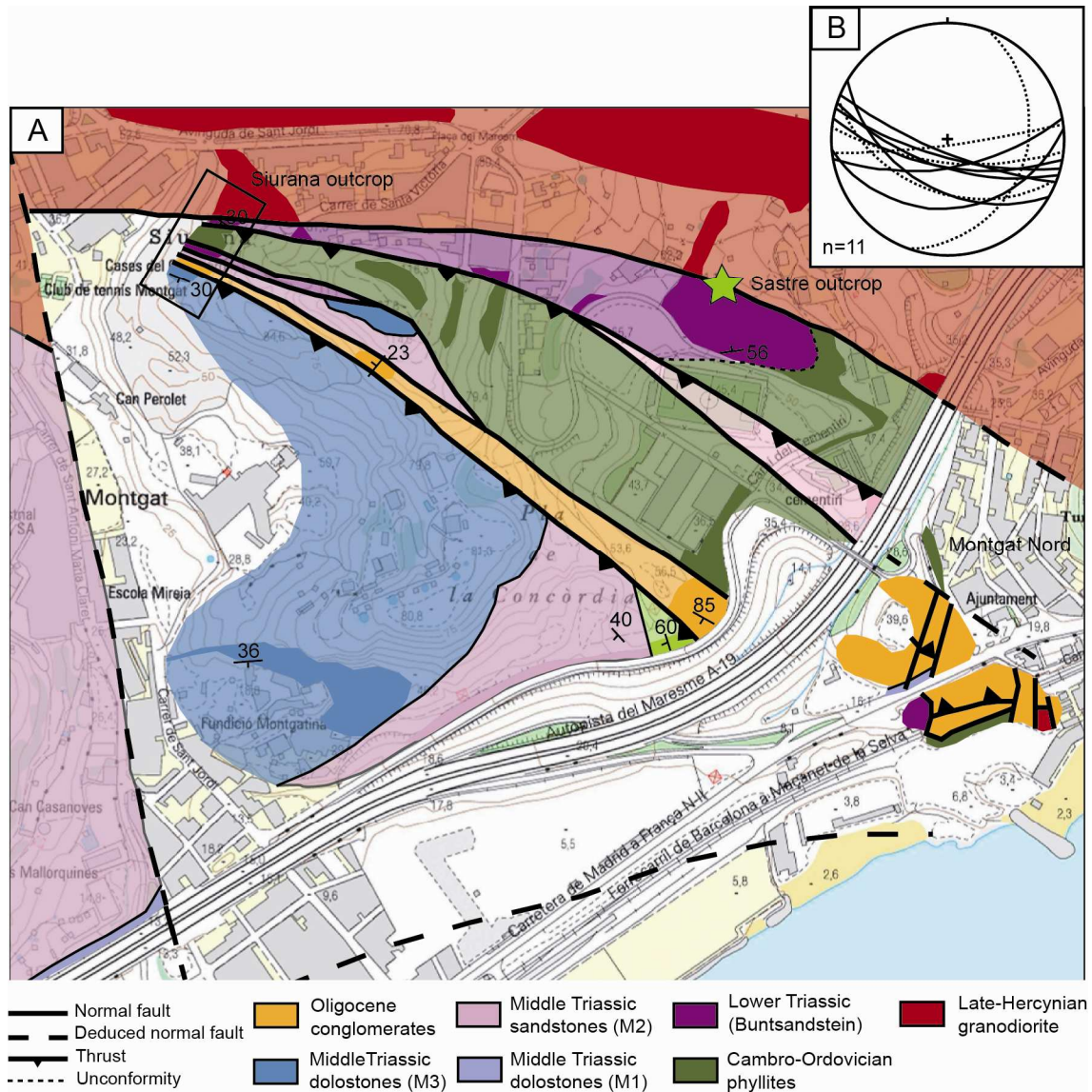
#### 4.3.4. Siurana outcrop

This outcrop is located at the beginning of the splay formation, at the northeastern ending of the Hospital fault (fig. 4.12). The outcrop consists in a steep trench dug out for the construction of a building. It shows a very complex zone due to the amalgamation of normal and reverse faults affecting rocks from Silurian to Oligocene ages in just a 150 m long outcrop (fig. 4.13A). These faults have a strike from E-W to NW-SE and have a high dip (fig. 4.12). From NNE to SSW, the following structures are found: 1) normal fault between the granodiorite and the Buntsandstein facies, 2) thrust of Ordovician and Silurian rocks over the Buntsandstein facies, 3) normal fault juxtaposing the Buntsandstein facies against the Ordovician and Silurian rocks, 4)



## 4. Results

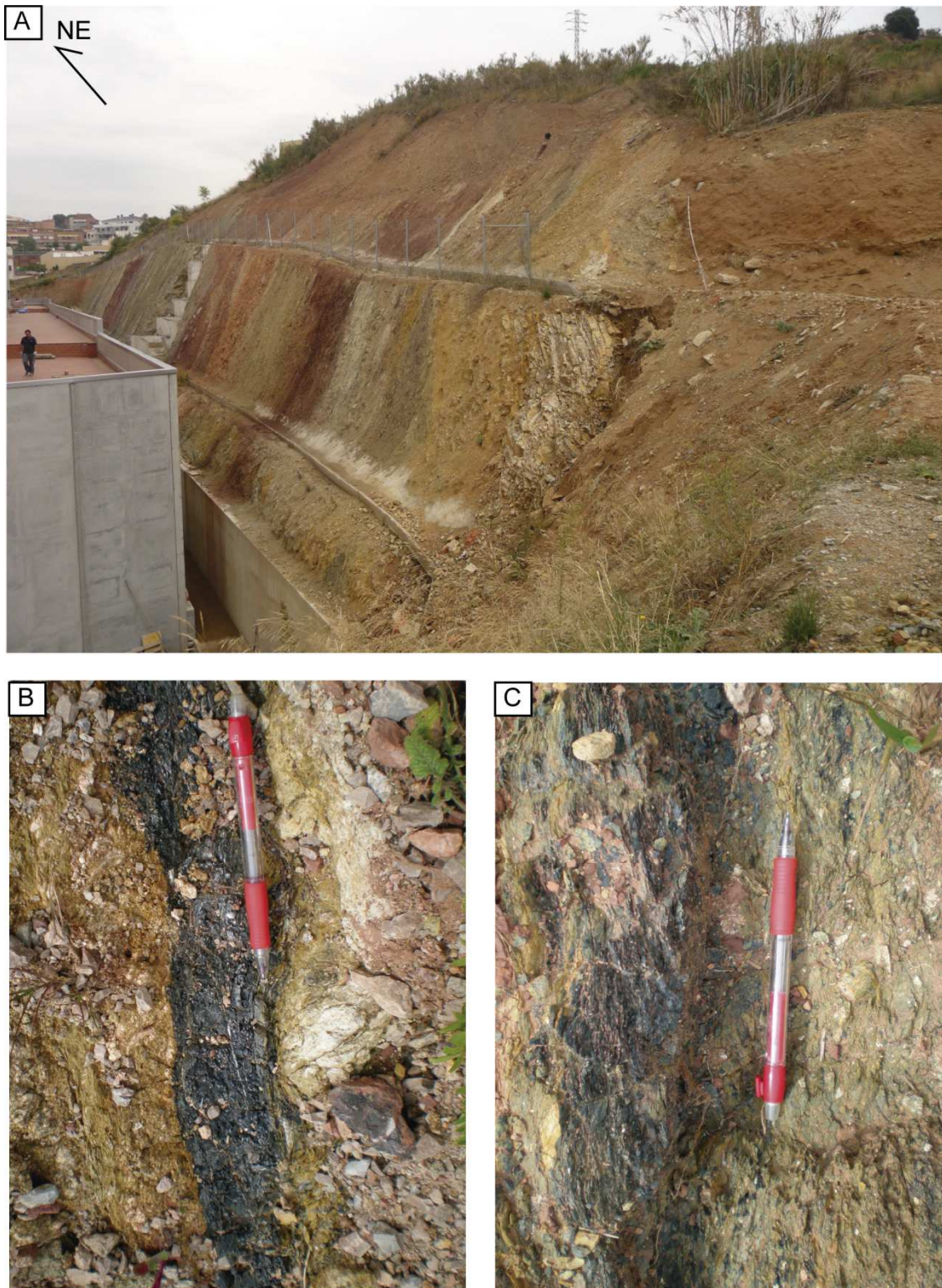
normal fault between the Buntsanstein and the M2 facies, 5) normal fault juxtaposing the Oligocene conglomerates against the M2 facies, and 6) thrust of M3 facies over the Oligocene rocks. All these faults have been linked with type 1B, 2B and possibly 3A faults.



**Figure 4.12.** A) Schematic geological map of the northeastern ending of the Barcelona Plain (enlarged from figure 4.2). The square marks the location of the Siurana outcrop and the star the Sastre outcrop. Darker patches indicate real outcrops. The detailed map of the hills at the SW of Montgat Nord is from Parcerisa (2002). B) Stereoplot of normal and inverse (dashed line) fault of the Siurana outcrop.

Fault rocks are poorly developed and cataclasites, gouges and veins have not been observed. Only, in two of the faults, one inside the granodiorite and one between the granodiorite and the Buntsandstein, a black shale material has been identified filling the fault (fig. 4.13B-C). In the former fault, it has a concoidal fracturation whereas in the





**Figure 4.13.** Siurana outcrop. A) Steep trench where the complex structure of the beginning of the splay crops out. B) Silurian rocks are sliced in a fault affecting the granodiorite. C) Silurian black shales in the fault that places the Buntsandstein on the granodiorite.

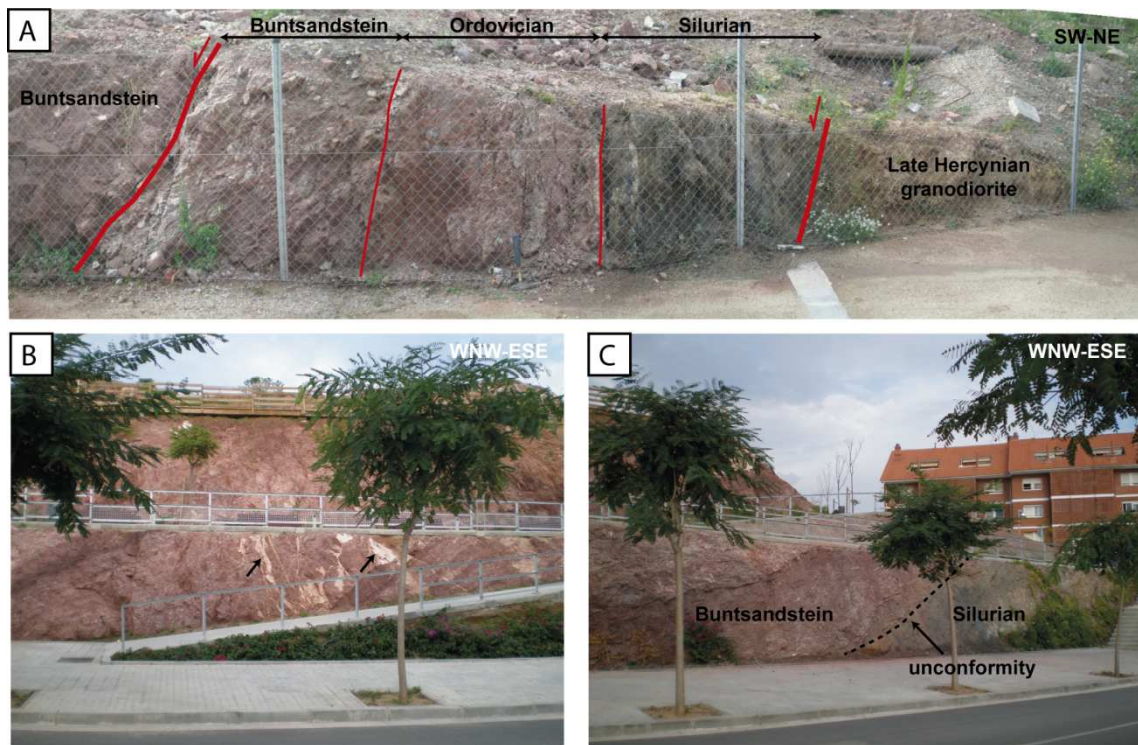
latter fault, this material is more clay-rich. The comparison of the X-Ray Fluorescence (FRX) analyses of these materials with Silurian rocks and the granodiorite indicates their origin from the Silurian black shales.



However, the importance of this ephemeral outcrop lies in that it shows, in a very narrow zone, at least two of the main deformation phases and their temporal relationships.

### 4.3.5. Sastre outcrop

The Sastre outcrop is located in the hill mainly constituted by Buntsandstein conglomerates in the northeast of the studied area (fig. 4.12). This hill is bounded to the northeast by a steep normal fault that places these conglomerates on the late Hercynian granodiorite, slicing in between Silurian and Ordovician rocks (fig. 4.14A). The fault zone, related to type 3A faults, is constituted by a 3 m thick fault core where several slip surfaces can be recognized. Silurian rocks consist of black shales that have developed a steep penetrative foliation parallel to the bounding fault. Within the Ordovician rocks irregular and steep fracture planes are also identified. The Buntsandstein conglomerates show a more cataclastic deformation and a certain preferential orientation parallel to fault core wall is observed.



**Figure 4.14.** Sastre outcrop. A) Fault zone between the late Hercynian granodiorite and the Buntsandstein conglomerates, slicing metamorphic Paleozoic materials. B) Type 2B faults with a white calcite film affecting the Buntsandstein conglomerates. C) Unconformity between the Silurian phyllites and the Buntsandstein basal conglomerates.

The Buntsandstein conglomerates are also affected by strike-slip faults related to the third deformation phase D<sub>3</sub>. These faults, of decimetric to metric spacing, have a planar surface that often is covered by a white and very thin and striated film of calcite (fig. 4.14B).

The unconformity between the Silurian phyllites and the Buntsandstein facies crops out further to the south of this hill (fig. 4.12 and 4.14C).

#### **4.3.6. Caritg outcrop**

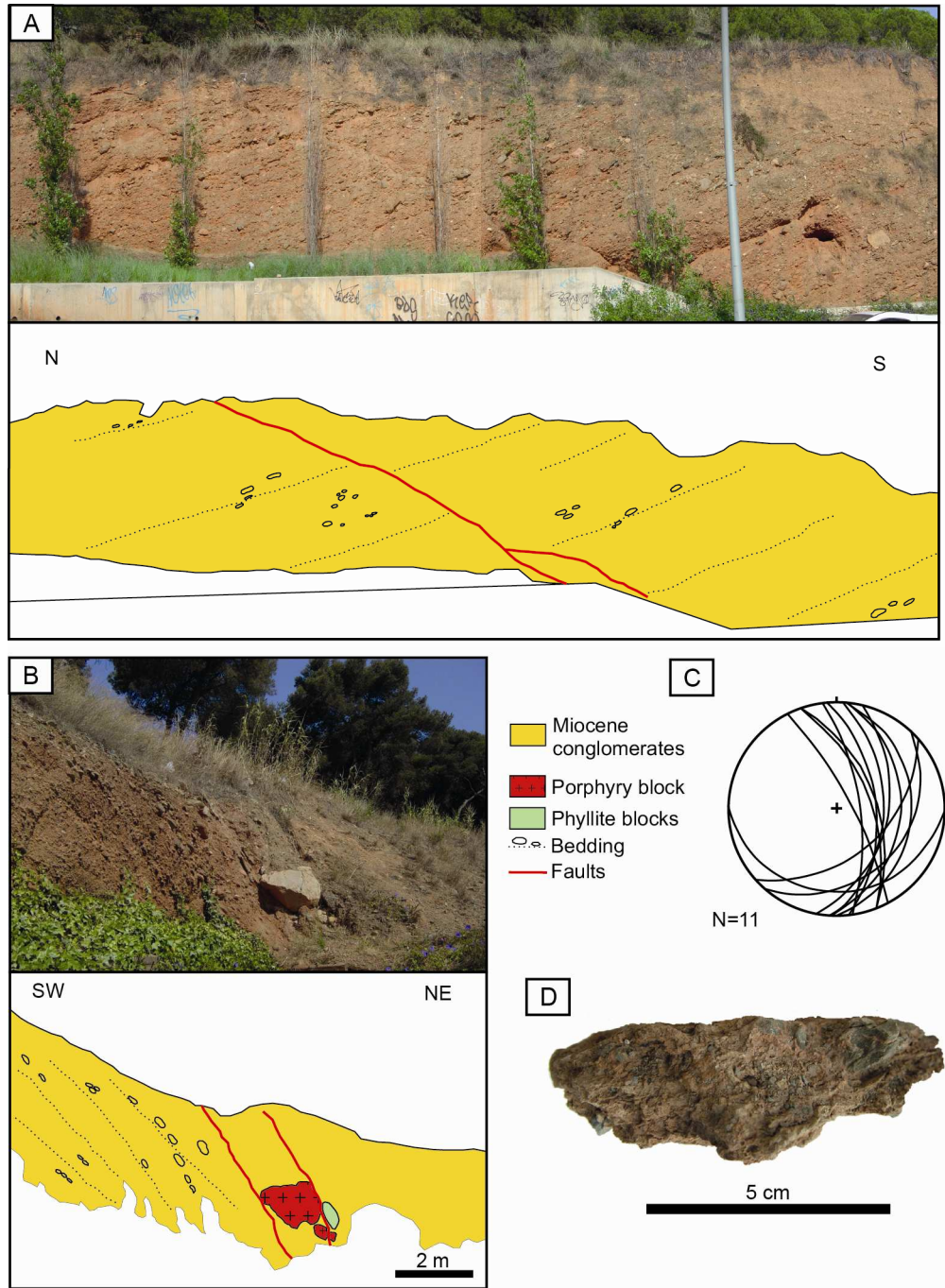
The Miocene conglomerates are affected by minor type 3D normal faults which show two main orientations: N-S striking faults and dip between 30 and 80° to the E and NE-SW striking faults with dip between 24 and 50° to the SE (fig. 4.15A-C). Faulting produced changes in bedding orientation and dip. Faults are discrete planes that generate a narrow fault core, from 0.5 to 7 cm wide, and no damage zone. The fault core is constituted of cohesive, reddish mud-to-sandy cataclasites with centimetric host rock clasts (fig. 4.15D).

#### **4.3.7. Guixeres outcrop**

This outcrop, located in the Hospital fault hangingwall, is formed by Triassic dolostones of M1 facies dipping to the north. They are affected by four deformation phases: D<sub>1</sub>, D<sub>3</sub>, D<sub>4</sub> and D<sub>6</sub>.

Normal faults 1A with sinistral component have both undulose and planar walls with smooth surfaces (fig. 4.16A-B). Deformation is localized in the footwall, generating a fault core formed by cataclasites (fig. 4.16B). Deformation decreases gradually across the first 6 cm. Type 2B reverse faults are centimetric faults of straight walls that are infilled by calcite cement. They usually have a step-like geometry indicative of their sense of movement (fig. 4.16C). Type 3A normal faults are discrete planes with undulose walls characterised by slickenside surfaces that denote their normal slip. Speleothems and karstic breccias usually cover their walls (fig. 4.16D). Type 3D normal faults are discrete planes with irregular walls that have little slip. They clearly crosscut previous faults (fig. 4.16A). Finally, 3E open joints have been identified (fig. 4.16E). The open joints usually have straight walls but some of them can be very irregular probably due to enlargement by dissolution. They can have a width up to 1.5 m and are

filled by the Triassic clays of the unit above (M2). Their planes are usually covered by speleothems.

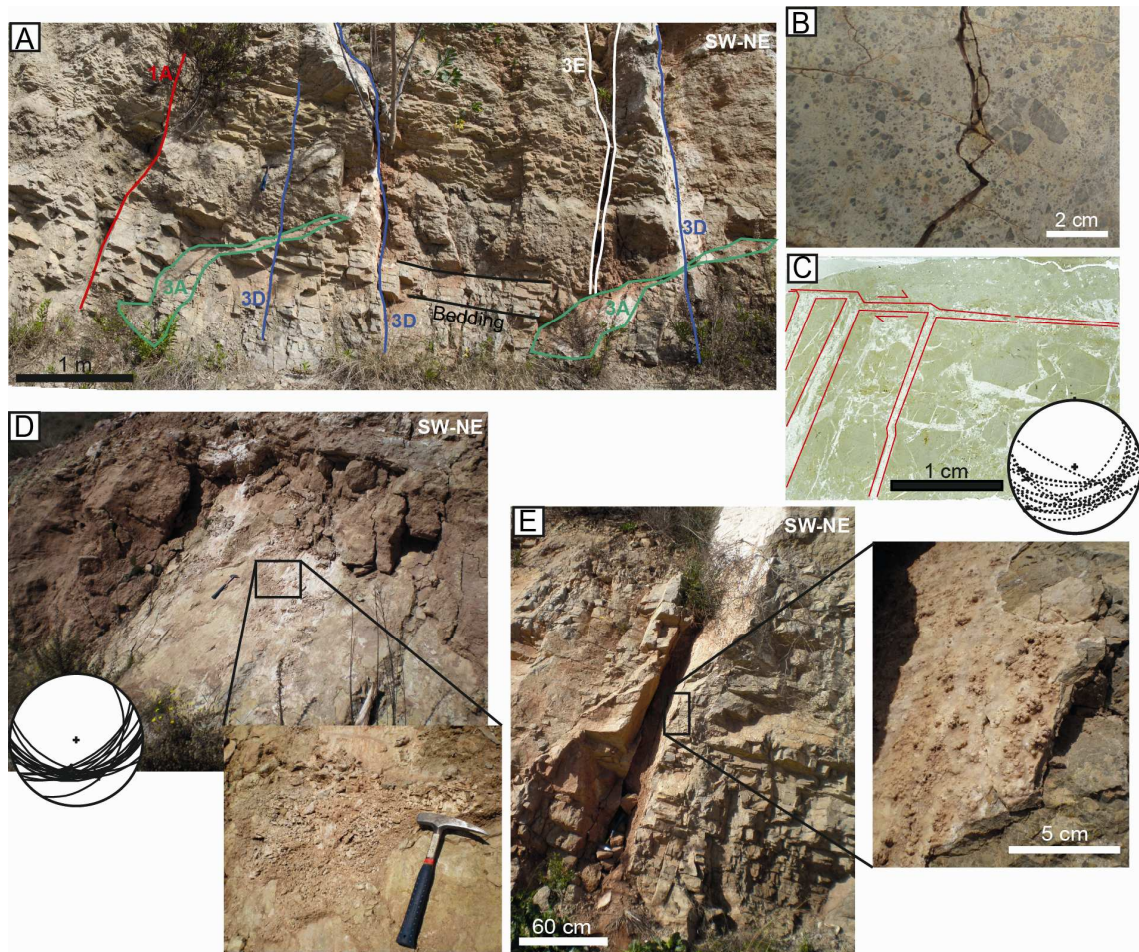


**Figure 4.15.** Caritg outcrop. A-B) Outcrop views of type 3D faults affecting Miocene conglomerates. C) Projection of the fault data in a stereoplot. D) Hand sample of a cataclasite. Observe the variability in clast size.

### 4.3.8. Torrent del Corró outcrop

The Torrent del Corró outcrop is located in the footwall, 50 m further to the north from the Neogene Vallès fault, where the Paleozoic basement exhibits an intense fracturation



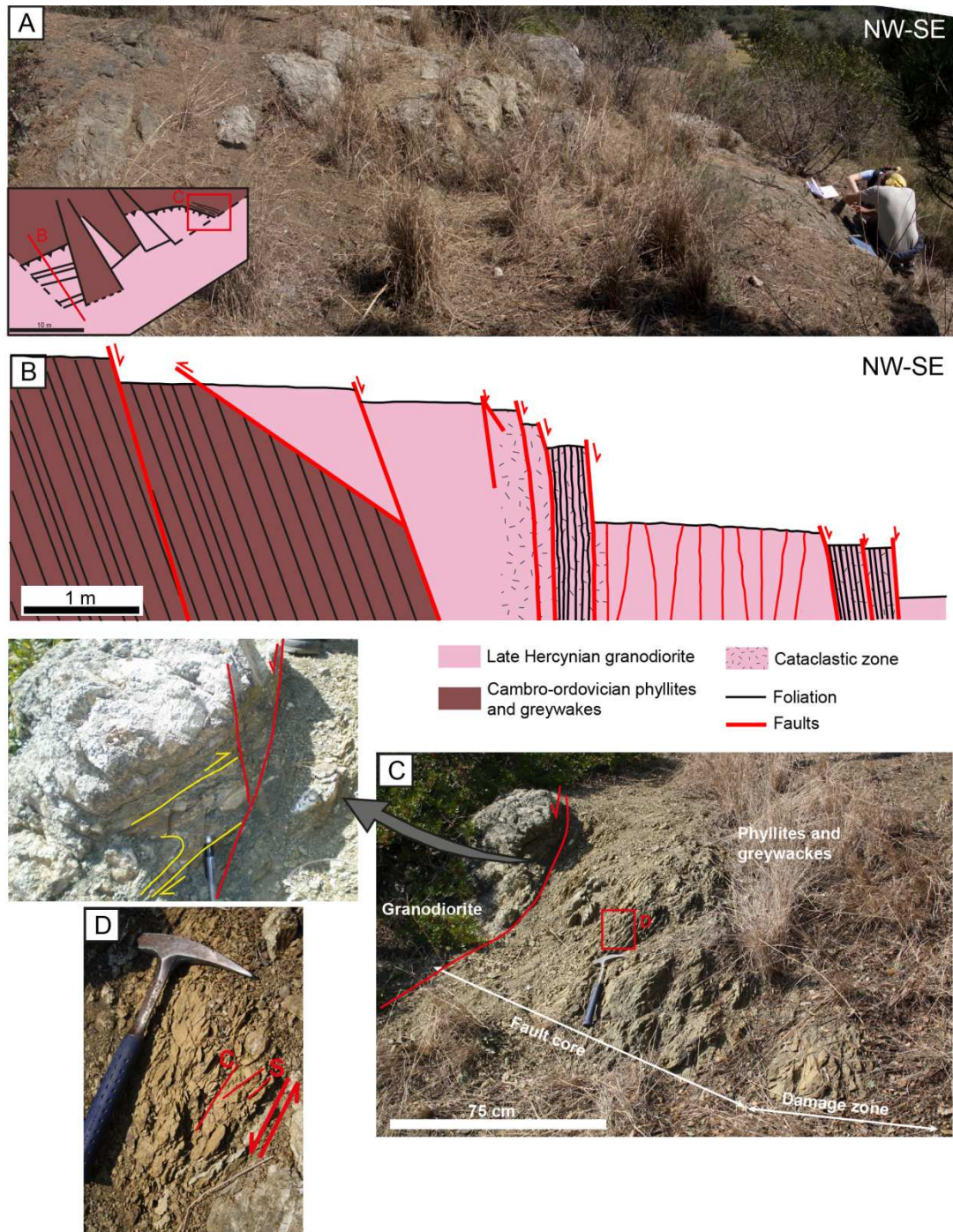


**Figure 4.16.** Generations of fractures affecting Triassic dolostones of M1 facies. A) Outcrop view affected by faults 1A, 3A, 3D and 3E. B) Cataclasite formed in the footwall of type 1A faults. C) Microfault of type 2B within M1 facies. This thin section is cut parallel to the strike of the fault, showing the sinistral component of displacement. D) Type 3A normal fault in M1 facies characterized by its undulating plane. Observe the detail of the karstic breccias on the fault plane. E) Type 3E open joint in M1 facies filled by clays of the M2 and detail of the speleothem covering the walls.

(fig. 4.5). The outcrop shows a step-like geometry, with blocks up to 2 m long that descend from NW to SE, caused by normal faults with a NE-SW strike and high dip to the SE (fig. 4.17A-B). Hercynian granodiorites and Ordovician phyllites and greywackes are involved in D<sub>2</sub>, D<sub>3</sub>, D<sub>4</sub> and D<sub>7</sub> deformation structures. Phyllites foliation has a NE-SW strike and high dip to the SE (155/71).

The granodiorite thrusts in a northwestern direction (D<sub>3</sub>) over the phyllites and greywackes. In the fault core, a black foliated gouge about 30 cm wide, resulting from the deformation of the Ordovician rocks, is developed (fig. 4.17C). Gouge foliation is parallel to the fault plane but also some folds are observed (fig. 4.17C).





**Figure 4.17.** Torrent del Corró outcrop. A) Lateral view of the outcrop where the step-like geometry can be observed and synthetic outcrop map indicating view location. B) Schematic cross-section of the outcrop shown in A, highlighting the step-like geometry and localization of foliation and cataclasis. C) Reactivated fault zone between the granodiorite and the phyllites and enlarged area showing the crosscutting relationship between the thrust fault and the later normal fault. Photograph location is shown in A. D) Detail of the S-C structure developed in the phyllites that indicates the normal displacement of the fault.

The deformation phase D<sub>4</sub> is characterized by normal faults with straight planes and dip-slip slickenlines. Within the footwall of the faults with the highest scarps (about 1 m high), a penetrative foliation parallel to the fault plane and a more apparent cataclasis are

developed (fig. 4.17B). Also, the block bounded by these faults is affected by minor faults with a spacing about 10 cm dipping to the SE and NW (fig. 4.17B). Cataclasites are very cohesive and have a dark green color. The normal fault zone between the granodiorite and phyllites and greywackes is about 2 m wide and clearly crosscuts the previous thrust. This fault mainly deforms the footwall rocks (fig. 4.17C). Phyllites develop a penetrative S-C structure indicative of the normal displacement of the fault (fig. 4.17D). Although in the field, these structures are related to D<sub>4</sub>, the petrologic and geochemical observations of fault rocks and cements have shown that D<sub>4</sub> faults have reactivated previous D<sub>2</sub> faults.

Finally, both normal and thrust faults are offset by a NW-SE system of dextral strike-slip faults that have been associated with the last deformation phase D<sub>7</sub>.

#### **4.3.9. Camí d'en Cisa outcrop**

This outcrop is located at the tectonic contact between the granodiorite and the Miocene rocks of the Vallès fault. This contact can not be observed as it is covered by farm fields and therefore, only structures in the granodiorite could be studied. The granodiorite is affected by subordinated normal faults of the main Vallès fault produced during the fourth deformation phase D<sub>4</sub>. The fault walls present two main morphologies, straight and undulose, and slickenlines are frequent (fig. 4.18). At the vicinity of the main fault, fracturation is more intense and the undulose surfaces generate a 1 m thick zone formed by sigmoids (fig. 4.18). These sigmoids indicate a certain left-lateral displacement during normal faulting, in accordance with slickenline orientations.

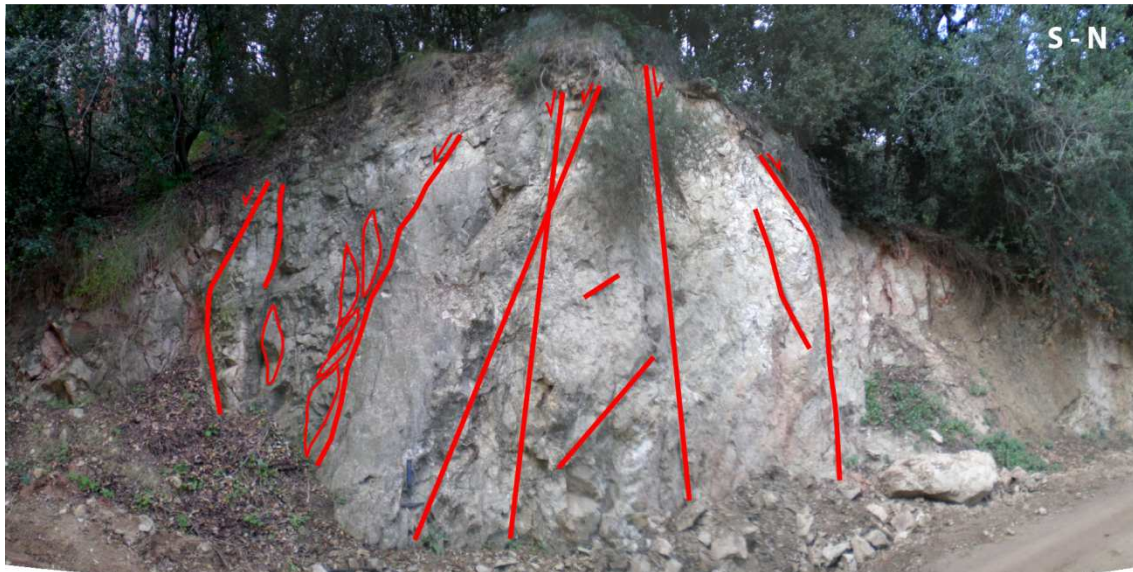
### **4.4. Petrology and geochemistry**

In this section are described the petrologic and geochemical characteristics of host rocks and fault rocks of the studied areas.

#### **4.4.1. Host rocks**

The host rocks that are involved in the studied fault zones are Paleozoic, Triassic and Miocene ages.





**Figure 4.18.** Camí d'En Cisa outcrop and interpretation of the main normal faults affecting the granodioritic footwall of the Vallès fault.

#### **Paleozoic rocks**

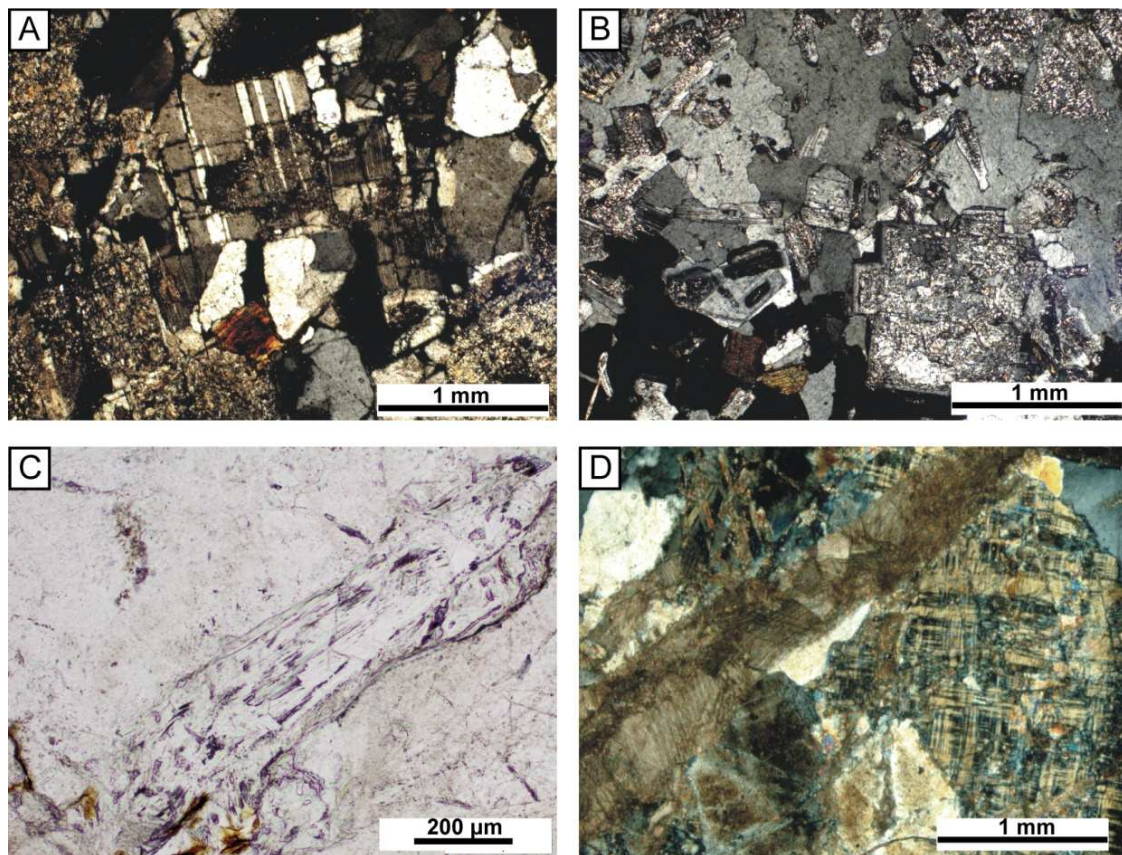
The late Hercynian granodiorite and the Silurian black shales are the two Paleozoic rocks that have been involved in a higher deformation. The former constitutes the footwall at the vicinity of major faults whereas the latter act as a plastic level clipped in faults zones.

The granodiorite is constituted by quartz, potassic feldspar, plagioclase and biotite (<5%) and shows granular texture (fig. 4.19). Grain size is mostly about 2-3 mm, but there are feldspars around 5 mm. Quartz crystals are allotriomorphic. The potassic feldspar, identified as orthose, is also allotriomorphic and has perthites. Some of the orthose crystals are poikilitic with inclusions of prismatic plagioclases and biotites (fig. 4.19B). The plagioclase has idiomorph prismatic crystals that show polysynthetic twins. Finally, the biotite show subidiomorphic shapes and has some interlayered epidote.

The granodiorite is poorly altered as shown by the partial replacement of orthose and plagioclase by kaolinite and sericite, respectively, and a very incipient alteration of biotite to chlorite. However, close to the Vallès fault, a localized alteration took place in some joints of the granodiorite previously to the defined deformation phases. This alteration is represented by the crystallization of coarse, between 0.2 and 1.1 mm long, idiomorphic K-white mica associated to microcline neoformation with tartan-like twin (fig. 4.19C-D).

The Silurian black shales are constituted by phyllosilicates, quartz, calcite, potassic feldspar, plagioclase, jarosite and hematites. Specifically, the phyllosilicates are 65% illite, 10% chlorite and 25% illite-smectite.

Ordovician rocks are phyllites and greywackes. Phyllites are aphanitic rocks that have a grey satined color and show a penetrative foliation. Greywackes are formed by quartz, quartzite and feldspar clasts, from rounded to subangulose, up to 1 mm in size and a slightly recrystallized quartzitic matrix. Greywackes show a rough cleavage, with a spacing about 1 mm, made of chlorite, white mica and oxides. Elongated clasts are disposed parallel to cleavage planes.



**Figure 4.19.** A) Microphotograph of the granodiorite under cross-polarized light. B) Poikilitic orthose crystals (cross-polarized light). C) K-white mica resulting from alteration at the vicinity of the Vallès fault. D) Microcline crystal with its characteristic tartan-like twin.

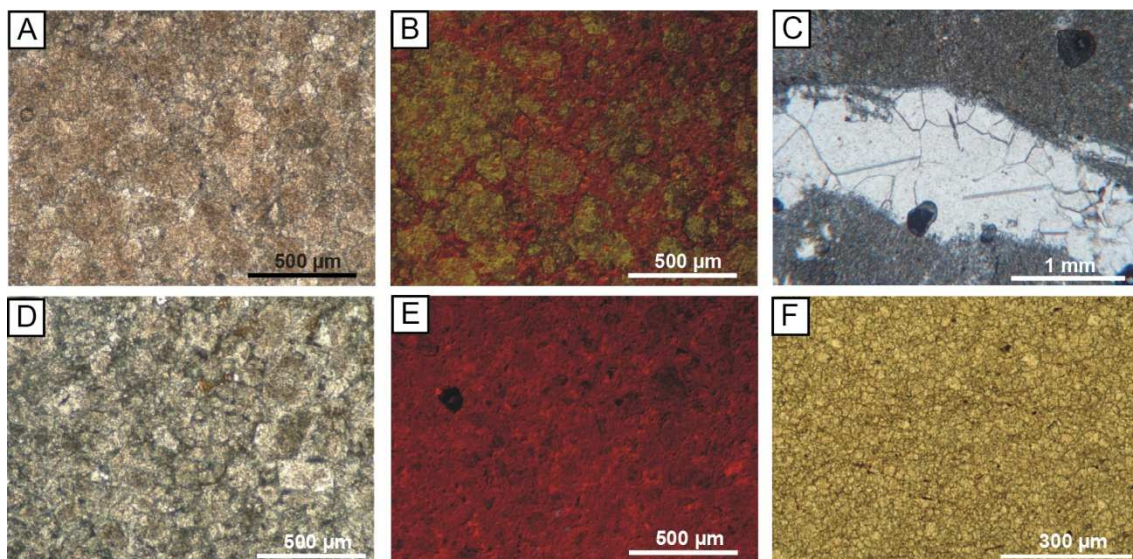
### Triassic

Middle Triassic materials are represented by Muschelkalk facies M1, M2 and M3. The Muschelkalk facies M2 are formed by lutites and layers of sandstones. Lutites are formed by clays, quartz, calcite, potassic feldspar and plagioclase, being the clays 65% illite, 20% illite-smectite, 10% chlorite-smectite and 5% chlorite. The red sandstones are



constituted by quartz, potassic feldspar, plagioclase, muscovite and biotite. Grains are 160  $\mu\text{m}$  in size and are cemented by orange luminescent calcite.

Muschelkalk facies M1 and M3 are formed by dolostones which consist of 2 to 50 cm thick beds. Four different types of dolostones (named HR) have been identified: HR1 and HR2 in the M1 and HR3 and HR4 in the M3. HR1 dolostone is constituted by clear anhedral crystals about 50  $\mu\text{m}$  thick and euhedral crystals with a cloudy nucleus and clear borders about 250  $\mu\text{m}$  thick (fig. 4.20A). HR1 shows a brown-yellowish luminescence (fig. 4.20B). HR2 consists of an orange luminescent dolmicrite (fig. 4.20C). HR3 dolostone is constituted of anhedral crystals about 80  $\mu\text{m}$  and euhedral crystals about 180  $\mu\text{m}$  in size with a cloudy nucleus and dull red luminescence (fig. 4.20D-E). Ghosts of coated grains indicate that the replaced rock was at least locally a grainstone and that dolomitization was non-destructive. Finally, HR4 is formed by anhedral crystals about 60  $\mu\text{m}$  in size with a orange dull luminescence (fig. 4.20F). The dolostones have  $\delta^{18}\text{O}$  values between -4.6 and -2.7‰ vPDB and  $\delta^{13}\text{C}$  values between +0.7 and +2.8‰ vPDB (table 1, appendix 1). With regard to their elemental geochemistry, HR3 shows higher contents in Mn and Fe and lower contents in Sr than the other host rocks. HR4 have contents of Na and Sr below the analytical detection limit (table 2, appendix 1). The dolostones of M1 are partially replaced by a clear anhedral dolomite with dull red luminescence (RD1) (fig. 4.20A-B).

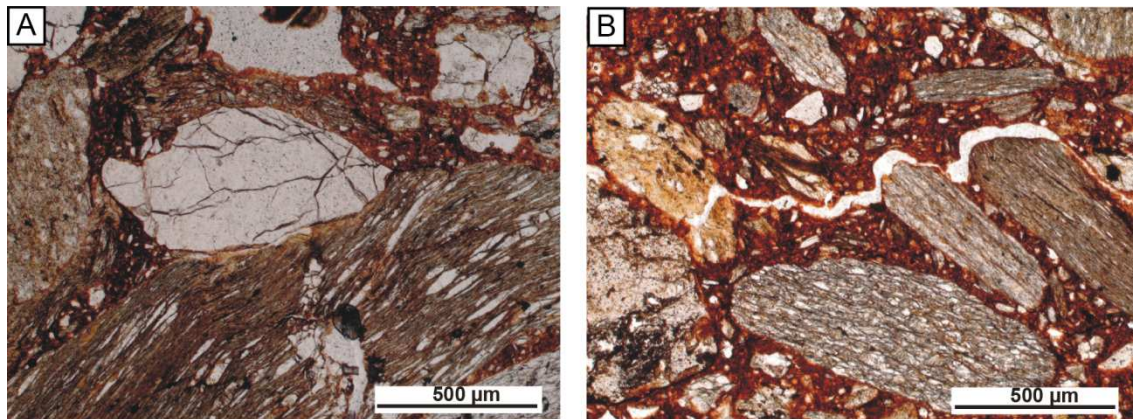


**Figure 4.20.** A-B) Microphotographs of dolostone HR1 (plane light and cathodoluminescence). HR1 in yellowish and replacive dolomite in red. C) Microphotograph of dolmicrite HR2 affected by a calcite fracture (plane light). D-E) Microphotographs of dolostone HR3 under plane light and cathodoluminescence, respectively. F) Microphotograph of dolostone HR4 (plane light).

## Miocene

The Miocene rocks of the Barcelona Plain are well-stratified conglomerates, probably of Langhian age (Parcerisa 2002; Parcerisa et al. 2007), interpreted as alluvial fan deposits of the Upper Continental Complexes. Conglomerates have intercalations of lentils of sandstones and clays. Bedding is of centimetric order and it is defined by clast alineations.

Conglomerates are matrix supported and heterometric (fig. 4.21). Clasts size range from cobble to granule and occasionally some of the clasts can reach a metric size. Clasts are derived from the Paleozoic basement and the most abundant are phyllites (45%) and quartzites (35%) followed by knotted hornfels (10%), quartz (7%) and porphyries (3%). Clasts usually are angular but phyllites and knotted hornfels are rounded. The matrix is formed by reddish mud-to-sandy material. The sand size is formed by grains of angular quartz and subrounded orthose. The smaller matrix fraction is constituted by quartz, potassium feldspar, illite, chlorite, kaolinite, mixed-layer of illite-chlorite, apatite, iron oxides and titanium oxides. Conglomerates have voids and fracture porosity. Voids are rounded and have a maximum diameter of 2.5 mm (fig. 4.21A). Fracture porosity is the most important and tend to border the clasts producing an anastomosing geometry (fig. 4.21B). Porosity is always open without any kind of cement.



**Figure 4.21.** Microphotographs of Miocene conglomerates under plane light. A) Subangular quartzite clast and phyllite clast with a concavo-convex contact. Observe at the top the irregular void within the matrix. B) Fracture porosity bordering the rounded phyllite clasts.

### 4.4.2. Fault rocks

Fault rocks developed within the studied outcrops were formed within the brittle regime and consist of gouges, cohesive breccias, cataclasites, ultracataclasites and

pseudotachylytes. The textural, mineralogical and geochemical features of the fault rocks and cements are briefly analyzed according to their relative chronology and their formation during the different deformation phases (fig. 4.22). This link between the different deformation phases and the different fault rocks and cements reveal the circulation of different fluids through time.

### **Deformation phase 1: cataclasites, ultracataclasites and D1, D2 and D3 cements**

This deformation phase has been recognized in the Triassic dolostones of the Barcelona Plain. Type 1A faults generated a cohesive cataclasite in the footwall formed by subrounded dolostone clasts up to 2 mm in size and a matrix generated by host rock comminution, which grains are about 100  $\mu\text{m}$  in size. Cataclasites are cemented by bright orange luminescent dolmicrite crystals D1 (fig. 4.23A-D, G). D1 has  $\delta^{18}\text{O}$  values between -5.9 and -5.4‰ vPDB and  $\delta^{13}\text{C}$  values between +2.3 and +2.4‰ vPDB (table 1, appendix 1). Later frictional processes produced ultracataclasites, which are constituted by subrounded dolostone clasts up to 500  $\mu\text{m}$  in size and a matrix formed by grains around 50  $\mu\text{m}$  in size. These fault rocks are cemented by a red luminescent dolmicrite D2 with  $\delta^{18}\text{O}$  values between -7.2 and -6.8‰ vPDB and  $\delta^{13}\text{C}$  values between +2.5 and +2.6‰ vPDB (fig. 4.23E-G). Dolomite D2 has different Fe content depending on the host rock. When precipitates in the dolostone HR2 (D2a) it has Fe contents up to 870 ppm and an average of 440 ppm whereas when precipitates in HR3 (D2b) it has Fe contents up to 7803 ppm and an average of 2813 ppm (table 2, appendix 1). Finally, dolomite cement D3 precipitated within micrometric type 1A veins. D3 is formed by anhedral crystals of dolomite, about 35  $\mu\text{m}$  in size, with a zoned orange and red luminescence, growing in optical continuity with the host rock (fig. 4.23D,G-I).

### **Deformation phase 2: breccia, cataclasite, gouge and C1, chlorite, illite and iron oxides cements**

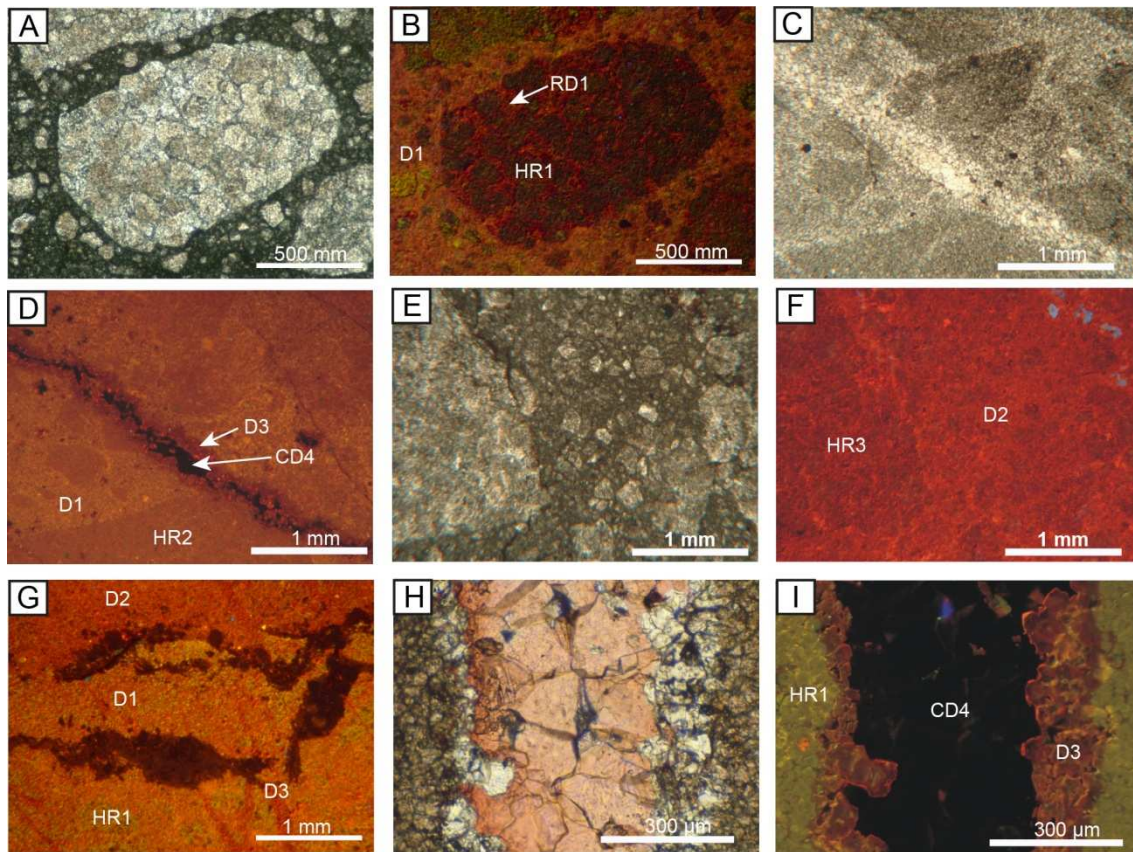
This deformation phase is present in both the Barcelona Plain and the Vallès Half-graben. It is localized in the granodioritic footwall and generates breccias, cataclasites, gouges and veins, which show similar cements.

In the Hospital outcrop, these faults generate a 70 cm wide core zone formed by a green cataclastic zone and a foliated gouge in the tectonic contact between the granodiorite and the Triassic clays and sandstones. This core zone developed in a zone where

	Pre-D <sub>1</sub>	D <sub>1</sub>	D <sub>2</sub>	D <sub>3</sub>	D <sub>4</sub>	D <sub>5</sub>	D <sub>6</sub>	D <sub>7</sub>
Microcline	—							
Coarse white mica M1-M2	—							
Triassic dolostones & RD1	—	—						
D1		—						
D2		—						
D3		—						
Small white mica M3-M4								
Chlorite			—					
Epidote			—					
Quartz			—					
Calcite C1 (a-f)			—					
Iron oxides			—					
Calcite C2 (a-c)				—				
Calcitized dolomite CD1 to CD4				—				
Stylolites				—				
Calcite C3 (a,b)								
Laumontite L1								
Calcite C4								
Laumontite L2								
Calcite C5								
Calcite C6								
Miocene diagenetic products								
Calcite PC1								
Calcite C7 and C8								
Speleothems								

**Figure 4.22.** Complete sequence of fracture-related cements for the different deformation phases and previous alteration and diagenetic products.



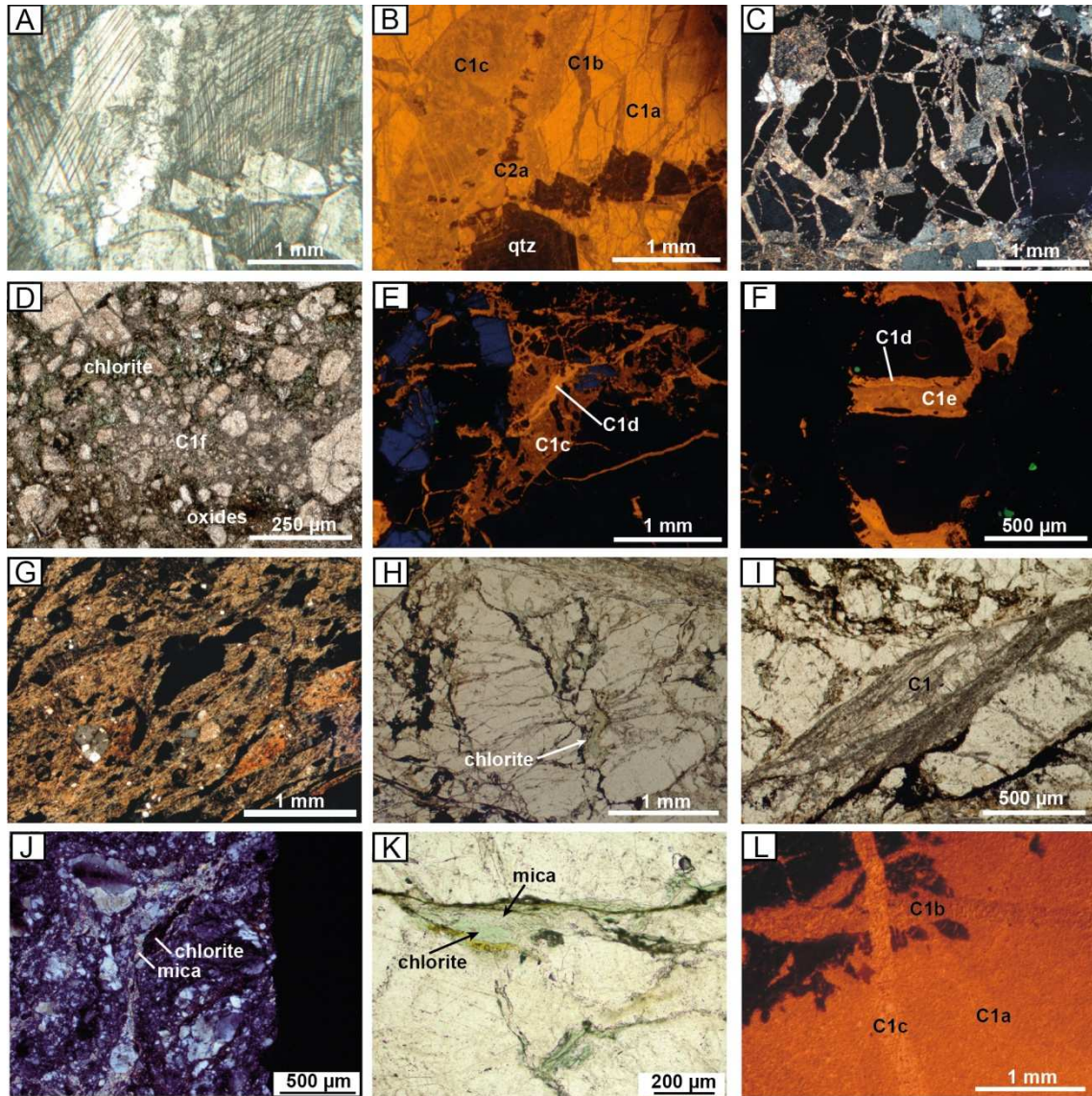


**Figure 4.23.** Dolomite cements related to the first deformation phase. A-B) Plane light and cathodoluminescence images of the cataclasite cemented by dolomite D1 in a HR1 dolostone. Within the clast, replacive dolomite RD1 is observed. C-D) Plane light and cathodoluminescence images of the cataclasite cemented by dolomite D1 in a HR2 dolmicrite. E-F) Plane light and cathodoluminescence images of the cataclasite cemented by dolomite D2 in a HR3 dolostone. G) Crosscutting relationships among the three cements in a HR1 dolostone. H-I) Plane light and cathodoluminescence images of a fracture cemented by dolomite D3 and a later generation of calcite CD4 affecting a HR1 dolostone.

previously quartz geodes had formed (fig. 4.24A-B). The cataclastic zone is the result of two successive reactivations that produced a dilatant cohesive random breccia and a consequent cohesive cataclasite. The dilatant random breccia is formed by angulose granodiorite clasts, between 300  $\mu\text{m}$  and 2 mm in size, separated by veins of calcite C1 around 50-100  $\mu\text{m}$  wide (fig. 4.24C). The cataclasite is formed by angulose granodiorite clasts and reworked subangulose clasts of the previous breccia and range from 100  $\mu\text{m}$  to 1 mm in size. The matrix is fine-grained and is predominantly cemented by calcite C1 and small amounts of chlorite and iron oxides (fig. 4.24D). Calcite C1 has crystals up to 1 mm in size and six generations of calcite C1 (from C1a to C1f) have been established from its variable luminescence from dull to bright (fig. 4.24A-B, E-F).



The gouge is localized in the Triassic clays and it is made up of quartz, calcite, potassic feldspar, plagioclase, anhydrite and clays. Clays constitute between 45 and 55% of the fault rock of which 65% is illite, 5% chlorite, 20% illite-smectite and 10% chlorite-smectite. These phyllosilicates form the S-C fabric observed in the field consistent with a normal slip (fig. 4.7D, 4.24G).



**Figure 4.24.** Fault rocks and cements related to D<sub>2</sub>. A-B) Plane light and cathodoluminescence images of quartz crystals (qtz), calcite cements C1a,b,c and later C2a related to deformation phase D<sub>3</sub>. C) Cross-polarized image of the dilatant random breccia. D) Plane light image of the cataclasite. Observe the three neoformed minerals linked to this fault rock: chlorite, calcite C1f and iron oxides. E) Cathodoluminescence of calcite cements C1c and C1d. F) Image of cathodoluminescence of calcites C1d and C1e. G) Foliated gouge with phyllosilicates displaying an S-C structure. H) Random breccia affected by fractures filled with chlorite. I) Multiepisodic pull-apart cemented by calcite C1 (plane polarized light). J) Cross-polarized light of the cataclasites and microfractures formed by chlorite and K-white mica. K) Vein filled with chlorite and K-white mica. L) Cathodoluminescence image of calcite C1 filling voids. As in the Hospital fault, several generations of calcite C1 with oscillating cathodoluminescence are observed.



In the Enric outcrop, a random breccia constituting the damage zone is found. Clasts, which range from 200  $\mu\text{m}$  to 3 mm in size, are formed by granodiorite and dynamically recrystallized quartz-feldspathic rocks. In the fractures, chlorite and epidote precipitated (fig. 4.24H). Affecting this breccia, millimetric multiepisodic pull-aparts are formed in type 1B faults. These pull-aparts are cemented by calcite C1, which is made of anhedral to euhedral bright orange luminescent calcite crystals up to 30  $\mu\text{m}$  in size (fig. 4.24I).

Within the Vallès Half-graben, type 1B faults have been only identified in the Torrent del Corró outcrop. They are characterized by the development of cataclasites, ultracataclasites and microfractures. Clasts of cataclasites and ultracataclasites derive from the granodiorite and previous pseudotachylytes (see below). The latter tend to be more subrounded. Clast size in the cataclasites is very heterometric ranging from 30  $\mu\text{m}$  to 1 mm whereas in the ultracataclasites clasts are from 40 to 150  $\mu\text{m}$  in size. In the fault rock matrix, amoeboid chlorite precipitates whereas within the microfractures, 15 to 90  $\mu\text{m}$  in size K-white mica flakes  $\pm$  amoeboid chlorite precipitates (fig. 4.24J-K). Also, during this phase, calcite C1 cemented irregular voids of about 2 cm of diameter localized next to the fault planes (fig. 4.24L).

It is difficult to establish the timing of the above mentioned pseudotachylytes because of the lack of preferential orientations and their later reworking. However, they clearly pre-date the cataclasites, ultracataclasites and fractures with chlorite and mica and post-date the previous coarse K-white mica. Pseudotachylyte veins show corroded quartz clasts and a very fine grained matrix clearly (fig. 4.25).



**Figure 4.25.** Pseudotachylyte microphotographs. A-B) Pseudotachylyte affected by later laumontite and calcite fractures (plane light and cross-polarized light, respectively). C) SEM image of the pseudotachylyte. Observe the fine-grained matrix where micrometric micacrystals have grown by later alteration and the corroded geometry of the quartz clast.

Calcite cement C1 has  $\delta^{18}\text{O}$  values between -16.4 and -15‰ vPDB and  $\delta^{13}\text{C}$  values between -6.9 and -5.9‰ vPDB. The isotopic values and elemental composition of this cement is shown in table 1 and 2 in appendix 1.

### **Deformation phase 3: gouge, breccia and C2, CD1-CD4 cements**

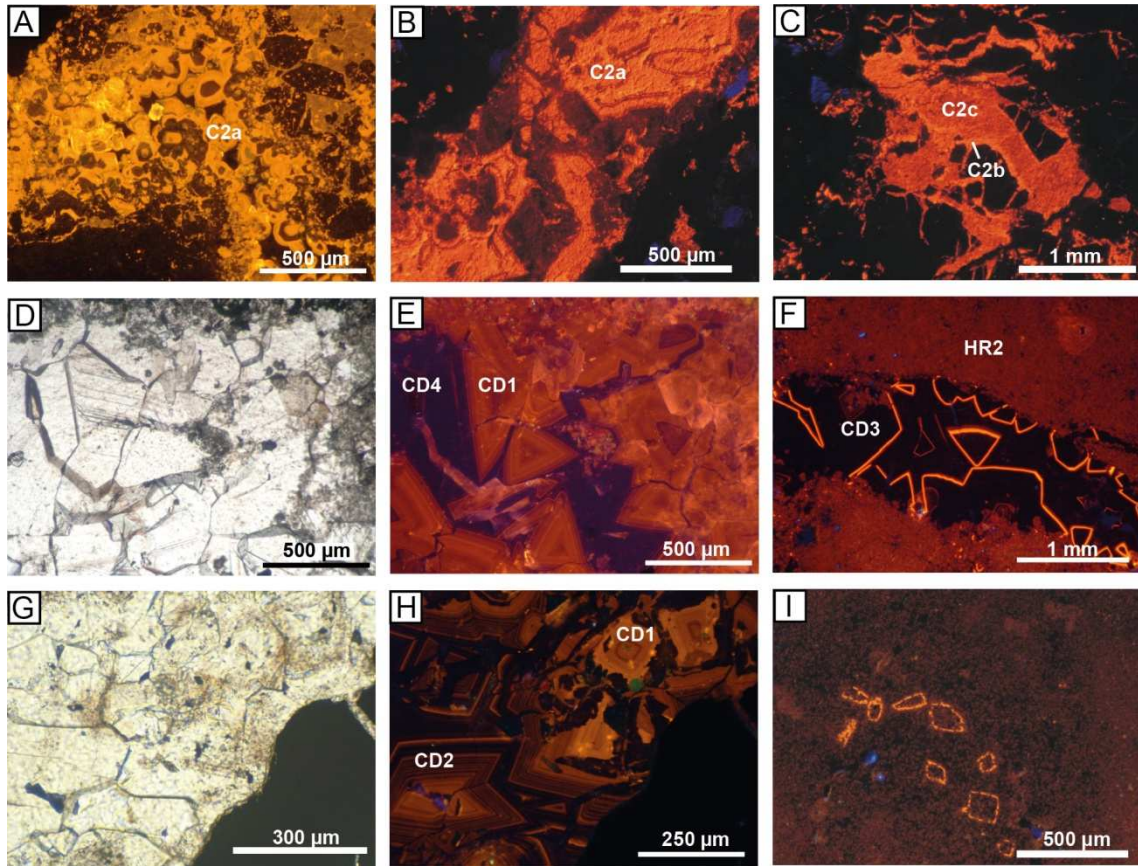
In the Vallès Half-graben, type 2A reverse faults developed gouge bands as a result of the deformation of the Ordovician phyllites. Also, subvertical stylolites have been recognized affecting the granodiorite and previous cataclasites.

In the Barcelona Plain, this deformation phase generates breccias and veins that are cemented with calcite C2 and calcitized dolomite cements CD1 to CD4.

In the Hospital outcrop, major type 2B reverse faults places the Silurian and Ordovician rocks over the M3 dolostones. The result is the generation of two breccias, FB2a and FB2b. Breccia FB2a is constituted by angulouse centimetric dolomite clasts from the M3 dolostones embedded in a yellow matrix resulting from an extreme comminution of the host rocks. Breccia FB2b contains subangulouse centimetric clasts of the Ordovician phyllites. Also, calcite cement C2 (C2a) fills vug porosity and joints within the dilatant breccia formed during the second deformation phase (fig. 4.26A) and joints of the Triassic sandstones of the hangingwall (fig. 4.26B). This cement is constituted by anhedral calcite crystals, between 100 and 500  $\mu\text{m}$  in size, with a zoned orange and brown luminescence. It has Mn values up to 7168 ppm and Fe values up to 6250 ppm.

In the Sariol outcrop, the main type 2B reverse fault produced a cohesive random breccia made of angulous, from 100 to 900  $\mu\text{m}$  in size, granodiorite clasts and a poorly developed matrix. Cohesion is given by the cementation of calcite C2 within the matrix and fractures up to 300  $\mu\text{m}$  wide across the clasts. Calcite C2 is constituted by twinned calcite crystals up to 300  $\mu\text{m}$ . Two generations have been identified: C2b and C2c, being C2b brighter orange luminescent than C2c (fig. 4.26C). C2b has higher contents of Mn and Fe, 3366 and 633 ppm on average, respectively than C2c, that has Mn values of 459 ppm in average and Fe contents below the detection limit.

In the Triassic dolostones, calcitized dolomite cements precipitated in reactivated 1A veins. Four generations of calcitized dolomite (from CD1 to CD4) have been associated with these faults. CD1 to CD4 cements are constituted by anhedral to subhedral crystals between 170 and 250  $\mu\text{m}$  in size, and idiomorphic rhombohedral crystals pseudomorphs of the previous dolomite. These cements differ from each other in their luminescence (fig. 4.26D-H). CD1 shows an orange bright zoned luminescence, CD2 shows a concentric zonation in orange and black, CD3 is non luminescent with a bright orange



**Figure 4.26.** Cements related to the third deformation phase. A) Void within the dilatant breccia filled with the zoned orange and brown luminescent calcite C2a. B) Fracture within the Triassic sandstones in the hangingwall of the Hospital fault filled with calcite C2a. C) Calcite cements C2b and C2c cementing the random breccia developed in the granodiorite at the Sariol outcrop. D-E) Fracture filled with calcitized dolomite CD1 and later CD4 under plane light and cathodoluminescence, respectively. F) Cathodoluminescence image of calcitized dolomite CD3 cementing a fracture. Plane light photograph is shown in figure 4.20C. G-H) Plane light and cathodoluminescence images of calcitized dolomite CD1 and CD2. Observe corrosion in the first cement. I) Patch of calcitized dolostone with luminescence similar to CD3.

luminescent thin line and CD4 is non luminescent. These cements have Na, Mn and Fe contents below the detection limit and Sr contents from 700 to 2200 ppm (table 2, appendix 1).

Calcitization of the Triassic dolostones have been also observed. In M1 facies calcitization is localized in small patches inside the original dolostone and has the cathodoluminescence similar to cement CD3 (fig. 4.26I). Calcitization of M3 facies is localized next to the main fault zone bounding the Triassic rocks and has orange luminescence.

The  $\delta^{18}\text{O}$  values of cements C2a,b,c and CD1-CD4 range between -5.9‰ and -4.6‰ vPDB and the  $\delta^{13}\text{C}$  between -7.4 and -5.4‰ vPDB. The  $\delta^{18}\text{O}$  and  $\delta^{13}\text{C}$  values of the calcitized M1 dolostones fall between the values of the dolostones and the calcite

cements, -4.1‰ vPDB and -3.2‰ vPDB, respectively. The  $\delta^{18}\text{O}$  and  $\delta^{13}\text{C}$  values of the calcitized M3 dolostones are between -9.5 and -9.3‰ vPDB and between -4.8 and -4.7‰ vPDB, respectively (table 1, appendix 1).

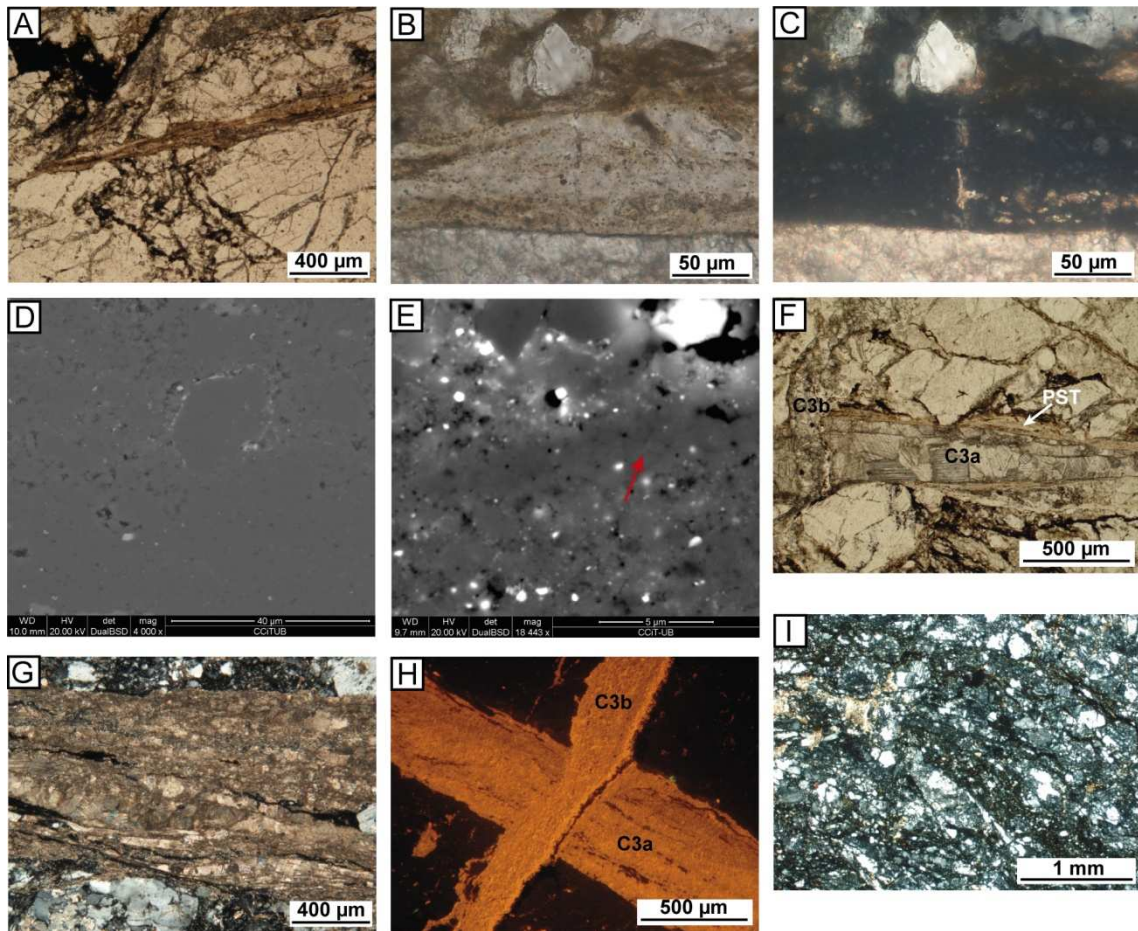
#### **Deformation phase 4: pseudotachylytes, cataclasites and C3, C4 and laumontite cements**

In the Barcelona Plain, type 3A faults have different size, geometries and products, depending on the outcrop.

In the Enric outcrop, centimetric 3A faults have straight walls and a sharp contact with the random breccia formed during the second deformation phase. They usually show bifurcations. Two pulses of activity have been recorded in these faults. The first one led to the development of pseudotachylytes. The pseudotachylytes are found in very thin up to 125  $\mu\text{m}$  wide fault veins and injection veins (fig. 4.27A). Under transmitted light, pseudotachylytes display yellow-brownish colours whereas under polarised light they show a dark aphanitic matrix that contain subrounded clasts of quartz and feldspar (fig. 4.27B-C). The observations with the optical and electronic microscopes point to the devitrification of the matrix (fig. 4.27C-E). The second pulse of activity consists of the development of crack-seal veins (fig. 4.27F-G). The crack-seals have internal shear planes and are cemented by the calcite cement C3a, which is a twinned anhedral to euhedral sparry calcite, from micrite to 200  $\mu\text{m}$  in size, with a bright orange luminescence (fig. 4.27H). It is characterized by  $\delta^{18}\text{O}$  values between -20.8‰ and -19.6‰ vPDB and  $\delta^{13}\text{C}$  values about -6.2‰ vPDB (table 1, appendix 1). The displacement produced during crack-seal formation caused the reorientation in localized zones of the previously formed random breccia. The result is the generation of a cataclasite with foliated fabric marked by planes of oxides, chlorites and epidotes (fig. 4.27I). The cataclasite is formed by a 50% of angulose to subrounded clasts between 50 and 500  $\mu\text{m}$  in size and 50% of fine-grained matrix. In a late stage, in a major 3A fault, a greenish-yellow semicohesive gouge was formed. It is formed by very fine-grained matrix constituted by smectite, chlorite and illite and isolated angulose clasts of granodiorite up to 300  $\mu\text{m}$  in size. It results from a completely comminution and alteration of the original granodiorite.

In the Guixeres outcrop, decimetric type 3A normal faults have been identified affecting M1 dolostones. These faults have undulose walls and are characterised by a localized



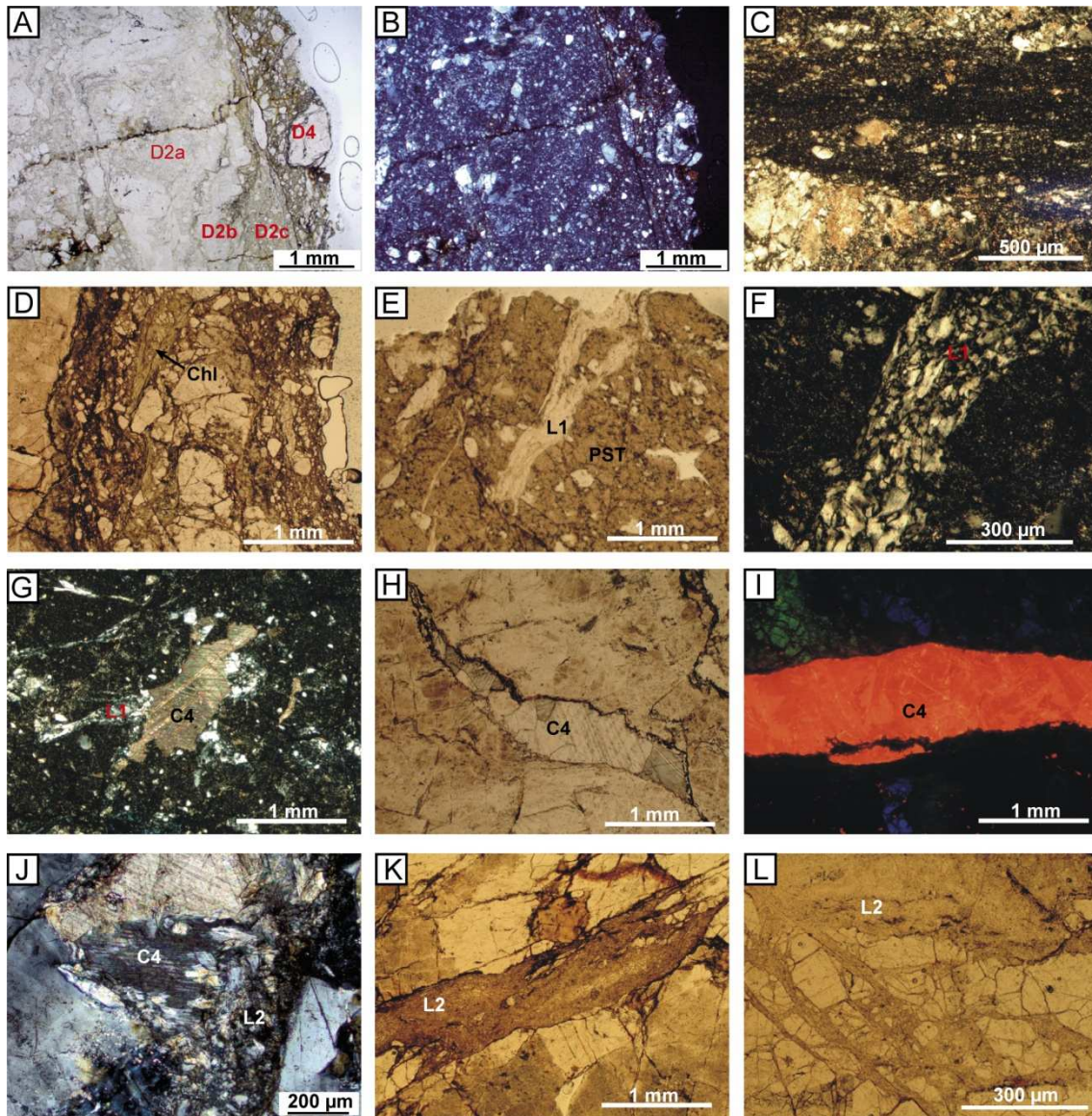


**Figure 4.27.** Fault rocks and cements of the Enric outcrop. A) Pseudotachylyte vein with banded structures crosscutting the previous random breccia. B) Plane light photograph of a pseudotachylyte vein. Observe the yellow color due to opaque inclusions. C) Under cross-polarized light, a micromosaic resulting of devitrification constituting the pseudotachylyte matrix is observed. D) SEM image of the pseudotachylyte. A clast of albite is embedded in the crystalline mosaic. Note the difference in size and morphology between the clast and the crystals of the mosaic. E) SEM image of the mosaic. It is formed by polygonal crystals (red arrow) that show triple points. F) Crack-seal veins of calcite C3a overprinting a pseudotachylyte vein and type 3B joint crosscutting both. G) Detail of the crack-seal structures and the internal shear planes (cross-polarized light). H) Cathodoluminescence image of calcite cements C3a and C3b showing their crosscutting relationship. I) Slightly foliated cataclasite coeval to crack-seal displacement.

deformation that generates slickensides.

In the Vallès Half-graben, this deformation phase is characterized by cataclasite, ultracataclasite and breccia development. Cataclasites are formed by subangulose clasts of granodiorite from 50 to 500  $\mu\text{m}$  in size which sum the 50% of rock volume and 50% of matrix (fig. 4.28A-B). Ultracataclasites are very fine-grained with clast size below 50  $\mu\text{m}$  and show banded structures (fig. 4.28C). The matrix of these two fault rocks was cemented by chlorite and laumontite L1 and less commonly by calcite C4. Also, along reactivated type 1B and new 3A fault veins, alternating precipitation of





**Figure 4.28.** Fault rocks and cements of the Vallès fault formed in D<sub>4</sub>. A-B) Cataclasite formed during D<sub>4</sub> that crosscuts three previous cataclasites formed during D<sub>2</sub>. Plane and cross-polarized light, respectively. C) Ultracataclasite (cross-polarized light). D) Cataclasite developed in type 3A normal fault and chlorite vein parallel to the fault plane (plane light). E) Vein formed by laumontite L1 (plane light). F) Detail of the laumontite crystals of the first generation (cross-polarized light). G) Calcite C4 crosscutting a laumontite L1 vein (cross-polarized light). H) Calcite vein resulting from the opening of a previous stylolite (plane light). I) Zoned cathodoluminescence of calcite C4. J) Calcite C4 replaced by laumontite L2. K) Vein formed by laumontite L2. Crystal size grows towards the center. L) Breccia cemented by laumontite L2.

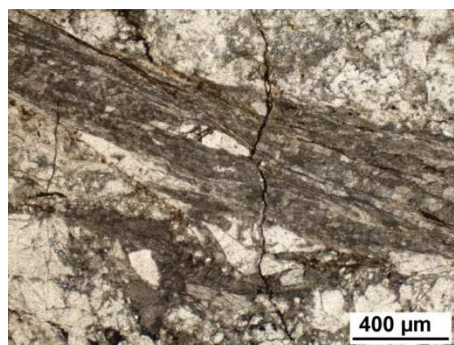
laumontite and calcite C4 coeval to irregular and ameboid chlorite crystals precipitation occurred (fig. 4.28D). The first generation of laumontite (L1) is made of translucent, anhedral and up to 50 µm in size crystals (fig. 4.28E-G). L1 precipitation was followed by calcite C4, which precipitated in fractures that in some cases are the result of the opening of the stylolites formed in the previous deformation phase (fig. 4.28H). Calcite C4 also constitutes the slickenlines observed in faults 3A. Calcite C4 is formed by

bright and dull orange zoned twinned calcite crystals with  $\delta^{18}\text{O}$  values about -23‰ vPDB and  $\delta^{13}\text{C}$  values about -7.5‰ vPDB (fig. 4.28I). Finally, the second generation of laumontite (L2) precipitated and replaced calcite C4 at the wall of some fractures (fig. 4.28J). Laumontite crystals are tabular, brownish under plane light and from cryptocrystalline to 70  $\mu\text{m}$  in size (fig. 4.28K-L). It cements joints up to 1 mm thick and dilatant breccias, which are formed by granodiorite clasts from 15 to 150  $\mu\text{m}$  in size separated by fractures up to 50  $\mu\text{m}$  wide cemented by laumontite L2 (fig. 4.28L). Chlorite, laumontite L1 and calcite C4 were mainly precipitated in the Torrent del Corró outcrop, whereas laumontite L2 is the main neoformed mineral cementing most of the fractures and breccias in the Camí d'en Cisa outcrop.

Type 3B joints have been only recognized in the Enric outcrop. They have irregular walls up to 250  $\mu\text{m}$  wide and are cemented by calcite C3b. This calcite is formed by anhedral crystals up to 30  $\mu\text{m}$  in size with orange luminescence increasing in brightness towards the borders (fig. 4.27H). This increase in luminescence is also reflected in the increase in Mn content, up to 6445 ppm (table 2, appendix 1). Its  $\delta^{18}\text{O}$  value is -18.4‰ vPDB and its  $\delta^{13}\text{C}$  value is -6.1‰ vPDB (table 1, appendix 1).

### **Deformation phase 5: iron oxide wispy seams**

Iron oxide seams are thin (<1 mm), undulose and discontinuous and have been classified as wispy seams (Koepnick 1984). They crosscut both type 3A crack-seals and type 3B joints filled by calcite C3b (fig. 4.29).



**Figure 4.29.** Wispy seam crosscutting a crack-seal vein (plane light).

### **Deformation phase 6: cataclasites and C5, C6, PC1 and diagenetic products**

Type 3D include the reactivation of previous main 3A faults and newly formed faults affecting the Miocene conglomerates.

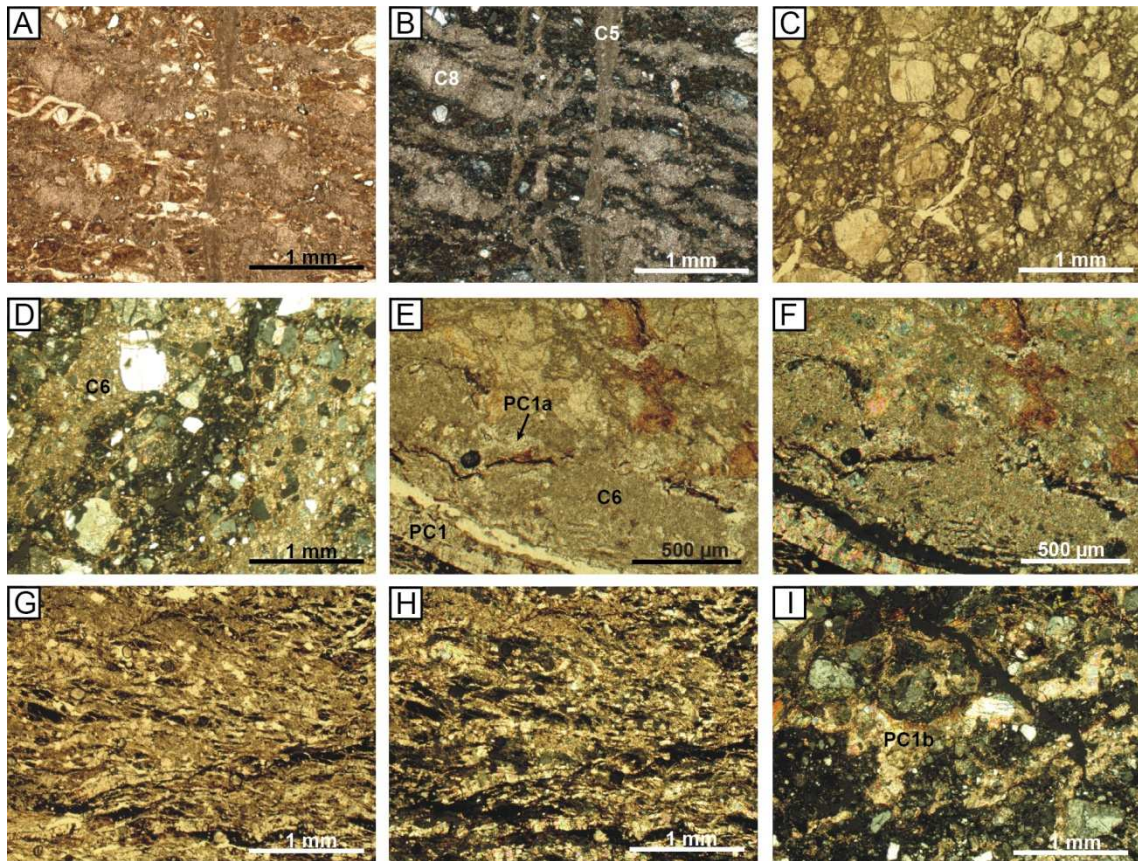
In the Hospital outcrop, a type 3D normal fault puts in contact Silurian rocks with late Miocene rocks. No deformation products have been observed in the Miocene rocks. On the opposite, the Silurian black shales accomodate all the deformation through the development of a penetrative foliation.

In the Enric outcrop, the gouge is affected by mode I fractures filled by cement C5 (fig. 4.30A-B). Cement C5 consists of bright orange luminescent microsparite calcite crystals with a  $\delta^{18}\text{O}$  value of  $-5.8\text{‰}$  vPDB and a  $\delta^{13}\text{C}$  value of  $-7.7\text{‰}$  vPDB (table 1, appendix 1). This cement has Mg content up to 9265 ppm (2981 ppm in average) (table 2, appendix 1).

In the Sariol outcrop, 3D faults generate up to 5 mm wide cataclasite bands in the previous breccia and in the calcitized dolostone. In the former, subangulous clasts, from 10  $\mu\text{m}$  to 2 mm in size, are contained in a fine grained matrix whereas in the cataclasite of the calcitized dolostone, subrounded clasts from 200  $\mu\text{m}$  to 5 mm in size have a heterogeneous distribution. Both fault rocks are cemented by a non-luminescent microsparitic calcite-to-dolomite cement C6 (fig. 4.30C-F). Fe content of cement C6 ranges from 576 to 8698 ppm and its  $\delta^{18}\text{O}$  values range from  $-2.9$  to  $-2.6\text{‰}$  vPDB and the  $\delta^{13}\text{C}$  is about  $-7.6\text{‰}$  vPDB. Finally, some faults were cemented by palisade cement PC1 (fig. 4.30G-H). This cement displays a laminar disposition parallel to the fault wall and it is formed by submillimetric thick laminae. The palisade is formed by 200  $\mu\text{m}$  long and 10  $\mu\text{m}$  wide bladed crystals of low-Mg calcite, high-Mg calcite and dolomite. The first laminae are constituted by non-luminescent dolomite and high-Mg calcite (PC1a) and the last laminae are constituted by orange luminescent low-Mg calcite (PC1b). Vug porosity in the calcitized dolostone cataclasite is cemented by the first cement (PC1a) (fig. 4.30E-F) whereas in the granodiorite cataclasite is cemented by the second cement (PC1b) (fig. 4.30I). PC1b has higher Mn and Fe contents than PC1a. The palisade cement has  $\delta^{18}\text{O}$  values between  $-2.7$  and  $-1.9\text{‰}$  vPDB and  $\delta^{13}\text{C}$  values around  $-7.8\text{‰}$  vPDB.

Type 3D faults affecting the rocks of the hangingwall, generally, do not develop fault cores and damage zone, with the exception of the Caritg outcrop, where cataclasites were formed. Cataclasites are formed by a red muddy matrix and clasts ranging from less than 1 mm to 3 cm that represent about 7 to 25% of the rock volume. As in the Miocene conglomerates, clasts have a wide range of lithologies with phyllites and

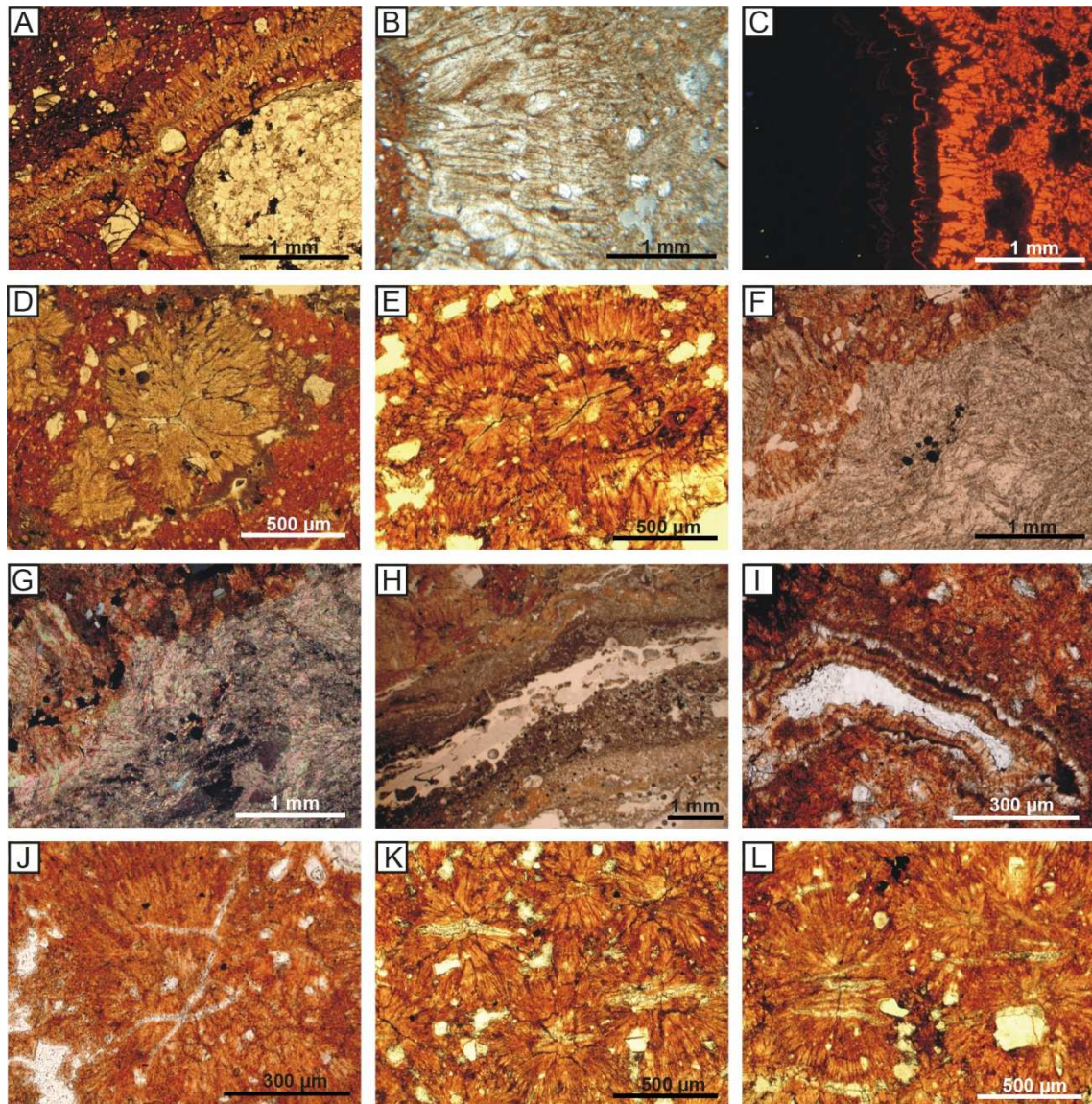




**Figure 4.30.** A-B) Plane and cross-polarized images of fractures filled with calcite C5 affecting the gouge. C-D) Plane and cross-polarized images of the cataclasite developed on the previous granodiorite random breccia. E-F) Plane and cross-polarized images of the cataclasite developed in the calcicite dolostone of the hanging-wall. Observe vug porosity filled with cement PC1a. G-H) Palisade PC1 domain. I) Porosity filled with calcite PC1b in the granodiorite cataclasite.

quartzites (approx. 43% each one) the dominant types. Other clasts are monocrystalline and polycrystalline quartz, knotted hornfels, orthose grains, sandstones and porphyries. As also occurs in the host rock, clasts are mostly angular but phyllites and hornfels are subrounded. Clasts show a random fabric. The matrix is formed by grains smaller than 50  $\mu\text{m}$ . These grains are quartz, potassium feldspar, apatite, iron oxides (probably goethite), titanium oxides, illite, chlorite, kaolinite, mixed-layers of illite–chlorite. However, the fabric of these fault rocks is overprinted by diagenetic processes. According to the texture and the delimitation of conspicuous domains, the main diagenetic products are (fig. 4.31A-I): 1) **orange bladed calcite aggregates**. Two aggregates are present, spherulites, up to 2-3 mm in diameter, and palisades. Orange bladed calcite is non-luminescent or bright orange luminescent. The former is found in all the aggregates, whereas the luminescent is only present in the nucleus of some spherulites and palisades; 2) **white bladed calcite domains**. Calcite crystals are translucent and show a bright orange luminescence. They form palisades but not so well





**Figure 4.31.** Diagenetic products developed in the cataclasites of the Caritg hill. A) Plane light image of a palisade aggregate formed by orange bladed calcite. B-C) Plane light and cathodoluminescence images of an orange bladed calcite palisade. Observe the luminescent nucleous and the non-luminescent borders. D-E) Plane light images of spherulites of orange bladed calcite. F-G) Plane and cross-polarized light images of the contact between the orange and white bladed calcites. H) Micrite strip and channel porosity. I) Vug porosity partially filled with bladed calcite alternating with clays (plane light). J-L) Plane light images of spherulites crosscut by microfractures.

defined as in the previous domain; 3) **micrite strips**. Micrite strips are 4 mm wide and are constituted by non-luminescent crystals; and, 4) **calcite cement filling vug and channel porosity**. Vugs are irregular and range from 0.3 to 2.5 mm in diameter. Channels have a variable width between 0.1 and 0.7 mm and generally have anastomosing arrangements. There are three types of cements in the porosity: blocky calcite, rim bladed calcite and alternating layers of clear bladed calcite with clays. All porosity cements are non-luminescent. These diagenetic products are aligned along two

main directions in the fault rock. One direction is subparallel to the fault plane, whereas the other forms at an angle of 30-45° relative to the fault plane. In turn, these products are crosscut by late microfractures filled with calcite cement (fig. 4.31J-L). Orange bladed calcite, white bladed calcite and micrite do not show important isotopic differences and plot in the same area. The  $\delta^{18}\text{O}$  ranges from -4.4 to -3.9‰ vPDB and the  $\delta^{13}\text{C}$  has negative values that range from -10.3 to -9.0‰ VPDB (table 1, appendix 1). Elemental composition of all the diagenetic products is shown in table 3 (appendix 1).

The second fracture family of this deformation phase are type 3E open joints, which result from the opening of previous faults (fig. 4.16E).

#### **Deformation phase 7: soils and karst**

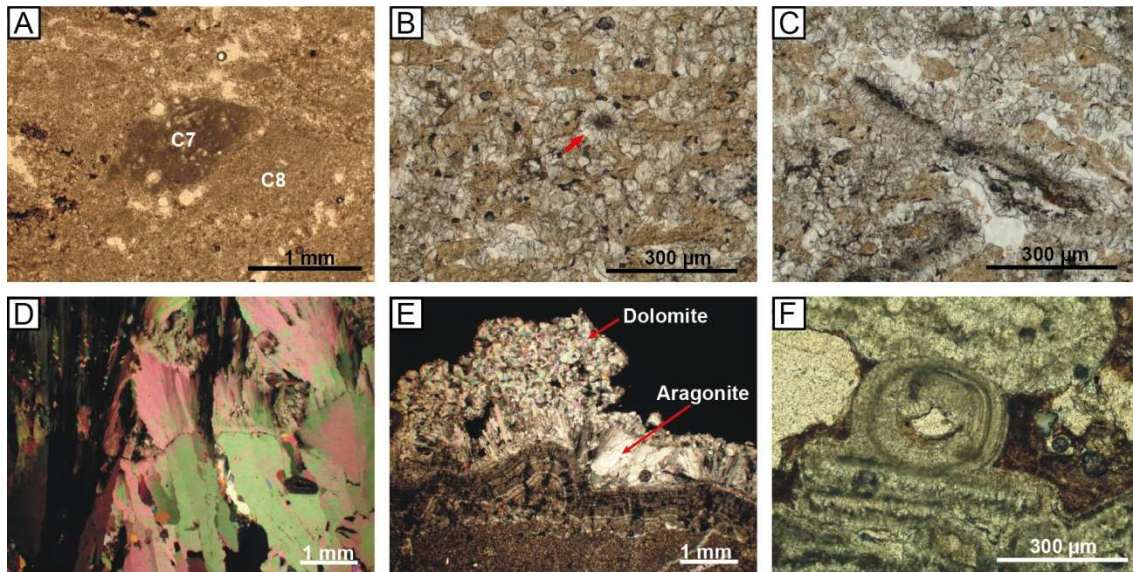
The last fault generation identified in the study areas is type 3F strike-slip faults.

Soil and karstic processes developed in previous fault planes after tectonic activity, as it is shown by the lack of fractures affecting them.

The event of soil development occurred in the fault gouge of the Enric outcrop, giving cohesivity to the fault rock. Two cements are recognised: cement C7 consists of micritic orange luminescent high-Mg calcite crystals that form nodules between 1 mm and 1 cm of diameter that include fragments of quartz and feldspar (fig. 4.32A). Cement C8 is constituted by anhedral sparitic non-luminescent high-Mg calcite crystals up to 30  $\mu\text{m}$  in size that forms a centimetric carbonate level that contains the nodules of cement C7 (fig. 4.32B). Crystals show spherulitic and “corn-cob” arrangements (fig. 4.32C). This cement has  $\delta^{18}\text{O}$  values between -2.9 and -2.5‰ vPDB and  $\delta^{13}\text{C}$  values between -8.5 and -8.3‰ vPDB.

The karstic system developed in M1 dolostones produced collapsed breccias and precipitation of speleothems on the fault planes of fractures 3A and 3E. Speleothems are made of calcite, aragonite, high-Mg calcite and dolomite and are formed by bladed and fibrous palisades, rafts or cavern pearls (fig. 4.32D-F). These speleothems have high Sr contents, especially the ones formed by high-Mg calcite and aragonite, which can reach 13800 ppm and has 7506 ppm in average.  $\delta^{18}\text{O}$  values of speleothems range between -5.3 and -2.6‰ vPDB (being the more enriched the dolomitic ones) and  $\delta^{13}\text{C}$  values between -9.8 and -8.2‰ vPDB.





**Figure 4.32.** Soil and karst products. A) Calcite nodule C7 embedded in an horizon formed by calcite C8 (plane light). B-C) Plane light images of calcite C8 with spherulitic (B) and corn-cob (C) arrangements. D) Cross-polarized image of speleothem formed by High-Mg calcite bladed crystals. E) Speleothem constituted of fibrous aragonite crystals and sparry dolomite and calcite crystals (cross-polarized light). F) Pearls and fragments of rafts (plane light).

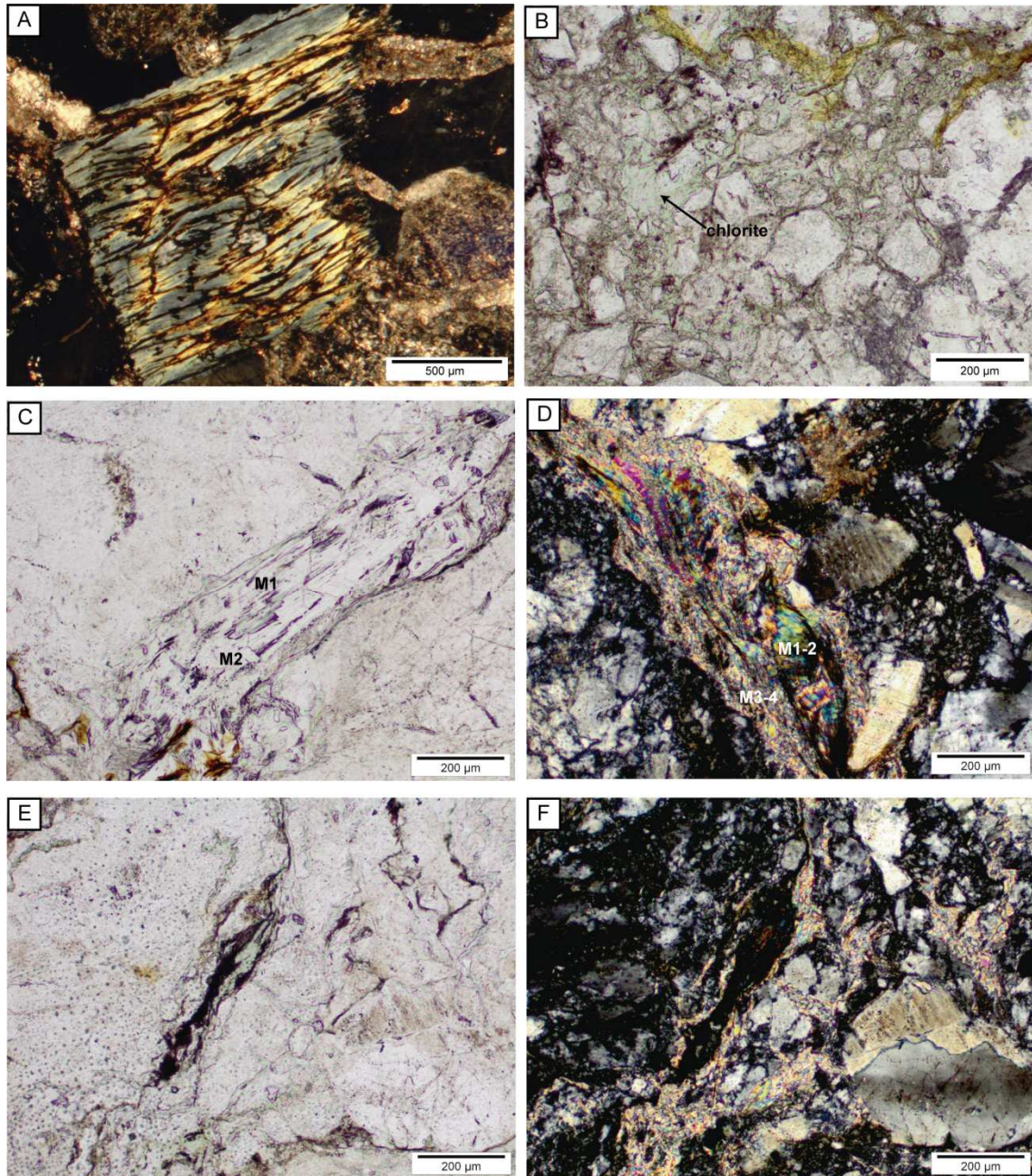
#### 4.5. Pressure and temperature estimates

As P-T conditions are estimated from chlorite and mica equilibrium, a brief petrographic description of these minerals is required.

Two types of chlorite were identified. The first one is the result of biotite alteration and it is only identified in the Hospital outcrop (fig. 4.33A). This chlorite is recognized because it alternates with biotite sheets and has prismatic morphology and/or a marked cleavage of the previous biotite. It has a strong pleochroism from yellow to bright or dark green. The second type is constituted by neofomed chlorite that precipitates in type 1B and type 3A faults or as patches in the cataclasite matrix (fig. 4.33B). The crystals are larger when precipitate in fractures (200  $\mu\text{m}$ -1 mm) than in the cataclasite matrix (7-150  $\mu\text{m}$ ). This chlorite usually shows an irregular and amoeboid morphology and has slight or no pleochroism.

Two groups of K-white mica have been texturally differentiated: a coarse idiomorphic K-white mica between 0.2 and 1.1 mm long in the slightly brecciated granodiorite of the Vallès fault and later small flakes of K-white mica between 15 and 90  $\mu\text{m}$  in size that crystallize along type 1B faults crosscutting or overgrowing detrital flakes of the previous mica (fig. 4.33C-D). The coarse K-white mica is formed by a core with marked cleavage (M1) rimmed by another white mica with poor cleavage (M2). The





**Figure 4.33.** Microphotographs of chlorite and mica from Hospital and Vallès faults. A) Chlorite resulting from biotite alteration. B) Neoformed chlorite between cataclasite clasts. C) Coarse white mica M1 rimmed by M2. D) Small white mica flakes overgrowing and crosscutting coarse detrital flakes of M1 and M2 mica. E-F) Plane and cross-polarized light photographs of chlorite and mica association in a type 1B fracture.

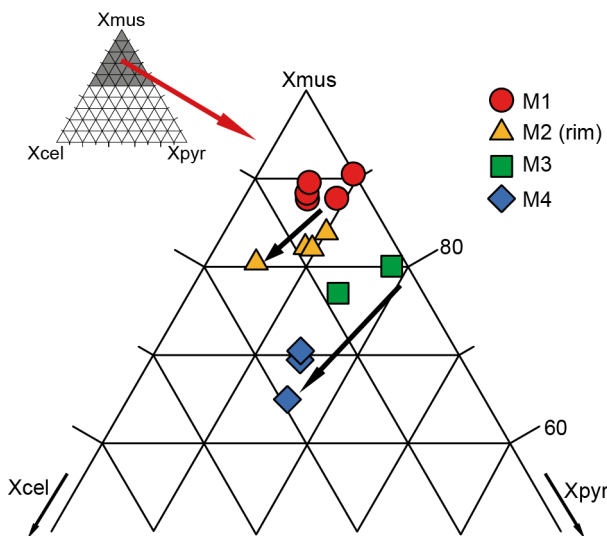
small flakes crystallize together with chlorite in type 1B faults (fig. 4.33E-F). These flakes are named M3 and M4 according to chemical criteria (see section 4.5.1).

### 4.5.1. Chemical variations and thermobarometry

#### K-white mica

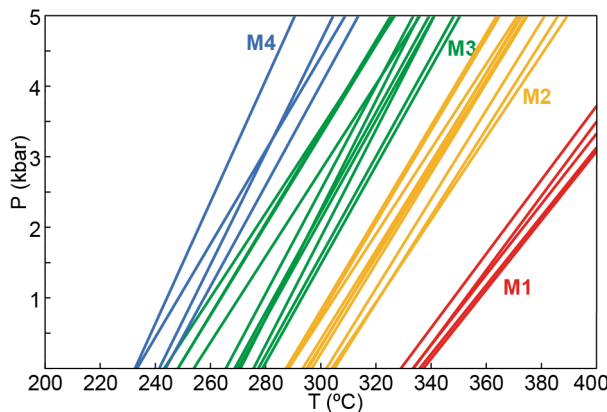
The two groups of K-white mica previously described, coarse idiomorphic (M1-M2)

and later small flakes (M3-M4), show muscovite/pyrophyllite ratios of 0.9 and 0.8, respectively (fig. 4.34). M1-M2 mica is muscovite-richer than M3-M4 mica. However, independently from this ratio, both kinds show the same trend, which is marked by an increase of the celadonite proportion associated with a decrease in muscovite and pyrophyllite end-member proportions from M1 to M2 and M3 to M4, respectively (black arrows, figure 4.34). The small flakes that postdate M1-M2 mica are named M3 and M4, where M4 are the celadonite-rich ones. These two trends correspond to two growing events characterized by different mica shapes, P-T conditions and probably bulk rock compositions. The average K-white mica compositions of each group and the corresponding structural formulas are listed in table 4 (appendix 1).



**Figure 4.34.** Ternary plot muscovite (mus)-celadonite (cel)-pyrophyllite (pyr) of mica in fault rocks of the Vallès fault.

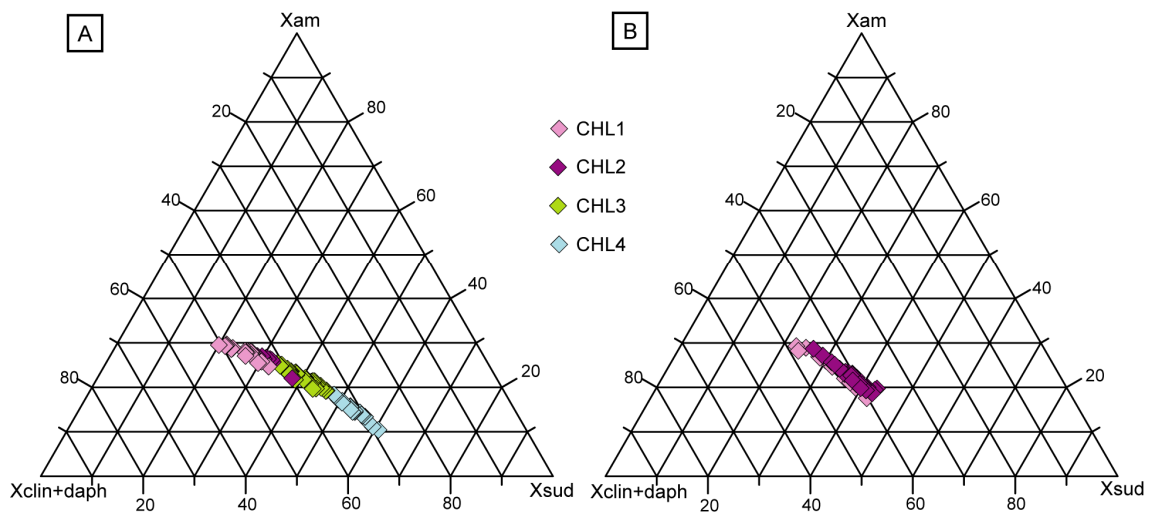
A P-T line corresponding to the equilibrium between K-white mica, quartz and water was calculated for each mica composition using the method proposed by Dubacq et al. (2010) (fig. 4.35). At a fixed pressure of 1 kbar, muscovite-rich M1 and M2 K-white mica show higher temperature (360 and 310°C, respectively) than the pyrophyllite-rich M3 and M4 K-white mica (270 and 250°C, respectively).



**Figure 4.35.** P-T diagram showing the results of mica-quartz-water thermometer for the four groups of mica.

## Chlorite

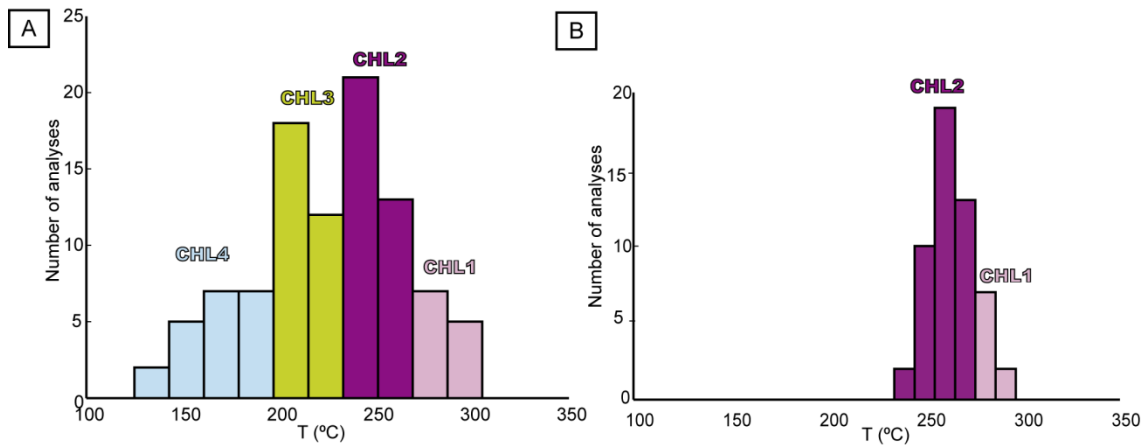
The chlorite compositions were plotted into a (Mg, Fe)-amesite, clinochlore+daphnite and (Mg, Fe)-sudoite ternary diagram, using the structural formulas calculated with the  $\text{Fe}^{3+}$  content predicted by the convergence of R1 to R4. The chlorite compositions evolve along a trend corresponding to a decrease in amesite, clinochlore and daphnite and an increase in sudoite end-member proportion (fig. 4.36). Sudoite proportion increases from 0.2 to 0.6 in the Vallès fault and 0.2 to 0.45 in the Hospital fault. The chlorite compositions and corresponding structural formulas are listed in table 5 and 6 (appendix 1).



**Figure 4.36.** Ternary plot amesite (am)-clinochlore+daphnite (clin+daph)- sudoite (sud) of chlorite in fault rocks. A) Vallès fault. B) Hospital fault.

The chlorite-quartz-water equilibria (R1 to R4) are located at temperatures between 125 and 310°C in the Vallès fault and between 240 and 310°C in the Hospital fault at 1 kbar (absolute error about  $\pm 50^\circ\text{C}$ ). The temperature histogram allows to differentiate four generations of chlorites within the Vallès fault: CHL1 from 260 to 310°C ( $\text{XFe}^{3+}=0.24$ ), CHL2 from 240 to 260°C ( $\text{XFe}^{3+}=0.28$ ), CHL3 from 190 to 240°C ( $\text{XFe}^{3+}=0.33$ ), and, CHL4 from 125 to 190°C ( $\text{XFe}^{3+}=0.41$ ) (fig. 4.37A, table 5 and 6 (appendix 1)). The former two groups, CHL1 and CHL2, were also identified in the Hospital fault (fig. 4.37B). The chlorite crystallization temperatures were estimated at 1 kbar, due to regional constraints. Changing the value of pressure within  $\pm 1$  kbar does not change significantly the temperature estimates, because equilibria R1 to R4 are mostly dependent on T over this range of P-T conditions.



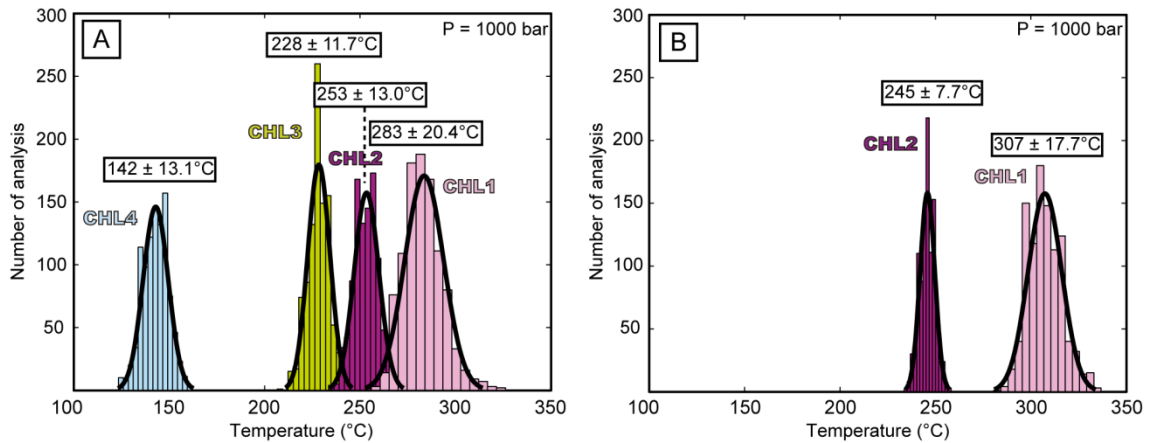


**Figure 4.37.** Histograms of chlorite temperatures. A) Vallès fault. B) Hospital fault.

The uncertainty on the chlorite temperature stemming from the analytical error was investigated in order to verify that the groups of composition-temperature identified above were not an artifact resulting from the analytical uncertainties of the EMPA measurements. A Monte Carlo method was used: 1000 compositions of chlorites were randomly simulated from the average group compositions using a normal distribution. The simulated distribution was set in order to reproduce the measured precision at  $\pm 1$  wt%. The temperature and  $\text{Fe}^{3+}$ -content of each composition was estimated and the results are plotted in the figure 4.38. The estimated temperatures of the groups of chlorite in the Vallès fault are  $283 \pm 20.4$  °C,  $253 \pm 13.0$  °C,  $228 \pm 11.7$  °C and  $142 \pm 13.1$  °C. The temperatures of the two groups in the Hospital fault are  $307 \pm 17.7$  °C and  $245 \pm 7.7$  °C. These results show that the identified groups of chlorites correspond to true distinct groups of composition and temperature of formation. The above Monte Carlo analysis does not take into account the errors resulting from the uncertainties of the thermodynamic data, which cannot be assessed. However, it is emphasized that such errors have a systematic effect on the absolute temperature, but not on the relative values of the chlorite groups. This is the reason why an absolute uncertainty on the temperature estimates of  $\pm 50$ °C was used.

The generations of chlorites are established by chemical criteria and do not correlate with the types of chlorites differentiate petrographically. The relationships with the structural locations are not easy to identify due to the complexity of the recrystallization of chlorite at low temperature (see example in Lanari et al. 2012). However, some 3A faults are mainly filled by low temperature chlorites (corresponding to the CHL4 group)





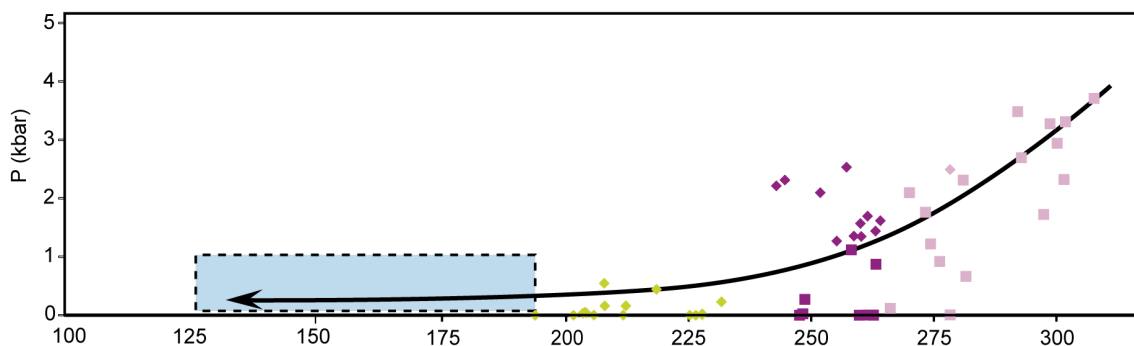
**Figure 4.38.** Histogram of chlorite temperature for each group of chlorite calculated with the compositions from the Monte Carlo simulation.

and most of these chlorites form a rim around high-T chlorites (CHL1 to CHL3 groups), indicating their later formation.

#### 4.5.2. P-T estimates

Chlorite-mica-quartz-water multi-equilibrium approach was applied to chlorite and mica of the Vallès fault. Only equilibrium between chlorite and M3 and M4 mica was obtained, which is coherent with the petrological observations, as only these mica show structural and spatial relationships with chlorite.

The P-T estimates from the chlorite-mica multi-equilibrium show groups of chlorite-mica associations coherent with the previously established chlorite generations (fig. 4.39). The first association is defined by the equilibrium between chlorite and M3 mica and ranges from 260 to 310°C at pressures between 0 and 3.5 kbar  $\pm$  2.5 kbar. The second is defined by the equilibrium between chlorite and M3 and M4 mica. This stage



**Figure 4.39.** P-T path of fault rocks in the Vallès fault. Squares represent chlorite in equilibrium with M3 mica and diamonds represents chlorite in equilibrium with M4 mica. The different colours represents the four chlorite generations. The blue area indicates the location of chlorites under 190°C, which are not in equilibrium with mica.

ranges from 240 to 260°C at P between 0 and  $1 \pm 2.5$  kbar with M3 and P between 1 and 3 kbar with M4. Finally, the third group is defined by chlorite in equilibrium with M4 mica. The P-T conditions of this stage ranges from 190 to 240°C at pressures between 0 and  $0.6 \pm 2$  kbar. Although the scatter and the uncertainty on the calculated P-T conditions are significant, the inferred P-T path followed by the fault rocks in the Vallès fault describes general trend of decreasing temperature and pressure (fig. 4.39).



## 5. DISCUSSION

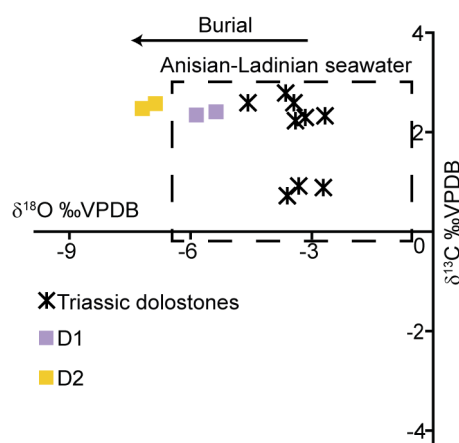
Several points can be discussed from the results presented in this thesis. Basically, there are three points to take into account as: 1) which is the origin of the fluids? 2) how do the fluids evolution during fault development? and, 3) why or how were faults reactivated?

### 5.1. Evolution and origin of fluids

In relation to fluids, this thesis questions the origin and timing for dolomitization, the effect of diagenetic processes in fault rocks and the timing of the different deformation phases from the geochemical characteristics of fluids and the degree of fluid-rock interaction.

#### 5.1.1. Diagenesis of the Triassic dolostones

Deposition of the Muschelkalk facies occurred in carbonate ramps during the Anisian (M1) and Ladinian (M3) (Calvet et al. 1990), synchronously to the first Mesozoic rifting event that lasted from Late Permian to Middle Jurassic (Salas & Casas 1993; Salas et al. 2001). Previous studies interpreted the dolomitization of M1 facies penecontemporaneous to sedimentation (Virgili 1957) and Ramon & Calvet (1987) specified that the lower dolomitic units were the result of a *mixed water* model of dolomitization. With regard to M3 facies, Tucker & Marshall (2004) proposed an early dolomitization process from seawater and a later



**Figure 5.1.**  $\delta^{18}\text{O}$ - $\delta^{13}\text{C}$  plot of the Triassic host rocks and the first fault-related dolomitic cements. Dolomitic cements (D1 and D2) are progressively more  $\delta^{18}\text{O}$ -depleted than the host rocks but maintain their  $\delta^{13}\text{C}$  values.

recrystallization process as the responsible of the  $\delta^{18}\text{O}$ -shift towards more depleted values. The  $\delta^{18}\text{O}$  and  $\delta^{13}\text{C}$  values of the M1 and M3 dolostones cropping out in the studied area fall within the box of the Anisian-Ladinian seawater (Veizer et al. 1999) (fig. 5.1). Moreover, these Triassic dolostones show non-destructive fabrics indicating that dolomitization occurred during an early event (Tucker & Marshall 2004). Both points suggest that dolomitization was produced by marine Triassic waters almost

coevally to sedimentation. However, M1 facies suffered two dolomitization processes as denoted by the presence of the replacive dolomite RD1, which is probably related with the dolomitization of M3 facies, and therefore not all the observed dolomitization is syn-sedimentary.

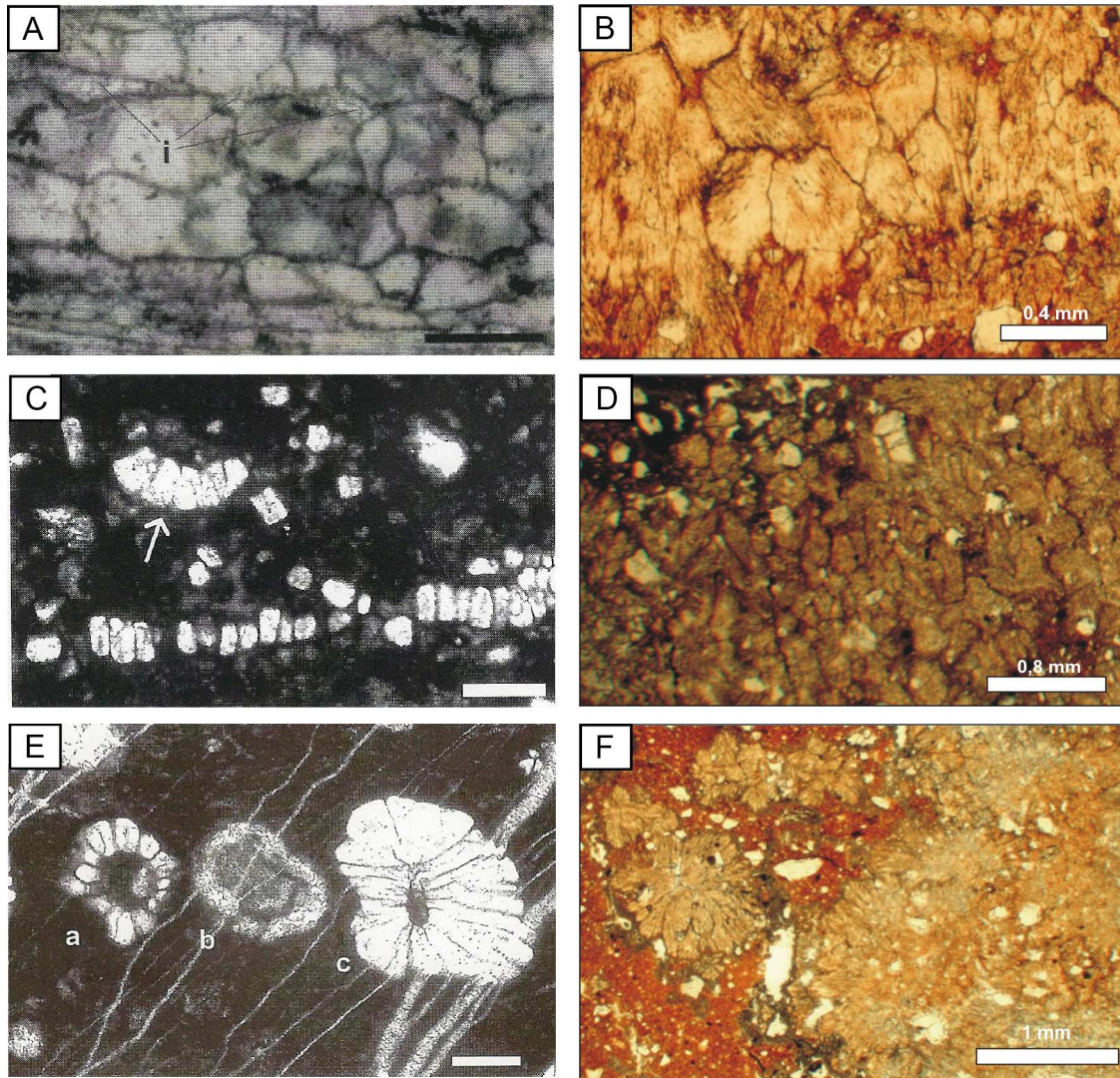
### 5.1.2. Diagenesis of the Miocene fault rocks

The Miocene fault rocks are affected by pedogenic processes. Overprinting relationships between fractures and diagenetic products modify the nature of the original fault rock and therefore also its preliminary classification.

The following features related to these diagenetic products support the interpretation of the textures as *Microcodium*: 1) the calcite mineralogy of crystals; 2) the equant and bladed habit of calcite crystals and their internal fibrous textures (Kabanov et al. 2008) (fig. 5.2 A-D); 3) the crystal arrangement forming spherulites, palisades and “corn-cobs” (fig. 5.2C-F) (Lucas & Montenat 1967; Bodergat 1974; Klappa 1978; Kabanov et al. 2008; Košir 2004); 4) the destructive and principally matrix selective replacement of the fault rock through the dissolution front surrounding the calcite crystals (Klappa 1978); and, 5) the concentration of replacement along discontinuity surfaces, fractures in this case (Alonso-Zarza & Jones 2007; Kabanov et al. 2008).

In the studied case, pedogenic products are only present in the faults. Inside the fault rock, they are oriented following two main directions, probably related to previous microfractures. However, typical *Microcodium* crystals have a rounded border and are translucent whereas the crystals here are orange and are formed by fibrous aggregates. The spherulites and palisades described here are also very similar to the pseudospherulitic fibrous calcite of Rossi and Cañaveras (1999) who interpreted them as the calcitization of bacterial colonies (fig. 5.3). In both cases, their cathodoluminescence behaviour shows concentric changes but their spherulites are composed of a single crystal and not polycrystalline aggregates (fig. 5.4).

Traditionally, the more extended interpretation of *Microcodium* is of originating as the result of the calcitization of root cells, with or without a mycorrhizal association (Calvet et al. 1975; Klappa 1978; Košir 2004). However, other investigations point to an induced mineralization driven by saprotrophic microorganisms or a microbial association (Lucas & Montenat 1967; Bodergat 1974; Kabanov et al. 2008). In this case,

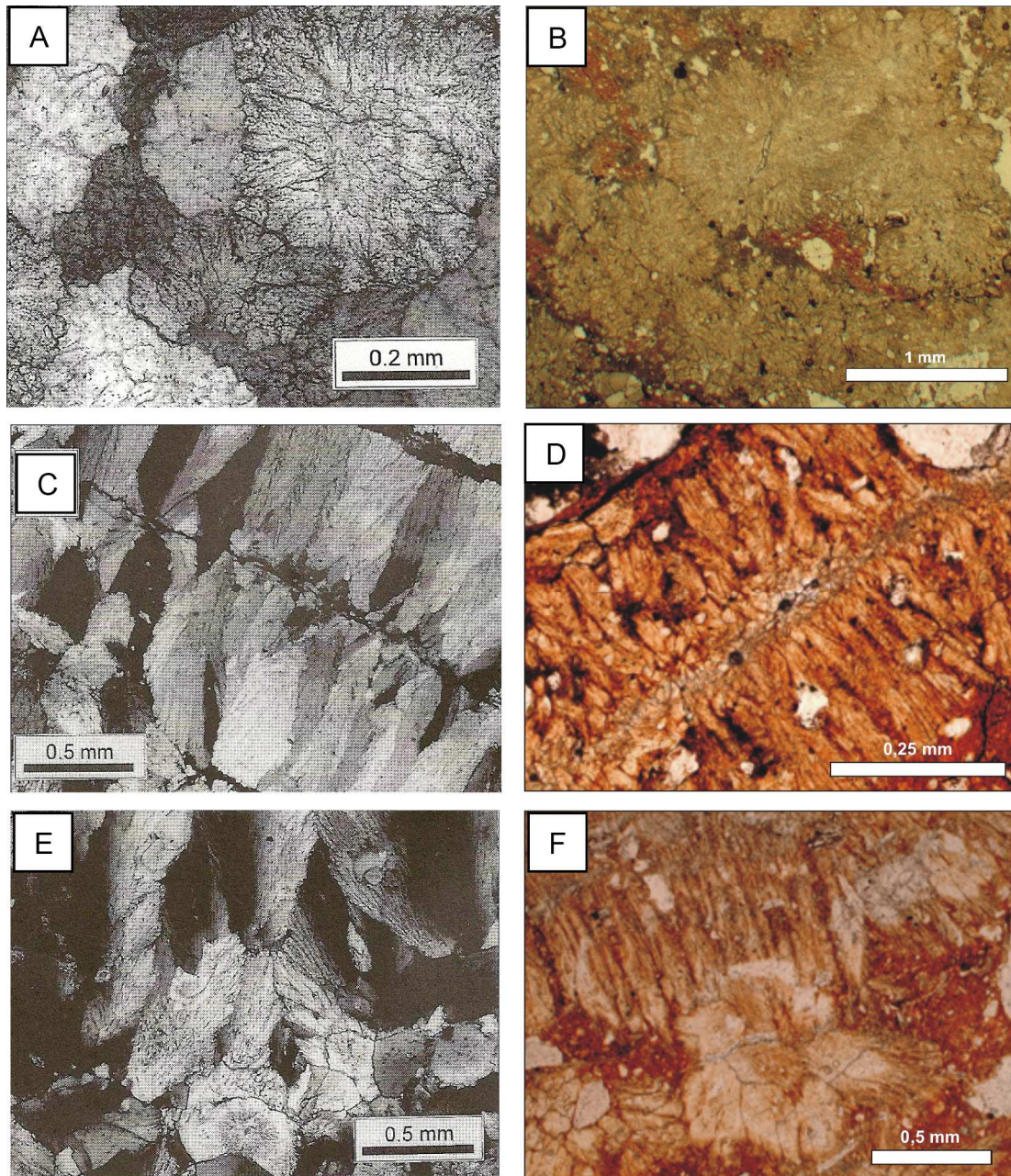


**Figure 5.2.** Comparison of *Microcodium* images of Košir (2004) (left column) with images of the pedogenic structures within the fault rocks of the Miocene conglomerates (right column, plane light). A-B) Equant calcite mosaic. Scale bar in A is 200  $\mu\text{m}$ . C-D) Bladed crystals forming palisades. Scale bar in C is 0.5 mm. E-F) Spherulites. Scale bar in E is 100  $\mu\text{m}$ .

the low  $\delta^{13}\text{C}$  values (from -10.3 to -9.0‰ VPDB) indicate the influence of soil-derived  $\text{CO}_2$ . Thus, a pedogenic process led to the growth of the calcite crystals that corroded the fault rock. This, together with the lack of microbial observations during the SEM analysis, point to processes associated with roots.

In the meteoric environment, where pedogenic processes take place, local waters have low Mg/Ca ratio, low content of Sr and  $\delta^{18}\text{O}$  values lower than -4‰ SMOW. Therefore, the dominant carbonate mineral is low-Mg calcite. Then, how to explain the presence of high-Mg calcite (up to 18766 ppm), high contents of Sr (up to 4311 ppm) and high values of  $\delta^{18}\text{O}$  (up to -3.9‰ VPDB) in a pedogenic environment? Watts (1980) showed the presence of high-Mg calcite, aragonite and dolomite in Quaternary calcretes from

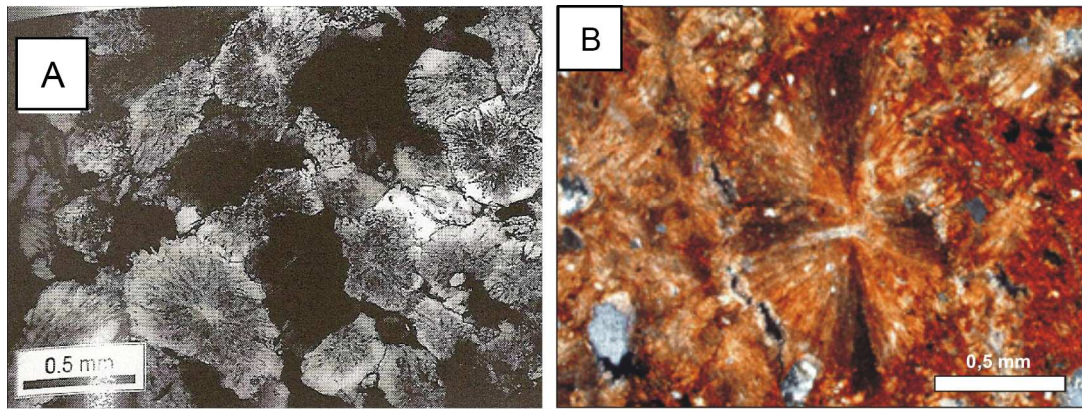




**Figure 5.3.** Comparison of the diagenetic features of Rossi & Cañaveras (1999) (left column) with images of the pedogenic structures within the fault rocks of the Miocene conglomerates showing clear resemblances.

the Kalahari area (southern Africa). He explained that high-Mg calcite and aragonite precipitate when there is a rapid evaporation and/or  $\text{CO}_2$  loss whereas low-Mg calcite precipitates when there is a slow evaporation and/or  $\text{CO}_2$  loss. In addition, McQueen et al. (1999) observed a vertical and lateral evolution of the carbonate mineralogy of regolith carbonates of southeastern Australia. They found an increase of the Mg content with depth due to changes in pH and  $\text{pCO}_2$  during the percolation of rainwater and argued that the lateral evolution was caused by lateral groundwater movements along the bedrock-alluvium boundary. None evidence of vertical and lateral evolution from



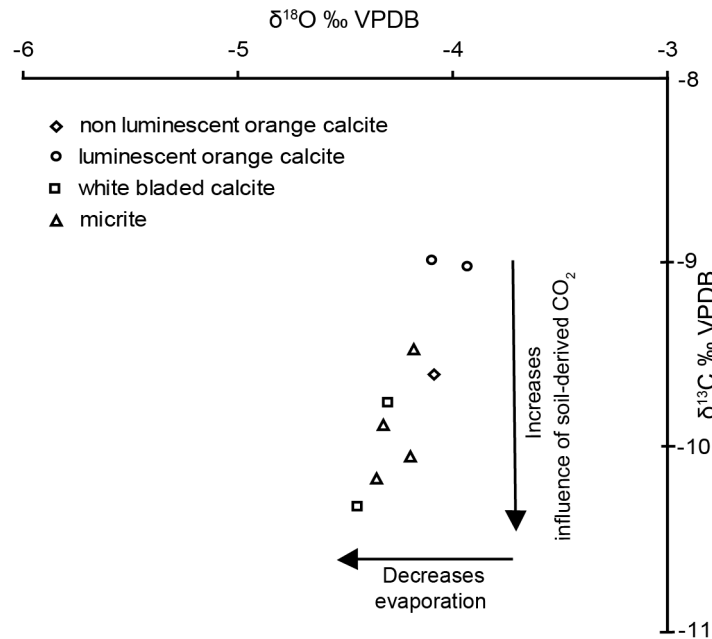


**Figure 5.4.** Difference between the pseudospherulites of Rossi & Cañaveras (1999) (left column) and spherulites of the fault rocks of the Miocene conglomerates. A) Spherulites are formed by an unique crystal (cross-polarized light). B) Spherulites are formed by different crystals showing independent extinction (cross-polarized light).

calcite to dolomite has been detected. So, to determine the origin of the fluid responsible for the calcite precipitation, we have compared the studied setting with the high-Mg calcite settings described by Watts (1980).

In the first setting, the calcretes described by Watts (1980) developed in Mg-rich host materials where high-Mg calcite precipitates from vadose waters enriched in Mg. The Miocene conglomerates have not sufficient Mg to produce this water enrichment. In addition, the fluids cannot be derived from the basement because faults are narrow, shallow and enclosed by clay-rich layers and the  $\delta^{18}\text{O}$  values, from -4.4 to -3.9‰ VPDB, do not support elevated temperatures.

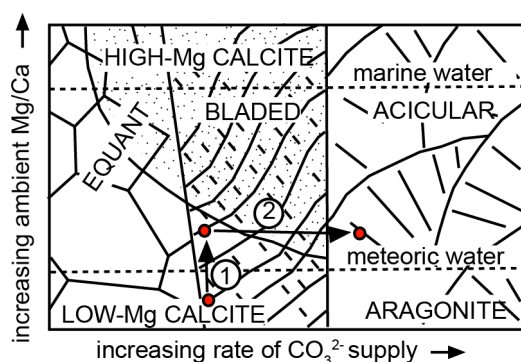
In a second case study, Watts (1980) outlines the development of calcretes in and around saline depressions where groundwaters are enriched in Mg compared to vadose water and carbonate precipitation is stimulated by  $\text{CO}_2$  loss during capillary rise. Although no brines have been identified, the outcrops are only 1.5 km far from the Mediterranean Sea. Moreover, during the late Burdigalian, Langhian and Serravallian, marine transgressions and highstand sea levels extended into the study area (Cabrera & Calvet 1996). It is therefore possible that the groundwaters were a mixture of meteoric and marine waters, which would be enriched in Mg and Sr. This would explain the mineralogy and elemental composition and also the  $\delta^{18}\text{O}$  values (James & Choquette 1990). In addition, cathodoluminescence would reflect the dominant water in the mixing zone, marine in luminescent cements and meteoric in non-luminescent cements. However, the elevated Sr contents of cements suggest a formation water composition for the fluid rather than a marine origin.



**Figure 5.5.** Stable isotope results of the main diagenetic products. For the orange bladed calcite, luminescence variations (from luminescent in the nucleus to non-luminescent in the borders) are related to an increase in the influence of soil-derived  $\text{CO}_2$  and a decrease of evaporation.

In the third case, high-Mg calcite appears in immature calcretes developed in Mg-poor sands with a low Mg/Ca ratio of vadose waters and carbonate precipitation occurs because of an enhanced evaporation. As earlier stated, the samples in this study have  $\delta^{18}\text{O}$  values ranging from -4.4 to -3.9‰ VPDB (fig. 5.5). If we assume precipitation temperature of 25°C, calcites would have precipitated from fluids with -2.2‰ SMOW, which marks the loss of  $^{16}\text{O}$  by evaporation. Moreover, paleoclimatic conditions between the Burdigalian and Langhian were warm, seasonal and arid tropical-subtropical with paleotemperatures between 15.5 and 24.6°C, even higher in the Serravallian (Cabrera & Calvet 1996). This paleoclimate could account for the required evaporation. In addition, the forced crystallization of carbonates in our study does not produce metastable thermodynamic equilibrium between high-Mg calcite and waters, so partition coefficients cannot be applied (Watts 1980; Tucker & Wright 1990). Finally, cathodoluminescence changes are probably related to oscillations of the water table that generate Eh-pH variations during the development of the diagenetic products. However, high-Mg calcite in this context was only formed as anhedral micrite. Although this third case is consistent with the observations in this study, we suggest that biota plays an important role and, together with evaporation, induces high-Mg calcite precipitation from a meteoric water. The  $\delta^{13}\text{C}$  values lower than -9‰ VPDB support biota implication. The luminescent calcite, the first to precipitate, is always low-Mg calcite

whereas the non-luminescent calcite is both low-Mg and high-Mg calcite. The mineralogical change is caused by an initial increase of temperature, followed by an increase of  $\text{CO}_3^{2-}$  supply rate. The  $\text{CO}_3^{2-}$  is the result of increased  $\text{CO}_2$  generation by plant respiration and the decomposition of organic acid anions exuded by the roots (Manning 2008). Luminescent cements precipitated from meteoric water that increased its Mg/Ca ratio because of evaporation but still precipitated low-Mg calcite (fig.5.6). As vegetation or microorganisms matured, the rate of  $\text{CO}_3^{2-}$  supply increased. This would have caused the change from low-Mg bladed calcite precipitation to high-Mg bladed calcite and to acicular aragonite precipitation (Tucker & Wright 1990) and would explain why crystals pass from bladed to an aggregate of fibres (fig.5.6). During this last period, evaporation decreased. The change of evaporation conditions and the influence of soil are marked by  $\delta^{18}\text{O}$  and  $\delta^{13}\text{C}$ , respectively. The luminescent nucleus of orange bladed calcites, the first to precipitate, have more enriched  $\delta^{18}\text{O}$  and  $\delta^{13}\text{C}$  values than non-luminescent calcites (fig.5.5). This change of evaporation implies a decrease of temperature that could be related to climatic or seasonal fluctuations.



**Figure 5.6.** Factors controlling the precipitation of the pedogenic products. 1) Evaporation increases the Mg/Ca ratio but still low-Mg calcite precipitates. 2) Biota activity become more important and increases the rate of  $\text{CO}_3^{2-}$  supply. This increase causes the change from low-Mg bladed calcite to high-Mg bladed calcite and to acicular aragonite precipitation. This explains the morphology zonations of the orange calcite aggregates (modified from Tucker & Wright 1990).

However, another hypothesis about calcite mineralogy is possible: a neomorphism process that begins in the nucleus of the aggregates and spreads towards the outer part. The reason is that the calcite of the nucleus is more metastable because: 1) it is the first to precipitate and 2) the organic matter of the nucleus is also the first to decompose. This process of neomorphism is similar to that described in calcareous red algae (Calvet 1979). This explanation is supported by a limit between both cements and because luminescent cements show a less preserved morphology. Up to now, we do not have

arguments to accept or reject one or another hypothesis about the initial mineralogy of the nucleus.

On the other hand, it is important to note that these fault rocks because of its cohesive appearance at the outcrop scale and the volume of clasts, from 7 to 25%, were preliminary classified as cataclasites (Sibson 1977). However, the petrologic study has revealed that cohesiveness was given later by the pedogenic products. Thus, the original fault rock was uncohesive, and therefore, it probably was an incohesive cataclasite in origin, which forms in shallower conditions than cohesive ones.

### 5.1.3. Relationships among fluids, deformation phases and tectonic events

The crosscutting relationships of fractures, the P-T estimates from chlorite and mica, and the fault rocks and cements characteristics established in this thesis, together with previous studies about sedimentology (Ramon & Calvet 1987; Calvet et al. 1990), diagenesis (Parcerisa 2002), petrology and geochemistry of veins (Cardellach et al. 2002; Solé et al. 2002; Baqués et al. 2012a,b) and structural works (Bartrina et al. 1992; Roca et al. 1999) has lead to reconstruct the link between paleofluids and fracturing in the studied areas through time.

The **Hercynian compression** is characterized by the development of a regional penetrative foliation associated with tight folds verging to the SW and a later crenulation cleavage (Julivert & Durán 1990a). Also, mylonitic bands of the Enric outcrop have been related to the this tectonic event. After deformation, late-Hercynian igneous rocks intruded the previous Paleozoic sequence and generated contact metamorphism (Enrique 1990). During magma solidification, due to thermal retraction, a network of joints is formed in the border of the igneous mass. In the Vallès fault, crystallization of muscovite, named M1 and M2, and microcline has been observed. Although these micas resemble result of igneous crystallization, two-mica granodiorites have never been described in the area (Enrique 1990). Therefore, these micas have been interpreted as deuterite minerals lining the granite thermal joints (Demange et al. 1996). This kind of alteration is produced by igneous water-rich fluids when the igneous mass is already solidified (Shelley 1983). Therefore, M1 muscovite is formed in fractures produced during the exhumation of the granodiorite at temperatures between 330 and 370°C (range established between the minimum temperature estimated with the mica-quartz-water equilibrium lines and the estimated temperature at 1.5 kbar, depth of

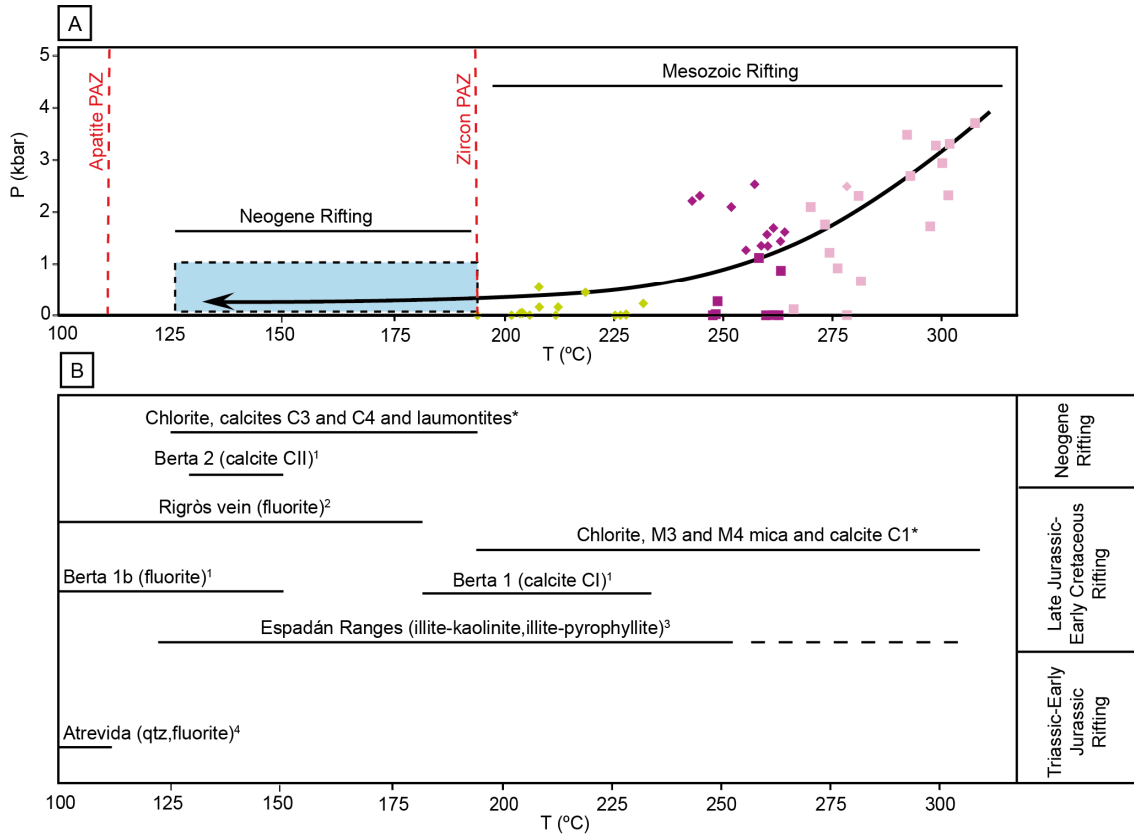


granodiorite emplacement). Pluton exhumation took place during the Permian and reached the surface as denoted by the unconformity between the granodiorite and Triassic materials of Buntsandstein facies outcropping in the area (Gómez-Gras & Ferrer 1999). During this exhumation, M1 muscovite was in turn partially overgrown by M2 muscovite at lower temperatures (between 290 and 330°C).

The first deformation phase is characterized by faults with NE-SW and NW-SE orientations and has been attributed to the **first Mesozoic rifting** because: 1) it has been only identified affecting Triassic rocks, and 2) the isotopic values of the dolomitic cements D1, D2 and D3 precipitated within these faults are consistent with Triassic seawater. The first dolomite cement D1 associated with fractures type 1A fall within the Triassic seawater values, indicating the onset of the Triassic rifting under marine conditions (fig. 5.1). Dolomite cement D2, and probably also D3, associated with fractures type 1A, show more  $\delta^{18}\text{O}$ -depleted values but the same  $\delta^{13}\text{C}$  values than the host rocks and cement D1. Moreover, the elemental geochemistry of dolomite cement D2 is controlled by the host rock in which is precipitating, indicating a high fluid-rock interaction. These facts point to the crystallization of dolomite cements from the Triassic marine water during increasing burial, produced by the rifting, in a closed hydrological regime.

The second deformation phase is characterized by the precipitation of chlorite (190-310°C), M3-M4 mica, calcite C1 and quartz in type 1B normal faults. Fission-track and (U-Th)/He studies with apatites and zircons show that the 190°C isotherm (closure temperature for zircon PAZ) was only crossed during the Mesozoic extension (Juez-Larré 2003), locating the neoformation of chlorite (and their associated minerals), and by extension the second deformation phase (D<sub>2</sub>), within this extensional tectonic event (Fig. 5.7A). However, as the Mesozoic extension is characterized by two rifting events, the obtained data were compared with other works on hydrothermal veins in the Catalan Coastal Ranges and the Iberian Chain in order to match the formation of these minerals with one of the two Mesozoic rift stages (Fig. 5.7B). Cardellach et al. (2002) have attributed temperatures between 190 and 230°C in calcites and quartz of the Berta mine (Montnegre Horst), named calcites CI, to the second Mesozoic rifting. These calcites CI have the same isotopic characteristics than the calcites C1 defined in this work, which are also associated with quartz. Similarly, Martín-Martín et al. (2008) have also associated temperatures between 120 and 300°C in illite-kaolinite and illite-pyrophyllite

associations of the Espadán Ranges (Iberian Chain) with this second Mesozoic rift stage. Comparison with these two areas suggests the formation of chlorite ( $T > 190^{\circ}\text{C}$ ), K-white mica M3 and M4 and calcite C1 in type 1B normal faults during this **second Mesozoic rift stage** (Late Jurassic-Late Cretaceous).



**Figure 5.7.** A) P-T path of fault rocks in the Vallès fault and interpretation of the age through fission-track constraints. Squares represent chlorite in equilibrium with M3 mica and diamonds represents chlorite in equilibrium with M4 mica. The different colours represents the four chlorite generations. The blue area indicates the location of chlorites under  $190^{\circ}\text{C}$ , which are not in equilibrium with mica. B) Temperature and age comparison with other mineralizations of the Catalan Coastal Ranges (Berta, Rigròs and Atrevida) and the Iberian Chain (Espadán Ranges). The asterisk marks the new data obtained in this thesis. 1) Cardellach et al. (2002); 2) Piqué et al. (2008); 3) Martín-Martín et al. (2006, 2008, 2009); 4) Canals et al. (1992).

The temperature estimates from chlorite, linked to a surface paleotemperature of  $20^{\circ}\text{C}$  and the depth conditions during the Mesozoic (up to 3.6 km), yields to a geothermal gradient higher than the regional gradient during the Mesozoic ( $27\text{-}35^{\circ}\text{C}/\text{km}$  according to Juez-Larré (2003)), indicating that hydrothermal fluids migrated upwards through the faults. The equations of Clayton et al. (1972) and O'Neil et al. (1969) were applied in quartz and calcite, respectively, to establish the parental fluid of the hydrothermal brine. The first equation gives values of  $\delta^{18}\text{O}_{\text{water}}$  between  $-1.2$  and  $+3.2\text{‰}$  SMOW indicating that the brine had a marine origin, as it was already postulated by Cardellach et al.

(2002). However, the equation of O'Neil et al. (1969) indicates that calcite C1 precipitated from water with  $\delta^{18}\text{O}$  values between +7 and +10‰ SMOW. Most granitic rocks have  $\delta^{18}\text{O}$  values between +7 and +13‰ SMOW and  $\delta\text{D}$  values between -85 and -50‰ SMOW (Taylor 1977). Isotopic studies of the Late Hercynian intrusive rocks of the Montnegre Horst (Catalan Coastal Ranges) show  $\delta^{18}\text{O}$  values up to +6.1‰ SMOW and  $\delta\text{D}$  values up to -35‰ SMOW suggesting the hydrothermal alteration of the rock by a  $\delta^{18}\text{O}$ -depleted fluid with a low water-rock ratio (Solé et al. 2002). The  $\delta^{18}\text{O}$ -depleted fluid could have had different origins as its original signal has been completely buffered by interaction with the granitic host rock. The low  $\delta^{13}\text{C}$  values of the calcite (from -7.8 to -5.9‰ VPDB) could result of this fluid-rock interaction due to influence of organic matter or be directly the meteoric water signal. If the former point occurred, the most probable source for the low  $\delta^{13}\text{C}$  is the Silurian black shales that crop out in the area, with TOC content between 3 and 8.6%.

Therefore, which is the origin of the fluids and the hydrothermalism during the second Mesozoic rifting?

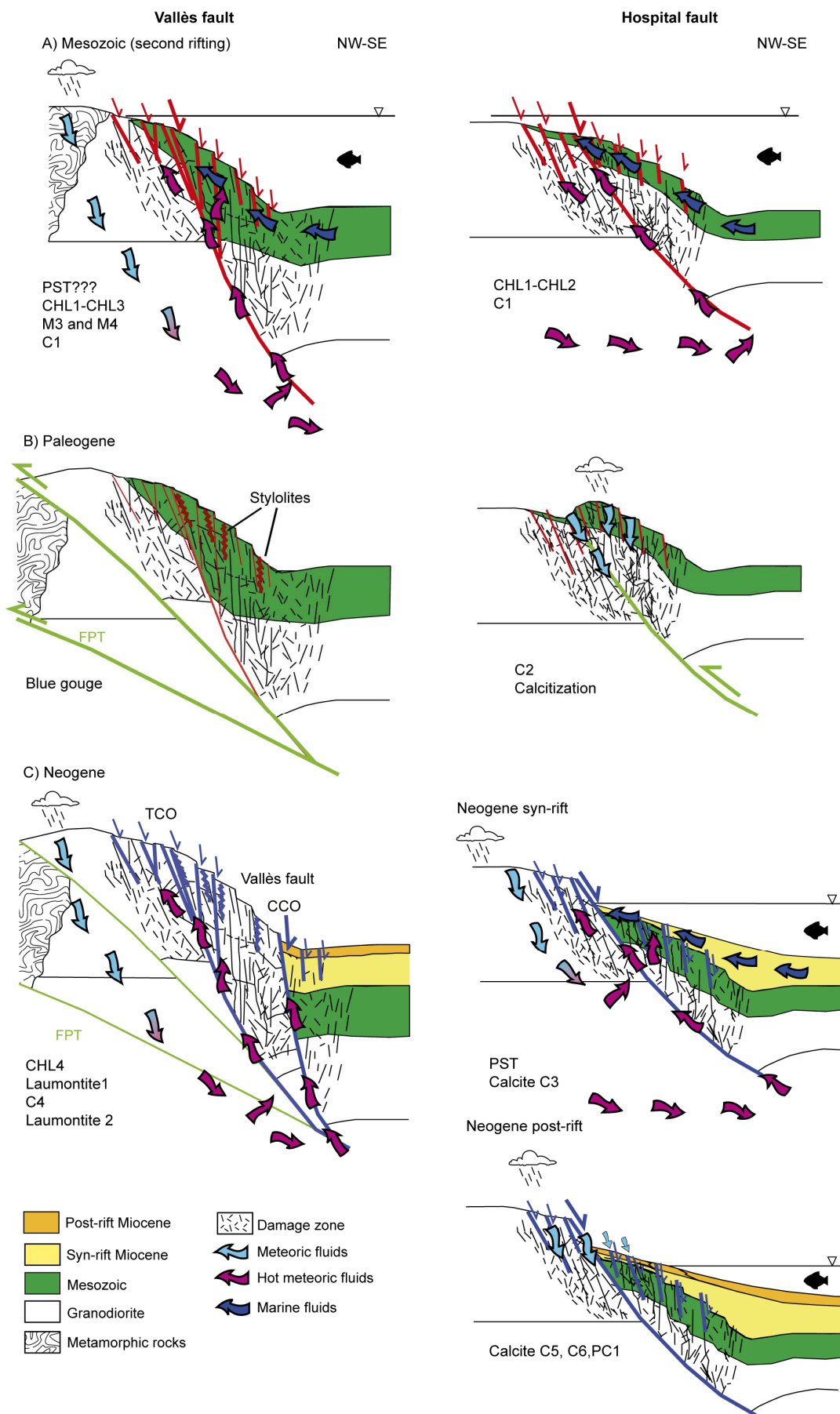
Crustal thinning and volcanism have been rejected to explain the Mesozoic hydrothermalism as the regional geothermal gradient can not produce such temperatures at 3.6 km depth (maximum depth previous to the Paleogene compression) and because magmatism has not been evidenced in the central Catalan Coastal Ranges. Moreover, fission-track data in this area are in agreement with structural and sedimentological observations and only next to fault zones, fission-track data are reset (Juez-Larré 2003). The second Mesozoic rifting mostly took place under marine conditions; however, prolonged periods of emersion occurred during Berriasian-Barremian times (Ebro Massif), probably controlled by normal faulting. These emersions are shown by the presence of karstification and bauxite formation in Kimmeridgian rocks outcropping close to the Barcelona Plain (Combes 1969; Molina & Salas 1993; Salas et al. 2004). Therefore, taking into account the geomorphological configuration during this period, the most plausible mechanism for hydrothermal fluids responsible of calcite C1 precipitation was the infiltration of meteoric waters through the emerged areas, which warmed at depth and interacted with the host rocks, and that upflow through the main fault. Possibly during their upflow, hot fluids mixed with marine waters expelled from the sediments by compaction (fig. 5.8A). This mixing between fluids could have been the responsible for the oscillating cathodoluminescence behavior of cements C1.

The third deformation phase ( $D_3$ ), characterized by type 2 reverse faults and their related cements C2a to C2c and CD1 to CD4 in the Hospital fault and by the gouge and stylolites in the Vallès fault, is attributed to the **Paleogene compression**. On one hand, orientation and compressional axes are coincident with the directions postulated for this tectonic event (Guimerà 1978; Guimerà & Santanach 1978; Anadón et al. 1979). On the other hand, these cements show  $\delta^{18}\text{O}$  and  $\delta^{13}\text{C}$  values ranging from -5.9 to -4.6‰ VPDB and -7.4 to -5.4‰ VPDB, respectively, coinciding with the values of the calcites described by Parcerisa (2002) affecting the Oligocene rocks of the horst (fig. 5.9), which were attributed to the last compressional stage that occurred during the Chattian. The isotopic signal indicates their meteoric origin. The  $\delta^{18}\text{O}$  and  $\delta^{13}\text{C}$  values of the calcitized dolostone, from -9.5 to -4.1‰ VPDB and from -4.8 to -3.2‰ VPDB, respectively, fall between those of the Triassic dolostones and those of the cements attributed to this period (fig. 5.9). In conclusion, the Paleogene compression is characterized by the opening of the hydrological system favoured by the uplift of the horst, which allows the percolation of meteoric fluids responsible of the calcite cements precipitation and the calcitization of the dolomite (fig. 5.8B).

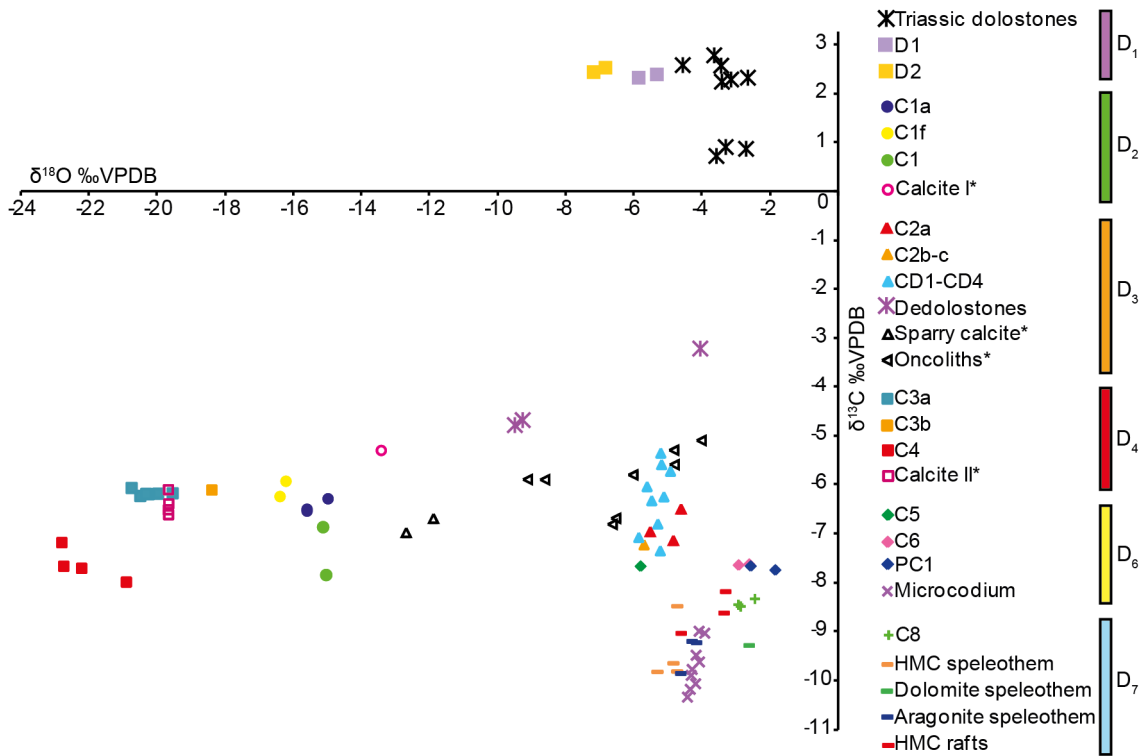
In the Vallès fault, the traces of the Mesozoic normal fault and the Paleogene thrust do not coincide in surface. The thrust fault occurred 125 m further to the north producing, during thrusting, the uplift of part of the footwall with the previous normal faults. This offset is the responsible of the lack of cements linked to compression overprinting the Mesozoic cements of the Vallès fault and of the formation of subvertical stylolites. Instead, a gouge is generated in the thrust planes (fig. 5.8B).

---

**Figure 5.8.** Evolution of the Vallès and Hospital faults from Mesozoic to Neogene. A) Mesozoic extensional event. Topographically driven meteoric fluids, percolating in emerged areas, are warmed at depth and upflow through faults. Due to the submarine conditions of the major part of the basin, these fluids are mixed with marine waters at shallower settings. B) Paleogene compressional event. In the Vallès fault a thrust system uplifts the previous normal fault. Deformation is localized in the thrust faults generating a blue gouge. In the Hospital fault, the previous Mesozoic fault is inverted and percolation of low-temperature meteoric waters occurs. C) Neogene extensional event. During this event, the Neogene normal Vallès fault is formed (CCO) and the reactivation of some of the Mesozoic structures occurs (TCO). Hydrothermal fluids are topographically driven meteoric fluids warmed at depth. In the Hospital fault, syn-rift and post-rift stages differ. During the syn-rift, meteoric hot fluids are mixed with marine waters, as occurred during the Mesozoic. On the opposite, the post-rift is dominated by low-temperature meteoric fluids. TCO, Torrent del Corró outcrop; CCO: Camí d'en Cisa outcrop; FPT, Frontal Paleogene thrust.







**Figure 5.9.** Stable isotope plot of the fault rock cements related to their deformation phase. Values of the cements studied by Parcerisa (2002) (sparry calcite and oncoliths) and Cardellach et al. (2002) (calcite I and calcite II) have been included and marked in the legend with an asterisk.

Normal faults belonging to deformation phases from D<sub>4</sub> to D<sub>7</sub> crosscut the previous reverse faults, pointing to their formation during the **Neogene extension**.

The fourth deformation phase (D<sub>4</sub>) is characterized by the formation of pseudotachylytes and the later precipitation of cements of chlorite ( $T < 190^{\circ}\text{C}$ ), calcite C3 and C4 and laumontite. The temperature conditions of low-temperature chlorite were achieved during both the Mesozoic and the Neogene extensions, as denoted by fission-track and fluid inclusion studies. Fission-track studies demonstrated that the  $110^{\circ}\text{C}$  isotherm (closure temperature for apatite PAZ) was crossed at the onset of the Neogene extension. Studies of fluid inclusions in veins of the Catalan Coastal Ranges have shown that temperatures between  $110^{\circ}\text{C}$  and  $190^{\circ}\text{C}$  were reached during both rifting events, i.e. Mesozoic fluorites of the Rigròs veins (Piqué et al. 2008) and Neogene calcites CII of the Berta mine (Cardellach et al. 2002) (Fig. 5.7B). However, fluorites are not present in the studied outcrops whereas calcite is a common neoformed mineral. Calcites C3 and C4 defined in this thesis show  $\delta^{18}\text{O}$ -depleted values similar to those reported by Cardellach et al. (2002) (fig. 5.9), who attributed these values to the Neogene syn-rift based on the fact that the  $^{87}\text{Sr}/^{86}\text{Sr}$  ratio of vein minerals reflects the Sr

isotopic composition of the host granodiorite nowadays. Summarizing, type 3A and 3B fracture development and their related cements low-temperature chlorite (+calcites C3 and C4 and laumontite) took place during the **Neogene syn-rift**.

The development of pseudotachylytes in type 3A faults of the Hospital fault indicates the seismic activity of some fault segments at the onset of the Neogene extension at about 2.3 km depth (maximum depth conditions according to Juez-Larré (2003)). The temperatures of the later cements, linked to a surface paleotemperature of 20°C and the depth conditions during the syn-rift, yields to a geothermal gradient higher than the regional geothermal gradient during the Neogene (30°C/km according to Juez-Larré (2003)), indicating the hydrothermal character of the fluids, as occurred during the Mesozoic. From the  $\delta^{18}\text{O}$  composition of calcites C3 and C4 (-20 and -23‰ VPDB, respectively) and the medium value of temperature obtained from chlorite (150°C), the origin of the parental fluid of these cements has been inferred applying the equation of Craig (1965). The results indicate fluids with  $\delta^{18}\text{O}$  values around 0‰ SMOW for C3 and -4.1‰ SMOW for C4.

These fluids have been interpreted as meteoric fluids infiltrated through the uplifted and subaerial exposed fractured horsts that during their circulation have suffered a strong interaction with host rocks, especially with the granodiorite, causing the buffering of their  $\delta^{18}\text{O}$  signal. As postulated for Mesozoic fluids during D<sub>2</sub>, the low  $\delta^{13}\text{C}$  values of these calcites (from -8 to -6.2‰ VPDB) can be due to the influence of organic matter widely present in the Silurian rocks or to soil-derived CO<sub>2</sub> present in these meteoric waters. These brines increased their temperature at depth and later upflowed through the main faults. In the Hospital fault, due to its position close to the Miocene shoreline, these fluids could have been mixed with marine water yielding to their more enriched  $\delta^{18}\text{O}$  values (fig. 5.8C). This mechanism of topographically-driven fluid flow has been also postulated at the onset of the Neogene in the Penedès half-graben (Bitzer et al. 2001).

Type 3C iron oxide wispy seams have been related to a small compression event (D<sub>5</sub>) that took place during the **early post-rift** (late Langhian to Serravalian) by comparison with similar type and orientation of fractures in the neighbour Penedès graben (Baqués et al. 2012a,b).

The sixth deformation phase (D<sub>6</sub>) has been linked with the **late post-rift** as faults affect Miocene conglomerates of the Upper Continental Complexes. Cements C5, C6, PC1 and *Microcodium* are characterized by an important increase of the Mg content (ranging from calcite to dolomite), more enriched  $\delta^{18}\text{O}$  values and more depleted  $\delta^{13}\text{C}$  values than the previous cements (fig. 5.9). These geochemical characteristics indicate the opening of the system and percolation of meteoric waters with a stronger influence of soil-derived CO<sub>2</sub> (fig. 5.8C). *Microcodium* development affected by later microfractures related to C5, C6 and PC1 cements and the morphology of palisade PC1 indicate that fault activity occurred under subaerial conditions, in the vadose zone. Also cathodoluminescence variations in *Microcodium* aggregates and the PC1 cements point to fluctuations of the water table during their formation.

Finally, the seventh deformation phase (D<sub>7</sub>) has been related to the small compression stage produced during the Messinian at the **end of the late post-rift**.

After cessation of fault activity, speleothems affecting the Triassic dolostones and soils developed within the Hospital fault in the Enric outcrop formed. Similar isotopic compositions to these diagenetic products have also been described in Pleistocene speleothems in the south of the Iberian Peninsula and in the Mallorca Island (Jiménez de Cisneros et al. 2003; Vesica et al. 2000) and in Tertiary speleothems developed in the Rmales Platform (Basque-Cantabrian Basin) (Dewit et al. 2012), suggesting a widespread event of karstification in the Iberian Peninsula from the Tortonian to recent. These values have been interpreted as originated from meteoric waters in a colder period than present (Jiménez de Cisneros et al. 2003; Vesica et al. 2000).

It is noteworthy that nowadays, hot springs along the Vallès fault have superficial temperatures up to 70°C and calculations of the reservoir temperature reach 110-120°C (Trilla 1974; Albert 1975). With the reservoir temperature and the -7‰ SMOW  $\delta^{18}\text{O}$  value of these thermal waters (Trilla 1974), the  $\delta^{18}\text{O}$  value of the calcites that could precipitate nowadays would be about -23‰ VPDB, which is also the value of calcites C4. In turn, calcite C4 is related to the presence of laumontite. The stability of laumontite is constrained at very low carbon dioxide contents in the solution (mole fraction of CO<sub>2</sub> below 0.1) and neutral to slightly alkaline waters in conditions of low pressure and low temperature (Liou et al. 1985). The present-day thermal waters of Caldes de Montbui have pH values between 7.9 and 8.35 and values of dissolved CO<sub>2</sub> of

0.88 mg/l, yielding in the laumontite stability field. In fact, the precipitation of calcite C4 or laumontite is caused by very low fluctuations in the CO<sub>2</sub> content of waters, as laumontite is very sensitive to these variations (Ivanov & Gurevich 1975). Thus hydrothermalism in the Vallès fault has remained active from the onset of the Neogene extension up to nowadays characterized by the precipitation of calcite C4, laumontite and LT chlorite. In contrast, hydrothermalism in the Hospital fault only took place during the Neogene syn-rift stage, as shown by precipitation of calcite C3 (fig. 5.8C).

## **5.2. Controls in the migration paths for fluids**

Along both the Vallès and Hospital faults different neoformed mineral associations are evidenced. These mineralogical differences along the fault mark preferential paths for fluids in certain periods of time, probably related to the independent tectonic activity of fault segments, fault zone architecture changes, inherited structures, and/or localized migration paths of certain fluids.

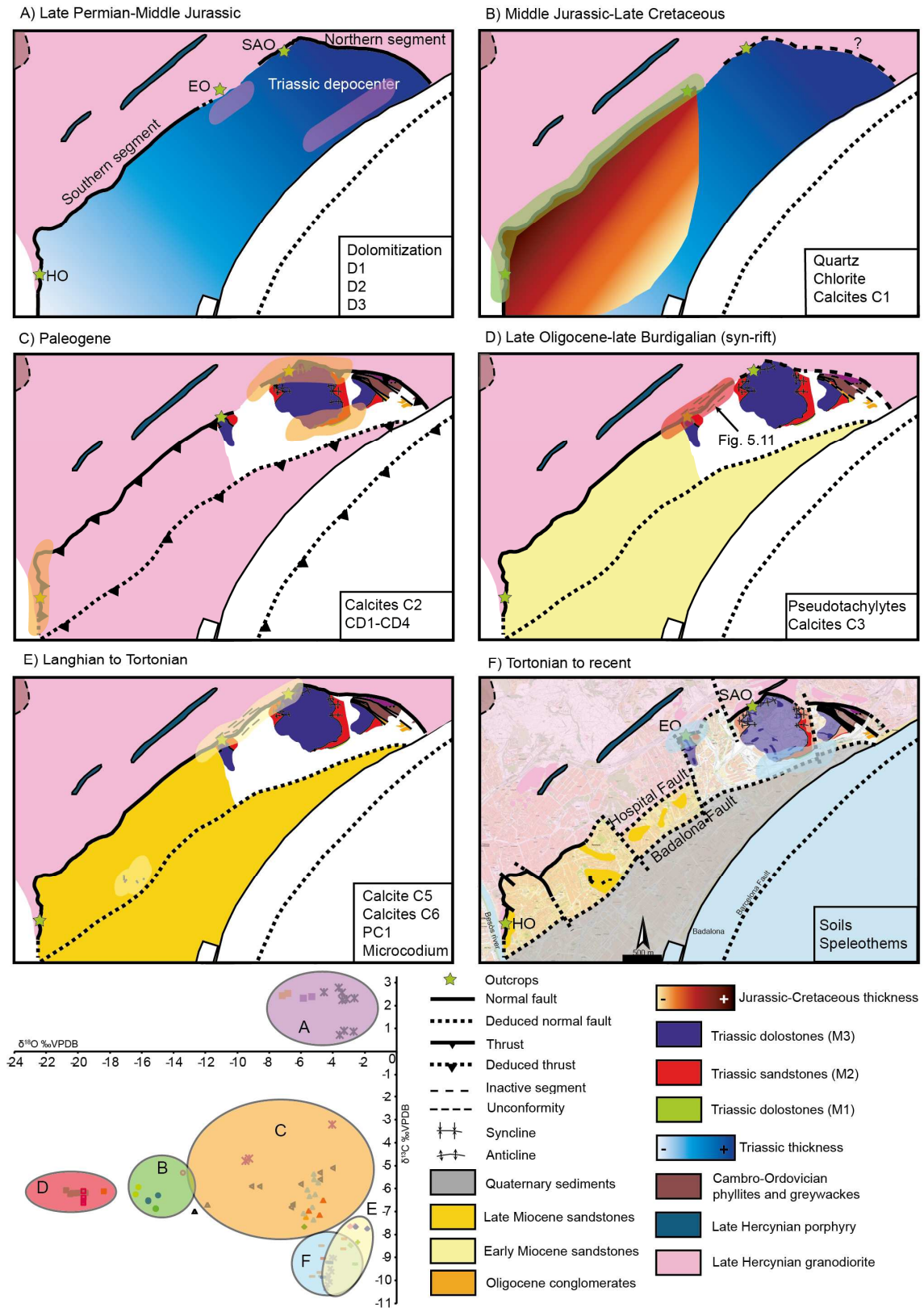
### **5.2.1. The Barcelona Plain**

The Hospital fault is formed by different fault segments with independent tectonic activity, which is evidenced by the differences in strike and dip between the fault segments and also by the thickness of the Triassic rocks and distribution of the cements.

During the Triassic extension, the Hospital fault was formed by two fault segments that controlled the Triassic sedimentation and therefore the variation in thickness of the Triassic rocks (fig. 5.10A). The low angle of the southern segment (<30°SE) led to a thinner accommodation space than in the northern segment (55°SE). The causes for such a low dip in a normal fault are discussed in section 5.3.1.

Cements associated with the Cretaceous rifting are only identified in the southern segment, indicating a localized migration of hot fluids ascending through the fault during its activity (fig. 5.10B). The lack of these cements in the north could be due to the inactivity of this segment or to the erosion of the cements associated with this period.

After the Mesozoic extension, the Paleogene compression inverted the previous normal faults and produced the exhumation and folding of the Triassic units. The uplift of the



Triassic rocks in the north favoured the percolation of meteoric fluids and the calcitization of the dolostones and dolomite cements (fig. 5.10C).

During the Miocene extension, the fault tip of the southern segment was located in the



area of the Enric outcrop controlling the thickness of the Miocene rocks, which decreases towards the northeast. Propagation of the fault tip to the north is also shown by the fault rocks and cements attributed to the Neogene syn-rift in the Enric outcrop.

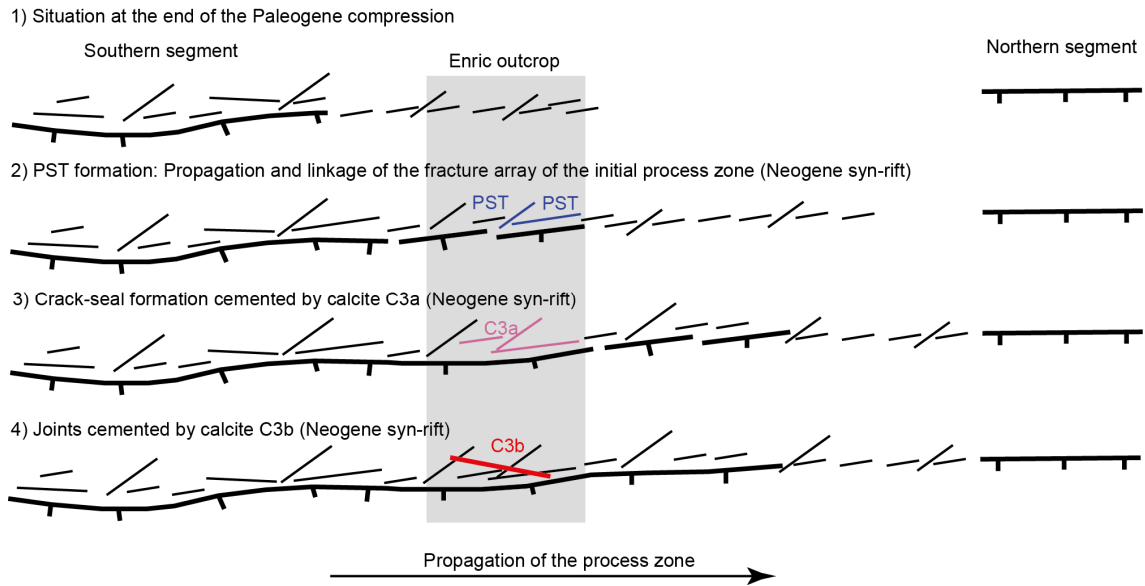
Tip propagation produced the migration of the process zone to the north, which is formed by fracture sets parallel to the southern segment and to the new fault trace that it is being formed between the two segments (fig. 5.10D, fig. 5.11). Each slip event of the main fault involved the propagation and linkage of the previous arrays generating 3A microfaults. These linking structures develop friction melts (Swanson 1992), what would explain the formation of pseudotachylytes in type 3A faults in this point. Studies in seismically active fault systems have also shown the spatial relationship between seismicity and linking structures between main faults (Tavarnelli & Pasqui 2000). Later crack-seals cemented by calcite C3a could have been generated during the pre-seismic stage of a new earthquake (Sibson 1986). Deformation under an extensional stress regime generates structures in the process zone that enhance dilation and therefore increase permeability, generating zones of localized hydrothermal upflow (Rowland & Sibson 2004). Moreover, outflows of water following earthquakes is a frequent phenomenon (seismic pumping (Sibson et al. 1975)), which can precipitate cement in the accessible extension fractures, such as 3B joints.

During the late post-rift, both segments had some displacement at shallow conditions in the presence of low-temperature meteoric fluids (fig. 5.10E). Minor faults affecting the Miocene conglomerates were formed with narrow and poorly developed fault cores and damage zones. This configuration before the precipitation of the pedogenic products allowed a cross-fault flux between the porous layers of the host rock (Rowland & Sibson 2004) (fig. 5.12). However, the later growth of vegetation and associated microorganisms induced the neoformation of different pedogenic products, which reduced the effective porosity of the fault rock and its permeability. The result was the

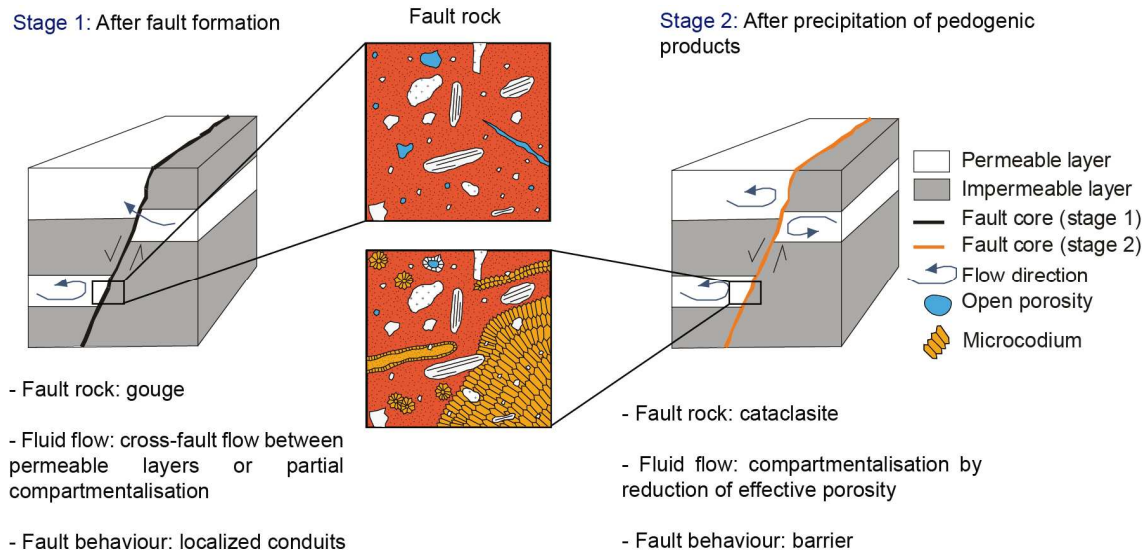
---

**Figure 5.10.** Structural evolution of the basin and distribution and evolution of fluids through time in the northern sector of the Barcelona Plain from Late Permian to recent. A) Deposition of the Triassic rocks and dolomitization during the first Mesozoic rifting event. B) Cretaceous rifting localized in the southern segment and circulation of ascending hot fluids. C) Basin inversion, folding, erosion and percolation of low-temperature meteoric fluids that produced the calcitization of previous dolomites. D) Segment connection through fault growth and upflow of hot fluids in the relay area during the Neogene syn-rift. E) Propagation of the Hospital fault to the surface and percolation of low-temperature meteoric fluids. F) Generation of the NW-SE set of fractures that segmented the Hospital fault and development of soil and speleothems.

---



**Figure 5.11.** Sketch of the mechanism of fault growth by tip propagation of the southern segment at kilometric scale. PST: pseudotachylite.



**Figure 5.12.** Effects of pedogenesis in cross-fault fluid flow within Miocene conglomerates.

sealing of the fault zones and the restriction of fluid flow (fig. 5.12).

Finally, NW-SE strike-slip faults segmented again the Hospital fault generating the current disposition probably during the Messinian compression (fig. 5.10F).

Large-scale horizontal fluid flow in the Hospital fault did not occur due to the marked structural heterogeneities produced by the variations of fault zone architecture along strike.

### 5.2.2. The Vallès fault

In the Vallès fault, the different associations of neoformed minerals are attributed to the different structural position of the outcrops within the footwall. The Camí d'En Cisa outcrop (CCO) is located in the contact with the Miocene rocks and only the formation of laumontite L2 related to the Neogene extension is registered. On the other hand, the Torrent del Corró outcrop (TCO), located 50 m from the contact, shows all the deformation stages, mainly chlorite-mica, chlorite and calcite veins. As mentioned above, mica-chlorite veins and calcite C1 have been related to the Mesozoic extension whereas low-T chlorite, laumontite and calcite C4 have been related to the Neogene extension. This means that the TCO outcrop represents the location of a Mesozoic fault zone reactivated during the Neogene deformation whereas the CCO outcrop represents the location of a newly formed Neogene fault. These observations point to an offset between the Mesozoic and the Neogene extensional faults (fig. 5.8).

### 5.3. Controls on fault reactivation

The stratigraphy, the fault rock kinematic indicators and the crosscutting relationships of cements point to successive reactivations of the Hospital and the Vallès faults. This fact perfectly fits with the evidence of reactivation of other main structures forming the Catalan Coastal Ranges proposed by other authors (Anadón et al. 1985; Bartrina et al. 1992; Roca 1996; Gaspar-Escribano et al. 2004; Santanach et al. 2011). However, nobody has focused in the controls for fault reactivation. In this section, a preliminary result about the causes for reactivation is proposed but further work needs to be done.

#### 5.3.1. The role of the Hercynian structures during the Mesozoic extension

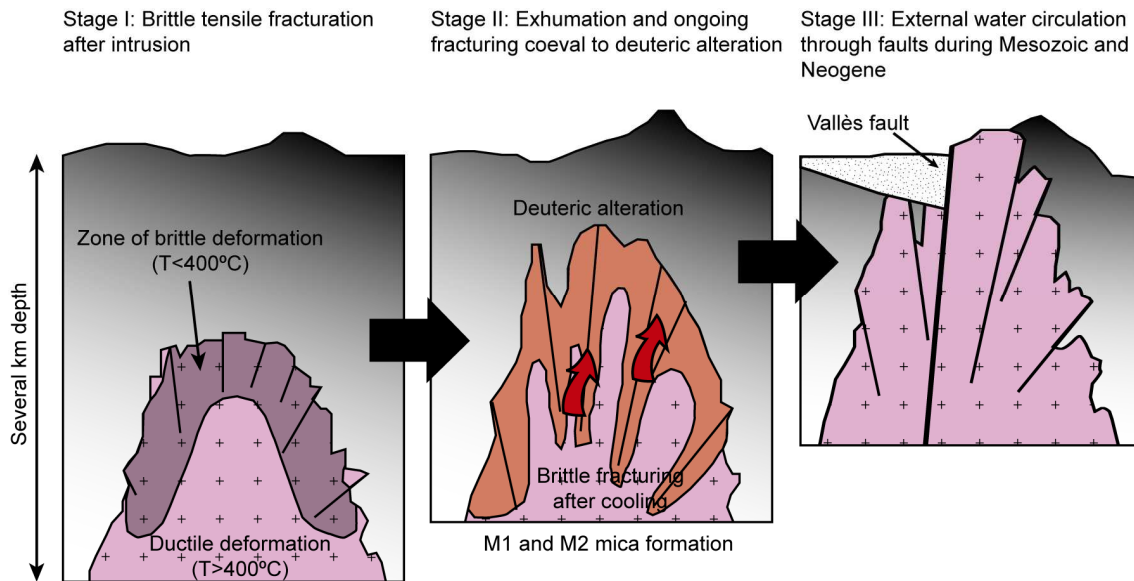
Although previous works in the Catalan Coastal Ranges agree in the reactivation of structures from Mesozoic to Recent (see references above), few authors have proposed the possible reactivation of Hercynian structures (Solé Sugañes 1978; Anadón et al. 1979). As shown in section 4.5, M1 and M2 muscovite resulting from deuteric alteration during pluton exhumation and later M3 and M4 phengite formed during deformation phase D2 are texturally and spatially related, indicating that Hercynian exhumation fractures were reactivated during the Mesozoic extension (fig. 5.13). This reactivation is favoured by two reasons. Firstly, exhumation fractures display a radial disposition around the pluton border generating a wide range of fracture orientations

with subvertical dips suitable for reactivation in an extensional regime. Secondly, exhumation produced dilatancy in the fractures, lowering the fault cohesion. Furthermore, the only minerals that precipitate along fractures are phyllosilicates which could reduce the friction coefficient.

In the Hospital fault, no mica precipitation has been observed though, in the Enric outcrop, Cenozoic and Mesozoic structures overprint ancient dynamically metamorphosed rocks, indicating also the reactivation of Hercynian structures. But, why is there no mica crystallization in the Hospital fault when both granodiorites are similar in composition? The location of M1 and M2 mica only in the Vallès fault probably indicates that the outcrops of the Vallès fault were near the pluton border, the highest fractured and altered area, whereas the outcrops of the Hospital fault were in an inner position or in a less fractured zone. This fact is supported by cartographic criteria. In the Hospital area, the contact between the granodiorite and the rocks forming the metamorphic contact aureole is about 2 km to the north and highly dips to the north (IGC 2011). The prolongation of this surface to the south simulating the concave shape of the pluton yields to a minimum distance from this surface to the current topography at the fault trace of about 1 km, far from the fractured and altered pluton border. On the opposite, in the Vallès fault, this contact aureole is even cut by the normal fault, clearly pointing that the outcrops are within the pluton border. This different location of the outcrops of both faults in the pluton is also reflected in the later fault zone architectures. The high density of fractures close to the pluton border would have been the responsible of the thicker fault zone in the Vallès fault (60 m) in front of the narrower Hospital fault zone (1-3 m). M1 and M2 muscovite formation changes the bulk rock composition of the granodiorite, controlling the crystallization of later M3 and M4 mica only in the Vallès fault and also explaining the lack of these late mica groups in the Hospital fault.

In conclusion, pre-existing Hercynian structures controlled the location and architecture of the Hospital and Vallès faults (fig. 5.13).

The Hospital fault in its southwestern section (Hospital outcrop) has a very low dip ( $<30^{\circ}\text{SE}$ ). Fault rocks developed within this fault plane have been interpreted as formed during the Mesozoic extension. Low-angle normal faults associated to the Mesozoic extension have been also described in other hills of the Barcelona Plain to the SW of the study area (Santanach et al. 2011) and in the Garraf Horst (Salas, personal



**Figure 5.13.** Schematic model of fracture formation during evolution of the granodiorite and reactivation of these previous structures during later tectonic events in the Vallès half-graben (modified from Yoshida et al. 2012).

communication). However, under an Andersonian regime, normal faults in the brittle regime should not form at dips below  $45^{\circ}$  (Anderson 1951).

Several hypothesis about the origin of this segment can be postulated: 1) As proposed by Santanach et al. (2011), these low angle normal faults are deep sections of listric faults that have been exposed due to the uplift and erosion produced during the Paleogene compression; 2) This segment is the result of the reactivation as a normal fault of the Permian unconformity between the granodiorite and the Triassic rocks that crops out along the Catalan Coastal Ranges; and, 3) It is the result of the reactivation of an Hercynian thrust.

If the second case is true, although the Permian unconformity is also a weak plane, other parameters must act in order to reactivate a plane dipping  $30^{\circ}$  as a normal fault. Probably, the exposure surface underwent meteoric alteration which could produce a certain disaggregation of the rock, reducing the cohesivity. Besides, upflowing hydrothermal brines could also increase the fluid pressure favouring reactivation.

The latter could be ruled out as thrusts only occurred at shallow structural levels in the Upper Paleozoic rocks whereas at deep-seated domains, only foliations with variable attitude and degree of penetration developed (Casas et al. 1989; Carreras & Debat 1995; Ábalos et al. 2002; Santanach et al. 2011).



### 5.3.2. Reactivation during the Paleogene

As pointed before, it is widely accepted the reactivation of Mesozoic normal faults as thrusts during the Paleogene compression along the Catalan Coastal Ranges. In the study areas, different fault behaviors have been observed associated with this tectonic event.

In the Vallès fault, Mesozoic structures close to the surface have a very high dip (between 70 and 90°) to be inverted during compression, causing the propagation to the north of thrust shortcuts. These newly formed structures profit the foliated and phyllosilicate-rich metamorphic rocks to develop and generate gouges.

In the Hospital outcrop, the pre-existing low-angle normal fault does not reactivate during this compressional event. This lock, despite the favourable orientation and dip of the fault, is probably due to the cementation produced by calcite cements C1, which increase the fault rock cohesion by hardening. Instead, new thrusts are formed using the plastic Silurian black shales as a detachment level. On the opposite, in the Sariol outcrop, the pre-existing Mesozoic normal fault, which has a higher dip (about 50°SE), is reactivated during the Paleogene. High-angle reverse faults are anomalous structures in the classical theory of Anderson (1951) and an increase in the fluid pressure is required to reactivate them (Sibson et al. 1988), as evidenced in this case by the dilatancy observed in the random breccia cemented by calcite C2b-c.

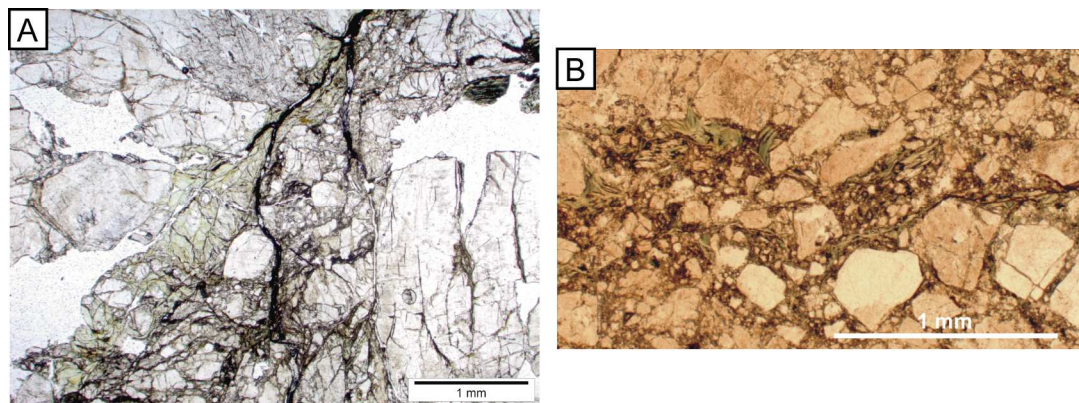
### 5.3.3. Reactivation during the Neogene

In the Vallès fault, most of the low temperature chlorites (125-190°C) form a rim around high temperature chlorites ( $T > 190^\circ\text{C}$ ), indicating the reactivation of the Mesozoic structures with phyllosilicates during the Neogene. This reactivation was possible due to the low friction coefficient of chlorite and K-white mica and their arrangement in localized fracture planes under hydrated conditions (fig. 5.14A) (Lacroix 2011; Behnsen & Faulkner 2012; Buatier et al. 2012). Nevertheless, despite this reactivation, a new Neogene fault was formed 50 m in front of the Mesozoic structures, as it is observed in the CCO outcrop. The presence in this outcrop of dilatant breccias cemented by laumontite L2 could indicate an increase in the fluid pressure that would induce the failure of the intact rock. This relay between the Mesozoic and Neogene

faults have been also described in the Penedès Half-graben (Baqués et al. 2012a), although no reasons have been postulated for the formation of a new fault.

In contrast to the Vallès fault, low temperature chlorites were not formed in the Hospital fault although both faults reached the same temperature conditions and both faults had previous chlorites, as observed in the Hospital and Enric outcrops. In the case of the Hospital outcrop, the absence of Neogene chlorite is due to: 1) the unfavorably oriented fault zone, with dip  $<30^\circ$ ; 2) the lack of a strong preferred orientation of chlorite crystals together with the lack of connection between them within the foliation, which could have reduced the friction coefficient to enhance failure (fig. 5.14B); and, 3) the hardening caused by calcite C1 cementation in fault rock matrix, which increased the fault zone cohesion. Therefore, during the Neogene extension a new fault was formed in this section of the Hospital fault, using the plastic Silurian black shales as a detachment level. The low friction coefficient of these Silurian rocks allowed the several reactivations of this fault during the Neogene.

In the Enric outcrop, together with the lack of a strong preferred orientation of chlorites, the canalization of fluids along well-defined veins (C3a crack-seals and C3b joints) avoided the circulation of fluids towards the chloritized random breccia that constitutes the veins host rock.



**Figure 5.14.** A) Plane light image of a fracture filled by chlorite in the Vallès fault. B) Foliation plane formed by chlorites in the Hospital fault. Chlorites are disconnected and misoriented avoiding sliding (plane light).



## 6. CONCLUSIONS

The Catalan Coastal Ranges display a horst and graben structure limited by NE-SW listric faults, which are offset by later NW-SE to NNW-SSE trending faults. This study is focused on two of these NE-SW faults, the Vallès and Hospital faults, that bound to the north the Vallès Half-graben and the Barcelona Plain, respectively.

The Vallès and the Hospital faults record successive reactivations linked with polyphasic fluid systems, which have been inferred from regional to thin section scale observations combined with geochemical analyses.

In these two faults, deformation is mainly localized in the basement granodiorite of the footwall, although minor faults have been also identified affecting the Triassic and Miocene rocks of the Hospital hangingwall.

The fault rocks identified in this study (gouges, cataclasites, breccias and pseudotachylytes) are not characteristic of the different deformation phases. However, pseudotachylytes have been only related to extensional events. On the opposite, the geochemistry of fault-related cements together with their crosscutting relationships have been useful to discern up to seven deformation phases encompassed within four tectonic events.

The Hercynian compression is characterised by a penetrative foliation linked with tight folds and dynamically metamorphosed rocks. After this first compressional event and during the exhumation of the pluton, crystallization of M1 and M2 muscovite and microcline occurred in the Vallès fault as result of deuteritic alteration, at temperatures between 330°C and 370°C.

The Mesozoic extension is divided into two deformation phases. Deformation phase D<sub>1</sub> corresponds to the Late Permian-Middle Jurassic rifting stage. During this phase, the Hospital fault controlled the thickness and distribution of the Triassic sediments, having their depocentre to the north. Early dolomitization produced by Triassic seawater took place at shallow conditions. Dolomite cements in type 1A fractures precipitated from the Triassic seawater during increasing burial in a relatively closed hydrological regime. The second deformation phase D<sub>2</sub>, related to the Late Jurassic-Late Cretaceous rifting, is

characterized by precipitation of M3 and M4 phengite together with chlorite and calcite C1 at temperatures between 190 and 310°C.

The Paleogene compression, or deformation phase D<sub>3</sub>, is characterized in the Hospital fault by percolation of low-temperature meteoric fluids favoured by tectonic uplift. These fluids are the responsible of precipitation of calcites C2 and calcitization of previous dolomite cements and Triassic host dolostones. In the Vallès fault, the Paleogene compression generated a shortcut that produced a gouge and the uplift of the Mesozoic structures, avoiding the reactivation of the former structures but generating subvertical stylolites.

The Neogene extension is subdivided into four deformation phases (D<sub>4</sub> to D<sub>7</sub>). During the syn-rift (D<sub>4</sub>), cements such as chlorite, calcite C4 and laumontite in the Vallès fault and calcite C3 in the Hospital fault precipitated at temperatures between 125 and 190°C. During this deformation phase, the southern segment of the Hospital fault grew by propagation of its northern tip generating pseudotachylytes and the later precipitation of calcite C3. Thus, the increase in dilatancy produced in the process zone together with a seismic pumping effect controlled the upflow during fault growth.

The post-rift is divided into three deformation phases, from which D<sub>5</sub> is related to a small compression stage during the early post-rift (Langhian-Serravalian), D<sub>6</sub> is related to the late post-rift (Serravalian-Tortonian) and D<sub>7</sub> is related to a new compressional period during the late post-rift (Messinian). Post-rift stages in the Barcelona Plain developed at shallow conditions under low-temperature meteoric regime. At the same period, the Vallès fault was dominated by hydrothermal fluids. This hydrothermalism remains active until nowadays.

The estimated temperatures of crystallisation of chlorites indicate that during the two extensional events (Mesozoic and Neogene) faults acted as conduits for hot fluids producing anomalous high geothermal gradients (50°C/km minimum). These hydrothermal fluids are the result of meteoric fluids moved by a topographically-driven mechanism, favoured by the shoulder uplift produced during normal faulting. During the flow, meteoric fluids warmed at depth and suffered a strong interaction with the host rocks. During the Mesozoic, the ascending warm fluids mixed with marine waters in both studied main faults. During the Neogene, the ascending fluids mixed with marine waters in the Hospital faults and with meteoric waters in the Vallès fault.



The estimated decrease of pressure from chlorite and mica equilibrium is consistent with exhumation produced during Alpine compression and Mesozoic and Neogene extensions. During the Neogene extension, exhumation of the granodiorite followed a nearly isobaric cooling path.

Most Neogene normal faults of the central Catalan Coastal Ranges are the reactivation of previous faults. In fact, in this thesis is demonstrated that Hercynian structures play an important role on the localization of later structures. The main controls that enable fault reactivation are the presence of phyllosilicates generating continuous planes and the increase in fluid pressure. On the other hand, cementation avoids reactivation because of a hardening effect. Silurian black shales are commonly sliced between rocks generating good detachment level due to their plastic, low frictional behavior.

Pedogenic products developed along the Neogene faults play an important control on cross-fault fluid flow by reducing the fault core permeability.

To summarize, the tectonic regime, the fault zone architecture, the seismic activity, the deuteric alteration processes and also pedogenic processes controlled the fluid regime and the fluid flow pathways through faults from Hercynian to recent.



## 7. REFERENCES

- Ábalos B, Carreras J, Druguet E, Escuder Viruete J, Gómez Pugnaire MT, Lorenzo Alvarez S, Quesada C, Rodríguez Fernández LR, Gil-Ibarguchi JI (2002) Variscan and Pre-Variscan Tectonics. In: Gibbons W. & Moreno M.T. (eds.), *The Geology of Spain*. Geological Society of London, 155-183.
- Agard P, Vidal O, Goffé B (2001) Interlayer and Si content of phengite in HP–LT carpholite-bearing metapelites. *Journal of Metamorphic Geology*, **19** (5), 479–496.
- Albert JF (1975) El equilibrio albita-anortita como termómetro hidrogeotérmico en zonas graníticas. *Acta Geològica Hispànica*, **X** (5), 170-174.
- Albert JF, Corominas J, París C (1979) El estudio hidrogeológico de los manantiales y su aplicación geológica: caso de las aguas termales, carbónicas y sulfhídricas de Cataluña. *Acta Geològica Hispànica. Homenatge a Lluís Solé i Sabarís*, **14**, 391-394.
- Allen MB, Vincent SJ (1997) Fault reactivation in the Junggar region, northwest China: the role of basement structures during Mesozoic–Cenozoic compression. *Journal of the Geological Society of London*, **154**, 151-155.
- Alonso-Zarza AM, Jones B (2007) Root calcrete formation on Quaternary karstic surfaces of Grand Cayman. *Geogaceta*, **5** (1), 77-88.
- Anadón P, Colombo F, Estaban M, Marzo M, Robles S, Santanach P, Solé Sugrañés LI (1979) Evolución tectonoestratigráfica de los Catalánides. *Acta Geològica Hispànica. Homenatge a Lluís Solé i Sabarís*, **14**, 242-270.
- Anadón P, Cabrera L, Guimerà J, Santanach P (1985) Paleogene strike-slip deformation and sedimentation along the southeastern margin of the Ebro Basin. In: Biddle K.T. & Christie-Blick N. (eds.). *Strike-slip Deformation, Basin Formation Sedimentation*. Special Publication of the Society of Economic Paleontologists and Mineralogists, **37**, 303-318.
- Anadón P (1986) Las facies lacustres del Oligoceno de Campins (Vallès Oriental, Provincia de Barcelona). *Cuadernos de Geología Ibérica*, **10**, 271-294.

- Anderson EM (1951) The dynamics of faulting and Dyke formation with applications to Britain. Ed. Olivier & Boyd, 206 p.
- Arnal I, Calvet F, Márquez L, Márquez-Aliaga A, Solé de Porta N (2002) La plataforma carbonatada epeírica (Formaciones Imón e Isábena) del Triásico superior del Noreste de la Península Ibérica. *Acta Geològica Hispànica*, **37** (4), 299-328.
- Ashauer H, Teichmüller R (1935) Die variszische und alpidische Gebirgsbildung Kataloniens. *Abhandlungen Gesellschaft Wissenschaften Göttingen, Math Phys.* K1, 3F, 16.
- Aydin A (2000) Fractures, faults, and hydrocarbon entrapment, migration and flow. *Marine and Petroleum Geology*, **17** (7), 797-814.
- Bando M, Bignall G, Sekine K, Tsuchiya N (2003) Petrography and uplift history of the Quaternary Takidani Granodiorite: could it have hosted a supercritical (HDR) geothermal reservoir? *Journal of Volcanology and Geothermal Research*, **120**, 215-234.
- Bartier D, Ledésert B, Clauer N, Meunier A, Liewig N, Morvan G, Addad A (2008) Hydrothermal alteration of the Soultz-sous-Forêts granite (Hot Fractured Rock geothermal exchanger) into a tosudite and illite assemblage. *European Journal of Mineralogists*, **20**, 131-142.
- Bartrina MT, Cabrera L, Jurado MJ, Guimerà J, Roca E (1992) Evolution of the central Catalan margin of the Valencia trough (western Mediterranean). *Tectonophysics*, **203**, 219-247.
- Baqués V, Travé A, Benedicto A, Labaume P, Cantarero I (2010) Relationships between carbonate fault rocks and fluid flow regime during propagation of the Neogene extensional faults of the Penedès basin (Catalan Coastal Ranges, NE Spain). *Journal of Geochemical Exploration*, **106**, 24-33.
- Baqués V, Travé A, Roca E, Marín M, Cantarero I (2012a) Geofluid behaviour in successive extensional and compressional events: a case study from the southwestern end of the Vallès-Penedès Fault (Catalan Coastal Ranges, NE Spain). *Petroleum Geoscience*, **18**, 17–31.

- Baqués V (2012b) Diagenesis and fluid-fracture evolution in an intracontinental basin: the Penedès half-graben, western Mediterranean. Dissertation, Universitat de Barcelona, 81 p.
- Behnsen J, Faulkner DR (2012) The effect of mineralogy and effective normal stress on frictional strength of sheet silicates. *Journal of Structural Geology*, **42**, 49-61.
- Berwouts I, van Noorden M, Muchez Ph, Boyce AJ, Sintubin M (2008) Inferring intermediate-scale fluid flow in a heterogeneous metasedimentary multilayer sequence during progressive deformation: evidence from the Monts d'Arrée slate belt (Britanny, France). *Geofluids*, **8**, 143-158.
- Bellahsen N, Fournier M, d'Acremont E, Leroy S, Daniel JM (2006) Fault reactivation and rift localization; Northeastern Gulf of Aden margin. *Tectonics*, **25**, TC1007, 14pp. Doi:10.1029/2004TC001626.
- Biddle KT, Rudolph KW (1988) Early Tertiary structural inversion in the Stord Basin, Norwegian North Sea. *Journal of the Geological Society of London*, **145** (4), 603-612.
- Bitzer K, Travé A, Carmona JM (2001) Fluid flow processes at basin scale. *Acta Geològica Hispànica*, **36** (1-2), 1-20.
- Bodergat AM (1974) Les microcodiums, milieux et modes de développement. *Documents des Laboratoires de Géologie de la Faculté des Sciences de Lyon*, **62**, 137-235.
- Bodnar RJ (2003) Reequilibration of fluid inclusions. In: Samson I., Anderson A., & Marshall D. (eds.) Fluid Inclusions: Analysis and Interpretation. *Mineralogical Association of Canada, Short Course*, **32**, 213-230.
- Breesch L, Swennen R, Vincent B (2009) Fluid flow reconstruction in hanging and footwall carbonates: Compartmentalization by Cenozoic reverse faulting in the Northern Oman Mountains (UAE). *Marine and Petroleum Geology*, **26** (1), 113-128.
- Buatier M, Lacroix B, Labaume P, Moutarlier V, Charpentier D, Sizun JP, Travé A (2012) Microtextural investigation (SEM and TEM study) of phyllosilicates in a

- major thrust fault zone (Monte Perdido, southern Pyrenees): impact on fault reactivation. *Swiss Journal of Geoscience*. doi: 10.1007/s00015-012-0098-0.
- Byerlee J (1978) Friction of rocks. *Pure and Applied Geophysics*, **116** (4-5), 615-626.
- Cabrera Ll (1981) Estratigrafia y características sedimentológicas generales de las formaciones continentales del Mioceno de la cuenca del Vallès-Penedès (Barcelona, España). *Estudios geológicos*, **37**, 35-43.
- Cabrera Ll, Calvet F (1996) Onshore Neogene record in NE Spain: Vallès-Penedès and El Camp half-grabens (NW Mediterranean). In: Friend P.F. & Dabrio C.J. (eds). *Tertiary Basins of Spain*. Cambridge University Press, 97-105.
- Cabrera Ll, Roca E, Garcés M, De Porta J (2004) Estratigrafia y evolución tectonosedimentaria oligocena superior-neógena del sector central del margen catalán (Cadena Costero-Catalana). In: Vera J.A. (ed.) *Geología de España*, SGE-IGME, 569-572.
- Caine JS, Evans JP, Forster CB (1996) Fault zone architecture and permeability structure. *Geology*, **24** (11), 1025-1028.
- Calvet F, Pomar L, Esteban M (1975) Las rizocreciones del Pleistoceno de Mallorca. *Inst. Invest. Geol. Univ. de Barcelona*, **30**, 35-60.
- Calvet F (1979) Evolució diagenètica en els sediments carbonatats del Pleistocè Mallorquí. Dissertation, Universitat de Barcelona, 273 p.
- Calvet F, March M, Pedrosa A (1987) Estratigrafia, sedimentología y diagénesis del Muschelkalk superior de los Catalánides. *Cuadernos de Geología Ibérica*, **11**, 171-197.
- Calvet F, Tucker ME, Henton JM (1990) Middle Triassic carbonate ramp systems in the Catalan Basin, northeast Spain: facies, systems tracts, sequences and controls. *Special Publications International Association of Sedimentologists*, **9**, 79-108.
- Calvet F, Marzo M (1994) El Triásico de las Cordilleras Costero Catalanas: Estratigrafia, sedimentología, y anàlisis secuencial. Guia de la excursión. III Col. Estrat. Paleog. Pérm. y Triás. Esp. 53 pp., Cuenca.



- Calvet F, Travé A, Roca E, Soler A, Labaume P (1996) Fracturación y migración de fluidos durante la evolución tectónica neógena en el Sector Central de las Cadenas Costero Catalanas. *Geogaceta*, **20** (7), 1715-1718.
- Calvet F, Travé A, Bitzer K, Roca E, Tritlla J, Baker J (2001) Dolomitization of detrital deposits related to Neogene extensional faults, Catalan Coastal Ranges (Spain). *Geo-Temas*, **3** (1), 109-111.
- Canals À, Cardellach E, Rye DM, Ayora C (1992) Origin of the Atrevida vein (Catalan Coastal Ranges, Spain): mineralogic, fluid inclusion and stable isotopy study. *Economic Geology*, **87**, 142-153
- Canals À, Cardellach E (1997) Ore lead and sulphur isotope pattern from the low-temperature veins of the Catalanian Coastal Ranges (NE Spain). *Mineralium Deposita*, **32**, 243-249.
- Cardellach E, Canals À, Grandia F (2002) Recurrent hydrothermal activity induced by successive extensional episodes: the case of the Berta F-(Pb-Zn) vein system (NE Spain). *Ore Geology Reviews*, **22**, 133-141.
- Carmona JM, Bitzer K, López E, Bouazza M (2000) Isotopic composition and origin of geothermal waters at Caldetes (Maresme-Barcelona). *Journal of Geochemical Exploration*, **69-70**, 441-447.
- Carreras J, Debat P (1995) Tectonique Hercynienne. In: Barnolas A. & Chiron J.C. (eds.) *Synthèse géologique et géophysique des Pyrénées, Tome I, Cycle Hercynien*, Edition BRGM-ITGE, 593-594.
- Casas JM, Domingo F, Poblet J, Soler A (1989) On the role of the Hercynian and Alpine thrusts in the Upper Paleozoic rocks of the Central and Eastern Pyrenees. *Geodinamica Acta*, **3** (2), 135-147.
- Cathalinea M, Nieva D (1985) A chlorite solid solution geothermometer the Los Azufres (Mexico) geothermal system. *Contributions to Mineralogy and Petrology*, **91** (3), 235-244.
- Cathalinea M (1988) Cation site occupancy in chlorites and illites as a function of temperature. *Clay minerals*, **23**, 471-485.

- Causse C, Moretti I, Eschard R, Micarelli L, Ghaleb B, Frank N (2004) Kinematics of the Corinth Gulf inferred from calcite dating and syntectonic sedimentary characteristics. *Comptes Rendus Geoscience*, **336**, 281-290.
- Cherchi A, Montadert L (1982) Oligo-Miocene rift of Sardinia and the early history of the Western Mediterranean Basin. *Nature*, **298**, 736-739.
- Clayton RN, O'Neil JR, Mayeda TK (1972) Oxygen isotope exchange between quartz and water. *Journal of Geophysical Research*, **77** (17), 3057-3067.
- Combes PJ (1969) Recherches sur la genèse des bauxites dans le nord-est de l'Espagne, le Languedoc et l'Ariège (France). Dissertation, Université de Montpellier, 342 p.
- Craig H (1965) The measurements of oxygen isotope paleotemperatures. In: Tongiorgi E (ed.) *Stable Isotopes in Oceanographic Studies and Paleotemperatures*. Consiglio Nazionale delle Ricerche, Laboratorio di Geologia Nucleare, Pisa, 161-182 p.
- Davis GH, Reynolds SJ (1996) *Structural Geology of Rocks and Regions*, 2<sup>nd</sup> edition. Ed. Wiley, New York, 800 p.
- Demange M, Alvarez JO, López L, Zarco JJ (1996) The Achala Batholith (Cordoba, Argentina): a composite intrusion made of five independent magmatic suites. Magmatic evolution and deuteric alteration. *Journal of South American Earth Sciences*, **9** (1-2), 11-25.
- Deming D (1994) Fluid flow and heat transport in the upper continental crust. In: Geofluids: Origin, Migration and Evolution of Fluids in Sedimentary Basins (ed. J. Parnell). *Geological Society Special Publication*, **78**, 27-42.
- Dewit J, Foubert A, El Desouky HA, Muchez Ph, Hunt D, Swennen R (2012) Dolomitisation model of hydrothermal dolomites (HTD) hosted by Aptian-Albian carbonates of the Ramales Platform (Basque-Cantabrian Basin, Northern Spain). VII Geofluids Conference, 75-78.
- Dickson JAD (1966) Carbonate identification and genesis as revealed by staining. *Journal of Sedimentary Research*, **36** (2), 491-505.
- Dias R, Ribeiro A (1995) The Ibero-Armorican Arc: a collision effect against an irregular continent? *Tectonophysics*, **246**, 113-128.

- Donath FA, Cranwell RM (1981) Probabilistic treatment of faulting in geologic media. In: Mechanical Behavior of Crustal Rocks (ed. NL Carter et al.). *Geophysical Monograph series*, **24**, 231-241.
- Drake H, Tullborg E (2009) Paleohydrogeological events recorded by stable isotopes, fluid inclusions and trace elements in fracture minerals in crystalline rock, Simpevarp area, SE Sweden. *Applied Geochemistry*, **24**, 715-732.
- Dubacq B, Vidal O, de Andrade V (2010) Dehydration of dioctahedral aluminous phyllosilicates: thermodynamic modelling and implication for thermobarometric estimates. *Contributions to Mineralogy and Petrology*, **159**, 159-174.
- Duddy IR, Green PF, Bray RJ, Hegarty KA (1994) Recognition of the thermal effects of fluid flow in sedimentary basins. In: Parnell J. (ed.) Geofluids: Origin, Migration and Evolution of Fluids in Sedimentary Basins. *Geological Society Special Publication*, **78**, 325-345.
- Duvall AR, Clark MK, van der Pluijm BA, Li C (2011) Direct dating of Eocene reverse faulting in northeastern Tibet using Ar-dating of fault clays and low-temperature thermochronometry. *Earth and Planetary Science Letters*, **304**, 520-526.
- ECORS team (1988) The ECORS deep reflection seismic survey across the Pyrenees. *Nature*, **331**, 508-510.
- Enrique P (1990) The Hercynian intrusive rocks of the Catalan Coastal Ranges (NE Spain). *Acta Geològica Hispànica*, **25** (1-2), 39-64.
- Etheridge MA (1986) On the reactivation of extensional fault systems. *Royal Society of London Philosophical Transactions, ser. A*, **317**, 179-194.
- Fernández M, Banda E (1989) An approach to the thermal field in northeastern Spain. *Tectonophysics*, **164**, 259-266.
- Faccena C, Funiciello F, Giardini D, Lucente P (2001) Episodic back-arc extension during restricted mantle convection in the Central Mediterranean. *Earth and Planetary Science Letters*, **187** (1-2), 105-116.

- Fyfe WS, Price NJ, Thompson AB (1978) Fluids in the Earth's crust. Their significance in metamorphic, tectonic and chemical transport processes. Developments in geochemistry 1. Elsevier Scientific Publishing Company, Amsterdam, 383 p.
- Garven G (1989) A hydrogeologic model for the formation of the giant oil sands deposits of the western Canada sedimentary basin. *American Journal of Science*, **289**, 105-166.
- Gaspar-Escribano JM, Garcia-Castellanos D, Roca E, Cloetingh S (2004) Cenozoic vertical motions of the Catalan Coastal Ranges (NE Spain): The role of tectonics, isostasy, and surface transport. *Tectonics*, **23**, 1-18.
- Gómez-Gras D, Ferrer C (1999) Caracterización petrológica de perfiles de meteorización antiguos desarrollados en granitos tardihercínicos de la Cordillera Costero Catalana. *Revista de la Sociedad Geológica de España*, **12** (2), 281-299.
- Gómez-Gras D, Parcerisa D, Bitzer K, Calvet F, Roca E, Thiry M (2000) Hydrogeochemistry and diagenesis of Miocene sandstones at Montjuïc, Barcelona (Spain). *Journal of Geochemical Exploration*, **69-70**, 177-182.
- Gómez-Gras D, Parcerisa D, Calvet F, Porta J, Solé de Porta N, Civís J (2001) Stratigraphy and petrology of the Miocene Montjuïc delta (Barcelona, Spain). *Acta Geologica Hispanica*, **36** (1-2), 115-136.
- Griggs DT (1967) Hydrolytic weakening of quartz and other silicates. *Geophysical Journal of the Royal Astronomical Society*, **14** (1-4), 19-31.
- Guimerà J (1978) Estudi estructural de les zones de fractura de Garraf i de Vallcarca, Massís de Garraf. Dissertation, Universitat de Barcelona, 124 p.
- Guimerà J, Santanach P (1978) Sobre la compresión alpina en el sector central de las Cadenas Costero Catalanas. *Acta Geològica Hispànica*, **XIII** (2), 33-42.
- Guimerà J (1984) Palaeogene evolution of deformation in the northeastern Iberian Peninsula. *Geol. Mag.*, **121** (5):413-420.
- Hills ES (1963) Elements of Structural Geology. Chapman and Hall, London, 483 p.

- Hoffmann DL, Spötl C, Mangini A (2009) Micromill and in situ laser ablation sampling techniques for high spatial resolution MC-ICPMS U-Th dating of carbonates. *Chemical Geology*, **259** (3-4), 253-261.
- IGC (2011) Geotrebball III. Mapa Geològic de zones urbanes 1:5000, Santa Coloma de Gramanet. Full 290-123 (421-2-3).
- Ivanov IP, Gurevich LP (1975) Experimental Study of T-X<sub>CO2</sub> Boundaries of Metamorphic Zeolite Facies. *Contributions to Mineralogy and Petrology*, **53**, 55-60.
- Iwatsuki T, Satake H, Metcalfe R, Yoshida H, Hama K (2002) Isotopic and morphological features of fracture calcite from granitic rocks of the Tono area, Japan: a promising palaeohydrogeological tool. *Applied Geochemistry*, **17**, 1241-1257.
- James NP, Choquette PW (1990) Limestones - The meteoric diagenetic environment. In: McIlreath, I.A. & Morrow, D.W. (eds.) *Diagenesis*. Canada Reprint Series 4, 35-73.
- Jiménez de Cisneros C, Caballero E, Vera JA, Durán JJ, Juliá R (2003) A record of Pleistocene climate from a stalactite, Nerja Cave, southern Spain. *Palaeogeography, Palaeoclimatology, Palaeoecology*, **189**, 1-10.
- Juez-Larré J (2003) Post Late Paleozoic tectonothermal evolution of the northeastern margin of Iberia, assessed by fission-track and (U-Th)/He analyses. A case history from the Catalan Coastal Ranges. Dissertation, Vrije Universiteit, 200 p.
- Julivert M, Durán H (1990a) Paleozoic stratigraphy of the Central and Northern part of the Catalanian Coastal Ranges (NE Spain). *Acta Geològica Hispànica*, **25** (1-2), 3-12.
- Julivert M, Durán H (1990b) The Hercynian structure of the Catalanian Coastal Ranges (NE Spain). *Acta Geològica Hispànica*, **25** (1-2), 13-21.
- Kabanov P, Anadón P, Krumbein WE (2008) Microcodium: An extensive review and a proposed non-rhizogenic biologically induced origin for its formation. *Sedimentary Geology*, **205**, 79-99.

- Klappa CF (1978) Biolithogenesis of Microcodium: elucidation. *Sedimentology*, **25**, 489-522.
- Koepnick RB (1983) Distribution and vertical permeability of stylolites within a Lower Cretaceous carbonate reservoir, Abu Dhabi, United Arab Emirates. In: Stylolites and associated phenomena: relevance to Hydrocarbon reservoirs, Abu Dhabi, UAE. Abu Dhabi Reservoir Research Foundation Special Publication, 261-278.
- Košir A (2004) Microcodium revisited: root calcification products of terrestrial plants on carbonate-rich substrates. *Journal of Sedimentary Research*, **74** (6), 845-857.
- Kristmannsdóttir H, Tómasson J (1978) Zeolite zones in geothermal areas in Iceland. In: Sand L.B. & Mumpton F.A. (eds.) *Natural Zeolites: Occurrence, Properties, Use*. Pergamon Press, Elmsford, New York, 277-284.
- Lacroix B (2011) Interaction fluide-roche et comportement des phyllosilicates à basses températures en contexte sédimentaire: exemple du prisme orogénique sud-pyrénéen. Dissertation, Université de Franche Comté.
- Lacroix B, Charpentier D, Buatier M, Vennemann T, Labaume P, Adatte T, Travé A, Dubois M (2012) Formation of chlorite during thrust fault reactivation. Record of fluid origin and P-T conditions in the Monte Perdido thrust fault (southern Pyrenees). *Contributions to Mineralogy and Petrology*, **163** (6), 1083-1102.
- Lanari P, Guillot S, Schwartz S, Vidal O, Tricart P, Riel N, Beyssac O (2012) Diachronous evolution of the alpine continental subduction wedge: Evidence from P-T estimates in the Briançonnais Zone houillère (France-Western Alps). *Journal of Geodynamics*, **56-57**, 39-54
- Lewis CJ, Vergés J, Marzo M (2000) High mountains in a zone of a extended crust: Insights into the Neogene-Quaternary topographic development of the northeastern Iberia. *Tectonics*, **19** (1), 86-102.
- Liou JG, Seki Y, Guillemette RN, Sakai H (1985) Compositions and parageneses of secondary minerals in the Onikobe geothermal system, Japan. *Chemical Geology*, **49**, 1-20.



- López de Azcona JM (1983) Consideraciones sobre el grupo de manatiales de aguas mineromedicinales de Caldas de Montbui. In: Monografía X Caldas de Montbui. *Monografías de aguas mineromedicinales*, pp 5-21
- Martín-Martín JD, Tritlla J, Cardellach E, Gómez-Gras D (2006) Tectonically driven fluid flow and associated low-grade metamorphism during the Alpine compression in the eastern Iberian Chain (Spain). *Journal of Geochemical Exploration*, **89**, 267-270
- Lucas G, Montenat C (1967) Observations sur les structures internes et de développement des Microcodium. *Bulletin de la Société Géologique de France*, **7** (9), 909-918.
- Manning DAC (2008) Biological enhancement of soil carbonate precipitation: passive removal of atmospheric CO<sub>2</sub>. *Mineralogical Magazine*, **72** (2), 639-649.
- Martín-Martín JD, Salas R, Gómez-Gras D (2008) Datación por K-Ar de la diagénesis y el metamorfismo de muy bajo grado en red-beds permo-triásicos de la Cadena Ibérica oriental (Castellón y Valencia): resultados preliminares. *Geo-Temas*, **10**, 257-260
- Martín-Martín J, Salas R, Gómez-Gras D, Zwingmann H (2009) K/Ar isotopic dating of very low-grade metamorphic and diagenetic conditions during the Mesozoic rifting evolution of the Iberian Chain, Spain. XIV International Clay Conference, Italia.
- Massone HJ, Schreyer W (1989) Stability field of the high-pressure assemblages talc-phengite and two new phengite barometers. *European Journal of Mineralogy*, **1**, 391-410
- Matte P (2001) The Variscan collage and orogeny (480-290 Ma) and the tectonic definition of the Armorica microplate: a review. *Terra Nova*, **13**, 122-128.
- McCrea JM (1950) On the isotopic chemistry of carbonates and a paleotemperature scale. *The Journal of Chemical Physics*, **18** (6), 849-857.
- McQueen KG, Hill SM, Foster KA (1999) The nature and distribution of regolith carbonate accumulations in southeastern Australia and their potential as a sampling

- medium in geochemical exploration. *Journal of Geochemical Exploration*, **67**, 67-82.
- Mercier J, Vergély P, Missenard Y (2011) *Tectonique 3e ed.* Ed. Dunod, Paris, 225 p.
- Molina JM, Salas R (1993) Bauxitas kársticas del Cretácico inferior en Fuentespalda (provincia de Teruel): Estratigrafia, origen y paleogeografia. *Cuadernos de Geología Ibérica*, **17**, 207-230.
- Morrow CA, Moore DE, Lockner DA (2000) The effect of mineral bond strength and adsorbed water on fault gouge frictional strength. *Geophysical Research Letters*, **27**, 815-818.
- Muñoz JA (1992) Evolution of a continental collision belt: ECORS-Pyrenees crustal balanced section. In: McClay K.R. (ed). *Thrust Tectonics*, 235-246.
- Muñoz JA (2002) The Pyrenees. In: Gibbons W. & Moreno T. (ed). *The Geology of Spain*, Geological Society of London, 370-385.
- Mutlu H, Uysal IT, Altunel E, Karabacak V, Feng Y, Zhao J, Atalay O (2010) Rb-Sr systematics of fault gouges from the North Anatolian Fault Zone (Turkey). *Journal of Structural Geology*, **32**, 216-221.
- Onasch CM, Dunne WM, Cook JE, O’Kane A (2009) The effect of fluid composition on the behavior of well cemented, quartz-rich sandstone during faulting. *Journal of Structural Geology*, **31**, 960-971.
- O’Neil JR, Clayton RN, Mayeda TK (1969) Oxygen isotope fractionation in divalent metal carbonates. *Journal of Chemical Physics*, **51** (12), 5547-5558.
- Parcerisa D (2002) Petrologia i diagènesi en sediments de l’Oligocè superior i del Miocè inferior i mitjà de la Depressió del Vallès i del Pla de Barcelona. Evolució de l’àrea Font i dinàmica dels fluids. Dissertation, Universitat Autònoma de Barcelona, 261 p.
- Parcerisa D, Gómez-Gras D, Travé A (2005) A model of early calcite cementation in alluvial fans: Evidence from the Burdigalian sandstones and limestones of the Vallès-Penedès half-graben (NE Spain). *Sedimentary Geology*, **178**, 197-217.

- Parcerisa D, Gómez-Gras D, Roca E, Madurell J, Agustí J (2007) The Upper Oligocene of Montgat (Catalan Coastal Ranges, Spain): new age constraints to the western Mediterranean Basin opening. *Geologica Acta*, **5** (1), 3-17.
- Parra T, Vidal O, Agard P (2002) A thermodynamic model for Fe-Mg dioctahedral K White micas using data from phase-equilibrium experiments and natural pelitic assemblages. *Contributions to Mineralogy and Petrology*, **143**, 706-732.
- Passchier C.W., Trouw R.A.J. (1996). *Microtectonics*. Ed. Springer-Verlog Berlin Heidelberg. 289 p.
- Piqué À, Canals À, Grandia F, Banks DA (2008) Mesozoic fluorite veins in NE Spain record regional base metal-rich brine circulation through basin and basement during extensional events. *Chemical Geology*, **257**, 139-152.
- Plawman TL (1983) Fault with reversal of displacement, Central Montana. In: Bally A.W. (ed.) *Seismic expression of structural styles – a picture and work atlas*. AAPG Studies in Geology, **15** (3).
- Powell CM (1987) Inversion tectonics in SW Dyfed. *Proceedings of the Geologists' Association*, **98** (3), 193-203.
- Putnis A (2002) Mineral replacement reactions: from macroscopic observations to microscopic mechanisms. *Mineralogical Magazine*, **66** (5), 689–708
- Ramon X, Calvet F (1987) Estratigrafia y sedimentología del Muschelkalk inferior del dominio Montseny-Llobregat (Catalánides). *Estudios geológicos*, **43** (5-6), 471-487.
- Roca E, Guimerà J (1992) The Neogene structure of the eastern Iberian margin: structural constraints on the crustal evolution of the Valencia trough (Western Mediterranean). *Tectonophysics*, **203**, 203-218.
- Roca E (1996) La evolución geodinámica de la Cuenca Catalano-Balear y áreas adyacentes desde el Mesozoico hasta la actualidad. *Acta Geológica Hispánica*, **29**, 3-25.

- Roca E, Sans M, Cabrera L, Marzo M (1999) Oligocene to Middle Miocene evolution of the central Catalan margin (Northwestern Mediterranean). *Tectonophysics*, **315**, 209-233.
- Rossi C, Cañaveras JC (1999) Pseudospherulitic fibrous calcite in paleo groundwater, unconformity-related diagenetic carbonates (Paleocene of the Áger Basin and Miocene of the Madrid Basin, Spain). *Journal of Sedimentary Research*, **69** (1), 224-238.
- Rossi C, Goldstein RH, Marfil R, Salas R, Benito MI, Permanyer A, de la Peña JA, Caja MA (2001) Diagenetic and oil migration history of the Kimmeridgian Ascla Formation, Maestrat Basin, Spain. *Marine and Petroleum Geology*, **18**, 287- 306.
- Rowland J.V., Sibson R.H. (2004). Structural controls on hydrothermal flow in a segmented rift system, Taupo Volcanic Zone, New Zealand. *Geofluids*, **4**, 259-283.
- Salas R, Casas A (1993) Mesozoic extensional tectonics, stratigraphy and crustal evolution during the Alpine cycle of the eastern Iberian basin. *Tectonophysics*, **228** (1-2), 33-55.
- Salas R, Guimerà J, Mas R, Martín-Closas C, Meléndez A, Alonso A (2001) Evolution of the Mesozoic central Iberian Rift System and its Cainozoic inversion (Iberian Chain). In: Ziegler P.A., Cavazza W., Robertson A.H.F. & Crasquin-Soleau S. (eds.) *Peri-Tethys Memoir 6: Peri-Tethyan Rift/Wrench Basins and Passive Margins*. Mem. Mus. natn. Hist. Nat., **186**, 145-185.
- Salas R, Vaquer R, Travé A (2004) Bauxitas kársticas y arcillas lateríticas barremienses de la Cadena Ibérica oriental y la Cadena Costero Catalana : relaciones genéticas y áreas de procedencia. *Geo-Temas*, **6** (2), 123-126.
- Santanach P, Casas JM, Gratacós O, Liesa M, Muñoz JA, Sàbat F (2011) Variscan and Alpine structure of the hills of Barcelona: geology in an urban area. *Journal of Iberian Geology*, **37** (2), 121-136.
- Scholz CH (2002) The mechanics of earthquakes and faulting. Cambridge University Press, p. 471.

- Schulz SE, Evans JP (1998) Spatial variability in microscopic deformation and composition of the Punchbowl fault, southern California: implications for mechanisms, fluid–rock interaction, and fault morphology. *Tectonophysics*, **295** (1-2), 223-244.
- Séguret M (1972) Etude tectonique des nappes et séries décollées de la partie centrale du versant sud des Pyrénées. Série géologie structurale, n°2. Publications de l'Université des Sciences et Techniques du Languedoc (Ustela), Montpellier.
- Serra PR, Enrique P (1989) Late hercynian intrusives from the Southern Catalanian coastal ranges (NE Spain), and their epiplutonic to subvolcanic level of magma emplacement. *Rendiconti della società italiana di mineralogia e petrologia*, **43-3**, 817-829.
- Shelley D (1983) Igneous and metamorphic rocks under the microscope: classification, textures, microstructures and mineral preferred orientations. Chapman and Hall, London.
- Sibson RH, Moore JMcM, Rankin AH (1975) Seismic pumping-a hydrothermal fluid transport mechanism. *Journal of the Geological Society of London*, **131**, 653-659.
- Sibson R.H. (1977). Fault rocks and fault mechanisms. *Geological Society of London*, **133**, 191-213.
- Sibson R.H. (1986) Earthquakes and rock deformation in crustal fault zones. *Ann. Rev. Planet. Sci.*, **14**, 149-175.
- Sibson RH, Robert F, Poulsen KH (1988) High-angle reverse faults, fluid-pressure cycling, and mesothermal gold-quartz deposits. *Geology*, **16**, 551-555.
- Sibson RH, Scott J (1998) Stress/fault controls on the containment and release of overpressured fluids: examples from gold-quartz vein systems in Juneau, Alaska; Victoria, Australia and Otago, New Zealand. *Ore geology Reviews*, **13**, 293-306.
- Sibson R.H. (2000) Fluid involvement in normal faulting. *Journal of Geodynamics*, **29**, 469-499.
- Siebel W, Hann HP, Danišík M, Shang CK, Berthold C, Rohrmüller J, Wemmer K, Evans NJ (2009) Age constraints on faulting and fault reactivation: a multi-

- chronological approach. *International Journal of Earth Sciences*, DOI 10.1007/s00531-009-0474-9.
- Solé Sugrañes L (1978) Alineaciones y fracturas en el sistema catalán según las imágenes LANDSTAT-1. *Tecniterrae*, **22**, 6-16.
- Solé J, Cosca M, Sharp Z, Enrique P (2002)  $^{40}\text{Ar}/^{39}\text{Ar}$  geochronology and stable isotope geochemistry of Late-Hercynian intrusions from north-eastern Iberia with implications for argon loss in K-feldspar. *International Journal of Earth Sciences (Geol Rundsch)*, **91**, 865-881.
- Swanson MT (1992) Fault structure, wear mechanisms and rupture processes in pseudotachylyte generation. *Tectonophysics*, **204**, 223-242.
- Sykes LR (1978) Intra-plate seismicity, reactivation of pre-existing zones of weakness, alkaline magnetism, and other tectonics post-dating continental separation. *Reviews of Geophysics and Space Physics*, **16**, 621-688.
- Tavarnelli E, Pasqui V (2000) Fault growth by segment linkage in seismically active settings: Examples from the Southern Apennines, Italy, and the Coast Ranges, California. *Journal of Geodynamics*, **29**, 501-516.
- Taylor HP Jr (1977) Water/rock interactions and the origin of  $\text{H}_2\text{O}$  in granitic batholiths. *Journal of the Geological Society of London*, **133**, 509-558.
- ter Voorde M, Gaspar-Escribano JM, Juez-Larré J, Roca E, Cloetingh S (2007) Thermal effects of linked lithospheric and upper crustal-scale processes: Insights from numerical modeling of the Cenozoic Central Catalan Coastal Ranges (NE Spain). *Tectonics*, **26**: TC5018.
- Travé A, Calvet F, Soler A, Labaume P (1998) Fracturing and fluid migration during Paleogene compression and Neogene extension in the Catalan Coastal Ranges, Spain. *Sedimentology*, **45**, 1063-1082.
- Travé A, Calvet F (2001) Syn-rift geofluids in fractures related to the early-middle Miocene evolution of the Vallès-Penedès half-graben (NE Spain). *Tectonophysics*, **336**, 101-120.



- Travé A, Roca E, Playà E, Parcerisa D, Gómez-Gras D, Martín-Martín JD (2009) Migration of Mn-rich fluids through normal faults and fine-grained terrigenous sediments during early development of the Neogene Vallès-Penedès half-graben (NE Spain). *Geofluids*, **9**, 303-320.
- Trilla J (1974) Sobre el origen de las aguas termales de Caldes de Montbui. *Acta Geològica Hispànica*, **IX** (4), 144-148.
- Tritlla J, Solé J (1999) A newly dated Cretaceous hydrothermal event in the Iberian Ranges (Eastern Spain) and its significance within the Mesozoic thermal history in the Iberian Peninsula. *Ore Geology Reviews*, **15**, 243-259.
- Tucker ME, Wright VP (1990) Carbonate sedimentology. Blackwell Scientific Publications, London.
- Tucker M, Marshall J (2004) Diagenesis and geochemistry of Upper Muschelkalk (Triassic) buildups and associated facies in Catalonia (NE Spain): a paper dedicated to Francesc Calvet. *Geologica Acta*, **2** (4), 257-269.
- Veizer J, Ala D, Azmy K, Bruckschen P, Buhl D, Bruhn F, Carden G, Diener A, Ebner S, Godderis Y, Jasper T, Korte C, Pawellek F, Podlaha O, Strauss H (1999)  $^{87}\text{Sr}/^{86}\text{Sr}$ ,  $\delta^{13}\text{C}$  and  $\delta^{18}\text{O}$  evolution of Phanerozoic seawater. *Chemical Geology*, **161**, 59-88.
- Vergés J (1993) Estudi geològic del vessant sud del Pirineu Oriental i Central: evolució en 3D. Dissertation, Universitat de Barcelona, 203 p.
- Vergés J, Sàbat F (1999) Constraints on the Neogene Mediterranean kinematic evolution along a 1000 km transect from Iberia to Africa. In: Durand B, Jolivet L, Horváth F and Séranne M (eds.) The Mediterranean basins: Tertiary Extension within the Alpine Orogen. *Geological Society of London Special Publications*, **156**, 63-80.
- Vergés J, García-Senz J (2001) Mesozoic evolution and Cainozoic inversion of the Pyrenean Rift. In: Ziegler P.A. et al. (eds.) *Peri-Tethys Memoir 6: Peri-Tethyan Rift/Wrench Basins and Passive Margins*. Mém. Mus. National Hist. Nat., **186**, 187-212.

- Vesica PL, Tuccimei P, Turi B, Fornós JJ, Ginés A, Ginés J (2000) Late Pleistocene Paleoclimates and sea-level change in the Mediterranean as inferred from stable isotope and U-series studies of overgrowths on speleothems, Mallorca, Spain. *Quaternary Science Reviews*, **19** (9), 865-879.
- Vidal O, Parra T, Trotet F (2001) A thermodynamic model for Fe-Mg aluminous chlorite using data from phase equilibrium experiments and natural pelitic assemblages in the 100-600°C 1-25 kbar range. *American Journal of Science*, **63**, 557-592.
- Vidal O, Parra T, Vieillard P (2005) Thermodynamic properties of the Tschermak solid solution in Fe-chlorite: Application to natural examples and possible role of oxidation. *American Mineralogist*, **90**, 347-358.
- Vidal O, De Andrade V, Lewin E, Munoz M, Parra T, Pascarelli S (2006) P-T-deformation-Fe<sup>3+</sup>/Fe<sup>2+</sup> mapping at the thin section scale and comparison with XANES mapping. Application to a garnet-bearing metapelite from the Sambagawa metamorphic belt (Japan). *Journal of Metamorphic Geology*, **24**, 669-683
- Watts NL (1980) Quaternary pedogenetic calcretes from the Kalahari (southern Africa): mineralogy, genesis and diagenesis. *Sedimentology*, **27**, 661-686.
- White SH, Bretan PG, Rutter EH (1986) Fault-zone reactivation: kinematic and mechanisms. *Philosophical Transactions of the Royal Society of London A*, **317**, 81-97.
- Wintsch RP, Christoffersen R, Kronenberg AK (1995) Fluid-rock reaction weakening of fault zones. *Journal of Geophysical Research*, **100** (B7), 13021-13032.
- Yoshida H, Metcalfe R, Ishibashi M, Minami M (2012) Long-term stability of fracture systems and their behaviour as flow paths in uplifting granitic rocks from the Japanese orogenic field. *Geofluids*, doi: 10.1111/gfl.12008.

## **Appendix 1: Geochemical data**



Table 1. Stable isotope data ( $\delta^{18}\text{O}$ - $\delta^{13}\text{C}$ ) of host rocks and cements of the studied area

Description	$\delta^{18}\text{O}\text{‰ VPDB}$	$\delta^{13}\text{C}\text{‰ VPDB}$	Sample	Outcrop
<b>HR1</b>	-3.6	0.7	G-12n42	Guixeres
	-3.4	2.2	G-12n44	Guixeres
	-4.6	2.6	G-15p3	Guixeres
<b>HR2</b>	-3.3	0.9	G-9p27	Guixeres
	-2.7	2.3	G-11p34	Guixeres
	-3.2	2.3	G-11p35	Guixeres
	-2.7	0.9	G-11p36	Guixeres
	-3.5	2.6	HOS-16E	Hospital
	-3.7	2.8	HOS-16C	Hospital
<b>D1</b>	-5.9	2.3	G-15p1	Guixeres
	-5.4	2.4	G-15p2	Guixeres
<b>D2</b>	-7.2	2.5	G-16n1	Guixeres
	-6.8	2.6	G-16n2	Guixeres
<b>C1a</b>	-15.6	-6.5	HOS-3	Hospital
	-15.6	-6.5	HOS-4	Hospital
	-15.0	-6.3	HOS-5	Hospital
<b>C1f</b>	-16.2	-5.9	HOS-10A	Hospital
	-16.4	-6.2	HOS-10B	Hospital
<b>C1</b>	-15.1	-6.9	EN-2E	Enric
	-15.0	-7.8	MTB-22	Torrent del Corró
<b>C2a</b>	-4.9	-7.1	HOS-6	Hospital
	-4.6	-6.5	HOS-7	Hospital
	-5.5	-7.0	HOS-8	Hospital
<b>C2b-c</b>	-5.8	-7.2	TS-2	Sariol
<b>CD1+CD2</b>	-5.9	-7.1	G-9p22	Guixeres
	-5.6	-6.1	G-9n13	Guixeres
<b>CD1+CD4</b>	-5.5	-6.3	G-12n38	Guixeres
<b>CD3</b>	-5.3	-6.8	G-9n11	Guixeres
	-5.2	-7.4	G-9n12	Guixeres
	-5.1	-6.3	G-9n17	Guixeres
	-5.2	-5.6	G-9p23	Guixeres
	-4.9	-5.7	G-11p33	Guixeres
	-5.2	-5.4	G-5p6	Guixeres
<b>Calcitized dolostones M1</b>	-4.1	-3.2	G-4n2	Guixeres
<b>Calcitized dolostones M3</b>	-9.3	-4.7	TS-1	Sariol
	-9.5	-4.8	TS-1	Sariol
<b>C3a</b>	-20.5	-6.2	EN-2A	Enric
	-20.0	-6.2	EN-2B	Enric
	-20.3	-6.2	EN-2C	Enric
	-20.8	-6.1	EN-2D	Enric
	-20.3	-6.2	EN-2G	Enric
	-19.6	-6.2	EN-2H	Enric
<b>C3b</b>	-18.4	-6.1	EN-2F	Enric
<b>C4</b>	-22.2	-7.7	MTB-1pA	Torrent del Corró
	-20.9	-8.0	MTB-1pB	Torrent del Corró
	-22.8	-7.2	MTB-2pB	Torrent del Corró
	-22.7	-7.7	MTB-21	Torrent del Corró
<b>C5</b>	-5.8	-7.7	EN-3D	Enric
<b>C6</b>	-2.6	-7.6	TS-1	Sariol
	-2.9	-7.6	TS-2	Sariol
<b>C8</b>	-2.9	-8.4	EN-1A	Enric

Description	$\delta^{18}\text{O}\text{‰ VPDB}$	$\delta^{13}\text{C}\text{‰ VPDB}$	Sample	Outcrop
<b>C8</b>	-2.9	-8.5	EN-1B	Enric
	-2.5	-8.3	EN-1C	Enric
<b>PC1</b>	-2.6	-7.7	TS-1	Sariol
	-1.9	-7.7	TS-1	Sariol
<b>Microcodium (luminescent spherulites)</b>	-4.1	-9.0	BAD-5E	Caritg
	-3.9	-9.0	BAD-5F	Caritg
<b>Microcodium (non-luminescent spherulites)</b>	-4.1	-9.6	BAD-1A	Caritg
<b>Microcodium (white bladed)</b>	-4.3	-9.8	BAD-1C	Caritg
	-4.4	-10.3	BAD-1D	Caritg
<b>Microcodium (micrite strips)</b>	-4.2	-10.1	BAD-5A	Caritg
	-4.3	-9.9	BAD-5B	Caritg
	-4.4	-10.2	BAD-5C	Caritg
	-4.2	-9.5	BAD-5D	Caritg
<b>HMC speleothem</b>	-4.7	-9.8	G-11p29	Guixeres
	-4.8	-9.6	G-11p30	Guixeres
	-4.7	-8.5	G-11p31	Guixeres
	-5.3	-9.8	G-11p32	Guixeres
<b>Dolomite speleothem</b>	-2.6	-9.3	G-12n39	Guixeres
<b>Aragonite speleothem</b>	-4.2	-9.2	G-12n41	Guixeres
	-4.3	-9.2	G-12n45	Guixeres
	-4.6	-9.8	G-12n40	Guixeres
<b>HMC rafts</b>	-4.6	-9.0	G-5p1	Guixeres
	-3.4	-8.6	G-5p2	Guixeres
	-3.3	-8.2	G-5p3	Guixeres



Table 2. Elemental composition of Triassic dolostones and calcite and dolomite cements

Label	Ca ppm	Mg ppm	Na ppm	Mn ppm	Fe ppm	Sr ppm	Total	Description
G-12n-c1-35	216464	131235	355	110	512	700	999000	HR1
G-12n-c1-36	211248	130316	369	45	496	597	982500	HR1
G-12n-c1-37	215610	131029	310	31	848	517	996300	HR1
G-12n-c2-38	216960	128308	410	114	150	531	989200	HR1
G-12n-c2-39	215464	132095	309	98	690	376	999200	HR1
G-12n-c2-40	212470	129624	370	88	447	548	983000	HR1
G-12n-c2-41	218109	129030	246	98	604	511	995100	HR1
G-15p-c3-55	218115	132250	212	0	131	677	1005300	HR1
G-15p-c5-64	217932	130315	297	0	17	621	998000	HR1
G-15p-c5-65	214437	152760	336	5	459	603	1068100	HR1
G-15p-c5-66	216099	152094	211	160	1269	543	1071500	HR1
G-15p-c5-67	214909	132630	454	58	223	591	999300	HR1
G-15p-c5-68	219995	129197	249	0	339	448	999500	HR1
G-15p-c5-69	217380	134259	116	36	3	509	1009700	HR1
G-15p-c5-70	218711	131904	66	0	280	568	1005300	HR1
G-11p-c1-24	214347	129776	235	24	923	457	988600	HR2
G-11p-c1-25	221167	129742	296	18	4800	354	1013500	HR2
G-11p-c1-27	216578	128544	299	110	1119	720	991100	HR2
G-11p-c1-28	202598	130245	350	115	17845	0	995700	HR2
G-9p1-c2-1	216348	125113	354	15	237	716	976700	HR2
G-9p1-c2-2	219617	131516	136	42	1047	584	1008100	HR2
G-9p1-c2-3	219683	128969	307	36	495	796	999000	HR2
G-9p1-c2-4	221559	131546	107	52	937	542	1012700	HR2
G-9p1-c2-5	219537	128200	289	169	329	857	996000	HR2
G-9p1-c1-19	216796	129849	111	150	1800	411	996700	HR2
G-9p1-c1-20	222456	121744	265	53	3455	544	986600	HR2
G-16n-c5-103	217435	128621	210	127	426	638	991800	HR2
G-16n-c5-104	218470	132336	292	38	593	32	1006600	HR2
G-16n-c5-105	217355	129542	247	4	436	551	994500	HR2
G-16n-c5-106	216185	127152	212	75	464	614	983500	HR2
G-16n-c5-107	219149	130720	295	63	375	462	1003000	HR2
G-16n-c6-112	222716	129071	208	0	0	554	1005200	HR2
G-16n-c6-113	216606	132719	166	188	760	474	1004400	HR2
G-16n-c6-114	220193	129270	211	43	50	475	999700	HR2
G-16n-c6-115	221784	130780	235	0	258	539	1009400	HR2
G-16n-c6-116	216089	131857	313	43	152	828	999500	HR2
G-16n-c6-117	218200	129841	311	113	592	546	998300	HR2
EN-5-c2-130	217476	128146	146	0	667	368	989900	HR3
EN-5-c2-131	218000	130392	182	0	977	550	1000000	HR3
EN-5-c2-132	216091	126129	76	350	3844	406	986600	HR3
EN-5-c2-133	217763	126860	217	242	2445	564	990800	HR3
EN-5-c3-136	216150	128766	330	39	597	525	989300	HR3
EN-5-c3-138	222811	126493	439	63	685	501	998500	HR3
EN-5-c3-139	214268	127659	382	14	736	326	980800	HR3
EN-5-c3-140	218074	128627	154	217	2114	553	996800	HR3
HOS-15-c1-165	220142	125106	517	496	1244	469	989200	HR3
HOS-15-c1-166	221015	131589	206	548	919	541	1012700	HR3
HOS-15-c3-174	221537	130146	207	435	1382	475	1009700	HR3
HOS-15-c3-176	214495	123851	145	486	3212	347	973800	HR3
HOS-15-c5-190	222072	126787	36	389	826	546	997800	HR3
HOS-15-c5-192	224409	129395	162	532	1159	525	1013900	HR3

## Appendix 1

Label	Ca ppm	Mg ppm	Na ppm	Mn ppm	Fe ppm	Sr ppm	Total	Description
HOS-15-c5-193	217189	127740	225	641	1721	545	991700	HR3
HOS-16-c3-210	217590	135569	85	56	759	335	1016000	HR3
HOS-16-c3-213	225332	120667	63	779	1950	283	987500	HR3
HOS-16-c3-214	215251	133237	25	135	1548	271	1003600	HR3
HOS-16-c3-215	217401	128792	111	187	874	367	992700	HR3
HOS-16-c4-222	213966	124982	201	165	699	309	970600	HR3
HOS-16-c4-224	245753	104916	100	960	2556	363	985700	HR3
EN-10-c2-1	220549	131053	-	205	1703	9	1009300	HR4
EN-10-c2-2	220404	128822	-	126	1731	0	1001000	HR4
EN-10-c2-3	221039	129583	-	173	2571	0	1007100	HR4
EN-10-c2-4	218605	129888	-	82	2240	0	1001200	HR4
EN-10-c2-5	217614	127839	-	188	3164	0	993800	HR4
EN-10-c2-6	218981	127827	-	242	1705	23	994300	HR4
EN-10-c2-7	216910	128990	-	337	939	0	991700	HR4
EN-10-c1-15	216001	126829	-	164	977	0	981600	HR4
EN-10-c1-17	220306	127589	-	325	1459	24	996400	HR4
EN-10-c1-20	215966	128276	-	398	1674	33	988600	HR4
EN-10-c1-21	217966	130337	-	252	1859	0	1000700	HR4
EN-10-c1-23	217515	128459	-	232	1412	0	992100	HR4
EN-10-c1-26	216868	128394	-	271	741	0	989000	HR4
EN-10-c1-27	217089	126808	-	195	923	64	984300	HR4
EN-10-c1-30	216517	130544	-	147	2065	15	998100	HR4
G-15p-c3-56	217625	130737	0	108	846	382	999500	RD1
G-15p-c5-57	222721	134409	0	35	422	506	1024100	RD1
G-15p-c5-58	217407	130630	30	205	922	405	999100	RD1
G-15p-c5-59	218325	132781	13	70	323	372	1007200	RD1
G-15p-c5-60	220982	131055	10	0	304	434	1007800	RD1
G-15p-c5-61	220087	132706	56	41	435	473	1011800	RD1
G-15p-c5-62	216438	131760	0	0	165	366	998400	RD1
G-15p-c5-63	222372	129305	130	67	97	485	1005200	RD1
EN-5-c3-134	217576	130622	0	53	1197	337	999500	RD1
EN-5-c3-135	216663	132160	0	30	927	268	1001900	RD1
EN-5-c3-137	220374	132307	0	156	1466	610	1013600	RD1
HOS-16-c3-209	221270	128123	0	61	322	305	998200	RD1
HOS-16-c3-211	218111	130453	62	47	442	416	999000	RD1
HOS-16-c3-212	219559	136806	200	42	273	248	1024300	RD1
HOS-16-c4-220	222747	130909	209	45	219	317	1011800	RD1
G-9p1-c1-13	217226	129033	0	63	1274	532	993600	D1
G-9p1-c1-14	219077	130125	263	18	1013	563	1002100	D1
G-9p1-c1-15	219908	129854	225	94	566	607	1002400	D1
G-9p1-c1-16	217744	129693	303	85	642	697	996900	D1
G-9p1-c1-17	221285	130660	277	120	462	776	1008900	D1
G-9p1-c2-6	216704	128429	336	62	906	618	990400	D1
G-9p1-c2-8	216990	129345	407	86	831	487	994100	D1
G-9p1-c2-9	220915	129244	290	56	578	606	1002900	D1
G-9p1-c2-10	213612	127664	256	93	1048	592	980200	D1
G-9p1-c2-11	218656	133086	73	38	168	475	1009000	D1
G-9p1-c2-12	221042	128069	470	95	418	732	999500	D1
G-11p-c1-29	216202	131606	202	54	1129	658	1000400	D1
G-11p-c1-30	219350	130367	73	127	730	628	1002900	D1
G-11p-c1-31	214654	132083	131	48	575	551	996700	D1
G-11p-c1-33	217947	131314	100	38	318	532	1001600	D1
G-11p-25-39	217400	130900	0	0	1200	700	1000500	D1

Label	Ca ppm	Mg ppm	Na ppm	Mn ppm	Fe ppm	Sr ppm	Total	Description
G-11p-26-45	216800	131500	100	0	1800	800	1002900	D1
G-11p-26-46	217800	129800	100	100	1100	600	997700	D1
G-11p-26-47	217600	129500	100	100	800	800	996000	D1
G-11p-26-48	221700	129600	100	200	700	500	1005800	D1
G-15p-c1-43	216946	130934	331	52	114	736	998200	D1
G-15p-c1-44	218754	132403	379	0	208	579	1007800	D1
G-15p-c1-45	221182	129710	115	37	197	544	1003900	D1
G-15p-c1-46	214113	134565	294	151	315	751	1004300	D1
G-15p-c1-47	217426	132032	261	162	299	571	1003400	D1
G-15p-c2-48	220081	131797	0	201	810	261	1009200	D1
G-15p-c2-49	218889	130874	153	113	639	515	1003300	D1
G-15p-c2-50	219604	129947	151	70	251	487	1000900	D1
G-15p-c2-51	218061	131039	125	104	551	499	1001500	D1
G-15p-c3-53	216695	129842	61	33	186	529	992900	D1
G-15p-c3-54	217198	130642	187	87	292	616	997700	D1
G-16n-c3-91	221213	128950	55	88	340	176	1001000	D1
G-16n-c3-92	217168	127909	221	147	78	559	987900	D1
G-16n-c3-93	217608	129193	216	73	419	457	993800	D1
G-16n-c3-94	221864	127591	61	94	552	0	998000	D1
G-16n-c3-95	219220	129727	258	20	237	517	999400	D1
G-16n-c1-74	218399	123803	138	74	374	525	976900	D2a
G-16n-c1-75	216961	127726	262	106	426	609	987500	D2a
G-16n-c1-78	222478	129215	187	41	362	589	1006000	D2a
G-16n-c1-79	221416	131422	256	14	493	681	1011500	D2a
G-16n-c1-80	220636	131800	50	72	554	454	1010300	D2a
G-16n-c2-81	219637	128219	102	67	560	128	994900	D2a
G-16n-c2-82	217962	129034	299	98	561	556	994800	D2a
G-16n-c2-84	214197	130083	113	177	870	639	989600	D2a
G-16n-c2-85	220986	127551	123	21	355	0	995300	D2a
G-16n-c2-86	216159	129627	304	37	324	481	991600	D2a
G-16n-c2-87	216995	129310	218	61	380	542	992700	D2a
G-16n-c1-73	220205	129240	257	56	379	667	1000800	D2a
G-16n-c4-96	217470	129766	56	92	657	392	995500	D2a
G-16n-c4-97	216875	127213	220	0	92	437	984200	D2a
G-16n-c4-98	218043	129238	0	22	222	352	993800	D2a
G-16n-c4-99	221684	130566	119	53	573	460	1008800	D2a
G-16n-c4-100	223924	129847	351	3	203	477	1011600	D2a
G-16n-c4-101	216647	126508	206	33	527	431	982100	D2a
EN-5-c1-118	220580	127711	106	225	2749	503	1001000	D2b
EN-5-c1-119	219723	127611	230	125	1960	30	996200	D2b
EN-5-c1-120	221205	132549	160	68	424	478	1014300	D2b
EN-5-c1-121	219581	128876	157	119	3095	422	1003100	D2b
EN-5-c1-122	217558	121831	98	173	7319	391	982300	D2b
EN-5-c1-123	217380	128270	27	20	1695	329	991900	D2b
EN-5-c1-124	220173	131383	79	0	883	384	1008100	D2b
EN-5-c5-148	221022	128229	156	247	3198	467	1005000	D2b
EN-5-c5-149	217407	128477	207	799	7803	294	1007300	D2b
EN-5-c5-150	216844	132860	223	86	1305	555	1006600	D2b
EN-5-c5-151	218507	130452	85	147	2299	0	1003400	D2b
EN-5-c5-152	216494	129271	0	313	2677	347	995800	D2b
EN-5-c5-153	218734	131168	0	103	1162	336	1004300	D2b
G-11p-c1-21	217637	132163	23	0	1103	464	1005000	D3
G-11p-c1-22	221626	129416	79	60	1061	612	1005800	D3

## Appendix 1

Label	Ca ppm	Mg ppm	Na ppm	Mn ppm	Fe ppm	Sr ppm	Total	Description
G-11p-c1-23	218857	129096	187	53	1185	548	998200	D3
G-11p-25-31	215800	132600	0	100	1500	700	1003100	D3
G-11p-25-32	213200	130900	0	0	1000	700	989700	D3
G-11p-25-33	220800	130000	100	200	1500	800	1007400	D3
G-11p-26-40	215400	132200	0	200	1500	800	1001100	D3
G-11p-26-43	218100	130300	0	100	1000	800	1000000	D3
G-11p-26-49	219700	129600	0	100	700	500	1000500	D3
G-11p-26-51	218700	129100	100	100	1000	700	997400	D3
G-11p-26-52	223500	129900	0	0	1200	700	1012100	D3
G-16n-c1-71	224203	128771	129	74	501	578	1009000	D3
G-16n-c1-72	220431	127827	84	115	573	448	996200	D3
G-16n-c3-88	219223	127422	44	0	452	477	991200	D3
G-16n-c3-89	219963	127234	67	128	605	528	993100	D3
G-16n-c3-90	219169	128591	130	29	630	490	995800	D3
G-16n-c6-109	219895	129188	122	54	474	557	999500	D3
G-16n-c6-110	218953	127341	126	103	478	488	990700	D3
G-16n-c6-111	224411	126284	149	66	631	536	1001100	D3
G-12n-30-202	210900	129800	200	100	900	800	980900	D3
G-12n-30-203	212000	129000	100	100	700	800	980000	D3
G-12n-30-204	212200	129900	0	0	1100	900	984100	D3
G-12n-30-205	216300	127900	0	100	400	800	985900	D3
HOS-6n-37-404	391591	0	168	1681	89	1199	984000	C1a
HOS-6n-37-405	396633	0	155	2080	172	1290	997700	C1a
HOS-6n-37-406	393495	0	43	2202	48	1342	989700	C1a
HOS-6n-37-410	394817	0	101	2673	18	1212	993800	C1a
HOS-6n-38-416	393057	0	241	3778	0	1113	991900	C1a
HOS-6n-38-417	395141	0	0	3156	37	1301	995600	C1a
HOS-6n-38-418	393016	0	241	4425	16	1261	993400	C1a
HOS-6n-38-420	392676	0	140	2566	170	1339	988900	C1a
HOS-6n-41-435	393278	105	11	3998	326	1154	993500	C1a
HOS-6n-41-436	394347	0	90	2812	67	968	992600	C1a
HOS-6n-41-437	396148	0	5302	300	2983	1044	1010100	C1b
HOS-6n-37-411	393691	0	133	1630	0	1055	988600	C1c
HOS-9p-57-311	394585	0	140	848	234	1454	990400	C1c
HOS-9p-57-312	391695	0	138	865	211	1687	983600	C1c
HOS-9p-57-313	393077	0	241	736	44	1463	986200	C1c
HOS-9p-57-314	391155	0	135	817	0	1519	981400	C1c
HOS-9p-57-315	391968	0	73	1230	64	1546	984300	C1c
HOS-9p-58-321	394791	0	133	905	333	1436	991200	C1c
HOS-9p-58-325	394013	0	159	821	518	1481	989600	C1c
HOS-9p-59-333	396970	0	243	853	39	1462	996200	C1c
HOS-9p-59-334	395331	0	86	1622	131	1557	993700	C1c
HOS-9p-59-335	396251	0	146	1279	23	1296	994800	C1c
HOS-9p-59-337	397361	0	163	821	0	1306	996600	C1c
HOS-9p-59-338	399890	0	0	1063	69	1553	1003600	C1c
HOS-9p-60-342	399557	0	217	880	87	1266	1002400	C1c
HOS-9p-60-343	403308	0	245	592	0	1409	1011300	C1c
HOS-9p-60-346	400551	0	168	274	30	1252	1003400	C1c
HOS-9p-60-348	399682	0	80	430	0	1283	1001300	C1c
HOS-9p-60-351	396242	0	178	394	46	1419	993200	C1c
HOS-9p-60-352	401906	0	26	751	2	1195	1007300	C1c
HOS-9p-60-353	397057	0	105	458	9	1496	995300	C1c
HOS-9p-60-354	400267	0	84	376	0	1280	1002700	C1c

Label	Ca ppm	Mg ppm	Na ppm	Mn ppm	Fe ppm	Sr ppm	Total	Description
HOS-9p-60-355	397457	0	103	459	0	1369	996000	C1c
HOS-9p-60-356	400588	0	15	439	131	1370	1003900	C1c
HOS-9p-60-356	397829	0	194	1476	156	1273	999500	C1c
HOS-9p-60-358	399198	0	71	344	23	1327	1000000	C1c
HOS-9n-51-359	396296	0	0	295	2	1248	992400	C1c
HOS-9n-51-360	393593	0	15	472	5	1172	985900	C1c
HOS-9n-51-361	400026	0	125	352	179	1299	1002500	C1c
HOS-9n-54-377	397089	0	189	255	48	1297	994900	C1c
HOS-9n-54-383	399166	0	0	190	186	1136	999500	C1c
HOS-6n-36-393	397867	16	58	735	0	1240	997400	C1c
HOS-6n-36-394	398202	0	161	406	0	1578	998300	C1c
HOS-6n-36-395	396280	0	125	910	0	1265	993900	C1c
HOS-6n-36-396	397354	0	157	269	0	1422	995600	C1c
HOS-6n-36-397	396799	0	13	367	96	1271	994000	C1c
HOS-6n-37-407	396109	0	93	717	1078	1043	994900	C1c
HOS-6n-37-408	399948	0	228	837	138	1410	1003700	C1c
HOS-6n-37-409	397761	0	275	869	0	1423	998100	C1c
HOS-6n-42-439	394057	0	262	2330	0	1250	991600	C1c
HOS-6n-42-442	396543	0	88	364	0	1396	993600	C1c
HOS-6n-42-443	393120	0	88	2998	0	1423	990600	C1c
HOS-6n-42-444	387489	180	366	3784	351	1626	980500	C1c
HOS-6n-42-447	395239	0	86	1178	67	1015	991500	C1c
HOS-6n-42-448	396789	0	198	1307	117	1208	996300	C1c
HOS-9p-57-318	387038	1049	0	4442	745	1388	983300	C1c
HOS-9n-55-387	393156	83	189	411	62	1401	981900	C1c
HOS-9n-56-389	390302	666	172	2246	459	293	983500	C1c
HOS-9n-56-391	389954	244	229	5031	1015	1365	990100	C1c
HOS-6n-40-427	396208	0	110	728	46	1512	993800	C1c
HOS-6n-40-428	402335	0	155	1240	119	1488	1010400	C1c
HOS-6n-40-429	396975	0	178	1186	94	1432	996800	C1c
HOS-6n-40-430	397885	0	69	1842	234	1388	1000400	C1c
HOS-9p-57-316	390171	8	45	1887	94	1580	981300	C1d
HOS-9p-57-317	393578	0	114	908	83	1517	987700	C1d
HOS-9p-59-340	395492	155	112	2487	697	1539	997700	C1d
HOS-9n-53-370	391514	849	95	3269	1000	1437	992200	C1d
HOS-9n-53-372	390573	234	108	3537	819	1141	987400	C1d
HOS-9n-54-382	386130	1367	149	3504	1034	1296	981000	C1d
HOS-9n-55-384	390706	266	140	2481	316	1438	985200	C1d
HOS-9n-55-385	394167	0	56	366	9	1331	987500	C1d
HOS-9p-58-324	391551	285	90	1738	179	1282	985100	C1e
HOS-9p-58-326	394000	0	116	1013	624	1426	990000	C1e
HOS-9p-58-327	393584	0	185	1771	427	1272	990000	C1e
HOS-9p-58-328	398156	5	103	761	236	1458	999100	C1e
HOS-9p-58-332	402147	0	211	594	317	1545	1009200	C1e
HOS-9n-54-375	391093	0	116	1160	195	1212	981800	C1e
HOS-9n-54-376	391509	2260	236	2120	734	1867	995200	C1e
HOS-10-2-42	403700	0	49	351	96	480	1010000	C1f
HOS-10-2-43	400000	0	230	342	54	413	1000900	C1f
HOS-10-2-44	402300	0	168	557	82	476	1007300	C1f
HOS-10-2-45	405700	0	35	233	87	299	1014300	C1f
HOS-10-2-46	397900	0	100	367	544	372	996500	C1f
HOS-10-3-50	414500	0	71	348	85	384	1036800	C1f
HOS-10-3-51	409300	0	123	263	0	282	1023300	C1f

## Appendix 1

Label	Ca ppm	Mg ppm	Na ppm	Mn ppm	Fe ppm	Sr ppm	Total	Description
HOS-10-3-52	390100	206	1888	640	823	300	982900	C1f
HOS-10-3-54	395700	0	1906	381	917	351	995800	C1f
HOS-10-3-55	402100	0	0	466	0	158	1005400	C1f
HOS-10-3-56	412300	0	38	391	42	417	1031300	C1f
EN-2-2-105	397700	0	68	1109	498	385	997300	C1
EN-2-2-106	404100	0	95	472	108	433	1011200	C1
EN-2-2-107	402000	0	216	798	59	590	1007000	C1
EN-2-2-108	397900	0	90	1066	183	590	997400	C1
EN-2-2-109	406200	0	149	1095	64	512	1018100	C1
EN-2-2-110	402700	2550	106	991	168	552	1018100	C1
EN-2-2-111	411300	98	111	1085	221	455	1031300	C1
EN-2-2-112	404200	0	114	1005	228	415	1013000	C1
EN-2-2-113	385500	4980	0	83	610	251	981900	C1
EN-2-2-114	396800	317	29	236	326	433	994000	C1
EN-2-2-115	398600	976	195	1160	398	523	1003400	C1
HOS-9p-60-344	384720	1982	125	4174	2535	1138	999300	C2a
HOS-9p-60-349	394661	1305	99	4617	1433	1309	981000	C2a
HOS-9p-60-350	397393	148	110	3019	1493	1310	999100	C2a
HOS-9n-52-364	386974	0	80	674	5895	1236	991100	C2a
HOS-9n-52-366	396375	0	346	1031	826	1880	982200	C2a
HOS-9n-52-367	398602	0	284	1202	466	1450	984900	C2a
HOS-9n-52-368	395607	12	145	488	4523	1615	990900	C2a
HOS-6n-37-399	386257	924	127	5134	1095	1170	983100	C2a
HOS-8-44-273	391273	672	233	2329	576	1438	988400	C2a
HOS-8-44-274	390594	385	17	815	6250	1275	993600	C2a
HOS-8-44-275	395121	1584	52	1939	0	1395	998700	C2a
HOS-8-44-276	387570	1535	104	7168	266	1137	990900	C2a
HOS-8-44-278	387077	966	103	4752	264	1225	982800	C2a
HOS-8-44-279	389931	1618	147	4266	1101	1187	992900	C2a
HOS-8-44-280	386093	1787	0	3350	854	1193	981100	C2a
HOS-8-44-281	393234	602	0	2491	569	1207	992500	C2a
HOS-8-44-282	393258	645	168	444	448	1238	988600	C2a
HOS-8-45-283	400837	718	92	454	23	1329	1006900	C2a
HOS-8-45-284	387247	2249	0	4232	1170	1178	988100	C2a
HOS-8-45-285	397487	154	131	780	83	1662	998000	C2a
HOS-8-45-286	389386	151	75	2255	647	1439	981600	C2a
HOS-8-45-287	392710	357	0	6144	21	971	996500	C2a
HOS-8-45-288	385352	595	114	6974	231	1452	982200	C2a
HOS-8-45-289	387575	636	4	5574	73	1233	984000	C2a
HOS-8-45-290	391682	1501	114	970	0	1498	988100	C2a
HOS-8-46-293	385374	492	231	4735	4326	1593	986200	C2a
HOS-8-46-295	385299	572	166	6800	0	1194	980800	C2a
HOS-8-47-297	386234	1458	145	4800	1909	1381	986200	C2a
HOS-8-47-298	388443	1976	0	2651	973	995	986100	C2a
HOS-8-48-301	394523	1263	185	3137	1103	1849	1002000	C2a
HOS-8-48-302	385544	2990	202	4397	1623	1581	988800	C2a
HOS-8-48-303	400536	575	114	78	324	1396	1005700	C2a
HOS-8-48-304	394164	0	297	877	365	1758	990500	C2a
HOS-8-49-305	387743	2657	362	4810	1201	1739	993800	C2a
HOS-8-49-306	389755	325	0	1991	638	1325	982100	C2a
HOS-8-49-307	388942	2213	179	4321	1377	1692	994100	C2a
HOS-8-49-308	393118	261	286	2398	653	1794	992700	C2a
HOS-8-50-309	391617	223	60	1094	294	1346	984000	C2a



Label	Ca ppm	Mg ppm	Na ppm	Mn ppm	Fe ppm	Sr ppm	Total	Description
HOS-8-50-310	393016	264	82	2091	578	1347	990400	C2a
TS-2-c3-41	386100	1239	0	5168	991	346	982000	C2b
TS-2-c3-43	393000	694	0	3877	608	313	993600	C2b
TS-2-c3-44	389900	127	0	2736	831	431	982400	C2b
TS-2-c3-45	398800	82	0	1086	95	184	998800	C2b
TS-2-c3-46	389800	1430	0	5629	1064	464	993000	C2b
TS-2-c3-49	388200	1128	0	3856	699	338	983300	C2b
TS-2-c3-50	400200	0	0	1212	142	157	1002500	C2b
TS-2-c3-32	403200	111	0	235	0	445	1008600	C2c
TS-2-c3-33	401900	0	0	263	119	389	1005200	C2c
TS-2-c3-34	399800	141	0	665	136	300	1001100	C2c
TS-2-C3-35	405600	215	0	232	0	288	1014500	C2c
TS-2-C3-36	402400	0	0	663	131	305	1007100	C2c
TS-2-C3-38	397800	170	0	525	138	229	995700	C2c
TS-2-C3-39	401300	128	0	770	152	340	1005100	C2c
TS-2-c3-47	400800	0	0	300	16	198	1001900	C2c
TS-2-c3-48	401600	186	0	446	12	280	1005000	C2c
TS-2-c3-51	401700	0	0	487	233	315	1005100	C2c
EN-2-6-137	398900	122	78	938	17	513	999700	C3a
EN-2-6-138	403000	0	16	768	97	506	1009000	C3a
EN-2-6-139	401800	0	73	832	50	418	1006000	C3a
EN-2-6-140	404100	0	33	791	89	497	1011800	C3a
EN-2-6-141	401800	0	82	1013	0	497	1006500	C3a
EN-2-6-142	403500	0	89	733	3	474	1010200	C3a
EN-2-6-143	400800	0	87	996	182	405	1004200	C3a
EN-2-6-144	397500	0	87	700	87	466	995300	C3a
EN-2-5-130	396900	0	197	1004	0	546	994600	C3a
EN-2-5-131	402000	0	168	656	150	562	1007000	C3a
EN-2-5-132	404900	0	144	963	93	410	1014300	C3a
EN-2-5-134	409300	0	97	885	65	528	1025100	C3a
EN-2-5-135	404300	0	125	1084	177	450	1013200	C3a
EN-2-7-154	404700	0	104	1645	6	379	1014900	C3a
EN-2-7-155	396900	0	20	641	30	581	993600	C3a
EN-2-7-156	397000	0	80	1379	72	434	995400	C3a
EN-2-7-157	402900	0	0	1133	81	320	1009200	C3a
EN-2-7-158	408300	97	136	885	58	445	1023100	C3a
EN-2-8-159	400100	0	154	1344	223	505	1003500	C3a
EN-2-8-160	399000	0	73	1305	0	582	1000200	C3a
EN-2-8-161	404200	0	127	1684	146	610	1014500	C3a
EN-2-8-162	402100	0	96	1132	313	351	1008000	C3a
EN-2-8-163	401200	0	0	2299	227	453	1007800	C3a
EN-2-8-164	400000	0	0	1047	82	396	1001800	C3a
EN-2-8-165	400700	0	68	1220	145	399	1004400	C3a
EN-2-8-168	403100	0	88	994	183	597	1010300	C3a
EN-2-10-169	402200	0	0	965	0	309	1006900	C3a
EN-2-10-171	396200	0	88	1196	58	449	993100	C3a
EN-2-10-172	399200	0	7	749	53	506	999500	C3a
EN-2-10-173	400800	0	1	1521	118	500	1005100	C3a
EN-2-10-174	404700	0	121	1775	57	376	1015300	C3a
EN-2-3-122	404900	0	97	1304	65	400	1015000	C3a
EN-2-3-123	409200	0	143	779	89	428	1024600	C3a
EN-2-3-124	400100	0	47	1162	137	409	1002600	C3a
EN-2-3-125	405000	0	143	1200	273	503	1015600	C3a

## Appendix 1

Label	Ca ppm	Mg ppm	Na ppm	Mn ppm	Fe ppm	Sr ppm	Total	Description
EN-2-3-126	402900	0	64	693	73	507	1008800	C3a
EN-2-3-128	401400	0	34	1709	272	317	1007000	C3a
EN-2-3-129	399700	0	123	740	0	468	1000900	C3a
EN-2-3-116	403000	0	163	1285	34	635	1010600	C3b
EN-2-3-117	400800	0	59	1185	635	568	1005800	C3b
EN-2-3-118	392100	0	297	1102	6576	0	995900	C3b
EN-2-3-119	402500	0	48	1199	115	574	1009000	C3b
EN-2-6-145	403300	0	105	925	131	391	1010100	C3b
EN-2-7-146	403000	0	50	1089	108	377	1009500	C3b
EN-2-7-147	397500	0	330	6445	496	879	1009300	C3b
EN-2-7-148	397400	0	155	1269	40	418	996100	C3b
EN-2-7-149	410400	0	226	1299	246	562	1029600	C3b
EN-2-7-150	396300	0	8	4954	347	432	1001600	C3b
EN-2-7-151	405000	0	0	1578	317	417	1016100	C3b
EN-2-7-152	406700	0	216	1786	194	641	1021400	C3b
EN-2-7-153	404300	0	112	5312	252	521	1022400	C3b
EN-2-8-166	404900	0	73	1041	280	485	1015000	C3b
EN-2-8-167	403100	0	0	1943	523	392	1012400	C3b
MTB-1b-c2-105	393200	26	0	1872	154	318	986700	C4
MTB-1b-c2-106	397700	88	0	1967	219	330	998500	C4
MTB-1b-c2-107	396100	0	0	1475	87	202	992800	C4
MTB-1b-c2-108	396000	0	0	2091	182	416	994500	C4
MTB-1b-c2-109	398000	0	0	1975	115	470	999200	C4
MTB-1b-c2-110	400300	0	0	908	124	865	1003300	C4
MTB-1b-c2-111	401000	0	0	802	80	546	1004100	C4
MTB-1b-c2-112	398700	0	0	709	16	599	998100	C4
MTB-1b-c2-113	401000	0	0	887	124	884	1005100	C4
MTB-1b-c2-114	398600	0	0	860	65	455	998100	C4
MTB-1b-c2-115	396100	0	0	943	45	620	992300	C4
MTB-1b-c3-116	397500	13	0	1957	144	216	997400	C4
MTB-1b-c3-117	397700	0	0	2107	233	273	998600	C4
MTB-1b-c3-118	399100	0	0	1881	202	385	1001500	C4
MTB-1b-c3-119	392900	155	0	1558	118	299	985800	C4
MTB-1b-c3-120	400800	0	0	717	21	288	1003000	C4
MTB-1b-c3-121	397400	0	0	1946	279	560	998000	C4
MTB-1b-c3-122	397200	0	0	587	69	539	994200	C4
MTB-1b-c5-123	392500	227	0	1752	129	258	985300	C4
MTB-1b-c5-124	398500	0	0	994	54	658	998400	C4
MTB-1b-c5-125	395100	0	0	1815	28	489	991400	C4
MTB-1b-c5-126	401300	0	0	1075	28	530	1005400	C4
MTB-1b-c5-127	398200	109	0	1539	0	274	998400	C4
MTB-1b-c5-128	398900	0	0	1002	159	369	999200	C4
MTB-1b-c5-129	395200	0	0	1338	31	245	990100	C4
MTB-1b-c5-130	390100	45	0	1453	82	37	977700	C4
MTB-1b-c5-131	402100	0	0	782	122	314	1006600	C4
MTB-1b-c5-132	397300	0	0	1020	103	529	995400	C4
MTB-1b-c5-133	392800	0	0	652	10	653	983300	C4
MTB-1b-c5-134	400900	0	0	909	117	259	1003600	C4
MTB-1b-c5-135	391200	56	0	2305	139	373	982900	C4
EN-3-5-3	381300	5131	83	613	255	559	973000	C5
EN-3-5-7	382800	3317	97	319	339	533	969900	C5
EN-3-2-24	390800	588	90	820	1579	410	983900	C5
EN-3-2-25	389000	1779	192	187	2475	601	984500	C5

Label	Ca ppm	Mg ppm	Na ppm	Mn ppm	Fe ppm	Sr ppm	Total	Description
EN-3-2-26	403600	235	145	1484	454	443	1013800	C5
EN-3-4-11	380400	5026	0	3735	814	561	977900	C5
EN-3-4-12	382900	2422	31	4569	1884	239	978400	C5
EN-3-4-18	383600	7635	0	0	0	657	985500	C5
EN-3-4-19	380500	8292	0	1589	223	550	983500	C5
EN-3-4-20	378100	6062	48	5421	2228	377	982000	C5
EN-3-3-23	403500	1970	0	3474	1311	423	1025100	C5
EN-3-2-28	385300	9265	230	81	286	714	996900	C5
EN-3-2-30	394200	994	126	4528	1409	420	1001300	C5
EN-3-1-40	390500	3162	0	2085	1038	195	993000	C5
EN-3-1-32	387800	1069	70	786	431	492	975600	C5
EN-3-1-33	407200	0	119	961	189	411	1020300	C5
EN-3-1-34	395900	0	107	851	1393	365	994100	C5
EN-1-5-87	400600	0	112	874	104	411	1003400	C5
EN-1-5-88	402700	0	191	1328	76	633	1010100	C5
EN-1-5-91	389200	2679	0	1611	400	577	986300	C5
TS-2-c5-20	341800	40327	0	946	1646	936	1000400	C6
TS-2-c5-21	268600	57314	0	262	8698	787	889600	C6
TS-2-c5-22	209200	104973	0	0	1083	1429	891100	C6
TS-2-c5-23	270400	84993	0	160	576	1191	973600	C6
TS-2-c5-24	370300	9174	0	4401	919	325	968100	C6
TS-2-c5-25	323400	33072	0	2704	2482	622	934100	C6
TS-2-c5-26	388600	761	0	3606	694	278	982500	C6
TS-1-c5-85	320900	49777	0	0	1298	721	978000	C6
TS-1-c1-58	237400	112418	0	41	1075	1019	986600	PC1a
TS-1-c1-60	380500	12859	0	118	834	223	997200	PC1a
TS-1-c1-64	336200	43256	0	61	2285	552	995500	PC1a
TS-1-c1-66	362200	24015	0	0	836	278	990000	PC1a
TS-1-c5-99	384900	358	0	6477	2764	298	982300	PC1a
TS-1-c6-101	234300	113885	0	0	470	916	982600	PC1a
TS-1-c6-102	392800	2916	0	87	446	252	992500	PC1a
TS-1-c6-103	388000	0	0	6644	941	92	985000	PC1a
TS-1-c6-104	395300	2600	0	89	433	195	997600	PC1a
TS-1-c5-90	239800	114046	0	0	306	735	996200	PC1a
TS-1-c5-91	225900	121058	0	0	91	625	985300	PC1a
TS-1-c5-92	242300	111994	0	0	179	730	995200	PC1a
TS-1-c5-93	228400	117914	0	48	178	1013	981600	PC1a
TS-2-c4-3	386200	203	0	3713	4351	347	982600	PC1b
TS-2-c4-5	384600	455	0	7766	1348	205	981400	PC1b
TS-2-c4-6	388700	655	0	5155	898	385	986300	PC1b
TS-2-c4-7	387300	752	0	4366	771	336	981000	PC1b
TS-2-c4-10	391600	0	0	4757	986	187	990300	PC1b
TS-2-c4-11	387300	152	0	5097	987	95	980500	PC1b
TS-2-c4-13	388300	342	0	5489	846	163	984500	PC1b
TS-2-c4-14	392000	1123	0	5548	2750	383	1000800	PC1b
TS-1-c1-53	385100	918	0	7088	1331	238	982900	PC1b
TS-1-c1-55	383400	492	0	7357	1402	283	977800	PC1b
EN-1-4-79	366700	20224	212	114	593	1159	989700	C7
EN-1-4-80	349700	39585	336	266	211	1599	1015100	C7
EN-1-4-81	340200	35703	238	0	395	1541	977300	C7
EN-1-4-82	382000	12986	0	0	0	0	999000	C7
EN-1-4-83	373400	24000	14	0	491	1191	1018800	C7
EN-1-5-92	406800	0	73	1000	89	500	1019200	C7

## Appendix 1

Label	Ca ppm	Mg ppm	Na ppm	Mn ppm	Fe ppm	Sr ppm	Total	Description
EN-1-5-93	397600	0	97	2381	148	488	999300	C7
EN-1-1-57	382800	17810	46	0	342	779	1019900	C8
EN-1-1-58	380600	17068	82	0	1066	762	1013400	C8
EN-1-1-61	383500	15759	0	61	580	655	1014800	C8
EN-1-1-62	370800	19999	141	0	744	975	998800	C8
EN-1-1-63	383900	12510	113	108	840	1064	1006100	C8
EN-1-1-64	370700	23823	38	0	206	348	1009400	C8
EN-1-1-65	361700	29628	0	59	179	864	1007900	C8
EN-1-2-72	365800	24249	0	0	76	281	998100	C8
EN-1-2-73	379300	11338	60	162	480	901	989600	C8
EN-1-3-74	376000	18457	108	27	315	819	1005300	C8
EN-1-3-75	371800	20032	157	0	275	1017	1000500	C8
EN-1-3-76	373100	19952	355	301	404	1271	1005500	C8
EN-1-3-77	384800	14764	0	0	381	179	1013300	C8
EN-1-4-85	374700	24602	51	0	1025	560	1024300	C8
EN-1-4-86	382500	12637	5	0	81	504	1000000	C8
EN-3-5-9	378200	11294	0	1573	528	782	989200	C8
EN-3-4-13	366700	17220	119	95	277	297	977000	C8
EN-3-4-16	371800	15225	122	49	240	511	983100	C8
EN-3-2-29	377600	19556	258	310	284	1056	1014400	C8
EN-3-1-41	366700	17903	101	111	520	793	980700	C8
EN-1-5-89	360100	29213	0	0	0	1041	1002400	C8
EN-1-5-90	366800	27758	0	0	0	1034	1013900	C8
G-11p-22-1	371400	18200	100	0	100	6800	1002900	High-Mg calcite speleothem
G-11p-22-2	366800	24900	400	100	200	6200	1014200	High-Mg calcite speleothem
G-11p-22-3	372900	21800	600	200	100	5300	1017500	High-Mg calcite speleothem
G-11p-22-4	367200	20900	400	100	0	6300	1000900	High-Mg calcite speleothem
G-11p-22-5	372200	19800	500	100	100	6500	1010500	High-Mg calcite speleothem
G-11p-22-6	369900	20500	500	100	100	6200	1006800	High-Mg calcite speleothem
G-11p-22-7	375000	19700	400	0	0	5500	1015200	High-Mg calcite speleothem
G-11p-22-8	377700	18400	200	100	100	7800	1020800	High-Mg calcite speleothem
G-11p-22-9	366000	18400	500	0	100	5400	988400	High-Mg calcite speleothem
G-11p-22-10	384000	10900	200	100	0	7500	1010000	High-Mg calcite speleothem
G-11p-24-23	384400	8800	200	100	0	8100	1004500	High-Mg calcite speleothem
G-11p-24-24	385800	12100	0	0	0	5900	1015600	High-Mg calcite speleothem
G-11p-24-25	383600	13000	200	100	100	8600	1018300	High-Mg calcite speleothem
G-11p-24-26	378500	14000	200	200	100	9000	1010000	High-Mg calcite speleothem
G-11p-24-27	380500	12600	0	100	100	9000	1009700	High-Mg calcite speleothem
G-11p-24-28	381700	14300	100	100	0	9700	1019600	High-Mg calcite speleothem
G-11p-24-29	360400	20300	300	0	100	13800	994600	High-Mg calcite speleothem
G-11p-27-54	396300	3500	100	0	100	2200	1005900	Calcite speleothem
G-11p-27-55	392200	3600	200	100	100	2500	996700	Calcite speleothem
G-11p-27-57	398700	3800	300	100	100	2600	1014400	Calcite speleothem
G-12n-29-192	388000	6700	0	100	100	2400	996600	Calcite speleothem
G-12n-29-189	250300	102900	500	0	0	2300	987000	Dolomite speleothem
G-12n-29-196	236600	110600	400	0	0	3700	981800	Dolomite speleothem
G-12n-34-228	389300	0	400	0	0	8200	987100	Aragonite speleothem
G-12n-34-229	393200	0	200	0	0	4800	990700	Aragonite speleothem
G-12n-34-230	395800	0	100	0	100	5500	998300	Aragonite speleothem
G-12n-34-231	393500	0	100	0	0	7700	996100	Aragonite speleothem
G-12n-34-232	390700	0	400	0	100	6900	988400	Aragonite speleothem
G-12n-34-233	392600	0	500	100	0	7600	994800	Aragonite speleothem

Label	Ca ppm	Mg ppm	Na ppm	Mn ppm	Fe ppm	Sr ppm	Total	Description
G-5p-4-84	309900	64300	600	0	300	3300	1004400	High-Mg rafts
G-5p-4-85	354600	31700	1300	200	0	2200	1002800	High-Mg rafts
G-5p-4-86	350300	29400	1000	0	100	2200	983100	High-Mg rafts
G-5p-4-87	357200	25800	1400	100	0	2500	989100	High-Mg rafts
G-5p-4-88	357400	29300	1100	0	0	2400	1000700	High-Mg rafts
G-5p-4-89	310100	62900	900	0	0	2800	999500	High-Mg rafts
G-5p-4-93	308600	63600	700	200	200	3100	998700	High-Mg rafts
G-5p-4-94	336200	42500	600	0	0	2700	992800	High-Mg rafts
G-5p-4-90	328900	52900	1000	200	100	2600	1011900	Pearls
G-5p-4-91	326300	53000	1100	400	100	3100	1007300	Pearls
G-5p-4-92	311900	61800	800	200	200	3500	1001900	Pearls





Table 3. Elemental composition of diagenetic products within the faults rocks developed in the Miocene conglomerates

Label	Ca ppm	Mg ppm	Na ppm	Fe ppm	Mn ppm	Sr ppm	Total	Description
BAD-1n-10-1	380000	3220	90	5190	10	0	971200	Non-luminescent orange bladed calcite
BAD-1n-10-6	380400	4360	140	3030	80	0	971700	Non-luminescent orange bladed calcite
BAD-1p-2-61	381400	6070	210	2730	10	0	979800	Non-luminescent orange bladed calcite
BAD-1p-8-72	380500	8040	110	1760	0	0	982000	Non-luminescent orange bladed calcite
BAD-1p-1-77	384100	4330	170	2460	40	0	979900	Non-luminescent orange bladed calcite
BAD-1p-1-82	381300	4620	140	1940	0	0	972500	Non-luminescent orange bladed calcite
BAD-1p-1-84	377900	6450	360	2670	0	0	972500	Non-luminescent orange bladed calcite
BAD-1p-1-85	377700	5820	90	3110	0	0	970000	Non-luminescent orange bladed calcite
BAD-1p-1-86	381600	5010	40	2080	10	0	974800	Non-luminescent orange bladed calcite
BAD-7n-1-108	382900	6190	60	3610	100	0	985500	Non-luminescent orange bladed calcite
BAD-7n-1-109	397900	4380	20	340	0	0	1009500	Non-luminescent orange bladed calcite
BAD-7n-1-112	386700	2930	70	2350	60	0	980900	Non-luminescent orange bladed calcite
BAD-7n-10-101	400300	1310	30	100	0	0	1004500	Non-luminescent orange bladed calcite
BAD-7n-10-102	400400	2210	50	200	0	0	1008100	Non-luminescent orange bladed calcite
BAD-1p-9-28	383900	10370	210	120	0	0	995400	Non-luminescent orange bladed calcite
BAD-1p-2-58	378300	9290	200	860	70	0	979400	Non-luminescent orange bladed calcite
BAD-11p-6-7	374241	10104	316	4781	20	1528	982900	Non-luminescent orange bladed calcite
BAD-11p-4-18	390739	2845	209	1149	0	1372	990800	Non-luminescent orange bladed calcite
BAD-11p-3-23	381577	10660	385	370	0	1935	994800	Non-luminescent orange bladed calcite
BAD-11p-3-26	389411	3017	207	4023	0	1262	993900	Non-luminescent orange bladed calcite
BAD-11p-3-27	389856	5974	229	5191	78	1497	1008300	Non-luminescent orange bladed calcite
BAD-11p-3-29	390323	6350	758	7619	79	1415	1016800	Non-luminescent orange bladed calcite
BAD-11p-2-35	391709	2466	168	3895	88	1421	997800	Non-luminescent orange bladed calcite
BAD-11p-2-39	377516	9969	261	2173	25	1617	985200	Non-luminescent orange bladed calcite
BAD-1p-17-82	399727	1844	85	0	0	1362	1007100	Non-luminescent orange bladed calcite
BAD-1p-17-83	396414	2339	134	1311	0	1170	1003000	Non-luminescent orange bladed calcite
BAD-11n-7-111	361634	18766	392	5127	20	1868	982900	Non-luminescent orange bladed calcite
BAD-11n-8-116	361267	14795	590	6272	0	1407	970200	Non-luminescent orange bladed calcite
BAD-11n-10-124	373820	8062	554	3245	0	1446	971900	Non-luminescent orange bladed calcite
BAD-11n-10-126	392200	1430	168	3620	6	1157	994200	Non-luminescent orange bladed calcite
BAD-11n-11-133	380436	7236	161	180	0	1358	978200	Non-luminescent orange bladed calcite
BAD-11n-11-139	396142	5013	145	1281	0	1542	1012200	Non-luminescent orange bladed calcite
BAD-11n-11-140	391110	4226	0	215	30	1450	994300	Non-luminescent orange bladed calcite
BAD-11n-12-150	389348	8207	480	444	58	2015	1006300	Non-luminescent orange bladed calcite
BAD-11p-5-9	376264	4371	199	6345	34	1477	971000	Non-luminescent orange bladed calcite
BAD-1n-10-2	380300	5940	90	300	1590	0	974300	Luminescent orange bladed calcite
BAD-11p-5-10	380452	5176	166	374	8691	1564	990000	Luminescent orange bladed calcite
BAD-11p-2-32	373704	2435	101	410	12431	1513	971300	Luminescent orange bladed calcite
BAD-11p-2-34	377240	1810	0	453	24912	1342	1003600	Luminescent orange bladed calcite
BAD-11p-1-41	392156	997	50	175	13972	1220	1014500	Luminescent orange bladed calcite
BAD-11p-1-42	373554	3514	10	278	25503	1270	1001100	Luminescent orange bladed calcite
BAD-11p-1-44	390366	3408	154	892	3860	1567	999600	Luminescent orange bladed calcite
BAD-11p-1-45	368791	4529	72	0	26870	1406	995400	Luminescent orange bladed calcite
BAD-1p-17-86	380257	3165	91	1307	5620	1191	977200	Luminescent orange bladed calcite
BAD-1p-17-88	379752	3246	0	684	5877	1099	975100	Luminescent orange bladed calcite
BAD-5n-15-102	375974	4077	192	1367	13036	1296	985800	Luminescent orange bladed calcite
BAD-11n-7-107	374824	2018	0	306	22622	1188	993000	Luminescent orange bladed calcite
BAD-11n-9-119	364479	3540	80	1338	26400	1193	982700	Luminescent orange bladed calcite
BAD-11n-9-120	391825	3365	4	825	16334	1377	1028400	Luminescent orange bladed calcite
BAD-1p-21-49	372761	3366	149	1418	12444	1327	974100	White bladed calcite
BAD-1p-21-50	393369	743	0	0	4702	1415	997100	White bladed calcite
BAD-1p-21-52	388346	6897	386	0	28	1336	996900	White bladed calcite
BAD-1p-18-76	378055	3319	183	0	16055	1822	992700	White bladed calcite

## Appendix 1

Label	Ca ppm	Mg ppm	Na ppm	Fe ppm	Mn ppm	Sr ppm	Total	Description
BAD-1p-18-78	374328	2366	155	586	13738	1305	975500	White bladed calcite
BAD-1p-18-79	392558	5716	95	115	9927	1330	1023600	White bladed calcite
BAD-1p-18-80	386246	3178	50	0	15921	1723	1011900	White bladed calcite
BAD-1p-18-81	390298	6285	314	227	260	1604	1000900	White bladed calcite
BAD-1p-7-54	378300	1680	30	0	12620	0	976900	White bladed calcite
BAD-1p-7-55	368500	5560	40	50	15060	0	971200	White bladed calcite
BAD-1p-7-56	373100	4250	0	70	12560	0	972900	White bladed calcite
BAD-5n-14-89	379608	9924	469	821	121	2333	989300	Micrite strips
BAD-5n-14-91	369380	18331	474	275	46	2652	992200	Micrite strips
BAD-5n-14-95	372578	12026	480	1223	0	2285	979600	Micrite strips
BAD-5n-14-98	389653	3846	230	277	0	1631	990200	Micrite strips
BAD-5n-14-100	376982	7954	508	2263	19	1955	978200	Micrite strips
BAD-5n-14-92	364326	16328	1396	122	89	4056	976900	Blocky calcite in micrite strips porosity
BAD-5n-14-93	369837	15974	924	252	0	2494	985800	Blocky calcite in micrite strips porosity
BAD-5n-14-96	376245	11493	1007	49	72	4311	989300	Blocky calcite in micrite strips porosity
BAD-5n-14-97	395756	2556	409	171	220	1641	1001700	Blocky calcite in micrite strips porosity
BAD-1p-20-54	395877	6573	245	160	0	1388	1014600	Sparry calcite in porosity
BAD-1p-20-55	387034	8014	368	69	0	1681	998100	Sparry calcite in porosity
BAD-1p-20-56	388786	6335	202	0	25	1532	996000	Sparry calcite in porosity
BAD-1n-10-7	379300	10350	170	110	0	0	983700	Sparry calcite in porosity
BAD-1p-9-34	379900	7540	220	210	70	0	975800	Sparry calcite in porosity
BAD-1p-5-41	377800	7370	340	240	190	0	970600	Sparry calcite in porosity
BAD-1p-5-42	377400	8770	210	180	0	0	973600	Sparry calcite in porosity
BAD-1p-8-65	389400	3340	60	100	0	0	984300	Sparry calcite in porosity
BAD-1p-8-67	392000	4060	70	90	50	0	993500	Sparry calcite in porosity
BAD-1p-8-68	389100	4310	100	0	0	0	986900	Sparry calcite in porosity
BAD-1p-8-69	394900	3940	140	0	0	0	1000100	Sparry calcite in porosity
BAD-1p-8-70	390400	3690	110	40	0	0	987900	Sparry calcite in porosity
BAD-7n-3-113	391500	4010	10	120	0	0	991700	Sparry calcite in porosity
BAD-7n-3-114	390300	7380	70	0	0	0	1000500	Sparry calcite in porosity
BAD-7n-3-115	394500	3790	30	100	60	0	998700	Sparry calcite in porosity
BAD-7n-3-116	394300	4640	60	0	20	0	1001000	Sparry calcite in porosity
BAD-5n-11-11	391400	4100	40	30	0	0	991800	Sparry calcite in porosity
BAD-5n-11-12	397900	4040	20	100	0	0	1007800	Sparry calcite in porosity
BAD-5n-11-13	393900	5460	120	140	0	0	1003200	Sparry calcite in porosity
BAD-1p-1-87	386900	6040	290	230	20	0	988400	Sparry calcite in porosity
BAD-1p-1-88	380800	6160	280	350	60	0	973700	Sparry calcite in porosity
BAD-1p-1-89	380700	9000	40	220	0	0	982400	Sparry calcite in porosity
BAD-7n-4-123	397700	5560	20	40	0	0	1012600	Sparry calcite in porosity
BAD-7n-4-124	390500	7090	140	0	0	0	1000000	Sparry calcite in porosity
BAD-7n-4-126	394600	4780	0	40	0	0	1002100	Sparry calcite in porosity
BAD-7n-4-127	393500	5300	0	0	0	0	1001100	Sparry calcite in porosity
BAD-7p-8-14	385800	7550	200	60	100	0	990300	Bladed calcite with clays in porosity
BAD-7p-8-15	386400	5310	60	2250	10	0	988200	Bladed calcite with clays in porosity
BAD-7p-8-16	395700	4500	110	270	0	0	1004500	Bladed calcite with clays in porosity
BAD-7p-9-22	370700	8070	550	8190	10	0	972000	Bladed calcite with clays in porosity
BAD-7p-9-25	380400	12040	80	100	0	0	992200	Bladed calcite with clays in porosity
BAD-7p-9-27	379300	6500	60	5630	0	0	981500	Bladed calcite with clays in porosity
BAD-11p-6-1	389345	7442	382	139	41	1837	1002400	Non-luminescent microfractures
BAD-11p-6-2	386786	9349	539	270	0	1904	1003300	Non-luminescent microfractures
BAD-11p-6-3	385463	11474	536	284	39	2159	1007900	Non-luminescent microfractures
BAD-11p-4-14	389555	4344	79	0	0	1292	990200	Non-luminescent microfractures
BAD-11p-4-15	381283	11409	467	257	46	2115	997000	Non-luminescent microfractures
BAD-11p-4-16	394722	3539	434	349	257	2559	1004500	Non-luminescent microfractures
BAD-11p-4-17	386154	11522	379	166	207	2286	1009800	Non-luminescent microfractures
BAD-11p-4-19	391652	7067	1819	217	0	1472	1009700	Non-luminescent microfractures

Label	Ca ppm	Mg ppm	Na ppm	Fe ppm	Mn ppm	Sr ppm	Total	Description
BAD-11p-4-20	384398	8906	333	298	60	2057	995800	Non-luminescent microfractures
BAD-11p-4-21	386432	9781	61	217	19	1582	1002200	Non-luminescent microfractures
BAD-11p-4-22	399520	350	146	721	16	1430	1003200	Non-luminescent microfractures
BAD-11p-3-25	373809	10801	652	185	108	2123	976600	Non-luminescent microfractures
BAD-11p-3-28	397855	973	0	55	0	1306	999200	Non-luminescent microfractures
BAD-11p-2-37	390110	8306	170	185	122	1811	1007100	Non-luminescent microfractures
BAD-11p-2-38	400523	5712	173	37	102	1591	1023400	Non-luminescent microfractures
BAD-11n-8-112	389784	9908	299	97	187	1698	1011900	Non-luminescent microfractures
BAD-11n-8-113	399108	3627	75	0	0	1215	1011500	Non-luminescent microfractures
BAD-11n-8-114	388555	12379	230	314	108	1877	1017800	Non-luminescent microfractures
BAD-11n-11-127	381462	10361	250	106	7	1588	992000	Non-luminescent microfractures
BAD-11n-11-129	396150	5173	253	74	52	1560	1010700	Non-luminescent microfractures
BAD-11n-11-130	387536	10112	421	155	215	2378	1008600	Non-luminescent microfractures
BAD-11n-11-131	395876	8394	355	49	180	1828	1022100	Non-luminescent microfractures
BAD-11n-11-132	380538	10698	358	324	0	1953	992200	Non-luminescent microfractures
BAD-11n-11-135	392465	6229	151	42	0	1410	1004500	Non-luminescent microfractures
BAD-11n-11-136	393550	4218	79	0	0	1368	999900	Non-luminescent microfractures
BAD-11n-11-137	397728	1707	0	157	0	1229	1001500	Non-luminescent microfractures
BAD-11n-11-138	392748	3053	212	37	10	1832	995000	Non-luminescent microfractures
BAD-11n-13-152	386120	8548	286	275	10	2092	998600	Non-luminescent microfractures
BAD-11n-13-153	377718	9899	248	312	24	1998	982200	Non-luminescent microfractures
BAD-11n-13-154	390146	9687	248	88	0	1658	1011400	Non-luminescent microfractures
BAD-11n-13-155	384691	12650	123	183	68	1781	1008300	Non-luminescent microfractures
BAD-11n-13-156	384617	12197	287	321	74	2210	1008000	Non-luminescent microfractures
BAD-11n-13-157	382948	10847	188	238	22	2089	998400	Non-luminescent microfractures
BAD-11n-13-159	390001	11728	484	229	200	1969	967700	Non-luminescent microfractures
BAD-11n-13-160	380212	9682	500	280	0	2006	1019900	Non-luminescent microfractures
BAD-11n-13-161	385368	6104	421	187	110	2057	988200	Non-luminescent microfractures
BAD-1p-20-59	390838	8669	55	28	896	1313	988600	Non-luminescent microfractures
BAD-1p-20-60	392958	9039	41	60	0	1229	1014900	Non-luminescent microfractures
BAD-1p-19-64	399809	1955	130	62	83	1669	1008600	Non-luminescent microfractures
BAD-1p-19-65	390560	7327	65	19	0	1289	1003100	Non-luminescent microfractures
BAD-1p-19-66	396899	3270	79	23	0	1319	1004900	Non-luminescent microfractures
BAD-1p-19-68	401213	3270	191	116	36	1435	1016400	Non-luminescent microfractures
BAD-1p-19-69	391858	7152	114	201	26	1457	1006500	Non-luminescent microfractures
BAD-1p-21-46	396088	6844	194	62	138	1630	1016500	Non-luminescent microfractures
BAD-1p-21-48	396157	4262	423	250	114	1306	1008000	Non-luminescent microfractures
BAD-1p-21-51	390007	7861	251	155	0	1415	1004500	Non-luminescent microfractures
BAD-1p-20-53	389103	8698	278	88	0	1686	1005500	Non-luminescent microfractures
BAD-1p-18-72	384764	9272	348	224	0	1474	996700	Non-luminescent microfractures
BAD-1p-18-73	387640	8039	125	18	0	1419	998600	Non-luminescent microfractures
BAD-1p-18-74	388751	10781	241	462	16	1515	1012300	Non-luminescent microfractures
BAD-1p-18-75	393055	6646	271	331	82	1608	1008800	Non-luminescent microfractures
BAD-11p-6-4	393552	2550	86	164	0	1502	994700	Non-luminescent microfractures
BAD-11p-6-5	397896	1984	238	171	53	1556	1004100	Non-luminescent microfractures
BAD-11p-2-30	394754	3270	134	331	92	1642	1001100	Non-luminescent microfractures
BAD-11p-2-31	398952	1841	118	125	0	1403	1005500	Non-luminescent microfractures
BAD-11n-12-147	380004	15631	339	125	66	1974	1007700	Non-luminescent microfractures
BAD-1p-20-57	384077	3357	169	0	14832	1144	1004100	Luminescent microfractures
BAD-1p-20-58	382366	3778	89	0	17146	1270	1006200	Luminescent microfractures
BAD-1p-20-61	389657	2407	56	0	12683	1179	1010100	Luminescent microfractures
BAD-1p-20-62	380025	3969	135	0	13636	1556	994200	Luminescent microfractures
BAD-1p-20-63	389736	4095	73	0	9903	1478	1010800	Luminescent microfractures
BAD-1p-19-67	374135	3336	0	0	18488	1298	986700	Luminescent microfractures
BAD-1p-19-70	389588	2957	107	46	18368	1240	1024000	Luminescent microfractures
BAD-1p-19-71	387097	0	0	0	15064	2066	1001700	Luminescent microfractures
BAD-7p-8-18	397600	2890	10	0	840	0	1004700	Luminescent microfractures

## Appendix 1

---

Label	Ca ppm	Mg ppm	Na ppm	Fe ppm	Mn ppm	Sr ppm	Total	Description
BAD-7p-8-20	389000	2270	60	0	870	0	981300	Luminescent microfractures
BAD-1p-5-44	370100	5190	50	0	15530	0	974700	Luminescent microfractures
BAD-1p-4-45-	386400	3960	30	0	6170	0	991600	Luminescent microfractures
BAD-1p-4-46	394300	3730	50	120	2610	0	1003400	Luminescent microfractures
BAD-1p-4-47	382300	1550	50	0	7180	0	975100	Luminescent microfractures

Table 4. Composition and atom site distribution of the four mica groups of the Vallès fault

	M1				M2				M3		M4			
SiO <sub>2</sub> (%wt)	46.72	46.32	46.85	45.11	44.34	48.21	49.05	42.2	43.58	44.23	48.34	49.39	50.69	50.07
Al <sub>2</sub> O <sub>3</sub> (%wt)	34.58	35.27	35.01	33.97	33.22	33.86	34.99	28.97	29.98	28.35	31.45	29.04	29.99	31.29
FeO (%wt)	2.2	2.2	2.18	2.05	1.99	2.74	1.99	1.79	2.7	3.95	2.76	3.61	2.2	2.23
MnO (%wt)	0.04	0.02	0.03	0.03	0.04	0.07	0.01	0.06	0.06	0.05	0.06	0.06	0.01	0.07
MgO (%wt)	0.79	0.5	0.52	0.48	0.44	0.88	0.67	1.09	1.21	2.17	1.72	2.56	2.12	1.9
CaO (%wt)	0	0.01	0.04	0	0.02	0	0.01	0	0.08	0.14	0.07	0.08	0.12	0.07
Na <sub>2</sub> O (%wt)	0.87	0.76	0.86	0.65	0.95	0.73	0.53	0.28	0.39	0.3	0.47	0.14	0.2	0.2
K <sub>2</sub> O (%wt)	9.8	9.61	9.87	9.86	8.84	9.88	10.23	9.46	9.14	8.38	9.39	9.76	9.67	9.92
Atom site distribution (11 anhydrous-oxygen basis including Fe <sup>3+</sup> )														
Si(T1+T2)	3.11	3.09	3.10	3.10	3.11	3.16	3.17	3.19	3.15	3.19	3.22	3.30	3.34	3.29
Al(T2)	0.89	0.91	0.90	0.90	0.89	0.84	0.83	0.81	0.85	0.81	0.78	0.70	0.66	0.71
V(M1)	0.98	0.97	0.99	0.99	0.99	0.99	1.00	1.00	1.00	0.93	1.00	0.96	1.00	0.99
Mg(M1)	0.01	0.01	0.00	0.00	0.01	0.01	0.00	0.00	0.00	0.05	0.00	0.03	0.00	0.01
Fe <sup>2+</sup> (M1)	0.01	0.01	0.01	0.01	0.01	0.01	0.00	0.00	0.00	0.02	0.00	0.01	0.00	0.00
Al(M2+M3)	1.82	1.85	1.84	1.84	1.85	1.78	1.83	1.77	1.71	1.60	1.68	1.59	1.67	1.71
Mg(M2+M3)	0.07	0.04	0.05	0.04	0.04	0.08	0.06	0.12	0.13	0.18	0.17	0.22	0.21	0.17
Fe(M2+M3)	0.05	0.05	0.06	0.05	0.05	0.07	0.05	0.06	0.08	0.09	0.07	0.09	0.06	0.06
K(A)	0.83	0.82	0.83	0.86	0.79	0.83	0.84	0.91	0.84	0.77	0.80	0.83	0.81	0.83
Na(A)	0.11	0.10	0.11	0.09	0.13	0.09	0.07	0.04	0.05	0.04	0.06	0.02	0.03	0.03
V(A)	0.06	0.08	0.05	0.05	0.08	0.08	0.09	0.05	0.10	0.18	0.14	0.14	0.15	0.14



Table 5. Composition (%wt), atom site distribution and estimated temperature of chlorites from the Hospital fault

	Atom site distribution (14 anhydrous-oxygen basis including Fe <sup>3+</sup> )																			CHL	
	SiO <sub>2</sub>	Al <sub>2</sub> O <sub>3</sub>	FeO	MnO	MgO	CaO	Na <sub>2</sub> O	K <sub>2</sub> O	Si(T1+T2)	Al(T2)	Al(M1)	Mg(M1)	Fe2+(M1)	V(M1)	Mg(M2+M3)	Fe(M2+M3)	Al(M2+M3)	Al(M4)	Fe <sup>3+</sup> (M4)		XFe <sup>2+</sup>
25.54	18.17	27.99	0.69	13.92	0.02	0.04	0.03		2.71	1.28	0.28	0.27	0.21	0.24	1.93	1.51	0.48	0.23	0.77	0.44	296
27.35	18.15	26.98	0.62	14.05	0.08	0.02	0.02		2.82	1.18	0.18	0.25	0.15	0.42	1.91	1.17	0.85	0.00	1.00	0.38	289
26.39	17.6	27.53	0.78	13.44	0.06	0.03	0.12		2.79	1.21	0.21	0.25	0.17	0.37	1.87	1.27	0.77	0.00	1.00	0.40	286
26.81	17.73	24.83	0.73	15.41	0.04	0	0		2.80	1.20	0.20	0.28	0.14	0.39	2.12	1.03	0.78	0.00	1.00	0.33	285
24.58	18.53	33.03	0.65	9.43	0.05	0	0.04		2.71	1.29	0.29	0.19	0.29	0.23	1.36	2.11	0.46	0.36	0.64	0.61	285
27.31	18.33	27.81	0.7	14.15	0.07	0.02	0.04		2.79	1.21	0.21	0.25	0.16	0.39	1.91	1.22	0.79	0.00	1.00	0.39	281
27.26	18.14	24.66	0.7	16.25	0.01	0.02	0.02		2.79	1.21	0.21	0.29	0.13	0.37	2.19	0.99	0.75	0.01	0.99	0.31	280
25.04	19.23	30.65	0.55	10.85	0.03	0.02	0.09		2.71	1.29	0.29	0.21	0.26	0.25	1.54	1.88	0.51	0.36	0.64	0.55	276
26.66	18.02	27.18	0.66	13.96	0.06	0.04	0.07		2.78	1.22	0.22	0.25	0.16	0.38	1.92	1.22	0.78	0.00	1.00	0.39	276
26.06	18.78	28.25	0.75	13.62	0.03	0	0.03		2.73	1.27	0.27	0.25	0.20	0.28	1.87	1.48	0.57	0.21	0.79	0.44	275
25.55	18.24	27.15	0.65	13.68	0.07	0.03	0.07		2.73	1.27	0.27	0.26	0.19	0.29	1.92	1.41	0.59	0.18	0.82	0.42	275
26.32	18.27	27.02	0.58	14.41	0.05	0.11	0.09		2.75	1.25	0.25	0.26	0.17	0.31	1.98	1.27	0.66	0.08	0.92	0.39	271
26.39	18.19	28.26	0.72	14.05	0.05	0	0.03		2.74	1.25	0.25	0.25	0.18	0.32	1.92	1.37	0.63	0.09	0.91	0.42	271
26.08	17.83	27.49	0.61	14.14	0.04	0	0.04		2.75	1.25	0.25	0.26	0.18	0.32	1.96	1.33	0.64	0.08	0.92	0.40	271
26.72	18.1	22.58	0.36	16.92	0.03	0.11	0.02		2.78	1.22	0.22	0.31	0.12	0.36	2.32	0.88	0.74	0.04	0.96	0.28	271
25.9	18.28	27.75	0.62	13.72	0.03	0.03	0.06		2.74	1.26	0.26	0.25	0.19	0.30	1.91	1.41	0.61	0.14	0.86	0.42	270
27.73	18.74	22.08	0.38	17.86	0.03	0.06	0.01		2.79	1.21	0.21	0.30	0.10	0.39	2.38	0.78	0.80	0.01	0.99	0.25	268
27.35	18.39	21.64	0.43	17.83	0.04	0.03	0.01		2.79	1.21	0.21	0.31	0.10	0.39	2.40	0.77	0.78	0.02	0.98	0.24	268
27	18.37	21.87	0.46	17.66	0.05	0.06	0		2.77	1.22	0.22	0.31	0.11	0.36	2.39	0.82	0.73	0.04	0.96	0.25	268
28	18.86	23.69	0.37	17.31	0	0.03	0		2.79	1.20	0.20	0.29	0.11	0.40	2.29	0.88	0.80	0.01	0.99	0.28	267
26.02	18.36	27.19	0.63	13.8	0.03	0.04	0.07		2.75	1.25	0.25	0.25	0.18	0.32	1.92	1.36	0.65	0.14	0.86	0.41	266
26.81	18.02	24.44	0.72	15.58	0.03	0	0.04		2.79	1.21	0.21	0.28	0.13	0.38	2.14	1.02	0.77	0.02	0.98	0.32	266
26.82	18.3	26.65	0.75	14.91	0.03	0.01	0.02		2.76	1.23	0.23	0.26	0.16	0.35	2.03	1.20	0.70	0.06	0.94	0.37	265
25.1	18.25	28.09	0.56	12.23	0.04	0.08	0.02		2.73	1.26	0.26	0.23	0.21	0.30	1.75	1.56	0.61	0.21	0.79	0.47	265
27.04	18.77	22.68	0.43	17.28	0.04	0.06	0		2.76	1.23	0.23	0.30	0.12	0.35	2.33	0.91	0.71	0.09	0.91	0.28	265
27.08	18.23	26.61	0.72	14.25	0.02	0.02	0.09		2.80	1.20	0.20	0.25	0.15	0.40	1.94	1.16	0.81	0.01	0.99	0.37	263
24.94	19.61	33.27	0.6	8.75	0.03	0.01	0.1		2.71	1.29	0.29	0.17	0.28	0.26	1.25	2.13	0.54	0.40	0.60	0.63	263
26.19	18.41	27.7	0.55	13.86	0.04	0	0.03		2.75	1.25	0.25	0.25	0.18	0.32	1.92	1.38	0.65	0.13	0.87	0.42	263
26.62	18.14	27.3	0.69	14.11	0.05	0.03	0.03		2.77	1.23	0.23	0.25	0.16	0.37	1.94	1.24	0.74	0.03	0.97	0.39	262
26.17	18.71	27.35	0.75	13.71	0.03	0.02	0.2		2.74	1.26	0.26	0.25	0.18	0.31	1.89	1.35	0.66	0.14	0.86	0.42	262



Atom site distribution (14 anhydrous-oxygen basis including Fe <sup>3+</sup> )																				
SiO <sub>2</sub>	Al <sub>2</sub> O <sub>3</sub>	FeO	MnO	MgO	CaO	Na <sub>2</sub> O	K <sub>2</sub> O	Si(T1+T2)	Al(T2)	Al(M1)	Mg(M1)	Fe2+(M1)	V(M1)	Mg(M2+M3)	Fe(M2+M3)	Al(M2+M3)	Al(M4)	Fe <sup>3+</sup> (M4)	XFe <sup>2+</sup>	T(°C)
26.35	18.25	27.85	0.58	13.77	0.05	0.05	0.06	2.76	1.24	0.24	0.25	0.17	0.34	1.90	1.34	0.69	0.07	0.93	0.41	262
26.74	18.13	28.2	0.48	13.48	0.07	0.07	0.07	2.78	1.22	0.22	0.24	0.17	0.38	1.85	1.30	0.77	0.02	0.98	0.41	262
27.34	18.52	22.55	0.5	17.18	0	0.03	0	2.79	1.21	0.21	0.30	0.11	0.39	2.32	0.85	0.78	0.04	0.96	0.27	261
CHL1																				
26.64	18.3	27.54	0.67	13.99	0.01	0.03	0.05	2.77	1.23	0.23	0.25	0.17	0.35	1.92	1.29	0.72	0.07	0.93	0.40	259
26.61	18.23	27.75	0.53	13.99	0.02	0	0.04	2.77	1.23	0.23	0.25	0.17	0.36	1.92	1.30	0.72	0.06	0.94	0.40	259
26.35	18.75	26.72	0.62	14.1	0.03	0.07	0.04	2.75	1.24	0.24	0.25	0.17	0.33	1.94	1.30	0.68	0.14	0.86	0.40	259
26.11	18.04	27.65	0.5	13.47	0.03	0.06	0.03	2.76	1.23	0.23	0.24	0.17	0.35	1.88	1.34	0.71	0.07	0.93	0.42	259
25.85	19.74	31.22	0.56	10.78	0.03	0.07	0.07	2.73	1.27	0.27	0.20	0.24	0.29	1.50	1.82	0.60	0.31	0.69	0.55	258
27.65	18.89	21.95	0.42	17.78	0.03	0.04	0.01	2.79	1.21	0.21	0.30	0.10	0.39	2.37	0.79	0.79	0.04	0.96	0.25	258
26.69	18.03	26.77	0.64	13.51	0.04	0.03	0.05	2.81	1.19	0.19	0.24	0.15	0.41	1.88	1.21	0.84	0.01	0.99	0.39	257
27.26	18.44	27.41	0.64	13.56	0.06	0	0.05	2.81	1.19	0.19	0.23	0.15	0.43	1.85	1.22	0.86	0.01	0.99	0.40	256
26.16	18.11	27.07	0.71	13.47	0.01	0.05	0.09	2.77	1.23	0.23	0.24	0.16	0.37	1.88	1.27	0.76	0.04	0.96	0.40	254
26.43	18.44	27.66	0.66	13.57	0.07	0.05	0.05	2.76	1.23	0.23	0.24	0.17	0.35	1.87	1.33	0.72	0.08	0.92	0.41	254
27.99	19.09	24.26	0.42	16.76	0	0.05	0	2.79	1.21	0.21	0.28	0.12	0.40	2.22	0.94	0.80	0.03	0.97	0.30	254
26.32	18.5	27.19	0.67	13.58	0.05	0	0.08	2.76	1.23	0.23	0.24	0.17	0.36	1.88	1.31	0.73	0.09	0.91	0.41	252
24.42	16.68	24.45	0.41	12.39	0.11	0.05	0.07	2.80	1.20	0.20	0.24	0.15	0.41	1.88	1.21	0.84	0.02	0.98	0.39	251
26.47	18.36	28.28	0.63	13.16	0.04	0.05	0.02	2.77	1.23	0.23	0.23	0.17	0.37	1.82	1.36	0.75	0.06	0.94	0.43	251
26.93	18.73	26.75	0.68	14.2	0.04	0.06	0.04	2.78	1.22	0.22	0.25	0.15	0.38	1.94	1.21	0.78	0.05	0.95	0.38	249
26.26	18.34	26.92	0.76	13.59	0.07	0	0.05	2.77	1.23	0.23	0.24	0.16	0.37	1.89	1.28	0.74	0.08	0.92	0.40	249
26.68	18.57	27.66	0.72	13.34	0.06	0.05	0.08	2.78	1.22	0.22	0.24	0.17	0.38	1.83	1.30	0.77	0.06	0.94	0.42	248
26.64	18.33	27.25	0.6	13.17	0.04	0.04	0.09	2.79	1.20	0.20	0.23	0.16	0.41	1.83	1.25	0.84	0.02	0.98	0.41	247
26.88	18.46	26.97	0.62	13.45	0.07	0	0.03	2.80	1.19	0.19	0.23	0.15	0.43	1.86	1.21	0.86	0.01	0.99	0.39	244
27.16	18.84	26.84	0.56	13.68	0.06	0	0.03	2.80	1.20	0.20	0.23	0.14	0.43	1.88	1.20	0.87	0.03	0.97	0.39	234

Table 6. Composition (%wt), atom site distribution and estimated temperature of chlorites from the Vallès fault

Atom site distribution (14 anhydrous-oxygen basis including Fe <sup>3+</sup> )																					CHI <sub>4</sub>
SiO <sub>2</sub>	Al <sub>2</sub> O <sub>3</sub>	FeO	MnO	MgO	CaO	Na <sub>2</sub> O	K <sub>2</sub> O	Si(T1+T2)	Al(T2)	Al(M1)	Mg(M1)	Fe2+(M1)	V(M1)	Mg(M2+M3)	Fe(M2+M3)	Al(M2+M3)	Al(M4)	Fe <sup>3+</sup> (M4)	XFe <sup>2+</sup>	T(°C)	
29.48	21.88	25.16	0.45	12.36	0.31	0.02	0.12	2.89	1.10	0.10	0.18	0.11	0.61	1.63	1.04	1.23	0.09	0.91	0.39	125	
28.32	21.42	23.83	0.44	12.08	0.18	0.04	0.09	2.89	1.11	0.11	0.18	0.12	0.59	1.66	1.06	1.20	0.15	0.85	0.39	136	
28.47	21.68	25.8	0.55	11.11	0.55	0.06	0.18	2.86	1.12	0.12	0.17	0.13	0.58	1.50	1.17	1.19	0.13	0.87	0.44	144	
28.78	22.13	25.44	0.46	11.83	0.22	0.04	0.26	2.86	1.13	0.13	0.17	0.13	0.57	1.58	1.14	1.17	0.15	0.85	0.42	146	
29.19	22.45	25.02	0.34	12.33	0.19	0.03	0.61	2.86	1.14	0.14	0.18	0.12	0.56	1.62	1.05	1.20	0.12	0.88	0.39	152	
27.37	20.84	26.8	0.4	10.1	0.22	0	0.46	2.86	1.14	0.14	0.16	0.15	0.55	1.41	1.30	1.16	0.11	0.89	0.48	155	
28.78	21.76	25.47	0.28	12.6	0.21	0.05	0.07	2.85	1.14	0.14	0.18	0.12	0.56	1.68	1.12	1.13	0.13	0.87	0.40	155	
28.27	21.6	24.65	0.48	12.43	0.26	0	0.09	2.85	1.14	0.14	0.19	0.13	0.54	1.68	1.14	1.09	0.19	0.81	0.40	164	
28.22	22.34	24.75	0.48	12.07	0.19	0.04	0.18	2.84	1.16	0.16	0.18	0.13	0.53	1.63	1.20	1.08	0.25	0.75	0.42	166	
28.71	21.58	25.72	0.52	12.51	0.45	0.02	0.12	2.84	1.15	0.15	0.19	0.13	0.54	1.66	1.13	1.10	0.13	0.87	0.40	167	
28.72	21.96	24.85	0.41	13.04	0.15	0.03	0.24	2.84	1.16	0.16	0.19	0.12	0.53	1.73	1.09	1.09	0.16	0.84	0.39	168	
28.18	21.43	25.96	0.43	12.05	0.23	0.05	0.05	2.84	1.16	0.16	0.18	0.14	0.53	1.63	1.22	1.07	0.17	0.83	0.43	169	
29.01	21.65	20.38	0.35	16.03	0.22	0	0.33	2.84	1.14	0.14	0.24	0.08	0.54	2.10	0.69	1.11	0.10	0.90	0.25	174	
29.04	21.71	21.8	0.32	15.36	0.19	0.01	0.3	2.84	1.15	0.15	0.23	0.09	0.53	2.01	0.80	1.10	0.11	0.89	0.28	177	
28.64	21.88	25.41	0.37	13.22	0.31	0.03	0.08	2.83	1.17	0.17	0.20	0.13	0.50	1.75	1.15	1.02	0.18	0.82	0.40	179	
28.08	21.65	25.05	0.5	12.84	0.18	0.02	0.07	2.83	1.17	0.17	0.20	0.14	0.50	1.73	1.19	1.00	0.22	0.78	0.41	183	
28.28	21.48	23.34	0.41	13.76	0.09	0	0.67	2.83	1.17	0.17	0.22	0.11	0.51	1.83	0.94	1.10	0.10	0.90	0.34	183	
28	21.65	24.56	0.44	13.15	0.23	0	0.19	2.82	1.18	0.18	0.20	0.13	0.48	1.77	1.15	0.99	0.21	0.79	0.39	187	
28.09	21.56	26.63	0.5	12.29	0.23	0.03	0.12	2.81	1.18	0.18	0.19	0.15	0.48	1.65	1.28	0.98	0.20	0.80	0.44	187	
28.18	21.67	26.34	0.45	12.93	0.13	0.05	0.11	2.81	1.19	0.19	0.20	0.15	0.46	1.72	1.26	0.95	0.21	0.79	0.42	195	
27.32	21.54	24.71	0.54	12.67	0.12	0	0.02	2.81	1.19	0.19	0.20	0.15	0.46	1.74	1.27	0.92	0.30	0.70	0.42	196	
27.62	21.95	25.52	0.43	12.59	0.13	0.02	0.11	2.80	1.20	0.20	0.20	0.15	0.45	1.70	1.32	0.91	0.31	0.69	0.44	199	
28.09	22	26.35	0.53	12.74	0.14	0	0.07	2.80	1.20	0.20	0.20	0.15	0.45	1.70	1.32	0.92	0.28	0.72	0.44	199	
27.5	21.5	26.25	0.49	12.38	0.21	0.03	0.06	2.79	1.20	0.20	0.20	0.16	0.45	1.68	1.34	0.90	0.26	0.74	0.44	200	
27.85	21.9	24.87	0.49	13.37	0.19	0.09	0.04	2.79	1.20	0.20	0.21	0.14	0.44	1.79	1.21	0.91	0.27	0.73	0.40	201	

Atom site distribution (14 anhydrous-oxygen basis including Fe <sup>3+</sup> )														CHI <sub>3</sub>						
SiO <sub>2</sub>	Al <sub>2</sub> O <sub>3</sub>	FeO	MnO	MgO	CaO	Na <sub>2</sub> O	K <sub>2</sub> O	Si(T1+T2)	Al(T2)	Al(M1)	Mg(M1)	Fe2+(M1)	V(M1)							
27.83	21.34	25.73	0.48	13.15	0.28	0.03	0.07	2.80	1.20	0.20	0.21	0.15	0.45	1.76	1.24	0.91	0.22	0.78	0.41	202
27.41	22.07	25.39	0.53	12.66	0.15	0	0.05	2.78	1.21	0.21	0.20	0.16	0.43	1.72	1.35	0.86	0.35	0.65	0.44	204
27.38	21.28	26	0.5	12.73	0.14	0	0.02	2.79	1.21	0.21	0.20	0.15	0.44	1.73	1.33	0.87	0.27	0.73	0.43	204
27.9	21.44	25.86	0.57	13.32	0.24	0.01	0.04	2.79	1.20	0.20	0.21	0.15	0.44	1.78	1.26	0.88	0.24	0.76	0.41	206
27.86	22.32	25.19	0.56	13.13	0.2	0.06	0.02	2.79	1.21	0.21	0.21	0.16	0.43	1.75	1.30	0.87	0.35	0.65	0.43	207
27.34	21.64	25.1	0.54	13.04	0.13	0.01	0.06	2.79	1.21	0.21	0.21	0.15	0.42	1.77	1.30	0.86	0.32	0.68	0.42	209
27.54	21.81	25.78	0.59	12.73	0.21	0.05	0.09	2.78	1.21	0.21	0.20	0.16	0.42	1.71	1.32	0.87	0.30	0.70	0.44	209
27.14	21.24	24.4	0.47	13.14	0.21	0	0.3	2.79	1.21	0.21	0.22	0.15	0.42	1.79	1.22	0.89	0.27	0.73	0.40	210
27.34	20.89	24.95	0.54	13.3	0.21	0.02	0.08	2.80	1.20	0.20	0.22	0.15	0.43	1.81	1.22	0.88	0.23	0.77	0.40	210
27.97	22.11	25.7	0.49	13.39	0.11	0.01	0.08	2.79	1.21	0.21	0.21	0.15	0.42	1.78	1.30	0.86	0.31	0.69	0.42	210
27.3	21.23	25.95	0.47	12.85	0.22	0	0.04	2.78	1.21	0.21	0.21	0.16	0.42	1.75	1.33	0.85	0.27	0.73	0.43	210
27.04	21.18	24.61	0.52	13.17	0.21	0	0.02	2.79	1.21	0.21	0.21	0.15	0.42	1.81	1.27	0.85	0.30	0.70	0.41	211
27.55	22.31	26.56	0.38	12.38	0.14	0.05	0.09	2.78	1.22	0.22	0.20	0.17	0.41	1.66	1.44	0.83	0.37	0.63	0.46	213
28.72	21.46	21.63	0.25	17.07	0.22	0	0.04	2.80	1.20	0.20	0.26	0.10	0.44	2.22	0.85	0.88	0.19	0.81	0.28	215
27.49	21.23	24.81	0.5	13.98	0.15	0.04	0.03	2.78	1.22	0.22	0.23	0.15	0.41	1.88	1.22	0.83	0.27	0.73	0.39	218
27.94	20.91	25.08	0.49	14.63	0.04	0	0	2.79	1.21	0.21	0.23	0.14	0.42	1.95	1.16	0.85	0.20	0.80	0.37	219
28.6	21.05	21.06	0.2	17.47	0.41	0.03	0.04	2.80	1.20	0.20	0.28	0.10	0.43	2.27	0.78	0.88	0.16	0.84	0.26	223
26.98	21.5	25.07	0.49	13.28	0.21	0.02	0.06	2.77	1.23	0.23	0.22	0.16	0.38	1.81	1.34	0.77	0.36	0.64	0.43	224
27.94	21.3	23.44	0.3	15.62	0.16	0.03	0.05	2.78	1.22	0.22	0.25	0.13	0.40	2.06	1.06	0.82	0.24	0.76	0.34	224
26.9	21.2	24.62	0.52	13.58	0.11	0.02	0.01	2.77	1.23	0.23	0.23	0.16	0.39	1.86	1.30	0.78	0.34	0.66	0.41	225
27.32	22.08	25.22	0.57	13.35	0.15	0	0.04	2.76	1.23	0.23	0.22	0.17	0.38	1.79	1.37	0.77	0.40	0.60	0.43	225
27.52	21.85	25.5	0.64	13.59	0.14	0.02	0	2.77	1.23	0.23	0.22	0.16	0.38	1.82	1.34	0.77	0.36	0.64	0.42	225
27.37	22.08	25.38	0.58	13.47	0.1	0.04	0.03	2.76	1.24	0.24	0.22	0.17	0.37	1.80	1.37	0.75	0.40	0.60	0.43	228
27.03	21.62	25.36	0.59	13.31	0.1	0	0.02	2.76	1.24	0.24	0.22	0.17	0.37	1.81	1.39	0.74	0.39	0.61	0.43	230
26.74	20.91	27.78	0.51	12.14	0.22	0	0.05	2.76	1.24	0.24	0.21	0.19	0.36	1.66	1.53	0.73	0.33	0.67	0.48	232
26.67	20.84	24.49	0.5	13.64	0.25	0.07	0.04	2.76	1.24	0.24	0.24	0.16	0.37	1.87	1.28	0.75	0.32	0.68	0.41	233
27.11	21.3	24.83	0.56	14.12	0.17	0	0.02	2.76	1.24	0.24	0.24	0.16	0.36	1.91	1.30	0.73	0.35	0.65	0.41	234



Atom site distribution (14 anhydrous-oxygen basis including Fe <sup>3+</sup> )																			CHL	
SiO <sub>2</sub>	Al <sub>2</sub> O <sub>3</sub>	FeO	MnO	MgO	CaO	Na <sub>2</sub> O	K <sub>2</sub> O	Si(T1+T2)	Al(T2)	Al(M1)	Mg(M1)	Fe2+(M1)	V(M1)	Mg(M2+M3)	Fe(M2+M3)	Al(M2+M3)	Al(M4)	Fe <sup>3+</sup> (M4)		
27.66	20.62	21.87	0.31	17.95	0.09	0.01	0.01	2.75	1.25	0.25	0.31	0.13	0.32	2.35	0.96	0.65	0.27	0.73	0.29	265
26.45	21.78	25.11	0.5	13.95	0.09	0.02	0.05	2.72	1.28	0.28	0.25	0.20	0.27	1.89	1.49	0.56	0.52	0.48	0.44	266
26.33	21.87	25.99	0.57	13.17	0.08	0.04	0.03	2.72	1.28	0.28	0.24	0.21	0.27	1.79	1.58	0.56	0.55	0.45	0.47	266
27.32	21.29	21.8	0.46	17.15	0.1	0.03	0.05	2.73	1.26	0.26	0.30	0.14	0.30	2.26	1.06	0.62	0.38	0.62	0.32	266
26.37	21.44	26.02	0.64	13.49	0.09	0.08	0.04	2.72	1.28	0.28	0.25	0.20	0.27	1.83	1.52	0.56	0.48	0.52	0.45	267
26.04	21.11	28.28	0.5	12.13	0.12	0.08	0.04	2.71	1.28	0.28	0.22	0.23	0.26	1.66	1.71	0.55	0.48	0.52	0.51	268
26.56	21.63	25.12	0.56	14.25	0.35	0	0	2.71	1.27	0.27	0.26	0.20	0.27	1.91	1.45	0.55	0.51	0.49	0.43	271
26.53	21.83	25.32	0.61	14.04	0.09	0.05	0.01	2.72	1.28	0.28	0.26	0.20	0.26	1.89	1.51	0.53	0.54	0.46	0.44	273
26.52	21.02	25.74	0.53	14.43	0.04	0.03	0.03	2.72	1.28	0.28	0.26	0.20	0.26	1.94	1.46	0.54	0.45	0.55	0.43	275
26.32	21.16	23.58	0.53	15.18	0.06	0.04	0.01	2.72	1.28	0.28	0.28	0.18	0.26	2.06	1.35	0.53	0.49	0.51	0.40	277
27.94	20.91	20.05	0.21	19.66	0.1	0	0.01	2.74	1.25	0.25	0.34	0.11	0.30	2.53	0.84	0.60	0.31	0.69	0.25	277
26.3	21.8	26.92	0.46	13.18	0.15	0	0.04	2.71	1.29	0.29	0.25	0.23	0.23	1.78	1.69	0.47	0.61	0.39	0.49	286
27.03	20.37	22.95	0.35	17.38	0.06	0.02	0.02	2.72	1.27	0.27	0.31	0.15	0.26	2.30	1.12	0.54	0.34	0.66	0.33	286
25.74	21.65	29.06	0.46	11.49	0.11	0	0.07	2.70	1.30	0.30	0.22	0.27	0.21	1.58	1.92	0.44	0.64	0.36	0.55	289
26.41	20.81	23.76	0.5	15.99	0.06	0.06	0.01	2.71	1.29	0.29	0.30	0.19	0.23	2.14	1.32	0.47	0.47	0.53	0.38	295
26.38	22	26.33	0.58	13.81	0.01	0	0.01	2.70	1.29	0.29	0.26	0.23	0.21	1.85	1.66	0.43	0.64	0.36	0.47	295
26.42	21.76	25.47	0.56	14.51	0.09	0.02	0	2.70	1.29	0.29	0.27	0.22	0.21	1.94	1.57	0.43	0.61	0.39	0.45	299
26.51	21.77	26.22	0.54	14.37	0.05	0.03	0	2.70	1.30	0.30	0.27	0.23	0.20	1.91	1.62	0.41	0.62	0.38	0.46	305

## **Appendix 2: Publications of this thesis**





### **Publication 1**

**Cantarero I**, Travé A, Alías G, Baqués V (2010) Pedogenic products sealing normal faults (Barcelona Plain, NE Spain). *Journal of Geochemical Exploration*, **106**,44-52.





# Pedogenic products sealing normal faults (Barcelona Plain, NE Spain)

I. Cantarero\*, A. Travé, G. Alías, V. Baqués

Departament de Geoquímica, Petrologia i Prospecció Geològica, Facultat de Geologia, Universitat de Barcelona, Martí i Franquès s/n, 08028, Spain

## ARTICLE INFO

### Article history:

Received 30 April 2009

Accepted 15 February 2010

Available online 25 February 2010

### Keywords:

Extensional tectonics

Fault rock

Pedogenic processes

Geofluids

Miocene

Fault seal

## ABSTRACT

Minor normal faults affecting Miocene conglomerates of the Barcelona Plain are constituted by a poorly developed fault core without a damage zone. Fault rocks are made of a red muddy material that has been obliterated by later diagenetic processes. The most important products are spherulites and palisades formed by orange bladed calcite crystals. These calcite crystals are interpreted as resulting from pedogenic processes, being similar to Microcodium. The precipitation of the calcite crystals was induced by evaporation together with biota activity. The presence of these pedogenic products has an important effect in fault evolution because: 1) they date fault evolution during the Miocene extension; 2) they indicate shallow burial depth and meteoric diagenetic environment during fault evolution; and, 3) they give the cohesiveness to the fault rock causing the sealing of the fault and its behaviour as a barrier to fluids.

© 2010 Elsevier B.V. All rights reserved.

## 1. Introduction

Brittle fault zones are composed of a fault core and a damage zone. The fault core, where most displacement is accommodated, is highly deformed and it is constituted by the fault rocks, as gouges, breccias, cataclases and pseudotachylites, whereas the damage zone is made up of little faults and joints, some with cementation, affecting the host rock or protolith (Caine et al., 1996; Labaume et al., 2004). The circulation of fluids during extensive fracturing is shown by the presence of minerals precipitating in veins or as cements.

Thus, fault rocks are the result, among others, of fault displacement, different events and mechanisms of deformation and different diagenetic processes related to different fluids that have circulated through the faults. Therefore, the microstructural, petrographic and geochemical study of fault rocks, together with the structural study of faults provides an understanding of the geodynamic and hydrogeologic evolution of the basin because faults can act successively as conduits or barriers for fluids (Caine et al., 1996; Rowland and Sibson, 2004).

This paper deals with the temporal relationship between pedogenic processes and the Neogene fracturing that affects Miocene conglomeratic deposits of the Caritg Hill (Barcelona) and the subsequent fault rock transformation, particularly on attributes such as chemical characteristics, reology and composition. The aims of this paper are: 1) to characterize petrologically and geochemically the fault rock and its diagenetic products; 2) to determine the composition of the fluids that circulated through the faults; and, 3) to determine the role of pedogenic processes in fault rock evolution.

## 2. Geological setting

The Valencia Trough is a NE–SW oriented basin generated during the Neogene extension (late Oligocene–middle Miocene). This basin, in the north-western Mediterranean between the Iberian Peninsula and the Balearic Promontory, is divided into two domains: the Betic–Balearic and the Catalan–Valencian (Bartrina et al., 1992). The Catalan margin forms the NW limit of the basin and is characterized by a complex system of horsts and grabens limited by listric faults striking NE–SW and NNE–SSW with a detachment level at 12–16 km (Gaspar-Escribano et al., 2004). One of these grabens corresponds to the Barcelona Plain, which is about 40 km long and 2–10 km wide. It consists mainly of Miocene continental-transitional siliciclastic deposits and Quaternary fluvio-deltaic deposits. To the NW, it is bounded by the SE-dipping Collserola Fault and the Collserola Horst, which is composed of Paleozoic materials (Fig. 1B).

The Neogene extension was divided into three stages: 1) syn-rift (late Oligocene–early Miocene); 2) early post-rift (Burdigalian–early Serravallian); and, 3) late post-rift (Serravallian–Pliocene) (Calvet et al., 1996).

The three outcrops selected for this study are located on a hill inside the city of Badalona, 8 km from Barcelona. The faults studied affect Miocene conglomerates, probably of Langhian age (Parcerisa, 2002; Parcerisa et al., 2007), which have been interpreted as alluvial fan deposits.

Two fault systems have been recognized in the studied outcrops. One system has a N–S striking direction and dips 30 to 60° towards the E–SE. The other system has a NW–SE striking direction and dips 60 to 80° towards the NE (Fig. 1B). Both systems have a fault core made of a cohesive, red mud-to-sandy material with centimetric host rock clasts and do not have a damage zone (Fig. 2).

\* Corresponding author. Tel.: +34 934031165; fax: +34 934021340.

E-mail addresses: [i.cantarero@ub.edu](mailto:i.cantarero@ub.edu) (I. Cantarero), [atrave@ub.edu](mailto:atrave@ub.edu) (A. Travé), [galias@ub.edu](mailto:galias@ub.edu) (G. Alías), [vbaques@ub.edu](mailto:vbaques@ub.edu) (V. Baqués).

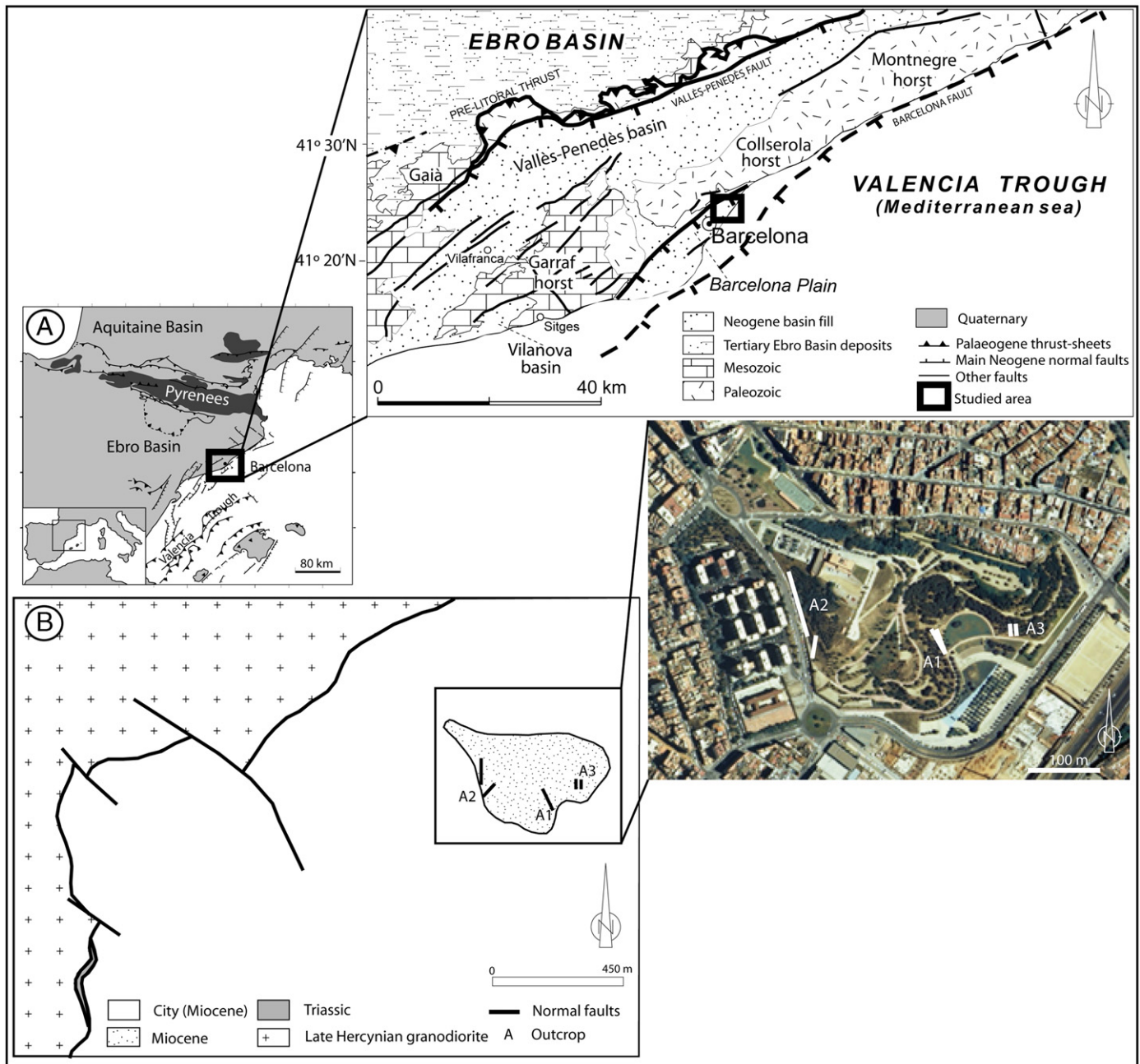


Fig. 1. A) Geological setting of the Barcelona Plain. B) Simplified geological map of the studied area and location of the outcrops.

### 3. Methods and analytical techniques

X-ray diffraction of bulk rock and oriented aggregates have been performed with a Bragg–Brentano PANalytical X'Pert PRO MPD alpha 1 operating at 1.5406 Å, 45 kV and 40 mA.

Thin sections of host rock and fault rock have been studied using optical and cathodoluminescence microscopes. A Technosyn Cold Cathodoluminescence Model 8200 MkII operating at 16–19 kV and 350 µA gun current was used. Some thin sections and chips were examined under ESEM Quanta 200 FEI, XTE 325/D8395 scanning electronic microscope.

After the petrographic study, some samples were selected for elemental analyses of the carbonate cements with a CAMECA model SX-50 microprobe. It was operated using 40 nA of current intensity and 20 kV of excitation potential. The detection limits are 140 ppm for

Na, 544 ppm for Ca, 517 ppm for Mg, 227 ppm for Fe, 160 ppm for Mn and 223 ppm for Sr.

Samples for carbon and oxygen stable isotopes were powdered with a microdrill. Collected samples were reacted with phosphoric acid at 70 °C for two minutes in an automated Kiel Carbonate Device attached to a Thermal Ionization Mass Spectrometer Thermo Electron (Finnigan) MAT-252. The results are expressed in ‰ VPDB standard. Standard deviation is ± 0.02‰ for  $\delta^{13}\text{C}$  and ± 0.05‰ for  $\delta^{18}\text{O}$ .

### 4. Host rock petrology

The conglomerates are matrix supported and heterometric. Clasts range from cobble to granule and occasionally some of the clasts are up to metric size. Clasts are derived from the Paleozoic basement and the most abundant lithologies are phyllites (45%) and quartzites

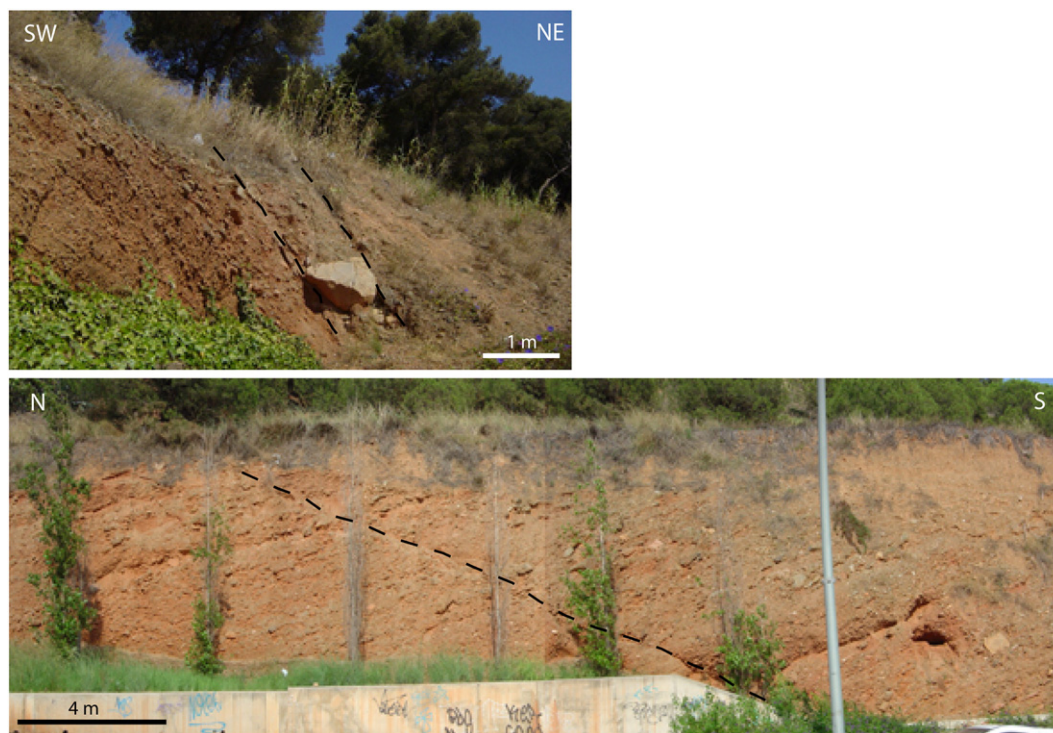


Fig. 2. Views of the outcrop showing the faults affecting the Miocene conglomerates.

(35%) followed by knotted hornfels (10%), quartz grains derived from quartzites and granodiorites (7%) and porphyries (3%). Clasts are usually angular but phyllites and knotted hornfels are rounded.

The matrix is formed by red mud-to-sandy material. The sand size includes grains of angular quartz and subrounded orthose. The smaller matrix fraction includes quartz, potassium feldspar, illite, chlorite, kaolinite, mixed-layer of chlorite–illite, mixed-layer of illite–chlorite, apatite, iron oxides and titanium oxides.

The conglomerates have vug and fracture porosity. Vugs are rounded and have a maximum diameter of 2.5 mm. Fracture porosity is the most significant and tends to border the clasts producing an anastomosing geometry. Porosity is open without cement.

## 5. Fault rock petrology

At the outcrop scale, the fault rocks form a narrow zone ranging from 0.5 to 7 cm width and are characterized by their red color. The petrologic study, however, has highlighted the presence of diagenetic products that have obliterated partially or totally the original fault rock fabric.

The preserved fault rock is formed by a red muddy matrix and clasts ranging from less than 1 mm to 3 cm that represent about 7 to 25% of the rock volume (Fig. 3A, C, E, F). As in the Miocene conglomerates, clasts have a wide range of lithologies with phyllites and quartzites (approx. 43% each one) the dominant types. Other clasts are monocrystalline and polycrystalline quartz, knotted hornfels, orthose grains, sandstones and porphyries. As also occurs in the host rock, clasts are mostly angular but phyllites and hornfels are subrounded. Clasts show a random fabric.

The matrix is formed by grains smaller than 50  $\mu\text{m}$ . These grains are quartz, potassium feldspar, apatite, iron oxides (probably goethite), titanium oxides, illite, chlorite, kaolinite, mixed-layers of illite–chlorite and mixed-layers of chlorite–illite (Fig. 3B). The fault rock matrix provides thinner peaks in the X-ray diffractogram of clays in contrast to the host rock matrix indicating a higher crystallinity.

Because of the cohesiveness of the rock, in addition to the proportion of matrix, the fault rock has been classified in the field as a cataclasite, according to Sibson's nomenclature (Sibson, 1977).

### 5.1. The diagenetic products

Diagenetic processes overprint the fault rock fabric. According to the texture and the delimitation of conspicuous domains, the main diagenetic products are: 1) orange bladed calcite aggregates; 2) white bladed calcite domains; 3) micrite strips; 4) calcite cement filling vug and channel porosity; and, 5) calcite cement filling late microfractures. These diagenetic products are aligned along two main directions in the fault rock. One direction is subparallel to the fault plane, whereas the other forms at an angle of 30–45° relative to the fault plane.

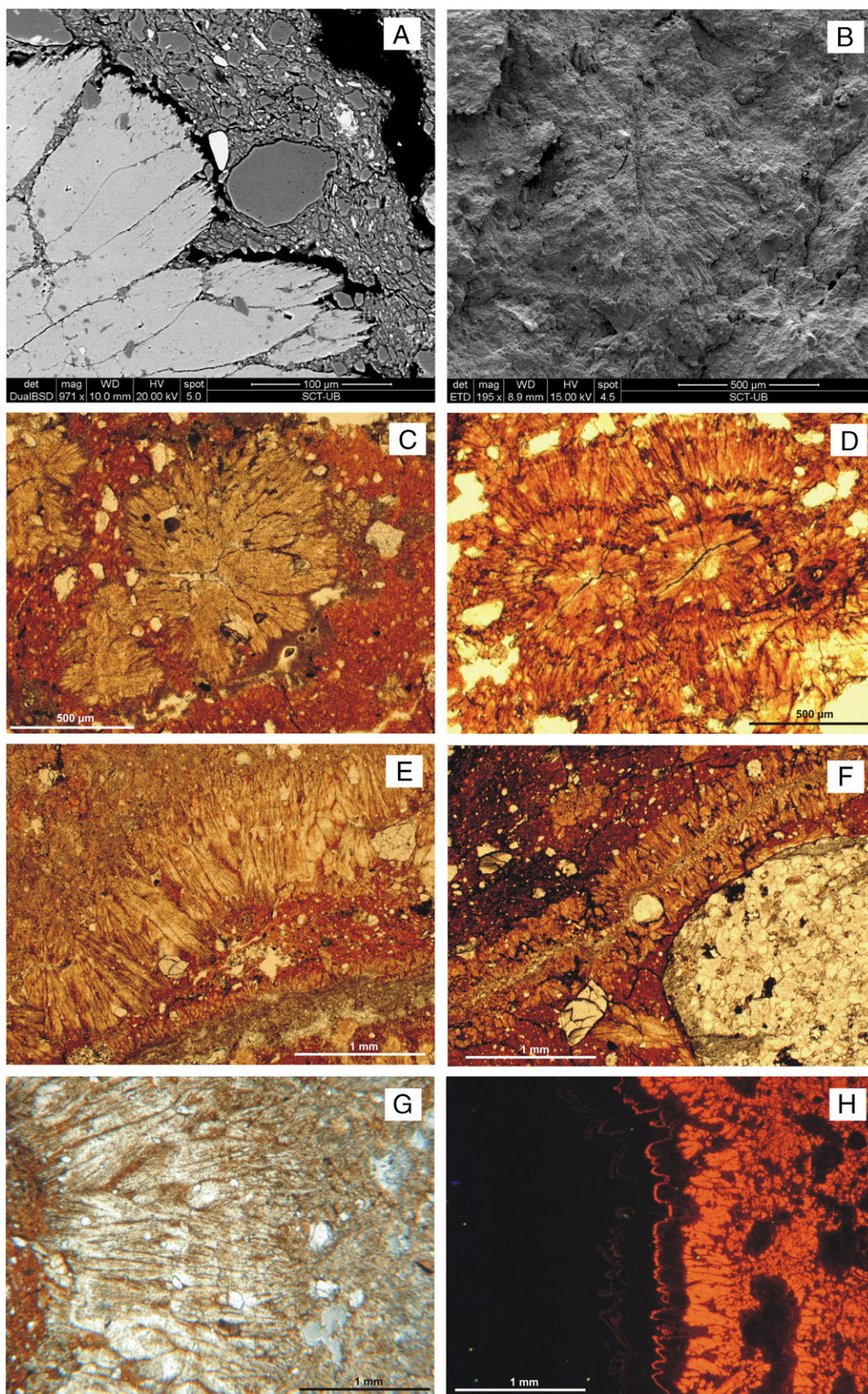
#### 5.1.1. Orange bladed calcite aggregates

The orange bladed calcite shows two main types of aggregates; spherulites and palisades, but also occasionally forms some “corn-cob” aggregates. In the inner part of these aggregates, crystals have bladed morphology and radial fibrous textures, whereas in the outer part, crystals became more acicular (Fig. 3A, E). Crystals show fan-like extinction with crossed-polarized light. These aggregates can be isolated or form dense masses in the matrix constituted by the original fault rock.

Spherulites are radial polycrystalline aggregates (Fig. 3B, C, D). They are typically formed by crystals of different sizes giving an asymmetric geometry. Spherulites have a maximum diameter of 2–3 mm in the NW–SE fault system and 1.5 mm in the N–S fault system. In the latter, the orange bladed calcite is also present as concentric spherulites formed by brown zonations in the bladed crystals (Fig. 3D).

Palisades form 0.25–1 mm wide strips with a minimum length of 2 mm. There are two kinds of palisades. The most abundant typically forms single thick palisade aggregates (Fig. 3E, G). The other forms a





**Fig. 3.** Orange bladed calcite aggregates. A) SEM photograph of the outer part of a palisade. Crystals are more acicular in the border. B) Spherulite aggregate under SEM. C) Spherulites isolated in the matrix of the fault rock. D) Concentric spherulites formed by brown zonations in the bladed crystals. E) Single thick palisade aggregates. F) Double palisade isolated in the matrix. G and H) Single palisade under transmitted light and cathodoluminescence microscopies. Only the nucleus of the palisade is bright orange luminescent.



double palisade with bladed crystals growing side by side from a central axis. This palisade describes straight and isolated strips in the matrix (Fig. 3F).

Orange bladed calcite is non-luminescent or bright orange luminescent. The former is found in all the aggregates, whereas the luminescent is only present in the nucleus of some spherulites and palisades (Fig. 3 G, H).

#### 5.1.2. White bladed calcite domain

The bladed calcite is translucent, has a grain size similar to the orange bladed calcite and also has fan-like extinction. It shows a bright orange luminescence (Fig. 4A, B) and it only constitutes palisades, although they are less defined than the ones formed from the orange calcite, producing a disordered appearance. This calcite borders fragmented clasts cemented by translucent blocky dull-orange luminescent calcite (Fig. 4C).

#### 5.1.3. Micrite strips

This product forms very thin to 4 mm wide micrite strips with a channel porosity in the center and micrite grains that increase their

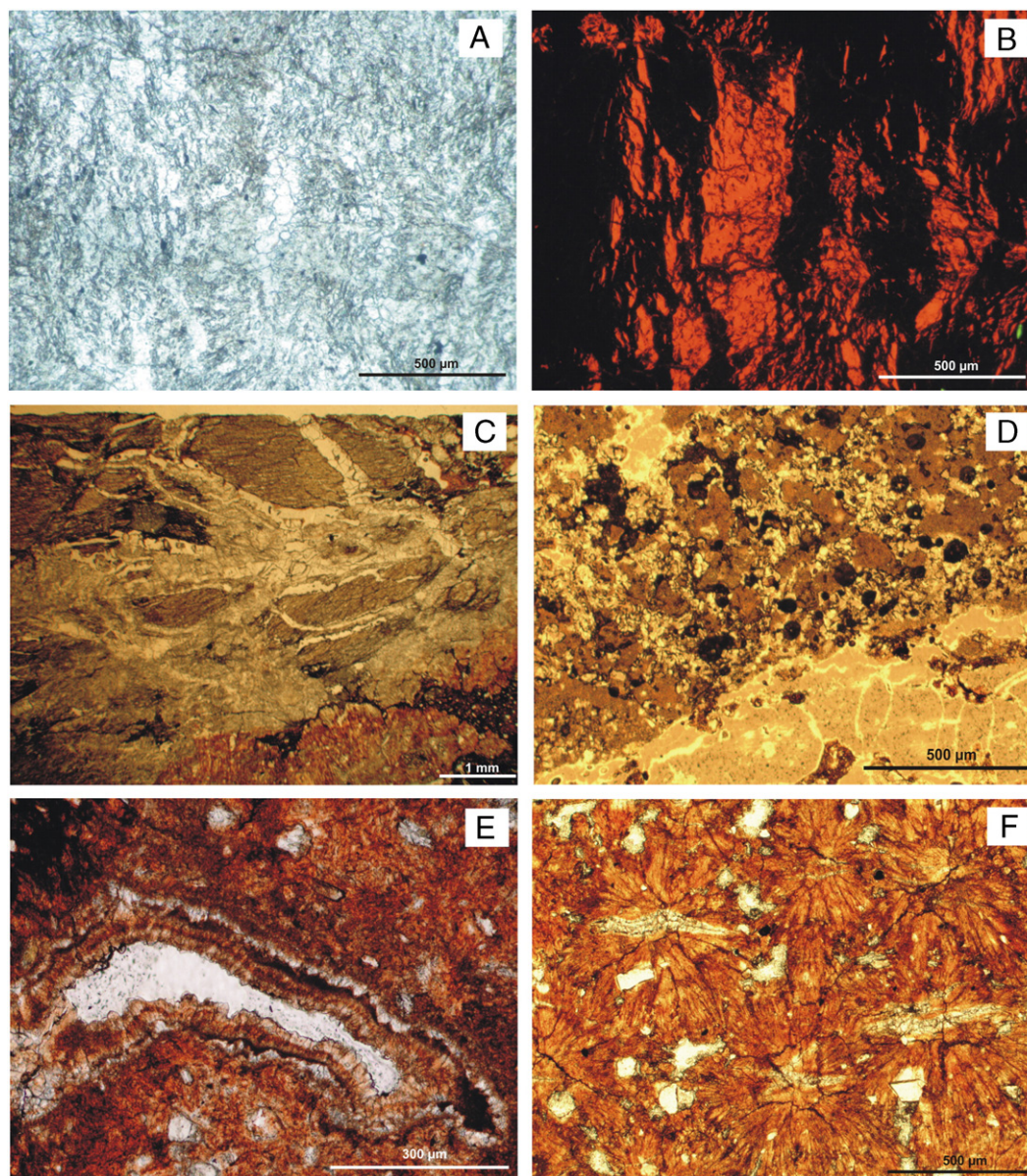
size from the site of the porosity towards the fault rock. Micrite strips show irregular vuggy porosity that is partially filled by blocky calcite (Fig. 4D). Micrite and blocky calcite are non-luminescent.

#### 5.1.4. Calcite cement filling vug and channel porosity

Porosity constitutes 25–30% of the rock volume. Vug and channel porosity within the fault rock can remain open or be cemented. Vugs are irregular cavities that range from 0.3 to 2.5 mm in diameter. Channels have a variable width between 0.1 and 0.7 mm and generally have anastomosing arrangements. There are three types of cements in the porosity: 1) blocky calcite; 2) rim bladed calcite; and, 3) alternating layers of clear bladed calcite with clays (Fig. 4E). All porosity cements are non-luminescent.

#### 5.1.5. Calcite cement filling late microfractures

Late microfractures affect the matrix and the previously described diagenetic products. They have rectilinear and sigmoidal morphologies which are consistent with a normal slip and follow the same



**Fig. 4.** A and B) White bladed calcite domain under transmitted light and cathodoluminescence microscopies. Bright orange luminescent crystals of this domain are cut by later non-luminescent blocky calcite microfractures. C) Relationship between fragmented clasts and white bladed calcite domain. D) Irregular vug porosity in the micrite strips cemented by blocky calcite. E) Bladed calcite alternating with clays in a vug porosity. F) Sigmoidal microfractures cutting orange bladed spherulites.



orientations as the diagenetic products (Fig. 4F). Microfractures are cemented by orange luminescent and non-luminescent blocky calcite.

## 5.2. SEM observations

Scanning electron microscopy has been performed in order to find further clues on the origin and development of the diagenetic products. The SEM study has revealed a dissolution front surrounding the calcite crystals that affects the fault rock matrix (Fig. 3A). On the other hand, it has not been observed the presence of microbial markers such as calcite rods, spheres or filaments which could be interpreted as bacteria or cyanobacteria (Travé, 1992; Rossi and Cañaveras, 1999).

## 6. Elemental geochemistry of carbonates

Non-luminescent cements are characterized by Mg contents between the analytical detection limit and 18,331 ppm (average 6000 ppm) and Mn contents in all cases below the analytical detection limit (Table 1). Orange bladed calcite and the clear bladed calcite alternating with clays have high contents of Fe, between 1310 and 18 766 ppm (average 6000 ppm) and between 4500 and 12,040 (average 7300 ppm) respectively. The remainder of the non-luminescent cements has very low or below analytical detection level Fe. Sodium is highly variable ranging from below analytical detection limit to 1900 ppm. Finally, Sr content is high (1500–3000 ppm).

By contrast, luminescent cements are characterized by contents of Na below the analytical detection limit and very high levels of Mn (Table 1). Manganese is especially abundant in orange bladed calcite (up to 25,400 ppm), which also has Fe contents up to 1367 ppm (average 662 ppm). The other luminescent cements have below analytical detection limit Fe. Magnesium contents are lower than in non-luminescent calcite but still high and do not show a clear relation with Ca. Finally, Sr remains constant at 1300 ppm.

## 7. Oxygen and carbon isotopes

Orange bladed calcite, white bladed calcite and micrite do not show important isotopic differences and plot in the same area (Fig. 5). The  $\delta^{18}\text{O}$  is of low variance, ranging from  $-4.4$  to  $-3.9\%$  VPDB, so it has a variability of  $0.5\%$  VPDB. The  $\delta^{13}\text{C}$  has highly negative values that range from  $-10.3$  to  $-9.0\%$  VPDB. Luminescent orange bladed calcite has the less negative values, around  $-9.0\%$  VPDB.

## 8. Discussion and interpretation

The main features of the diagenetic products affecting the fault rocks suggest a pedogenic origin and permit speculation about the origin of the fluids. On the other hand, overprinting relationships between fractures and diagenetic products modify the nature of the parent rock and therefore the preliminary classification of the fault rock in the field as a cataclastite.

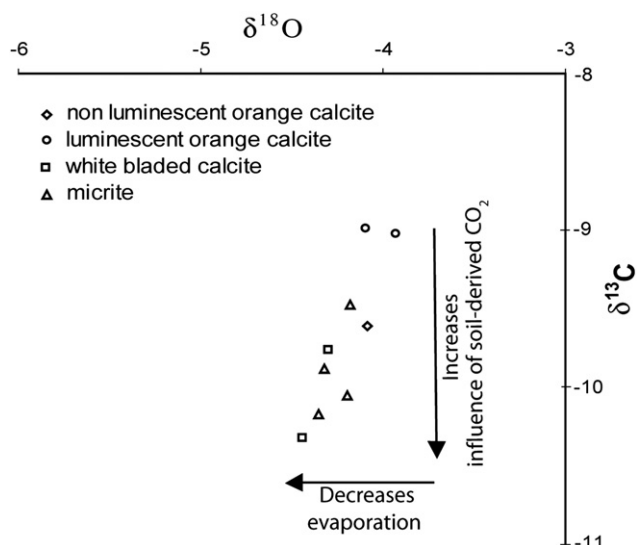
### 8.1. Pedogenic origin of the diagenetic products

The following features related to these diagenetic products support our interpretation of the textures as Microcodium: 1) the calcite mineralogy of crystals; 2) the bladed habit of calcite crystals and their internal fibrous textures (Kabanov et al., 2008); 3) the crystal arrangement forming spherulites, palisades and “corn-cobs” (Lucas and Montecat, 1967; Bodergat, 1974; Klappa, 1978; Kabanov et al., 2008; Košir, 2004); 4) the destructive and principally matrix selective replacement of the fault rock through the dissolution front surrounding the calcite crystals (Klappa, 1978); and, 5) the concentration of replacement along discontinuity surfaces, fractures in our case (Alonso-Zarza and Jones, 2007; Kabanov et al., 2008).

In our case, pedogenic products are only present in the faults. Inside the fault rock, they are oriented following two main directions, probably related to previous microfractures. However, typical Microcodium crystals have a rounded border and are translucent while the

**Table 1**  
Synthesis of the elemental composition of the diagenetic products (<d.l. means below the detection limit).

		Mg(ppm)	Ca(ppm)	Mn(ppm)	Fe(ppm)	Se(ppm)	Na(ppm)
Non-luminescent-cements							
Orange bladed calcite (n = 36)	Minimum	1310	361,267	<d.l.	<d.l.	1157	<d.l.
	Maximum	18,766	400,400	100	7619	2015	758
	Average	6065	384,544	<d.l.	2565	1489	212
Micrite (n = 5)	Minimum	3846	369,380	<d.l.	275	1631	230
	Maximum	18,331	389,653	<d.l.	2263	2652	508
	Average	10,416	377,640	<d.l.	972	2171	434
Blocky calcite in micrite porosity (n = 4)	Minimum	2556	364,326	<d.l.	<d.l.	1641	409
	Maximum	16,328	395,756	220	252	4311	1396
	Average	11,588	376,541	<d.l.	<d.l.	3125	934
Blocky calcite in microfractures (n = 56)	Minimum	<d.l.	373,809	<d.l.	<d.l.	1215	<d.l.
	Maximum	15,631	401,213	896	721	2559	1819
	Average	7438	390,175	<d.l.	<d.l.	1700	274
Sperry calcite in porosity (n = 26)	Minimum	3340	377,400	<d.l.	<d.l.	1215	<d.l.
	Maximum	10,350	397,900	190	350	1618	368
	Average	5832	389,246	<d.l.	<d.l.	1699	<d.l.
Clear bladed calcite alternating with clays (n = 6)	Minimum	4500	370,700	<d.l.	<d.l.	–	<d.l.
	Maximum	12,040	395,700	<d.l.	8190	–	550
	Average	7328	383,050	<d.l.	2750	–	177
Luminescent cements							
Orange bladed calcite (n = 14)	Minimum	997	364,479	1590	<d.l.	1099	<d.l.
	Maximum	5940	392,156	26,870	1367	1567	192
	Average	3375	378,834	14,837	622	1325	<d.l.
White bladed calcite (n = 11)	Minimum	743	368,500	<d.l.	<d.l.	1305	<d.l.
	Maximum	6897	393,369	16,055	1418	1822	386
	Average	3942	381,442	10,301	<d.l.	1483	<d.l.
Blocky calcite in microfractures (n = 14)	Minimum	<d.l.	370,100	840	<d.l.	1144	<d.l.
	Maximum	5190	397,600	18,488	<d.l.	2066	169
	Average	3106	385,456	10,951	<d.l.	1404	<d.l.



**Fig. 5.** Stable isotope results of the main diagenetic products. For the orange calcite luminescence, ranging from luminescent to non-luminescent cements, there are an increase in the influence of soil-derived  $\text{CO}_2$  and a decrease of evaporation.

crystals here are orange and seem to be formed by fibrous aggregates. The spherulites and palisades described here are also very similar to the pseudospherulitic fibrous calcite of Rossi and Cañaveras (1999) who interpreted them as the calcitization of bacterial colonies. In both cases, their cathodoluminescence behaviour shows concentric changes but their spherulites are composed of a single crystal and not polycrystalline aggregates.

Traditionally, the more extended interpretation of Microcodium is of originating as the result of the calcitization of root cells, with or without a mycorrhizal association (Calvet et al., 1975; Klappa, 1978; Košir, 2004). However, other investigations point to an induced mineralization driven by saprotrophic microorganisms or a microbial association (Lucas and Montenat, 1967; Boderat, 1974; Kabanov et al., 2008). We are not concerned here about the origin, type or textures of Microcodium. In this case, the low  $\delta^{13}\text{C}$  values indicate the influence of soil-derived  $\text{CO}_2$ . Thus, a pedogenic process led to the growth of the calcite crystals that corroded the fault rock. This, together with the lack of microbial observations during the SEM analysis, point to processes associated with roots.

## 8.2. Fluids origin

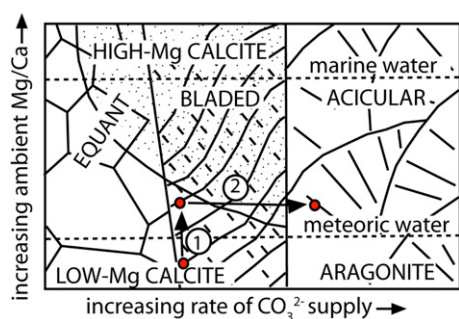
Determining the fluid origin is difficult because of the complexity of the elemental composition of diagenetic products and the  $\delta^{18}\text{O}$  values. In the meteoric environment, where pedogenic processes take place, local waters have a low Mg/Ca ratio, a low content of Sr and  $\delta^{18}\text{O}$  values lower than  $-4\text{‰}$  SMOW. Therefore, the dominant carbonate mineral is low-Mg calcite. Then, how to explain the presence of high-Mg calcite, high contents of Sr and high values of  $\delta^{18}\text{O}$  in a pedogenic environment? Watts (1980) showed the presence of high-Mg calcite, aragonite and dolomite in Quaternary calcretes from the Kalahari (southern Africa). He explained that high-Mg calcite and aragonite precipitate when there is a rapid evaporation and/or  $\text{CO}_2$  loss whereas low-Mg calcite precipitates when there is a slow evaporation and/or  $\text{CO}_2$  loss. In addition, McQueen et al. (1999) observed a vertical and lateral evolution of the carbonate mineralogy of regolith carbonates of southeastern Australia. They found an increase of the Mg content with depth due to changes in pH and  $\text{pCO}_2$  during the percolation of rainwater and argued that the lateral evolution was caused by lateral groundwater movements along the bedrock-alluvium boundary. We did not detect any evidence of vertical and lateral evolution from calcite to dolomite in our case. So,

to determine the origin of the fluid responsible for the calcite precipitation, we have compared our setting with the high-Mg calcite settings described by Watts (1980).

In case one, the calcretes described by Watts (1980) developed in Mg-rich host materials where high-Mg calcite precipitates from vadose waters enriched in Mg. The host rock in our study is not sufficiently enriched in Mg to form this water composition. In addition, for our case the fluids cannot be derived from the basement because the faults are small and enclosed by clay rich layers and the  $\delta^{18}\text{O}$  values do not support elevated temperatures.

In a second case study, Watts (1980) outlines the development of calcretes in and around saline depressions where groundwaters are enriched in Mg compared to vadose water and carbonate precipitation is stimulated by  $\text{CO}_2$  loss during capillary rise. No brines were identified in our setting; however, the outcrops are only 1.5 km from the Mediterranean Sea. Moreover, during the late Burdigalian, Langhian and Serravallian, marine transgressions and highstand sea levels extended into the study area (Cabrera and Calvet, 1996). It is therefore possible that the groundwaters were a mixture of meteoric and marine waters, which would be enriched in Mg and Sr. This would explain the mineralogy and elemental composition and also the  $\delta^{18}\text{O}$  values (James and Choquette, 1990). In addition, cathodoluminescence would reflect the dominant water in the mixing zone, marine in luminescent cements and meteoric in non-luminescent cements. However, the elevated Sr contents of cements in our case suggest a formation water composition for the fluid rather than a marine origin.

In the third case, high-Mg calcite appears in immature calcretes developed in Mg-poor sands with a low Mg/Ca ratio of vadose waters and carbonate precipitation occurs because of an enhanced evaporation. As earlier stated, the samples in this study have  $\delta^{18}\text{O}$  ranges from  $-4.4$  to  $-3.9\text{‰}$  VPDB. If we assume precipitation temperature of  $25^\circ\text{C}$ , calcites would have precipitated from fluids with  $-2.2\text{‰}$  SMOW, which marks the loss of  $^{16}\text{O}$  by evaporation. Moreover, paleoclimatic conditions between the Burdigalian and Langhian were warm, seasonal and arid tropical-subtropical with paleotemperatures between  $15.5$  and  $24.6^\circ\text{C}$ , even higher in the Serravallian (Cabrera and Calvet, 1996). This paleoclimate could account for the required evaporation. In addition, the forced crystallization of carbonates in our study does not produce metastable thermodynamic equilibrium between high-Mg calcite and waters, so partition coefficients cannot be applied (Watts, 1980; Tucker and Wright, 1990). Finally, cathodoluminescence changes are probably related to oscillations of the water table that generate Eh-pH variations during the development of the diagenetic products. However, high-Mg calcite in this context was only formed as anhedral micrite. Although this third case is consistent with the observations in this study, we suggest that biota plays an important role and, together with evaporation, induces high-Mg calcite precipitation from a meteoric fluid. The  $\delta^{13}\text{C}$  values lower than  $-9\text{‰}$  VPDB support this theory. The luminescent calcite, the first precipitate, is always low-Mg calcite and non-luminescent calcite can be of low-Mg calcite or high-Mg calcite. The mineralogical change is caused by an initial increase of temperature, followed by an increase of  $\text{CO}_3^{2-}$  supply rate. The  $\text{CO}_3^{2-}$  is the result of increased  $\text{CO}_2$  generation by plant respiration and the decomposition of organic acid anions exuded by the roots (Manning, 2008). Luminescent cements precipitated from meteoric water that increased its Mg/Ca ratio because of evaporation but still precipitated low-Mg calcite (Fig. 6). As vegetation or microorganisms matured, the rate of  $\text{CO}_3^{2-}$  supply increased. This would have caused the change from low-Mg bladed calcite precipitation to high-Mg bladed calcite and to acicular aragonite precipitation (Tucker and Wright, 1990) and would explain why crystals pass from bladed to an aggregate of fibres (Fig. 6). During this last period, evaporation decreased. The change of evaporation conditions and the influence of soil are marked by  $\delta^{18}\text{O}$  and  $\delta^{13}\text{C}$ , respectively. Looking at the isotopes of orange bladed calcites, it is observed that the luminescent nucleus, the first to precipitate, has



**Fig. 6.** Factors controlling the precipitation of the pedogenic products. 1) Evaporation increases the Mg/Ca ratio but still low-Mg calcite precipitates. 2) Biota activity become more important and increases the rate of  $\text{CO}_3^{2-}$  supply. This increase causes the change from low-Mg bladed calcite to high-Mg bladed calcite and to acicular aragonite precipitation. This explains the morphology zonation of the orange calcite aggregates (modified from Tucker and Wright, 1990).

more enriched  $\delta^{18}\text{O}$  and  $\delta^{13}\text{C}$  values than non-luminescent calcites (Fig. 5). This change of evaporation implies a decrease of temperature that could be related to climatic or even seasonal fluctuations.

However, another hypothesis about calcite mineralogy is possible: a neomorphism process that begins in the nucleus of the aggregates and spreads towards the outer part. The reason is that the calcite of the nucleus is more metastable because: 1) It is the first to precipitate and 2) the organic matter of the nucleus is also the first to decompose. This process of neomorphism is similar to that described in calcareous red algae (Calvet, 1979). This explanation is supported by a limit between both cements and because luminescent cements show a less preserved morphology. Up to now, we do not have arguments to accept or reject one or another hypothesis about the initial mineralogy of the nucleus.

### 8.3. Implications of pedogenic processes in understanding fault and fault rock evolution

The presence of pedogenic products is important in understanding the fault and fault rock evolution. They constrain the fault age, the formation conditions and the fault rock classification.

We can limit the formation of the fault and the pedogenic processes to the Miocene extension because: 1) faults affect Miocene conglomerates; 2) pedogenic products follow two main orientations which were probably previous microfractures of the fault rock; 3) pedogenic products are also affected by microfractures with the same orientations; and, 4) restitution of microfractures show normal slip.

In addition, pedogenesis develops in surface conditions, typically within the uppermost 10 m, and here the pedogenic products are affected by microfractures associated with fault displacement. This indicates a shallow burial depth of the fault and a meteoric diagenetic environment during fault evolution.

Finally, the fault rock, because of its cohesive appearance in the outcrop and the volume of clasts, was preliminary classified as a cataclasite (Sibson, 1977). However, the petrologic study has revealed that cohesiveness was given by the pedogenic products. The original fault rock was uncohesive, and therefore, it was probably a gouge, which forms in shallower conditions than cataclasites.

The change in fault rock properties implies a change in fault permeability. Before the precipitation of the pedogenic products, the narrow and poorly developed fault core was a gouge. This, together with the absence of a damage zone, allowed a cross-fault flux between the porous layers of the host rock. The growth of plants and microorganisms induced the neoformation of the different pedogenic products which reduced the effective porosity of the fault rock and its permeability. The result was the sealing of the fault zones and the restriction of fluid flow.

## 9. Conclusions

The studied normal faults affecting Miocene conglomerates of the Caritg Hill are formed by a poorly developed fault core without a damage zone. Fault rocks are characterized by their red colour, a clast volume under 25% and their cohesive appearance in the outcrop. The petrologic study of the fault rocks has highlighted the presence of diagenetic products that have obliterated partially or totally the fault rock fabric.

The main and most obvious diagenetic product is palisades and spherulites of orange bladed calcite. The others are white bladed calcite, micrite strips, porosity and microfractures. Luminescent cements of low-Mg calcite were the first to precipitate whereas non-luminescent low-Mg and high-Mg calcite precipitated later. Non-luminescent cements are characterized by high contents of Mg and Sr and the absence of Mn and only bladed calcite has Fe. In contrast, luminescent cements have lower values of Mg and below analytically detectable Fe and Na. Therefore, there is an incompatibility between Fe and Mn and between Mn and Na.

Biota, together with evaporation, is considered to have induced the precipitation of the pedogenic products from meteoric water. Luminescent low-Mg calcite precipitated with  $\delta^{18}\text{O}$  of  $-3.9\%$  VPDB when evaporation increased the Mg/Ca ratio. Later, the growth of biota in the fractures caused an increase of the  $\text{CO}_3^{2-}$  supply rate. This increment induced the precipitation of non-luminescent bladed calcite and fibres of aragonite, now transformed to calcite with high Sr content and an acicular morphology. However, a neomorphism process from high-Mg calcite to low-Mg calcite is also taken into account.

All these diagenetic processes have strong implications in understanding fault and fault rock evolution. Firstly, the relationship between pedogenic products and microfractures date the formation of the faults and of the pedogenic processes to the Miocene. Secondly, the presence of microfractures affecting the pedogenic products indicates a shallow burial depth and meteoric diagenetic environment during fault evolution. Thirdly, pedogenic products are responsible for the cohesiveness of the fault rocks, causing a change in fault rock classification from cataclasite to gouge. This change of properties of the fault rock had an important effect on the fault zone permeability. The neoformation of the diagenetic products reduced the permeability of the fault rock causing the sealing of the fault and forming a barrier to fluid flow.

## Acknowledgements

We thank Pere Anadón for discussion on the Microcodium, Montserrat Inglés, Ramon Vaquer and Juan Diego Martín for help in clays interpretation and Eduard Roca for his comments. We also thank Steven Hill and an anonymous reviewer for their constructive reviews. The isotopic, electron microprobe and SEM analyses were carried out at "Serveis Científicotècnics" of the Universitat de Barcelona. This research was performed within the framework of DGICYT Spanish Project CGL2006-04860, Grup Consolidat de Recerca "Geologia Sedimentària" (2009SGR-1451) and the 2009FI\_B00241 supported by the Comissionat per a Universitats i Recerca del Departament d'Innovació, Universitats i Empresa de la Generalitat de Catalunya i el Fons Social Europeu.

## References

- Alonso-Zarza, A.M., Jones, B., 2007. Root calcrete formation on Quaternary karstic surfaces of Grand Cayman. *Geogaceta* 5 (1), 77–88.
- Bartrina, M.T., Cabrera, L., Jurado, M.J., Guimerà, J., Roca, E., 1992. Evolution of the Central Catalan margin of the Valencia trough (Western Mediterranean). *Tectonophysics* 203, 219–247.
- Bodergat, A.M., 1974. Les microcodiums, milieux et modes de développement. *Docum. Lab. Géol. Fac. Sci. Lyons*. 62, 137–235.
- Cabrera, L., Calvet, F., 1996. Onshore Neogene record in NE Spain: Vallès-Penedès and El Camp half-grabens (NW Mediterranean). In: Friend, P.F., Dabrio, C.J. (Eds.), *Tertiary*

- basins of Spain: The stratigraphic record of crustal kinematics. Cambridge University Press.
- Caine, J.S., Evans, J.P., Forster, C.B., 1996. Fault zone architecture and permeability structure. *Geology* 24 (11), 1025–1028.
- Calvet, F. 1979. Evolució diagenètica en els sediments carbonatats del Pleistocè Mallorquí. PhD Thesis, p. 273.
- Calvet, F., Pomar, L., Esteban, M., 1975. Las rizocreciones del Pleistoceno de Mallorca. *Inst. Invest. Geol. Univ. de Barcelona* 30, 35–60.
- Calvet, F., Travé, A., Roca, E., Soler, A., Labaume, P., 1996. Fracturación y migración de fluidos durante la evolución tectónica neógena en el Sector Central de las Cadenas Costero Catalanas. *Geogaceta* 20, 1715–1718.
- Gaspar-Escribano, J.M., García-Castellanos, D., Roca, E., Cloetingh, S., 2004. Cenozoic vertical motions of the Catalan Coastal Ranges (NE Spain): the role of tectonics, isostasy, and surface transport. *Tectonics* 23, TC1004. doi:10.1029/2003TC001511.
- James, N.P., Choquette, P.W., 1990. Limestones – the meteoric diagenetic environment. In: McIlreath, I.A., Morrow, D.W. (Eds.), *Diagenesis Geosc. Canada Reprint Series*, 4, pp. 35–73.
- Kabanov, P., Anadón, P., Krumbein, W.E., 2008. Microcodium: an extensive review and a proposed non-rhizogenic biologically induced origin for its formation. *Sed. Geol.* 205, 79–99.
- Klappa, C.F., 1978. Biolithogenesis of Microcodium: elucidation. *Sedimentology* 25, 489–522.
- Košir, A., 2004. Microcodium revisited: root calcification products of terrestrial plants on carbonate-rich substrates. *J. Sed. Res.* 74 (6), 845–857.
- Labaume, P., Carrio-Schaffhauser, E., Gamond, J.F., Renard, F., 2004. Deformation mechanisms and fluid-driven mass transfers in the recent fault zones of the Corinth Rift (Greece). *Comptes Rendus Géoscience* 336 (4/5), 375–383.
- Lucas, G., Montenat, C., 1967. Observations sur les structures internes et de développement des Microcodium. *Bull. Soc. Géol. France* 7 (9), 909–918.
- Manning, D.A.C., 2008. Biological enhancement of soil carbonate precipitation: passive removal of atmospheric CO<sub>2</sub>. *Mineral. Mag.* 72 (2), 639–649.
- McQueen, K.G., Hill, S.M., Foster, K.A., 1999. The nature and distribution of regolith carbonate accumulations in southeastern Australia and their potential as a sampling medium in geochemical exploration. *J. of Geochem. Explor.* 67, 67–82.
- Parcerisa, D., 2002. Petrologia i Diagenèsi en sediments de l'Oligocè superior i del Miocè inferior i mitjà de la Depressió del Vallès i del Pla de Barcelona. Evolució de l'àrea font i dinàmica dels fluids. Universitat Autònoma de Barcelona. PhD Thesis, p. 288.
- Parcerisa, D., Gómez-Gras, D., Roca, E., Madurell, J., Agustí, J., 2007. The Upper Oligocene of Montgat (Catalan Coastal Ranges, Spain): new age constrains to the western Mediterranean Basin opening. *Geogaceta* 5 (1), 3–17.
- Rossi, C., Cañaveras, J.C., 1999. Pseudospherulitic fibrous calcite in paleo groundwater, unconformity-related diagenetic carbonates (Paleocene of the Áger Basin and Miocene of the Madrid Basin, Spain). *J. Sed. Res.* 69 (1), 224–238.
- Rowland, J.V., Sibson, R.H., 2004. Structural controls on hydrothermal flow in a segmented rift system, Taupo Volcanic Zone, New Zealand. *Geofluids* 4, 259–283.
- Sibson, R.H., 1977. Fault rocks and fault mechanisms. *Geol. Soc. Lond.* 133, 191–213.
- Travé, A., 1992. Sedimentologia, petrologia i geoquímica (elements traça i isòtops) dels estromatòlits de la conca eocena sudpirinenca. Universitat de Barcelona. PhD Thesis, p. 388.
- Tucker, M.E., Wright, V.P., 1990. Carbonate sedimentology. Blackwell Scientific Publications, London.
- Watts, N.L., 1980. Quaternary pedogenetic calcretes from the Kalahari (southern Africa): mineralogy, genesis and diagenesis. *Sedimentology* 27, 661–686.



## **Publication 2**

**Cantarero I**, Travé A, Alías G, Baqués V (2013) Polyphasic hydrothermal and meteoric fluid regimes during the growth of a segmented fault involving crystalline and carbonate rocks (Barcelona Plain, NE Spain). *Geofluids* (accepted)





**Polyphasic hydrothermal and meteoric fluid regimes during the growth of a segmented fault involving crystalline and carbonate rocks (Barcelona Plain, NE Spain)**

Journal:	<i>Geofluids</i>
Manuscript ID:	GFL-2012-041.R1
Manuscript Type:	Geofluids VII: Paris 2012
Date Submitted by the Author:	n/a
Complete List of Authors:	Cantarero, Irene; Facultat de Geologia (UB), Geoquímica, Petrologia i Prospecció Geològica Trave, Anna; Facultat de Geologia (UB), Geoquímica, Petrologia i Prospecció Geològica Alías, Gemma; Facultat de Geologia (UB), Geoquímica, Petrologia i Prospecció Geològica Baqués, Vinyet; Facultat de Geologia (UB), Geoquímica, Petrologia i Prospecció Geològica
Key words:	fracture-related cements, segmented fault, crystalline basement, carbonate rocks, hydrothermal fluids, Barcelona Plain



# **Polyphasic hydrothermal and meteoric fluid regimes during the growth of a segmented fault involving crystalline and carbonate rocks (Barcelona Plain, NE Spain)**

I. Cantarero\*, A. Travé, G. Alías, V. Baqués

Departament de Geoquímica, Petrologia i Prospecció Geològica, Facultat de Geologia, Universitat de Barcelona (UB), Martí i Franquès s/n, 08028, Spain (E-mail: i\_cantarero@ub.edu, atrave@ub.edu, galias@ub.edu, vbaques@ub.edu).

\* Corresponding author. E-mail address: i\_cantarero@ub.edu. Tel.: 0034934031165; FAX: 0034934021340

## **Abstract**

A polyphasic tectonic-fluid system of a fault that involves crystalline and carbonate rocks (Hospital fault, Barcelona Plain) has been inferred from regional to thin section scale observations combined with geochemical analyses. Cathodoluminescence, microprobe analyses and stable isotopy in fracture-related cements record the circulation of successive alternations of hydrothermal and low-temperature meteoric fluids linked with three main regional tectonic events. The first event corresponds to the Mesozoic extension, which had two rifting stages, and it is characterized by the independent tectonic activity of two fault segments, namely southern and northern Hospital fault segments. During the Late Permian-Middle Jurassic rifting, these segments controlled the thickness and distribution of the Triassic sediments. Also, dolomitization was produced in an early stage by Triassic seawater at shallow

## **Geofluids**

conditions. During increasing burial, formation of fractures and their dolomite-related cements took place. Fault activity during the Middle Jurassic-Late Cretaceous rifting was localized in the southern segment and it was characterized by hydrothermal brines, with temperatures over 180°C, which ascended through this fault segment precipitating quartz, chlorite and calcite. The second event corresponds to the Paleogene compression (Chattian), which produced exhumation, folding and erosion, favouring the percolation of low temperature meteoric fluids which produced the calcitization of the dolostones and of the dolomite cements. The third event is linked with the Neogene extension, where three stages have been identified. During the syn-rift stage, the southern segment of the Hospital fault grew by tip propagation. In the relay zone, hydrothermal brines with temperature around 140°C upflowed. During the late post-rift, the Hospital fault acted as a unique segment and deformation occurred at shallow conditions and under a low-temperature meteoric regime. Finally, and possibly during the Messinian compression, NW-SE strike-slip faults offset the Hospital fault to its current configuration.

**Keywords:** fracture-related cements, segmented fault, crystalline basement, hydrothermal fluids, Barcelona Plain

## **1. Introduction**

Fault zones play an important control in fluid flow because of their behaviour as conduits or barriers to fluids (Caine et al. 1996, Rowland & Sibson 2004). The behaviour of the fault zone is controlled by its architecture (Berg & Skar 2005) and the petrophysical properties of the fault rocks (porosity, permeability, cohesivity, etc.),

### **Geofluids**

which vary spatially and temporally along the fault. The petrophysical properties can change due to grain comminution and mineral neoformation, processes that are in turn controlled by the lithology, pressure-temperature conditions and physico-chemical characteristics of fluids. Minerals formed during circulation of fluids coeval to fracturing record important information about the evolution of the fault zone architecture, the deformation mechanisms and the types of fluids during fault history (O’Kane et al. 2007, Travé et al. 2009, Breesch et al. 2009). The reactivation of faults can produce changes in fault behaviour and the mobilization of fluids, consequently controlling fluid flow and preservation of structural traps, point of high interest due to their relation with economic geology and petroleum geology (Zhang et al. 2009). In addition, most of the works that study the fault-fluid evolution within the brittle regime, which are focused on one lithology, normally in carbonate rocks (Labaume et al. 2004, Micarelli et al. 2006, Bussolotto et al. 2007, Bastesen et al. 2009, Breesch et al. 2009, Andre et al. 2010, Billi 2010, Baqués et al. 2010, 2012, Rodríguez-Morillas et al. 2013) or siliciclastic rocks (Labaume & Moretti 2001, Travé & Calvet 2001, Boles et al. 2005, Davatzes & Aydin 2005, Eichhubl et al. 2009, Onasch et al. 2009, Travé et al. 2009), as these rocks constitute most of reservoirs. However, due to the high demand of energetic resources, unconventional reservoirs, such as crystalline basement reservoirs, have increased their interest and more studies about deformation and fluids in crystalline rocks need to be done. Therefore a multidisciplinary study based on multiscale structural analysis and petrological and geochemical data of fracture-related cements leads to decipher the origin and the pathways of fluids.

### **Geofluids**

The present study has been focused on unravel the successive fault-fluid systems on a segmented fault that grew and was reactivated by two extensional and one compressional event. This fault is located at the Barcelona Plain (Catalan Coastal Ranges) and juxtaposes Triassic carbonates and Miocene siliciclastic rocks against basement granodiorites. The presence of different lithologies forming the footwall and hanging-wall of the fault zone allows us to study the host rock influence on the mineralogical changes and precipitation of neoformed minerals within the fault zone and the effects of the fluids circulating through the faults, that is, it allows us to study the fault-fluid-rock interaction through time from the cover to the basement. The aims of this study are fourfold: 1) to characterize petrologically and geochemically the successive generations of fault rocks and cements along a segmented fault and its hanging-wall; 2) to determine the composition and origin of the fluids that circulated through the faults; 3) to establish the hydrogeological regimes and the fluid pathways as a function of the involved tectonic event; and, 4) to determine the factors that control fault zone heterogeneities.

## **2. Geological setting**

The Barcelona Plain and its boundary faults locate within the Catalan Coastal Ranges (CCR). These ranges form the western margin of the Valencia Trough (fig. 1), an extensional basin located between the Iberian Peninsula and the Balearic Promontory. The CCR are the result of the superposition of three main tectonic events. During the Mesozoic, two rift stages related with the opening of the western Tethys and of the North Atlantic took place (Salas & Casas 1993, Rossi et al. 2001). The first rift stage lasted from Late Permian to Middle Jurassic and the second one occurred during the

Late Jurassic-Late Cretaceous times. The normal faults generated during this period were later reactivated as thrust faults during the N-S compression caused by the collision of the Iberian and European plates (Late Cretaceous-early Oligocene) (Bartrina et al. 1992). This positive inversion had a limited left-lateral motion (Ashauer & Teichmüller 1935, Anadón et al. 1985, Roca 1996). In the studied area, the compressive structures correspond to the very late compressive stage (Chattian) (Parcerisa 2002). During the Neogene extension (late Oligocene-middle Miocene), faults were again reactivated as normal faults. This late extensional process, responsible of the opening of the Valencia Trough, is related to the southwestward propagation of the Western European rift system and the Burdigalian oceanic accretion associated with the counterclockwise rotation of the Corsica-Sardinia block from the European margin to its current position (Cherchi and Montadert 1982; Roca et al. 1999). This last event of deformation was the responsible of the actual morphology of the Catalan Coastal Ranges, which is characterized by a system of horsts and grabens limited by listric faults striking NE-SW and NNE-SSW with a detachment level at 12-16 km (fig. 1) (Gaspar-Escribano et al. 2004). This structure is also offset by later faults trending NW-SE to NNW-SSE. The tectonic evolution of the CCR during the Neogene extension is divided into a syn-rift stage (late Oligocene-late Burdigalian), an early post-rift stage (late Burdigalian-early Serravalian) and a late post-rift stage (Serravalian to Present). Within the post-rift, two small compressional stages have been recognised, one during the early post-rift (Langhian-Serravalian) and one during the late post-rift (Messinian) (Calvet et al. 1996; Gaspar-Escribano et al. 2004).

Abundant springs, some of them of hot water (up to 70°C), occur in the intersection between the main faults limiting the grabens and the last NW-SE faults (Fernández &

### **Geofluids**



Banda 1989). These hot springs, which are exploited as spa since the roman times, are preferably located in the igneous basement, which constitutes the footwall of the faults, i.e. Caldes de Montbui, La Garriga, Caldes d'Estrac (fig. 1) (Albert et al. 1979, Carmona et al. 2000). Fault-controlled barite-fluorite-sulphur veins along the Catalan Coastal Ranges (Canals & Cardellach 1997, Piqué et al. 2008) have been interpreted as the result of two hydrothermal events: a Mesozoic (at least Jurassic) and a Neogene (lower Miocene) event (Cardellach et al. 2002).

The studied area is located within the Barcelona Plain, a graben about 40 km long and 2-10 km wide situated in the central sector of the Catalan Coastal Ranges (fig. 1 and 2). Its filling mainly consists of Miocene continental-transitional siliciclastic deposits and Quaternary fluvio-deltaic deposits. Its northern boundary is limited by the Collserola-Montnegre Horst, which is mainly formed by Paleozoic rocks consisting of Cambro-Ordovician shales and phyllites, Silurian black shales and phyllites, Devonian carbonates, Carboniferous Culm facies and late Hercynian leucogranites, tonalites and granodiorites (Julivert & Durán 1990). In this horst, the Mesozoic cover has been almost completely eroded.

The present study concerns the NE-SW segmented fault that defines the northern boundary of the Barcelona Plain in its north-eastern sector, the Hospital fault. This fault juxtaposes Triassic rocks in the north and Miocene rocks in the south against the basement granodiorite and it is crosscut by an orthogonal fault system (fig. 2).

### **3. Methods and analytical techniques**

Fifty-two samples were collected from the outcrops and two samples of the unaltered granodiorite were obtained from boreholes. Thirty of these samples are from the fault

core between the late Hercynian granodiorite and the Triassic rocks, twenty samples are from faults affecting middle Triassic dolostones and two are from the fault core between the Triassic and Silurian rocks. Thirty-nine thin sections were studied using optical and cathodoluminescence microscopes. Some of the thin sections were stained with Alizarine Red-S and potassium ferricyanide to distinguish calcite and dolomite and their ferroan equivalents (Dickson, 1966). A Technosyn Cold Cathodoluminescence Model 8200 MkII operating at 16-19 kV and 350  $\mu$ A gun current was used. Some thin sections were also examined under ESEM Quanta 200 FEI, XTE 325/D8395 scanning electronic microscope.

X-ray diffraction of bulk rock and oriented aggregates have been performed with a Bragg-Brentano PANalytical X'Pert PRO MPD alpha 1 operating at 1.5406 Å, 45 kV and 40 mA.

After the petrographic study, carbon-coated thin sections were used for elemental analyses of carbonate cements with a CAMECA model SX-50 microprobe. It was operated using 15 nA of current intensity, 20 kV of acceleration voltage and a beam diameter of 10  $\mu$ m. The detection limits are 99 ppm for Na, 312 ppm for Ca, 436 ppm for Mg, 149 ppm for Fe, 107 ppm for Mn and 124 ppm for Sr. The precision of major elements is about 0.64% (at 2 $\sigma$  level).

Sixty-eight microsamples for carbon and oxygen stable isotopes were powdered with a microdrill. Collected samples were reacted with 100% phosphoric acid at 70° C for two minutes in an automated Kiel Carbonate Device attached to a Thermal Ionization Mass Spectrometer Thermo Electron (Finnigan) MAT-252. The results are expressed in  $\delta\text{‰}$  VPDB standard. Standard deviation is  $\pm 0.02\text{‰}$  for  $\delta^{13}\text{C}$  and  $\pm 0.05\text{‰}$  for  $\delta^{18}\text{O}$ . Cements

## **Geofluids**

C6 and D3 could not be sampled due to the micrometric thickness of fractures and their spatial relationship with other carbonatic cements.

#### **4. Lithology and petrography of the host rocks**

The granodiorite shows a phaneritic and granular texture. The grain size is mostly about 2-3 mm but there are feldspars around 5 mm. It is constituted by quartz, potassic feldspar, plagioclase and biotite (<5%). The potassic feldspar, identified as orthose, has perthites and is partially replaced by kaolinite. Some of them are poikilitic. The plagioclase shows polysynthetic twins and it is partially altered to sericite. Finally, the biotite has some interlayered epidote and shows a very incipient alteration to chlorite.

Silurian rocks consist on phyllites and clay-rich black shales. Phyllites are only present as clasts in fault-related breccias. The Silurian black shales are constituted by phyllosilicates, quartz, calcite, potassic feldspar, plagioclase, jarosite (oxidation of iron sulfides) and hematites. Specifically, the phyllosilicates are 65% illite, 10% chlorite and 25% illite-smectite.

Middle Triassic rocks are represented by Muschelkalk facies M1, M2 and M3. The Muschelkalk facies M2 is formed by lutites and layers of sandstones. Lutites are formed by quartz, calcite, potassic feldspar, plagioclase and clays (65% illite, 20% illite-smectite, 10% chlorite-smectite and 5% chlorite). The red sandstones are constituted by quartz, potassic feldspar, plagioclase, muscovite and biotite. Grains are 160 µm in size and are cemented by orange luminescent calcite.

Muschelkalk facies M1 and M3 are formed by dolostones which consist of 2 to 50 cm thick beds that form NE-SW oriented folds. Four different types of dolostones have been identified: host rocks HR1 and HR2 in the M1 and HR3 and HR4 in the M3. HR1

#### **Geofluids**

dolostone is constituted by clear anhedral crystals about 50  $\mu\text{m}$  thick and euhedral crystals with a cloudy nucleus and clear borders about 250  $\mu\text{m}$  thick. HR1 shows a brown-yellowish luminescence. HR2 consists of an orange luminescent dolmicrite. HR3 dolostone is constituted of anhedral crystals about 80  $\mu\text{m}$  and euhedral crystals about 180  $\mu\text{m}$  in size with a cloudy nucleus and dull red luminescence. Ghosts of coated grains indicate that the replaced rock was at least locally a grainstone and that dolomitization was non-destructive. Finally, HR4 is formed by anhedral crystals about 60  $\mu\text{m}$  in size with a orange dull luminescence. The dolostones have  $\delta^{18}\text{O}$  values between -4.6 and -2.7‰ vPDB and  $\delta^{13}\text{C}$  values between +0.7 and +2.8‰ vPDB. With regard to their elemental geochemistry, HR3 shows higher contents in Mn and Fe and lower contents in Sr than the other host rocks (table 1). HR4 have contents of Na and Sr below the analytical detection limit. The dolostones of M1 are partially replaced by a clear anhedral dolomite with dull red luminescence (replacive dolomite RD1).

Finally, the Miocene rocks are represented by matrix supported and heterometric conglomerates. Clasts range from cobble to granule and are mainly derived from the Paleozoic basement although some clasts of the Triassic rocks are identified. The most abundant lithologies are phyllites (40%) and quartzites (35%) followed by knotted hornfels (10%), quartz grains derived from quartzites and granodiorites (7%), porphyries (4%), granodiorite (1%), Muschelkalk (2%) and Buntsandstein (1%) clasts. Clasts are usually angular except phyllites and knotted hornfels which are rounded. The matrix is formed by red shales and silts. The sand-sized grains include angular quartz and subrounded orthose. The smaller matrix fraction includes quartz, potassium feldspar, illite, chlorite, kaolinite, mixed-layer of illite-chlorite, apatite, iron oxides and titanium oxides. Cretaceous clasts are absent.

### **Geofluids**

## 5. Fracture sets analysis

Nine generations of fractures have been identified in the studied area and have been arranged in chronological order according to their crosscutting relationships (fig. 3).

The first three generations have been attributed to the **first tectonic event**, which is characterized by extensional axes from ENE-WSW to WNW-ESE direction. Type 1A fractures have only developed in the Triassic dolostones of the hanging-wall of the Hospital fault and they are represented by NE-SW normal faults with dip about 49°SE and by NW-SE normal faults with a certain right-lateral component with dip from 60 to 90° to the SW and NE. Type 1B fractures are normal faults with NE-SW trending and dip between 24 and 67° to the SE. In the Hospital outcrop, slickenlines with 14/076 orientation indicate a certain left-lateral motion during normal faulting. Although the similar orientation of 1A and 1B faults, the study of their cements demonstrated their activity during different stages.

The **second tectonic event** shows NNE-SSW compressional axes. It is constituted by type 2 fractures which are reverse faults with NE-SW trend and dip towards the SE, which have a strong left-lateral component. This faulting episode is the responsible of the formation of the NE-SW oriented folds in the Muschelkalk units. Minor faults of this group affecting Triassic rocks of the horst reactivate previous 1A faults.

The **third tectonic event** has variable extensional axes from NNW-SSE to NE-SW and is represented by five generations of fractures. Type 3A fractures are the most abundant in the Barcelona Plain. They are from NE-SW to E-W striking normal faults with a steep dip, mostly, to the SE. The second generation, type 3B fractures, is made of joints with a WNW-ESE trend and elevated dip to the NE whereas type 3C fractures are NE-SW seams with low dip to the NW. The fourth generation, type 3D, is represented by a

### Geofluids

set of mainly oriented N-S normal faults dipping from 30 to 80° to the east and barely to the SW and NE-SW normal faults that are the reactivation of previous 3A and 2 faults. Type 3E fractures are open joints with NW-SE trend and dip about 60° to the SW that result from the opening of previous 1A faults. Finally, type 3F strike-slip faults formed and offset previous type 3A main normal faults. These faults however do not crop out in the Barcelona Plain but are deduced from regional mapping.

## **6. Fault zones: structure, microstructures and chemistry**

This section has been divided in two parts: the Hospital fault and the horst between the Hospital and the Badalona faults (or Hospital hanging-wall).

### **6.1. The Hospital fault**

The Hospital fault is a NE-SW fault zone with increasing dip towards the northeast from 29 to 63°SE. It shows in its northern ending a splay structure as a result of thrusting with a left lateral component and later N-S extension (fig. 2). This fault separates the late Hercynian granodiorite from the Triassic rocks. To describe the deformation along this main fault zone we have studied three outcrops settled at different segments of the fault. In the Hospital and Enric outcrops, the granodiorite is in tectonic contact with the M2 unit, whereas in the Sariol outcrop is in tectonic contact with the M3 unit.

#### **6.1.1 The Hospital outcrop**

The fault zone architecture in this segment of the Hospital fault is very complex due to the concentration of the three tectonic events in a reduced area (~20 m) (fig. 4A-B). The first tectonic event is represented by type 1B faults. One of these faults juxtaposes the

## **Geofluids**

Middle Triassic clays and sandstones against the late Hercynian granodiorite. This major normal fault has low dip (about 30°SE) and generates a core zone about 70 cm width (FC1) with well-defined and sharp boundaries. The core is formed by 60 cm of a cataclastic green material and by 10 cm of a discontinuous foliated red and black clay gouge (fig. 4C-D). Also compressive type 2 faults are present and develop two decimetric-scale duplexes in the hanging-wall that locates the Silurian phyllites on top of the Middle Triassic dolostones (fig. 4B). Each duplex is constituted by different breccias. Breccia FB2a is constituted by dolomitic clasts from the Triassic unit M3 whereas breccia FB2b contains clasts of the Silurian phyllites. Finally, a type 3D extensional fault, reactivation of a previous 3A fault, settles the Miocene in contact with the Silurian black shales. The Silurian acts as a detachment level and accommodates all the deformation. In the Miocene conglomerates minor type 3D normal faults are present. These minor faults do not develop fault cores in this outcrop.

The study is centred in the analysis of the fault core FC1. The cataclastic band resulting from granodiorite deformation shows that the type 1B fault was successively reactivated generating different fault rocks and cements.

During a first stage, took place the precipitation in geodes of euhedral quartz crystals, up to 1 mm in size, with concentric bands of fluid inclusions, the overgrowth of albites and the precipitation of orthose in mode I fractures up to 50 µm wide affecting the feldspars. Moreover, orthose was more altered to kaolinite and albite to sericite in the deformed granodiorite.

During a second stage, a dilatant random breccia was formed and cemented by five calcite cements C1 (fig. 5A-D). Cement C1a is constituted by twinned bright orange luminescent calcite filling vugs and mode I fractures (opening). Crystal size is 1-2 mm,

### **Geofluids**



$\delta^{18}\text{O}$  values range between -15.6 and -15.0‰ vPDB and  $\delta^{13}\text{C}$  values between -6.5 and -6.3‰ vPDB. Cement C1b, which fills fractures in cement C1a, is only visible under the cathodeluminescence microscope by its dark brown luminescence. It shows high values of Na and Fe, averaging 5302 and 2983 ppm, respectively. Cement C1c is constituted by twinned sparitic brownish-orange luminescent calcite. This cement has crystals up to 1 mm when cementing mode I fractures and mode II fractures (sliding), where it is syn-kynematic, and crystals about 100  $\mu\text{m}$  when cementing small patches of cataclasite inside the dilatant breccia. Cement C1d is formed by euhedric orange luminescent calcite crystals smaller than 50  $\mu\text{m}$  that fills mode I fractures. Finally, cement C1e is constituted by euhedric brownish-orange luminescent calcite, 125  $\mu\text{m}$  in size, that fills mode I fractures. The detailed elemental geochemistry of all these calcite cements is summarized in Table 1.

Later, the previously formed dilatant breccia was further deformed as a slightly foliated cataclasite constituted by reworked clasts of both the granodioritic host rock and the dilatant breccia. The foliation is oblique to the main fault plane and indicates the normal slip of the fault (fig. 4C2). It is constituted by calcite cement C1f, iron oxides and chlorites (fig. 5E). The cement C1f is constituted by twinned brownish-orange luminescent sparitic calcite about 100  $\mu\text{m}$ .  $\delta^{18}\text{O}$  and  $\delta^{13}\text{C}$  values are nearly constant about -16.3‰ vPDB and -6.0‰ vPDB, respectively. Unlike the previous cements, C1f calcite has Mn values below the detection limit and lower values of Sr, about 357 ppm (table 1). The iron oxides occur in the cataclasite matrix defining the foliation and also form envelops around the reworked clasts of the cataclasite (fig. 4C2). Chlorites are both detrital and neoformed as patches growing within the cataclastic matrix.

## Geofluids

The red and black clay gouge has an S-C fabric consistent with a normal slip (fig. 4D). It is made up of quartz, calcite, potassic feldspar, plagioclase, anhydrite and clays. Clays constitute between 45 and 55% of the fault rock of which 65% is illite, 5% chlorite, 20% illite-smectite and 10% chlorite-smectite. This clay composition is similar than in the lutites of the M2 unit, indicating that this gouge represents the deformation of the hanging-wall coeval to the generation of the green cataclastic band.

During the last stage, vug porosity within the dilatant breccia and mode I fractures of the Triassic sandstones of the hanging-wall were cemented by cement C2a. This cement is constituted by anhedral calcite crystals between 100 and 500  $\mu\text{m}$  in size with a zoned orange and brown luminescence (fig. 5B, F). It has Mn values up to 7168 ppm and Fe values up to 6250 ppm. The  $\delta^{18}\text{O}$  values of C2a range between -5.5 and -4.6‰ vPDB and the  $\delta^{13}\text{C}$  between -7.2 and -6.5‰ vPDB.

#### **6.1.2. The Enric outcrop**

The Hospital fault in this outcrop dips 55° towards the SE. At outcrop scale two fault rocks are recognised: a first generation of a 2 m thick dark green cohesive breccia with irregular boundaries and a later 20 cm thick greenish-yellow semicohesive gouge with sharp and well delimited boundaries (fig. 6A). Both fault rocks resulted from the brittle deformation of the granodiorite. Five sets of fractures were measured in the cohesive breccias (fig. 6B).

The dark green cohesive breccia was formed from several stages of deformation. Deformation began with the development of a random cataclastic breccia, which microfractures were cemented by epidotes (clinozoisites and epidotes s.s.) and chlorites (fig. 7A). Some of the clasts of this breccia are of mylonite, indicating a previous

### **Geofluids**

deformation stage within the ductile regime. Quartz and feldspar recrystallisation of the mylonite was mainly produced by bulging and some subgrain rotation. Affecting this breccia, multiepisodic pull-aparts were formed in type 1B faults of little slip. These pull-aparts are cemented by calcite C1 (fig. 7B). The cement is formed by anhedral to euhedral bright orange luminescent calcite crystals up to 30  $\mu\text{m}$  in size. Geochemically, this cement has higher Mg content than the cements C1 of the Hospital outcrop (table 1). It has a  $\delta^{18}\text{O}$  value of -15.1‰ vPDB and a  $\delta^{13}\text{C}$  value of -6.9‰ vPDB.

Later, the development of pseudotachylytes took place in type 3A normal faults (fig. 7C), which usually show bifurcations (fig. 6B). They form very thin fault veins and injection veins. Pseudotachylyte fault veins have a width up to 125  $\mu\text{m}$  and have sharp and straight walls. Under transmitted light, pseudotachylytes display yellow-brownish colours whereas under polarised light they show a dark aphanitic matrix that contain subrounded clasts of quartz and feldspar. The study under the optical microscope points to the devitrification of the matrix. The discontinuities generated by these fault rocks were later profit for crack-seal veins to develop (fig. 7C). These crack-seals have internal shear planes and produce the reorientation in localized zones of the previously formed cataclastic breccia. The result is the generation of a cataclasite with foliated fabric marked by planes of oxides, chlorites and epidotes. The crack-seals are cemented by the calcite cement C3a, which is a twinned anhedral to euhedral sparry calcite, from micrite to 200  $\mu\text{m}$  in size, with a bright orange luminescence (fig. 7C-D). It is characterized by  $\delta^{18}\text{O}$  values between -20.8‰ and -19.6‰ vPDB and  $\delta^{13}\text{C}$  values about -6.2‰ vPDB. The next stage generated the development of type 3B joints, which are cemented by calcite C3b. This calcite is formed by anhedral crystals up to 30  $\mu\text{m}$  in size which bright orange luminescence increases towards the borders (fig. 7D). This increase

in luminescence is also reflected in the increase in Mn content, up to 6445 ppm. Its  $\delta^{18}\text{O}$  value is -18.4‰ vPDB and its  $\delta^{13}\text{C}$  value is -6.1‰ vPDB. Finally, 3C seams of iron oxides were formed.

The greenish-yellow semicohesive gouge, generated in type 3A normal faults, is constituted by smectite, chlorite and illite and results from a completely comminution and alteration of the original granodiorite. The gouge is affected by mode I fractures filled by cement C4 (fig. 7E). Cement C4 consists of microsparite calcite crystals with bright orange luminescence that shows a  $\delta^{18}\text{O}$  value of -5.8‰ vPDB and a  $\delta^{13}\text{C}$  value of -7.7‰ vPDB. This cement also has Mg content up to 9265 ppm (2981 ppm in average). After all the mentioned deformation events a soil developed in the gouge, giving cohesivity to the fault rock. Two cements are recognised: cement C6 consists of micritic orange luminescent high-Mg calcite crystals that form nodules between 1 mm and 1 cm of diameter that include fragments of quartz and feldspar. Cement C7 is constituted by anhedral sparitic non-luminescent high-Mg calcite crystals up to 30  $\mu\text{m}$  in size that forms a centimetric carbonate level that contains the nodules of cement C6. Crystals show spherulitic and “corn-cob” arrangements (fig. 7E-F). This cement has  $\delta^{18}\text{O}$  values between -2.9 and -2.5‰ vPDB and  $\delta^{13}\text{C}$  values between -8.5 and -8.3‰ vPDB.

### **6.1.3. The Sariol outcrop**

The Hospital fault in this outcrop has an E-W striking and dips about 60°S. Fault zone thickness is about 1 m thick and both footwall and hanging-wall of the Hospital fault have been deformed, unlike the previous outcrops (fig. 8A-B). The Triassic dolostone constituting the hanging-wall next to the fault zone has been completely calcitized. It shows orange luminescence and has  $\delta^{18}\text{O}$  values between -9.5 and -9.3‰ vPDB and

## **Geofluids**

$\delta^{13}\text{C}$  values between -4.8 and -4.7‰ vPDB. The first fracture generation identified in this outcrop are type 2 reverse faults (fig. 8B). These faults generate a random breccia made of angular granodiorite fragments cemented by two generations of calcite, C2b and C2c (fig. 8C). Both generations are constituted by twinned calcite crystals up to 500  $\mu\text{m}$ , being C2b brighter orange luminescent than C2c (fig. 8D). C2b has higher contents of Mn and Fe, 3366 and 633 ppm on average, respectively than C2c, that has Mn values of 459 ppm in average and Fe contents below the detection limit. The high crosscutting relationship between both cements made impossible to pick them separately for isotopic analyses. The average values from both are of -5.8‰ vPDB for  $\delta^{18}\text{O}$  and -7.2‰ vPDB for  $\delta^{13}\text{C}$ . The second generation identified are type 3D normal faults, which produced cataclasites in the previous breccia and in the calcitized dolostone (fig. 8B). In the former, subangular clasts, from 10  $\mu\text{m}$  to 2 mm in size, are contained in a fine grained matrix. In this matrix, parallel planes to the fracture border are cemented by a non-luminescent calcite-to-dolomite cement C5 (fig. 8E). The cataclasite in the calcitized dolostone has a heterogeneous distribution of subrounded clasts from 200  $\mu\text{m}$  to 5 mm in size, cemented by cement C5 (fig. 8F). Fe values range from 576 to 8698 ppm.  $\delta^{18}\text{O}$  values range from -2.9 to -2.6‰ vPDB whereas the  $\delta^{13}\text{C}$  is about -7.6‰ vPDB. Finally, the Hospital fault was cemented by palisade cement PC1. This cement displays a laminar disposition parallel to the main fault and it is formed by submillimetric thick laminae (fig. 8F). The palisade is formed by bladed crystals of low magnesium calcite, high magnesium calcite and dolomite 200  $\mu\text{m}$  long and 10  $\mu\text{m}$  wide. The first laminae are constituted by non-luminescent dolomite and high-Mg calcite (PC1a) and the last laminae are orange luminescent and are constituted by low-Mg calcite (PC1b). Vug porosity is cemented by the first cement (PC1a) in the calcitized dolostone cataclasite

### **Geofluids**

and by the second cement (PC1b) in the granodiorite cataclasite. PC1b has higher Mn and Fe contents than PC1a (table 1). The palisade cement has  $\delta^{18}\text{O}$  values between -2.7 and -1.9‰ vPDB and  $\delta^{13}\text{C}$  values around -7.8‰ vPDB.

## **6.2. The Hospital fault hanging-wall**

The horst is formed by Miocene rocks in the south and mostly Triassic rocks in the north (fig. 2). As shown in figure 2, the boreholes reveal a major thickness of Miocene rocks in the southwest than in the northeast of the studied area and the lack of Triassic rocks in the southeast. In this domain we have focused the study on the diagenesis of the Triassic dolostones and the evolution of deformation and fracture-related cements affecting these host rocks.

Deformation of the Miocene conglomerates and interpretation of the diagenetic processes sealing the faults in these conglomerates have been already published (Cantarero et al. 2010). The Miocene conglomerates are affected by minor type 3D normal faults constituted by a poorly developed fault core (up to 7 cm width) without a damage zone (fig. 9A). Fault rocks are made of a red muddy material that has been obliterated by later diagenetic processes. The most important products are spherulites and palisades formed by orange bladed calcite. These crystals are non-luminescent although some of the spherulite nucleus are orange luminescent. Calcite ranges from low to high-Mg calcite. The  $\delta^{18}\text{O}$  ranges from -4.4 to -3.9‰ vPDB whereas the  $\delta^{13}\text{C}$  has highly negative values that range from -10.3 to -9.0‰ vPDB. Luminescent orange bladed calcite has the less negative values, around -9.0‰ vPDB. These products result from pedogenic processes similar to *Microcodium*. The precipitation of the calcite crystals was induced by evaporation from meteoric water together with biota activity

although a neomorphism process from high-Mg calcite to low-Mg calcite was also taken into account. The presence of these pedogenic products has an important effect in fault evolution because: 1) they date fault evolution during the Miocene extension; 2) the presence of microfractures affecting the pedogenic products indicates a shallow burial depth and meteoric diagenetic environment during fault evolution; and, 3) they give the cohesiveness to the fault rock causing the sealing of the fault and its behavior as a barrier to fluids.

Within the Triassic rocks, different generations of fractures corresponding to three tectonic events have been identified. During the first tectonic event, type 1A faults generated cataclasites cemented by bright orange luminescent dolmicrite crystals D1 (fig. 9B-C, 10A-B). D1 has  $\delta^{18}\text{O}$  values between -5.9 and -5.4‰ vPDB and  $\delta^{13}\text{C}$  values between +2.3 and +2.4‰ vPDB. Later frictional processes produced ultracataclasites cemented by a red luminescent dolmicrite D2 with  $\delta^{18}\text{O}$  values between -7.2 and -6.8‰ vPDB and  $\delta^{13}\text{C}$  values between +2.5 and +2.6‰ vPDB (fig. 10B). Dolomite D2 has different Fe content depending on the host rock. When precipitates in HR2 (D2a) it has Fe contents up to 870 ppm and an average of 440 ppm whereas when precipitates in HR3 (D2b) it has contents up to 7803 ppm and an average of 2813 ppm. Finally, dolomite cement D3 precipitated within micrometric type 1A fractures. D3 is formed by anhedral crystals of dolomite, about 35  $\mu\text{m}$  in size, which shows a zoned orange and red luminescence and grows in optic continuity with the host rock (fig. 10B-C).

Minor type 2 reverse faults, which are the reactivation of the previous type 1A faults, have been also identified (fig. 9D). Four generations of calcitized dolomite (from CD1 to CD4) have been associated with these faults. CD1 to CD4 cements are constituted by anhedral to subhedral crystals between 170 and 250  $\mu\text{m}$  in size, with some idiomorphic

### **Geofluids**



rombohedral crystals pseudomorphs of the previous dolomite. These cements differ from each other in their luminescence behaviour (fig. 10C-E). CD1 shows an orange bright zoned luminescence, CD2 shows a concentric zonation in orange and black, CD3 is non luminescent with a bright orange luminescent thin line and CD4 is non luminescent. These cements have Na, Mn and Fe contents below the detection limit and high contents of Sr, from 700 to 2200 ppm. It was difficult to sample these cements separately for isotopic analysis, and only cement CD3 could be sampled alone. However, the plot of all the values in a well-constrained area validates the use of all the data. The  $\delta^{18}\text{O}$  values range between -5.9 and -4.9‰ vPDB, with an average about -5.3‰ vPDB whereas the  $\delta^{13}\text{C}$  values range between -7.4 and -5.4‰ vPDB, with an average about -6.3‰ vPDB.

Calcitization of the host dolostone has been locally observed in small patches. Under cathodoluminescence the calcitized dolostone shows a bright orange thin line similar to cement CD3 (fig. 10F). The  $\delta^{18}\text{O}$  and  $\delta^{13}\text{C}$  values are between the host rock and the calcite cements signatures, -4.1‰ vPDB and -3.2‰ vPDB respectively.

During the third tectonic event, type 3A and 3D normal faults and type 3E open joints were formed (fig. 9E-F). Type 3A normal faults have a much localized deformation and generate slickensides.

After tectonic deformation, a karstic system was installed producing collapsed breccias and precipitating speleothems on the fault planes of fractures 3A and 3E (fig. 9G-H). Speleothems are made of calcite, aragonite, high-Mg calcite and dolomite and are formed by bladed and fibrous palisades, rafts or cavern pearls. These speleothems have high Sr contents, especially the ones formed by high-Mg calcite and aragonite, which can reach 7506 ppm in average and up to 13800 ppm (table 1). HMC speleothems with

### **Geofluids**

bladed morphology have  $\delta^{18}\text{O}$  values between -5.3 and -4.7‰ vPDB and  $\delta^{13}\text{C}$  values between -9.8 and -8.5‰ vPDB whereas the HMC rafts have more enriched values, between -4.6 and -3.3‰ vPDB of  $\delta^{18}\text{O}$  and between -9.0 and -8.2‰ vPDB of  $\delta^{13}\text{C}$ . The dolomite speleothems have the most  $\delta^{18}\text{O}$  enriched values, about -2.6‰ vPDB, and  $\delta^{13}\text{C}$  values about -9.3‰ vPDB. Finally, the aragonite speleothems show  $\delta^{18}\text{O}$  values between -4.6 and -4.2‰ vPDB and  $\delta^{13}\text{C}$  values between -9.8 and -9.2‰ vPDB.

## 7. Discussion

### 7.1. Evolution of fluids and relationships with tectonic events

The crosscutting relationships of fractures and the description of their fault rocks and cements presented in this paper, together with the knowledge of the sedimentology (Ramon & Calvet 1987, Calvet et al. 1990), diagenesis (Parcerisa 2002), petrology and geochemistry of veins (Cardellach et al. 2002, Solé et al. 2002, Baqués et al. 2012) and structural works (Bartrina et al. 1992, Roca et al. 1999) of the Vallès-Penedès basin has allowed reconstructing the timing and characteristics of the paleofluids linked to fracturing in the studied area.

**Mesozoic extension.** Deposition of the Muschelkalk facies occurred in carbonate ramps during the Anisian (M1) and Ladinian (M3) (Calvet et al. 1990), synchronously to the first Mesozoic rifting event that lasted from Late Permian to Middle Jurassic (Salas & Casas 1993, Salas et al. 2001). Previous studies interpreted the dolomitization of M1 facies penecontemporaneous to sedimentation (Virgili 1957). On the other hand, Ramon & Calvet (1987) suggested that the upper dolomititic units were of primary origin but the lower ones were the result of a *mixed water* model of dolomitization. With regard to M3 facies, Tucker & Marshall (2004) proposed an early dolomitization from seawater and a

## Geofluids

later recrystallization as the responsible of the  $\delta^{18}\text{O}$ -shift towards more depleted values. The  $\delta^{18}\text{O}$  and  $\delta^{13}\text{C}$  values of the M1 and M3 dolostones cropping out in the studied area fall within the box of the Anisian-Ladinian seawater (Veizer et al. 1999) (fig. 11). Moreover, HR1 and HR3 show non-destructive fabrics indicating that dolomitization occurred during an early event (Tucker & Marshall 2004). Both points suggest that dolomitization was produced by marine Triassic waters almost coevally to sedimentation. However, M1 facies suffered two dolomitization processes as denoted by the presence of the replacive dolomite RD1, which is probably related with the dolomitization of M3 facies.

Also, the first dolomite cement D1 associated with fractures type 1A fall within the seawater values, indicating the onset of the Triassic rifting under marine conditions (fig. 11). Dolomite cement D2, and probably also D3, associated with fractures type 1A, show more  $\delta^{18}\text{O}$ -depleted values but the same  $\delta^{13}\text{C}$  values than the host rocks and cement D1. Moreover, the elemental geochemistry of dolomite cement D2 is controlled by the host-rock in which is precipitating, suggesting a high fluid-rock interaction. These facts point to the crystallization of dolomite cements from the marine water during increasing burial, produced by the rifting, in a closed hydrological regime.

The cements attributed strictly to the Hospital fault during the Mesozoic are quartz and later calcites C1 and chlorites in type 1B faults. This association of quartz and later calcite has been also described in the Montnegre Horst associated with the second Mesozoic rifting event (Late Jurassic-Late Cretaceous) (Cardellach et al. 2002). Calcites C1 show  $\delta^{18}\text{O}$ -depleted values (fig. 11) that combined with fluid inclusion data in quartz and calcites (Cardellach et al. 2002) points to hydrothermal fluids (180-230°C). The solubility/precipitation of vein minerals is dependent on fluid temperature, pressure and

### **Geofluids**

composition (Parry 1998). Taking into account that these rocks have not been subjected to important changes of pressure (Juez-Larré 2003), temperature and composition are the most important factors in our context. The equations of Clayton et al. (1972) and O'Neil et al. (1969) were applied in quartz and calcite, respectively, to establish the parental fluid of the hydrothermal brine. The first equation gives values of  $\delta^{18}\text{O}_{\text{water}}$  between -1.2 and +3.2‰ SMOW indicating that the brine had a marine origin, as it was already postulated by Cardellach et al. (2002). However the equation of O'Neil et al. (1969) indicates that calcite C1 precipitated from water with  $\delta^{18}\text{O}$  values between +7 and +10‰ SMOW. Most granitic rocks have  $\delta^{18}\text{O}$  values between +7 and +13‰ SMOW and  $\delta\text{D}$  values between -85 and -50‰ SMOW (Taylor 1977). Isotopic studies of the Late Hercynian intrusive rocks of the Montnegre Horst (Catalan Coastal Ranges) show  $\delta^{18}\text{O}$  values up to +6.1‰ SMOW and  $\delta\text{D}$  values up to -35‰ SMOW suggesting the hydrothermal alteration of the rock by a  $\delta^{18}\text{O}$ -depleted fluid with a low water-rock ratio (Solé et al. 2002). The  $\delta^{18}\text{O}$ -depleted fluid could have got different origins as its signal has been completely buffered by the granitic host rock.

**Paleogene compression.** Type 2 reverse faults and their related cements C2a to C2c and CD1 to CD4 are attributed to this period. These cements show  $\delta^{18}\text{O}$  and  $\delta^{13}\text{C}$  values ranging from -5.9 to -4.6‰ VPDB and -7.4 to -5.4‰ VPDB, respectively, coinciding with the values of the calcites defined by Parcerisa (2002) affecting the Oligocene rocks of the horst (fig. 11), which were attributed to the last compressional stage that occurred during the Chattian. The isotopic signal indicates their meteoric origin. The  $\delta^{18}\text{O}$  and  $\delta^{13}\text{C}$  values of the calcitized dolostone, from -9.5 to -4.1‰ VPDB and from -4.8 to -3.2‰ VPDB, respectively, fall between those of the Triassic dolostones ( $\delta^{18}\text{O}$  between -4.6 and -2.7 ‰ VPDB and  $\delta^{13}\text{C}$  between +0.7 and +2.8‰ VPDB) and those of the

### Geofluids

cements attributed to this period. In conclusion, the Paleogene compression is characterized by the opening of the hydrological system, which allows the percolation of meteoric fluids responsible of the calcite cements and the calcitization of the dolomite, which is favoured by the uplift of the horst. This conclusion is in agreement with the results of the work of Baqués et al. (2012) about the southwestern end of the Penedès fault affecting Cretaceous rocks.

**Neogene extension.** Type 3 fractures have been associated with the Neogene extension because of the implied host rocks, their extensional character and the crosscutting relationships with previous fractures. Type 3A normal faults and 3B joints have been related to the syn-rift stage produced during the Aquitanian?- late Burdigalian. The development of pseudotachylytes in type 3A faults indicates the seismic activity of some fault segments at the onset of the Neogene extension at about 2.3 km depth (maximum depth conditions according to Juez-Larré (2003)). Later calcites associated with these fractures (C3a and C3b, respectively) show  $\delta^{18}\text{O}$ -depleted values (fig. 11) similar to the ones reported by Cardellach et al. (2002) and Travé & Calvet (2001), both attributing these values to the Neogene syn-rift. Temperatures of these calcites obtained from fluid inclusion data by Cardellach et al. (2002) range between 130 and 150°C. Taking into account these temperatures, a surface paleotemperature of 20°C and the depth conditions during the syn-rift, the calculated geothermal gradient ranges between 47-56°C/km, higher than the estimated geothermal gradient during the Neogene (30°C/km according to Juez-Larré (2003)), indicating the hydrothermal character of the fluids. With regard to their origin, applying the equation of O'Neil et al. (1969) results of  $\delta^{18}\text{O}$  of the waters between -0.9 and +1.5‰ SMOW are obtained what would imply a seawater source. Although sedimentation from Chattian to late Miocene has been

### Geofluids

dominated by alluvial fans, during the late Burdigalian shore environments existed in the area (Parcerisa 2002; Riba & Colombo 2009 and references therein). Thus, waters responsible of the precipitation of calcites C3a and C3b during the syn-rift were topographically-driven meteoric waters, warmed at depth and buffered by the host granodiorites, and mixed with marine waters during their upflow. Moreover, these waters were partially yielding to such a positive values. This significant water-rock interaction is also recorded by the low  $\delta^{13}\text{C}$  values of these calcites, which are probably due to the influence of organic matter. The most probable source for the low  $\delta^{13}\text{C}$  is the Silurian black shales that crop out in the area, with TOC content between 3 and 8.6%. The same phenomenon is recorded in the Mesozoic calcites.

Type 3C seams have been related to a small compression event that took place during the early post-rift (late Langhian to Serravalian) by comparison with similar type and orientation of fractures in the neighbour Penedès graben (Baqués et al. 2012).

Finally, type 3D normal faults, type 3E open joints and later speleothem and soil development formed during the late post-rift (Serravalian to recent). Their related low-Mg calcite, high-Mg calcite, dolomite and aragonite cements are characterized by an important increase of the Mg content (from calcite to dolomite) and they are significantly more enriched in the  $\delta^{18}\text{O}$  content and depleted in the  $\delta^{13}\text{C}$  content than the previous cements (fig. 11). Therefore, these geochemical characteristics indicate again the opening of the system and the percolation of meteoric waters with a strong influence of soil-derived  $\text{CO}_2$ . In consequence, during this last stage of the Neogene extension, fault activity occurred under subaerial conditions. Also the palisade cement PC1 with morphology and mineralogy indicating their formation in the vadose zone, with fluctuating water conditions, supports this hypothesis. With regard to the  $\delta^{18}\text{O}$  values,

### **Geofluids**

they are slightly enriched with respect to the common meteoric waters. Microcodium formed in minor faults affecting the Miocene conglomerates occurred during the beginning of the late post-rift in a temperate climate, explaining the enriched  $\delta^{18}\text{O}$  values by an evaporation effect (Cantarero et al. 2010). Calcite cement C5 and palisade cement PC1, probably related to the sigmoidal microfractures affecting the Microcodium, formed in the same context. On the opposite, speleothems affecting the Triassic dolostones and the soil developed within the Hospital fault in the Enric outcrop formed later, after the cessation of fault activity. Similar isotopic compositions to these features have also been described in Pleistocene speleothems in the south of the Iberian Peninsula and in the Mallorca Island (Jiménez de Cisneros et al. 2003, Vesica et al. 2000) and Tertiary speleothems developed in the Rmales Platform (Basque-Cantabrian Basin) (Dewit et al. 2012), suggesting a widespread event in the Iberian Peninsula from the Tortonian to recent. These values have been interpreted as originated from meteoric waters in a colder period than present (Jiménez de Cisneros et al. 2003, Vesica et al. 2000).

## **7.2. The Hospital fault growth and fluid flow paths**

Fault rocks show differences on neoformed minerals between the outcrops studied in the Hospital fault. These mineralogical differences along the fault mark preferential paths for fluids in certain periods of time, probably related to the independent tectonic activity of fault segments or different fluid origin through time related to intermittent pulses of fluids.

The independent origin and tectonic activity of the fault segments is supported by the differences in strike and dip between the fault segments but also by the thickness of the

## **Geofluids**



Triassic rocks and distribution of the cements. There is a strong difference in the thickness of the Triassic rocks along the horst. In the south, they are almost absent whereas in the north they have a thickness up to 200 m (fig. 12A). In the Catalan Coastal Ranges, the changes in thickness within the Triassic rocks have been related to the influence of NE-SW and NW-SE normal faults (Calvet et al. 1990). So probably, in the studied sector of the Barcelona Plain, during the Triassic extension, the Hospital fault was formed by two fault segments that controlled the sedimentation. The southern segment, where the Hospital outcrop is settled, is a low-angle normal fault ( $<30^{\circ}\text{SE}$ ) whereas the northern segment (Sariol outcrop location) has a dip around  $55^{\circ}\text{SE}$ . This difference in dip control the vertical throw of the fault and could lead to a thicker accommodation space in the northern segment. The southern segment has low dip probably because: 1) it is the deep section of a listric Mesozoic fault, or 2) it is the rework as a normal fault of the Permian unconformity between the granodiorite and the Triassic rocks that crops out along the CCR.

Cements associated with the Cretaceous rifting are only identified in the Hospital and Enric outcrops (southern segment), indicating a localized migration of hot fluids ascending through the fault during its displacement (fig. 12B). The lack of these cements in the north could be due to the inactivity of this segment or the erosion of the cements associated with this period. After these rifting events, the Paleogene compression, inverted the previous normal faults and produced the exhumation and folding of the Triassic units. In the southern segment the erosion of the Triassic rocks was almost complete as it is shown by the boreholes. The uplift of the Triassic rocks in the north favoured the percolation of meteoric fluids and the calcitization of the dolostones and dolomite cements (fig.12C).

### **Geofluids**

The thickness of the Miocene rocks decreases towards the northeast (fig. 2) due to the differential displacement of the fault segment, indicating the presence of the fault tip in the area of the Enric outcrop. The fault rocks and cements attributed to the Neogene syn-rift (PST and calcite C3a and C3b) have only been identified in the Enric outcrop. This fact has been interpreted as the result of fault growth by tip propagation of the southern segment (fig. 12D and 13). Tip propagation produces the migration of the process zone to the north, which is formed by arrays of fractures constituted by fracture sets parallel to the southern segment and to the new fault trace that is forming between the two segments (fig. 13). Each slip event of the main fault involves the propagation and linkage of the previous arrays generating 3A microfaults. These linking structures have been demonstrated to develop friction melts (Swanson 1992), what would explain the formation of pseudotachylytes in type 3A faults in this point. Studies in seismically active fault systems have also shown the spatial relationship between seismicity and linking structures between main faults (Tavarnelli & Pasqui 2000). Following crack-seals cemented by calcite C3a could be generated during the pre-seismic stage of a new earthquake (Sibson 1986). Deformation under an extensional stress regime generates structures in the process zone that enhance dilation and therefore permeability, generating zones of localized hydrothermal upflow (Rowland & Sibson 2004). Moreover, outflows of water following earthquakes are not an infrequent phenomenon (seismic pumping (Sibson et al. 1975)), which enter and cement accessible extension fractures such as 3B joints.

During the late post-rift, both segments had some displacement (fig. 12E). This displacement was produced at shallow conditions in the presence of low-temperature

### **Geofluids**

meteoric fluids. Finally, NW-SE strike-slip faults segmented again the fault generating the current disposition probably during the Messinian compression (fig. 12F).

Large-scale horizontal fluid flow is prevented by the marked structural heterogeneities produced by the variations of fault zone architecture along strike.

### **7.3. Origin of the hydrothermalism**

The onshore of the Catalan Coastal Ranges is characterized by the presence of hot water springs, up to 70°C, mainly along the main bounding faults. And, although Miocene crustal thinning and Miocene and Quaternary volcanism have been reported in the area, this region of the Iberian Peninsula cannot be defined as a high-temperature geothermal province (Fernández & Banda 1989). All the studies support the origin of these springs as meteoric waters infiltrated through fractured elevated areas (horsts) that have been warmed at greater depths by a normal geothermal gradient (Fernández & Banda 1989; Carmona et al. 2000). This mechanism of fluid flow has been also postulated at the onset of the Neogene in the Penedès half-graben (Bitzer et al. 2001), where meteoric waters would have been topographically driven, through the fault zones, thanks to the elevation of the shoulders and the subsidence of the basin during the extensional event. In the case of the Barcelona Plain, meteoric waters were mixed with seawater due to its position at the shoreline. In later stages due to erosion and the consequent loss of topographic gradient this mechanism stops, explaining the lack of hot waters during the post-rift.

Crustal thinning and geothermal gradients during the Mesozoic and the Neogene extension were quite similar and therefore indicating crustal thinning was neither the reason for Mesozoic hydrothermalism (Roca 1996; Juez-Larré 2003). Mesozoic

## **Geofluids**

volcanism has been identified related to the first rifting in the southern Catalan Coastal Ranges (150 km to the south of the Barcelona Plain) and in the Iberian Chain (Ortí & Vaquer 1980; Mitjavila & Martí 1986). This volcanism was produced by an extended volcanic complex in this area (Ortí & Vaquer 1980). Also in the Iberian Chain, Albian-Coniacian volcanism, metamorphism and Hg-Sb deposits have been related to the emplacement of a hot spot in the offshore opposite to San Sebastian (northern Spain) which would produce the emplacement of a basic pluton below the Iberian Chain and the extrusion of alkali basalts in the Pyrenees (Aller & Zeyen 1996; Salas et al. 2005). However, in the central Catalan Coastal Ranges, where this work is performed, there are no evidences of such magmatism. Moreover, fission-track data in this area perfectly link with structural and sedimentological observations and only in specific points, generally next to fault zones, fission-track data are reset (Juez-Larré 2003). The second Mesozoic rifting mostly took place under marine conditions; however, prolonged periods of emersion occurred during Berriasian-Barremian times (Ebro Massif), probably controlled by normal faulting. This emersion is shown by the presence of karstification and bauxite formation in Kimmeridgian rocks outcropping close to the Barcelona Plain (Combes 1969, Molina & Salas 1993, Salas et al. 2004). As discussed in section 7.1, fluids responsible of calcite C1 precipitation during the second Mesozoic rifting were brines highly interacted with the host rock that could have got several origins. Taking into account the geomorphological configuration during this period, the most plausible mechanism for such hydrothermal fluids was the infiltration of meteoric waters through the emerged areas (topography driven) that have been warmed at depth, and that during their upflow through the main fault mixed with marine waters expelled from the

### **Geofluids**

sediments by compaction. This mixing between fluids could have been the responsible for the oscillating cathodoluminescence behavior of cements C1.

## **8. Conclusions**

The Hospital fault and its hanging-wall in the northern sector of the Barcelona Plain recorded three main tectonic events characterized by cements resulting from successive circulation of hydrothermal and low-temperature meteoric fluids. Hydrothermal fluids are characteristic of extensional events whereas low-temperature meteoric fluids are found in both extensional and compressional events. A topographically-driven fluid mechanism, favoured by the shoulder uplift produced during normal faulting, was the responsible for the hydrothermal fluids.

During the Late Permian-Middle Jurassic rifting stage, the Hospital fault controlled the thickness and distribution of the Triassic sediments, having their depocentre to the north. Their early dolomitization produced by Triassic seawater took place at shallow conditions. Dolomite cements in type 1A fractures were produced by the Triassic seawater during increasing burial in a relatively closed hydrological regime. Fault activity during the second Mesozoic rifting stage (Late Jurassic-Late Cretaceous) was localized in the southern segment and it is represented by type 1B faults. This stage is characterized by hydrothermal brines of meteoric origin, with temperatures over 180°C, which ascended through the southern fault segment and mixed with marine water, precipitating quartz, chlorite and calcite C1.

The Paleogene compression in this area was late (Chattian) and it is marked by type 2 fractures. The compression produced exhumation, folding and erosion of the Cretaceous and almost all the Triassic rocks in the south of the studied area. The uplift favoured the

percolation of low temperature meteoric fluids which produced the calcitization of the dolostones and of the dolomite cements.

During the Aquitanian-late Burdigalian syn-rift stage, the southern segment of the Hospital fault grew by propagation of its northern tip. Fault growth generated minor type 3A and 3B fractures in the relay zone which are characterized by the formation of pseudotachylytes and the later precipitation of calcite C3. This calcite is the result of the localized upflow of hydrothermal brines with temperature about 140°C, which are the result of warmed meteoric waters at depth mixed with marine waters during their upflow. Thus, the increase in dilatancy produced in the process zone together with a seismic pumping effect control the upflow during fault growth. Type 3C seams have been related to a small compressional stage within the early post-rift. During the late post-rift, the Hospital fault acted as a unique segment. Type 3D and 3E fractures were formed at shallow conditions and under a low-temperature meteoric regime. Later, possibly during the Messinian, the NW-SE strike-slip faults were formed and offset the Hospital fault to its current configuration.

In conclusion, the tectonic regime, the fault zone architecture and the seismic activity controlled the fluid regime and the fluid flow pathways in the Barcelona Plain from Mesozoic to recent.

### **Acknowledgements**

We are grateful with Jordi Illa for sample preparations and with the Thin Section Service of the Universitat de Barcelona. The stable isotopy, the electron microprobe and the SEM analyses were carried out at “Serveis Científic-Tècnics” of the Universitat de Barcelona. We also thank Jordi Jubany from GISA, Estibalitz Allende from Payma and

Geotec-262 for the information and core samples provided from the boreholes of the several ongoing civil engineering works in Barcelona. This research was performed within the framework of DGICYT Spanish Project CGL2010-18260, *Grup Consolidat de Recerca "Geologia Sedimentària"* (2009SGR-1451) and the 2010FI\_B2 00179 supported by the Comissionat per a Universitats i Recerca del Departament d'Innovació, Universitats i Empresa de la Generalitat de Catalunya i el Fons Social Europeu. The constructive comments of two anonymous referees helped to improve the quality of the manuscript.

## References

- Albert JF, Corominas J, París C (1979) El estudio hidrogeológico de los manantiales y su aplicación geológica: caso de las aguas termales, carbónicas y sulfhídricas de Cataluña. *Acta Geològica Hispànica. Homenatge a Lluís Solé i Sabarís*, **14**, 391-394.
- Aller J & Zeyen HJ (1996) A 2.5-D interpretation of the Basque country magnetic anomaly (northern Spain): geodynamical implications. *Geologische Rundschau*, **85**, 303-309.
- Anadón P, Cabrera L, Guimerà J, Santanach P (1985) Paleogene strike-slip deformation and sedimentation along the southeastern margin of the Ebro Basin. In: *Strike-slip Deformation, Basin Formation Sedimentation* (eds. K.T. Biddle & N. Christie-Blick), Special Publication of the Society of Economic Paleontologists and Mineralogists, **37**, 303-318.
- Andre G, Hibsich C, Fourcade S, Cathelineau M, Buschaert S (2010) Chronology of fracture sealing under a meteoric fluid environment: microtectonic and isotopic



evidence of major Cainozoic events in the eastern Paris basin (France). *Tectonophysics*, **490**, 214-228.

Ashauer H & Teichmüller R (1935) Die variszische und alpidische Gebirgsbildung Kataloniens. Abhandlungen Gesellschaft Wissenschaften Göttingen, Math Phys. K1, 3F, 16.

Baqués V, Travé A, Benedicto A, Labaume P, Cantarero I (2010) Relationships between carbonate fault rocks and fluid flow regime during propagation of the Neogene extensional faults of the Penedès basin (Catalan Coastal Ranges, NE Spain). *Journal of Geochemical Exploration*, **106**, 24-33.

Baqués V, Travé A, Roca E, Marín M, Cantarero I (2012) Geofluid behaviour in successive extensional and compressional events: a case study from the southwestern end of the Vallès-Penedès Fault (Catalan Coastal Ranges, NE Spain). *Petroleum Geoscience*, **18**, 17-31.

Bartrina MT, Cabrera L, Jurado MJ, Guimerà J, Roca E (1992) Evolution of the central Catalan margin of the Valencia trough (western Mediterranean). *Tectonophysics*, **203**, 219-247.

Bastesen E, Braathen A, Nøttveit H, Gabrielsen RH, Skar T (2009) Extensional fault cores in micritic carbonate-case studies of the Gulf of Corinth, Greece. *Journal of Structural Geology*, **31**, 403-420.

Berg SS & Skar T (2005) Controls on damage zone asymmetry of a normal fault zone: outcrop analyses of a segment of the Moab fault, SE Utah. *Journal of Structural Geology*, **27**, 1803-1822.

Billi A (2010) Microtectonics of low-P low-T carbonate fault rocks. *Journal of Structural Geology*, **32**, 1392-1402.

## Geofluids

- Bitzer K, Travé A, Carmona JM (2001) Fluid flow processes at basin scale. *Acta Geologica Hispanica*, **36** (1-2), 1-20.
- Boles JR, Eichhubl P, Garven G, Chen J (2005) Evolution of a hydrocarbon migration pathway along basin-bounding faults: evidence from fault cement. *AAPG Bulletin*, **88** (7), 947-970.
- Breesch L, Swennen R, Vincent B (2009) Fluid flow reconstruction in hanging and footwall carbonates: Compartmentalisation by Cenozoic reverse faulting in the Northern Oman Mountains (UAE). *Marine and Petroleum Geology*, **26**, 113-128.
- Bussolotto M, Benedicto A, Invernizzi C, Micarelli L, Plagnes V, Deiana G (2007) Deformation features within an active normal fault zone in carbonate rocks: the Gubbio fault (Central Apennines, Italy). *Journal of Structural Geology*, **29**, 2017-2037.
- Caine JS, Evans JP, Forster CB (1996) Fault zone architecture and permeability structure. *Geology*, **24** (11), 1025-1028.
- Calvet F, Tucker ME, Henton JM (1990) Middle Triassic carbonate ramp systems in the Catalan Basin, northeast Spain: facies, systems tracts, sequences and controls. *Special Publications International Association of Sedimentologists*, **9**, 79-108.
- Calvet F, Travé A, Roca E, Soler A, Labaume P (1996) Fracturación y migración de fluidos durante la evolución tectónica neógena en el Sector Central de las Cadenas Costero Catalanas. *Geogaceta*, **20** (7), 1715-1718.
- Canals À & Cardellach E (1997) Ore lead and sulphur isotope pattern from the low-temperature veins of the Catalanian Coastal Ranges (NE Spain). *Mineralium Deposita*, **32**, 243-249.
- Cantarero I, Travé A, Alías G, Baqués V (2010) Pedogenic products sealing normal faults (Barcelona Plain, NE Spain). *Journal of Geochemical Exploration*, **106**, 44-52.

- Cardellach E, Canals À, Grandia F (2002) Recurrent hydrothermal activity induced by successive extensional episodes: the case of the Berta F-(Pb-Zn) vein system (NE Spain). *Ore Geology Reviews*, **22**, 133-141.
- Carmona JM, Bitzer K, López E, Bouazza M (2000) Isotopic composition and origin of geothermal waters at Caldetes (Maresme-Barcelona). *Journal of Geochemical Exploration*, **69-70**, 441-447.
- Cherchi A, Montadert L (1982) Oligo-Miocene rift of Sardinia and the early history of the Western Mediterranean Basin. *Nature*, **298**, 736-739.
- Clayton RN, O'Neil JR, Mayeda TK (1972) Oxygen isotope exchange between quartz and water. *Journal of Geophysical Research*, **77** (17), 3057-3067.
- Combes PJ (1969) Recherches sur la genèse des bauxites dans le nord-est de l'Espagne, le Languedoc et l'Ariège (France). Dissertation, Université de Montpellier, 342 p.
- Davatzen NC & Aydin A (2005) Distribution and nature of fault architecture in layered sandstone and shale sequence: an example from the Moab fault, Utah. In: *Faults, fluid flow, and petroleum traps* (eds. R. Sorkhabi & Y. Tsuji) AAPG Memoir, **85**, 153-180.
- Dewit J, Foubert A, El Desouky HA, Muchez Ph, Hunt D, Swennen R (2012) Dolomitisation model of hydrothermal dolomites (HTD) hosted by Aptian-Albian carbonates of the Ramales Platform (Basque-Cantabrian Basin, Northern Spain). VII Geofluids Conference, 75-78.
- Dickson JAD (1966) Carbonate identification and genesis as revealed by staining. *Journal of Sedimentary Research*, **36** (2), 491-505.
- Eichhubl P, Davatzen NC, Becker S (2009) Structural and diagenetic control of fluid migration and cementation along the Moab fault, Utah. *AAPG Bulletin*, **93** (5), 653-681.

- Fernández M & Banda E (1989) An approach to the thermal field in northeastern Spain. *Tectonophysics*, **164**, 259-266.
- Gaspar-Escribano JM, García-Castellanos D, Roca E, Cloetingh S (2004) Cenozoic vertical motions of the Catalan Coastal Ranges (NE Spain): The role of tectonics, isostasy, and surface transport. *Tectonics*, **23**, 1-18.
- Jiménez de Cisneros C, Caballero E, Vera JA, Durán JJ, Juliá R (2003) A record of Pleistocene climate from a stalactite, Nerja Cave, southern Spain. *Palaeogeography, Palaeoclimatology, Palaeoecology*, **189**, 1-10.
- Juez-Larré J (2003) Post Late Paleozoic tectonothermal evolution of the northeastern margin of Iberia, assessed by fission-track and (U-Th)/He analyses. A case history from the Catalan Coastal Ranges. Dissertation, Vrije Universiteit, 200 p.
- Julivert M & Durán H (1990) Paleozoic stratigraphy of the Central and Northern part of the Catalanian Coastal Ranges (NE Spain). *Acta Geologica Hispanica*, **25** (1-2), 3-12.
- Labaume P & Moretti I (2001) Diagenesis-dependence of cataclastic thrust fault zone sealing in sandstones. Example from the Bolivian Sub-Andean Zone. *Journal of Structural Geology*, **23**, 1659-1675.
- Labaume P, Carrio-Schaffhauser E, Gamond JF, Renard F (2004) Deformation mechanisms and fluid-driven mass transfers in the recent fault zones of the Corinth Rift (Greece). *Comptes Rendus Geoscience*, **336**, 375-383.
- Micarelli L, Benedicto A, Wibberley CAJ (2006) Structural evolution and permeability of normal fault zones in highly porous carbonate rocks. *Journal of Structural Geology*, **28**, 1214-1227.
- Mitjavila J & Martí J (1986) El volcanismo triásico del sur de Catalunya. *Revista d'Investigacions Geològiques.*, **42-43**, 89-103.

- Molina JM, Salas R (1993) Bauxitas kársticas del Cretácico inferior en Fuentespalda (provincia de Teruel): Estratigrafía, origen y paleogeografía. *Cuadernos de Geología Ibérica*, **17**, 207-230.
- O’Kane A, Onasch CM, Farver JR (2007) The role of fluids in low temperature, fault-related deformation of quartz arenite. *Journal of Structural Geology*, **29**, 819-836.
- O’Neil JR, Clayton RN, Mayeda TK (1969) Oxygen isotope fractionation in divalent metal carbonates. *Journal of Chemical Physics*, **51** (12), 5547-5558.
- Onasch CM, Dunne WM, Cook JE, O’Kane A (2009) The effect of fluid composition on the behaviour of well cemented, quartz-rich sandstone during faulting. *Journal of Structural Geology*, **31**, 960-971.
- Ortí F & Vaquer R (1980) Volcanismo jurásico del sector valenciano de la Cordillera Ibérica. Distribución y trama estructural. *Acta Geológica Hispánica*, **XV** (5), 127-130.
- Parcerisa D (2002) Petrologia i diagènesi en sediments de l’Oligocè superior i del Miocè inferior i mitjà de la Depressió del Vallès i del Pla de Barcelona. Evolució de l’àrea Font i dinàmica dels fluids. Dissertation, Universitat Autònoma de Barcelona, 261 p.
- Parry WT (1998) Fault-fluid compositions from fluid-inclusion observations and solubilities of fracture-sealing minerals. *Tectonophysics*, **290**, 1-26.
- Piqué A, Canals A, Grandia F, Banks DA (2008) Mesozoic fluorite veins in NE Spain record regional base metal-rich brine circulation through basin and basement during extensional events. *Chemical Geology*, **257**, 139-152.
- Ramon X & Calvet F (1987) Estratigrafia y sedimentología del Muschelkalk inferior del dominio Montseny-Llobregat (Catalánides). *Estudios geológicos*, **43** (5-6), 471-487.

Riba O & Colombo F (2009) *Barcelona: la Ciutat Vella i el Poblenou. Assaig de geologia urbana*, 1st edn. Institut d'Estudis Catalans. Reial Acadèmia de Ciències i Arts de Barcelona, Barcelona.

Roca E (1996) La evolución geodinámica de la Cuenca Catalano-Balear y áreas adyacentes desde el Mesozoico hasta la actualidad. *Acta Geológica Hispánica*, **29**, 3-25.

Roca E, Sans M, Cabrera L, Marzo M (1999) Oligocene to Middle Miocene evolution of the central Catalan margin (Northwestern Mediterranean). *Tectonophysics*, **315**, 209-233.

Rodríguez-Morillas N, Playà E, Travé A, Martín-Martín JD (2013) Diagenetic processes in a partially dolomitized carbonate reservoir: Casablanca oil field, Mediterranean Sea, offshore Spain. *Acta Geologica*, 11. doi: 10.1344/0.000001833.

Rossi C, Goldstein RH, Marfil R, Salas R, Benito MI, Permanyer A, de la Peña JA, Caja MA (2001) Diagenetic and oil migration history of the Kimmeridgian Ascla Formation, Maestrat Basin, Spain. *Marine and Petroleum Geology*, **18**, 287- 306.

Rowland JV & Sibson RH (2004) Structural controls on hydrothermal flow in a segmented rift system, Taupo Volcanic Zone, New Zealand. *Geofluids*, **4**, 259-283.

Salas R & Casas A (1993) Mesozoic extensional tectonics, stratigraphy and crustal evolution during the Alpine cycle of the eastern Iberian basin. *Tectonophysics*, **228** (1-2), 33-55.

Salas R, Guimerà J, Mas R, Martín-Closas C, Meléndez A, Alonso A (2001) Evolution of the Mesozoic central Iberian Rift System and its Cainozoic inversion (Iberian Chain). In: *Peri-Tethys Memoir 6: Peri-Tethyan Rift/Wrench Basins and Passive Margins* (eds. P.A. Ziegler, W. Cavazza, A.H.F. Robertson, S. Crasquin-Soleau) Mémoires du Muséum National d'Histoire Naturelle, **186**, 145-185.

Salas R, Vaquer R, Travé A (2004) Bauxitas kársticas y arcillas lateríticas barremienses de la Cadena Ibérica oriental y la Cadena Costero Catalana : relaciones genéticas y áreas de procedencia. *Geo-Temas*, **6** (2), 123-126.

Salas R, Caja MA, Martín JD, Mas R, Permanyer A (2005) Mid-Late Cretaceous volcanism, metamorphism and the regional thermal event affecting the Northeastern Iberian basins (Spain). In: *Global events during the quiet Aptian-Turonian superchron* (ed A. Arnaud-Vanneau, N. Arndt & I. Zghal). Série spéciale colloques et excursions, **6**, 55-58.

Santanach P, Casas JM, Gratacós O, Liesa M, Muñoz JA, Sàbat F (2011) Variscan and Alpine structure of the hills of Barcelona: geology in an urban area. *Journal of Iberian Geology*, **37** (2), 121-136.

Sibson RH, Moore JMcM, Rankin AH (1975) Seismic pumping-a hydrothermal fluid transport mechanism. *Journal of the Geological Society of London*, **131**, 653-659.

Sibson RH (1986) Earthquakes and rock deformation in crustal fault zones. *Annual Review of Earth and Planetary Sciences*, **14**, 149-175.

Solé J, Cosca M, Sharp Z, Enrique P (2002)  $^{40}\text{Ar}/^{39}\text{Ar}$  geochronology and stable isotope geochemistry of Late-Hercynian intrusions from north-eastern Iberia with implications for argon loss in K-feldspar. *International Journal of Earth Sciences (Geol Rundsch)*, **91**, 865-881.

Swanson MT (1992) Fault structure, wear mechanisms and rupture processes in pseudotachylyte generation. *Tectonophysics*, **204**, 223-242.

Tavarnelli E, Pasqui V (2000) Fault growth by segment linkage in seismically active settings: Examples from the Southern Apennines, Italy, and the Coast Ranges, California. *Journal of Geodynamics*, **29**, 501-516.



- Taylor HP Jr (1977) Water/rock interactions and the origin of H<sub>2</sub>O in granitic batholiths. *Journal of the Geological Society of London*, **133**, 509-558.
- Travé A, Calvet F (2001) Syn-rift geofluids in fractures related to the early-middle Miocene evolution of the Vallès-Penedès half-graben (NE Spain). *Tectonophysics*, **336**, 101-120.
- Travé A, Roca E, Playà E, Parcerisa D, Gómez-Gras D, Martín-Martín JD (2009) Migration of Mn-rich fluids through normal faults and fine-grained terrigenous sediments during early development of the Neogene Vallès-Penedès half-graben (NE Spain). *Geofluids*, **9**, 303-320.
- Tucker M & Marshall J (2004) Diagenesis and geochemistry of Upper Muschelkalk (Triassic) buildups and associated facies in Catalonia (NE Spain): a paper dedicated to Francesc Calvet. *Geologica Acta*, **2** (4), 257-269.
- Veizer J, Ala D, Azmy K, Bruckschen P, Buhl D, Bruhn F, Carden G, Diener A, Ebner S, Godderis Y, Jasper T, Korte C, Pawellek F, Podlaha O, Strauss H (1999) <sup>87</sup>Sr/<sup>86</sup>Sr,  $\delta^{13}\text{C}$  and  $\delta^{18}\text{O}$  evolution of Phanerozoic seawater. *Chemical Geology*, **161**, 59-88.
- Vesica PL, Tuccimei P, Turi B, Fornós JJ, Ginés A, Ginés J (2000) Late Pleistocene Paleoclimates and sea-level change in the Mediterranean as inferred from stable isotope and U-series studies of overgrowths on speleothems, Mallorca, Spain. *Quaternary Science Reviews*, **19** (9), 865-879.
- Virgili C (1957) El Triásico de los Catalánides. Dissertation, Universitat de Barcelona.
- Zhang Y, Gartrell A, Underschultz JR, Dewhurst DN (2009) Numerical modelling of strain localisation and fluid flow during extensional fault reactivation: implications for hydrocarbon preservation. *Journal of Structural Geology*, **31** (3), 315-327.

## FIGURE CAPTIONS

Figure 1. Schematic geological map of the Catalan Coastal Ranges with localization of the studied area and cross-section (Santanach et al. 2011). T: Tagamanent; MT: Martorell; BT: Berta Mine; CM: Caldes de Montbui; LG: La Garriga; CE: Caldes d'Estrac.

Figure 2. Detailed geological map of the northern sector of the Barcelona Plain with outcrop and borehole locations. Schematic columns of four of the boreholes are shown. F.Z.: fault zone.

Figure 3. Stereoplots of the different generations of fractures in Schmidt lower hemisphere projections with strain directions. The “r” marks reactivated fractures.

Figure 4. Hospital outcrop. A) General view of the Hospital outcrop. Legend: Pink: granodiorite; Purple: deformation zone formed by Triassic and Silurian rocks; Yellow: Miocene conglomerates. Faults are in red and bedding in black. B) Enlarged area marked in A, where most of deformation is concentrated, and stereoplot of the sets of fractures. Legend: Grd: granodiorite; Si: Silurian; M1: Lower Muschelkalk dolostones; M2: Middle Muschelkalk clays and sandstones; M3: Upper Muschelkalk dolostones; Mi: Miocene conglomerates; FC1: fault core 1; FB2a: fault breccias with carbonate clasts; FB2b: fault breccias with phyllite clasts. C) Photograph of the cataclastic green band of the fault core FC1. Observe the different degrees of comminution: C1) Thin section of the breccia. C2) Thin section of the slightly foliated cataclasite. D) Foliated red and black gouge of the fault core FC1.

Figure 5. Microphotographs of the minerals cementing the Hospital fault rocks in the Hospital outcrop. A-B) Plane polarized light and cathodoluminescence images of calcite cements C1a,b,c and later C2a. C) Cathodoluminescence of calcite cements C1c, which cements patchy cataclasites, and C1d. D) Image of cathodoluminescence of calcites C1d and C1e. E) Plane polarized light image of the cataclasite. Observe the three neoformed minerals linked to this fault rock: chlorite, calcite C1f and iron oxides. F) Vug porosity infilled by the zoned cement C2a in the cataclastic band (cathodoluminescence).

Figure 6. Enric outcrop. A) Poorly outcropping of the Hospital fault in the Enric outcrop and hand samples of the cohesive breccia and semicohesive gouge. Each bar subdivision is 1 cm. B) Synthetic cross-section of the fault zone, with sample location and projection of the identified sets of fractures.

Figure 7. Microphotographs of the minerals cementing the Hospital fault rocks in the Enric outcrop. A) Random breccia cemented by epidotes (plane polarized light). B) Multiepisodic pull-apart cemented by calcite C1 (plane polarized light). C) Type 3A microfault formed by pseudotachylyte (PST) and later calcite cement C3a, which is crosscut by a type 3B open joint cemented by calcite C3b (plane polarized light). D) Cathodoluminescence image of cements C3a and C3b. E) Semicohesive breccia with fractures cemented by calcite C4. Calcite cement C7 partially replaces calcite C4 during soil development (plane polarized light). F) Corn-cob aggregate formed by calcite C7 interpreted as a soil developed in the semicohesive gouge (plane polarized light).

Figure 8. Sariol outcrop. A) View of the Hospital fault from the Sariol outcrop to the southwest. B) Synthetic sketch of the fault zone at the Sariol outcrop and stereoplot of the sets of fractures. Red faults are type 2 faults reactivated during development of type

3D faults (in black). C) Thin section of fault rocks developed within the granodiorite. D) Random breccia cemented by the two generations of calcite cement C2b and C2c (cathodoluminescence image). E) Cataclasite developed in the granodiorite cemented by non-luminescent calcite-dolomite cement C5 (cross polarized light). F) Cataclasite in the calcitized dolostone cemented by calcite-dolomite cement C5 and succession of palisades PC1 (plane polarized light).

Figure 9. Fractures of the hanging-wall. A) Type 3D faults affecting the Miocene conglomerates. B) Type 1A normal fault affecting carbonates of the M3 facies. C) Cataclasite formed in the footwall of type 1A faults. D) Microfault of type 2 within M1 facies. E) Type 3A normal fault in M1 facies characterized by its undulating plane. F) Type 3E open joint in M1 facies filled by clays of the M2. G) Karstic breccias on a fault plane. H) Speleothem covering one of the walls of a type 3E joint.

Figure 10. Microphotographs of the minerals cementing minor fractures within Triassic dolostones of the Hospital hanging-wall. A) Cataclasite cemented by dolomite cement D1 developed in type 1A faults. Observe the red dull replacive dolomite within the clasts (cathodoluminescence). B) Cataclasite and later ultracataclasite cemented by dolomite cements D1 and D2 respectively. Also, later fractures cemented by dolomite cement D3 are observed (cathodoluminescence). C) Dolomite cement D3 and later calcitized dolomite CD4 (cathodoluminescence). D) Cathodoluminescence image of calcitized dolomite cements CD1 and CD2. E) Cathodoluminescence image of calcitized dolomite cement CD3. F) Patch of calcitized dolostone with the same cathodoluminescence behaviour than the CD3 cement.

## Geofluids

Figure 11.  $\delta^{18}\text{O}$  versus  $\delta^{13}\text{C}$  plot of the different carbonate cements and host rocks. The asterisk marks the values of the calcites of Parcerisa (2002). Anisian-Ladinian seawater values are according to Veizer et al. (1999).

Figure 12. Structural evolution of the basin and distribution and evolution of fluids through time in the northern sector of the Barcelona Plain from Late Permian to Recent.

A) Deposition of the Triassic rocks and dolomitization during the first Mesozoic rifting event. B) Cretaceous rifting localized in the southern segment and circulation of ascending hot fluids. C) Basin inversion, folding, erosion and percolation of low-temperature meteoric fluids that produce the calcitization of previous dolomites. D) Segment connection through fault growth and upflow of hot fluids in the relay area during the Neogene syn-rift. E) Propagation of the Hospital fault to the surface and percolation of low-temperature meteoric fluids. F) Generation of the NW-SE set of fractures that segment the Hospital fault and development of soil and speleothems.

Figure 13. Sketch of the mechanism of fault growth by tip propagation of the southern segment at kilometric scale. PST is the abbreviation of pseudotachylyte.

#### TABLE CAPTIONS

Table 1. Elemental geochemistry and  $\delta^{18}\text{O}$ - $\delta^{13}\text{C}$  composition of the carbonate cements and host rocks.

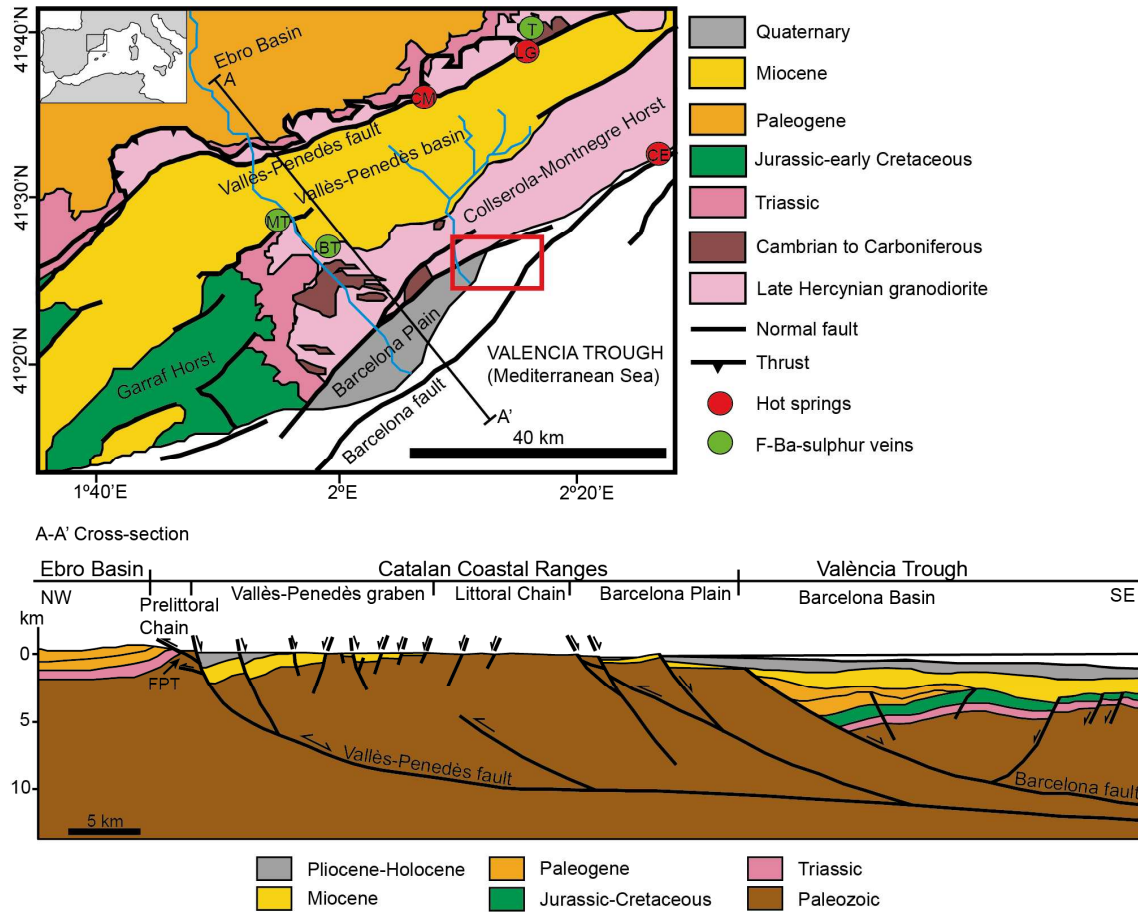
**Figure 1**

Figure 2

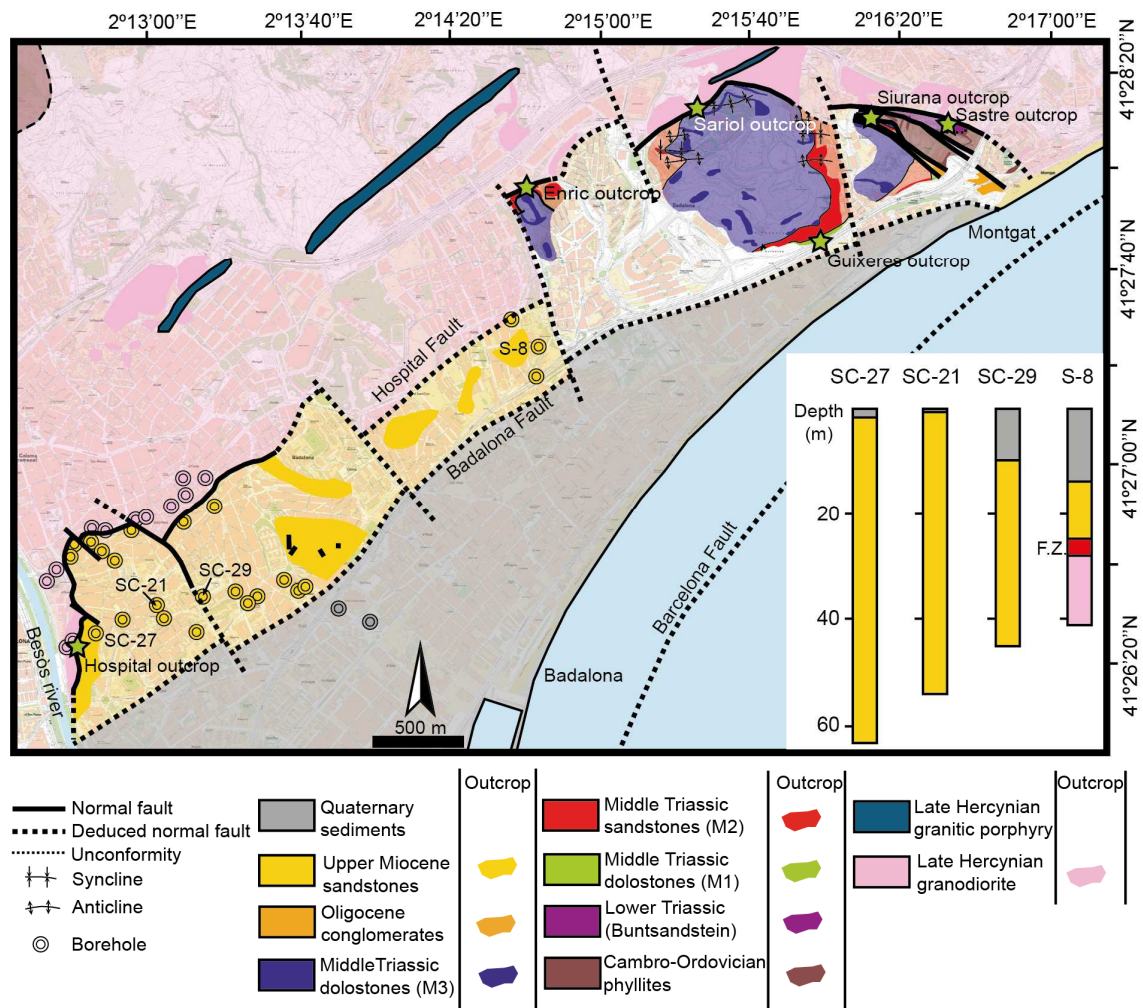


Figure 3

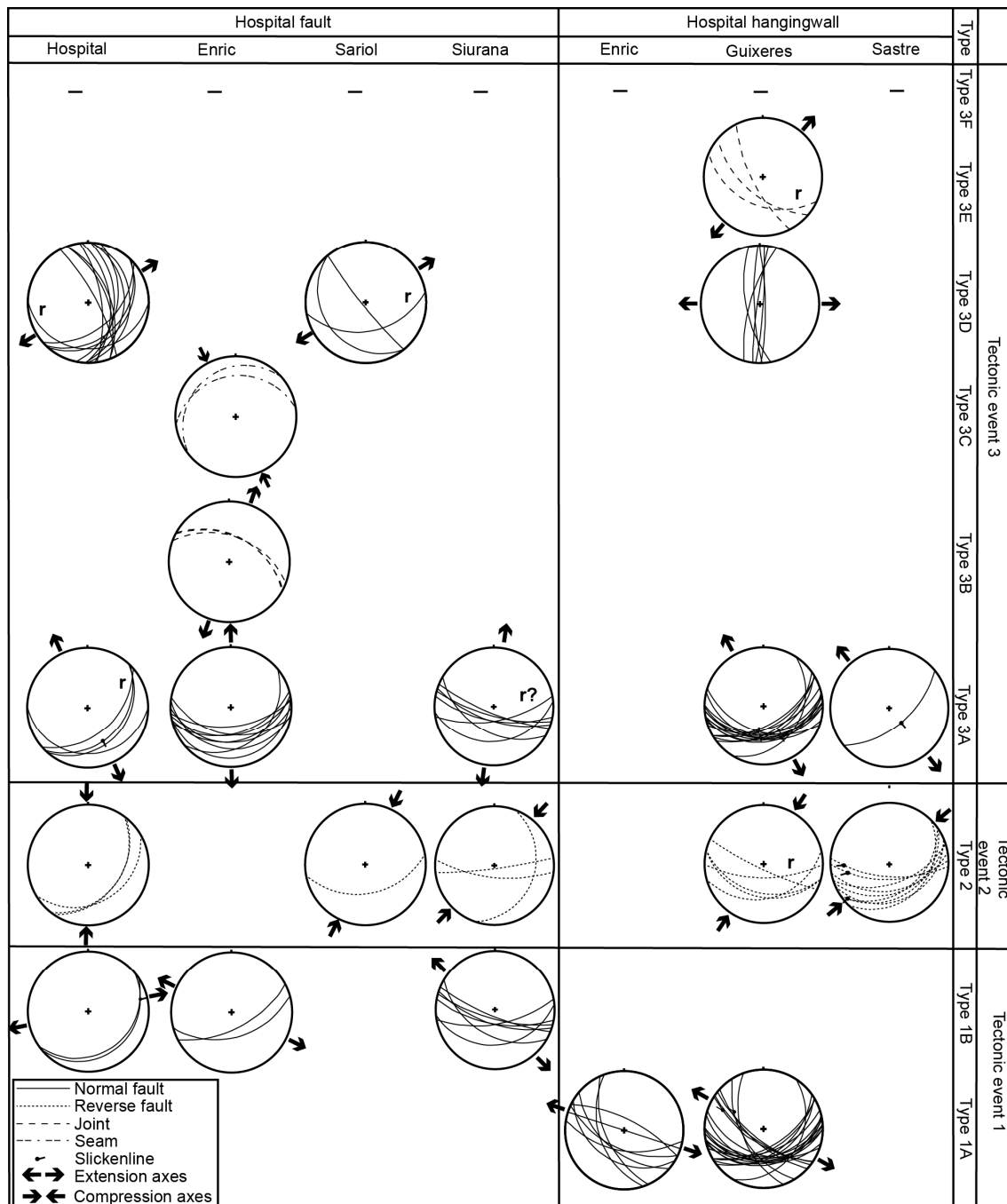
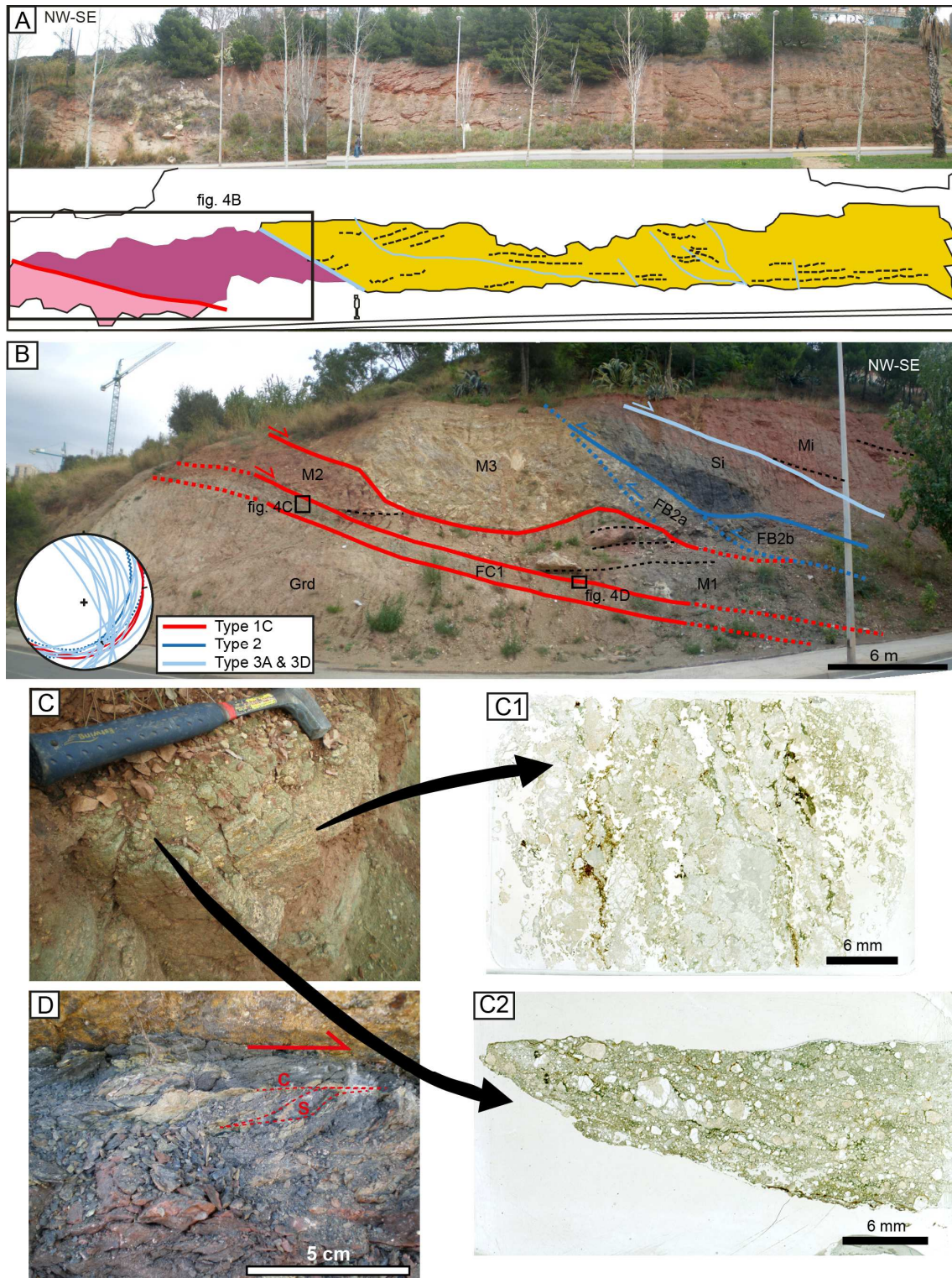


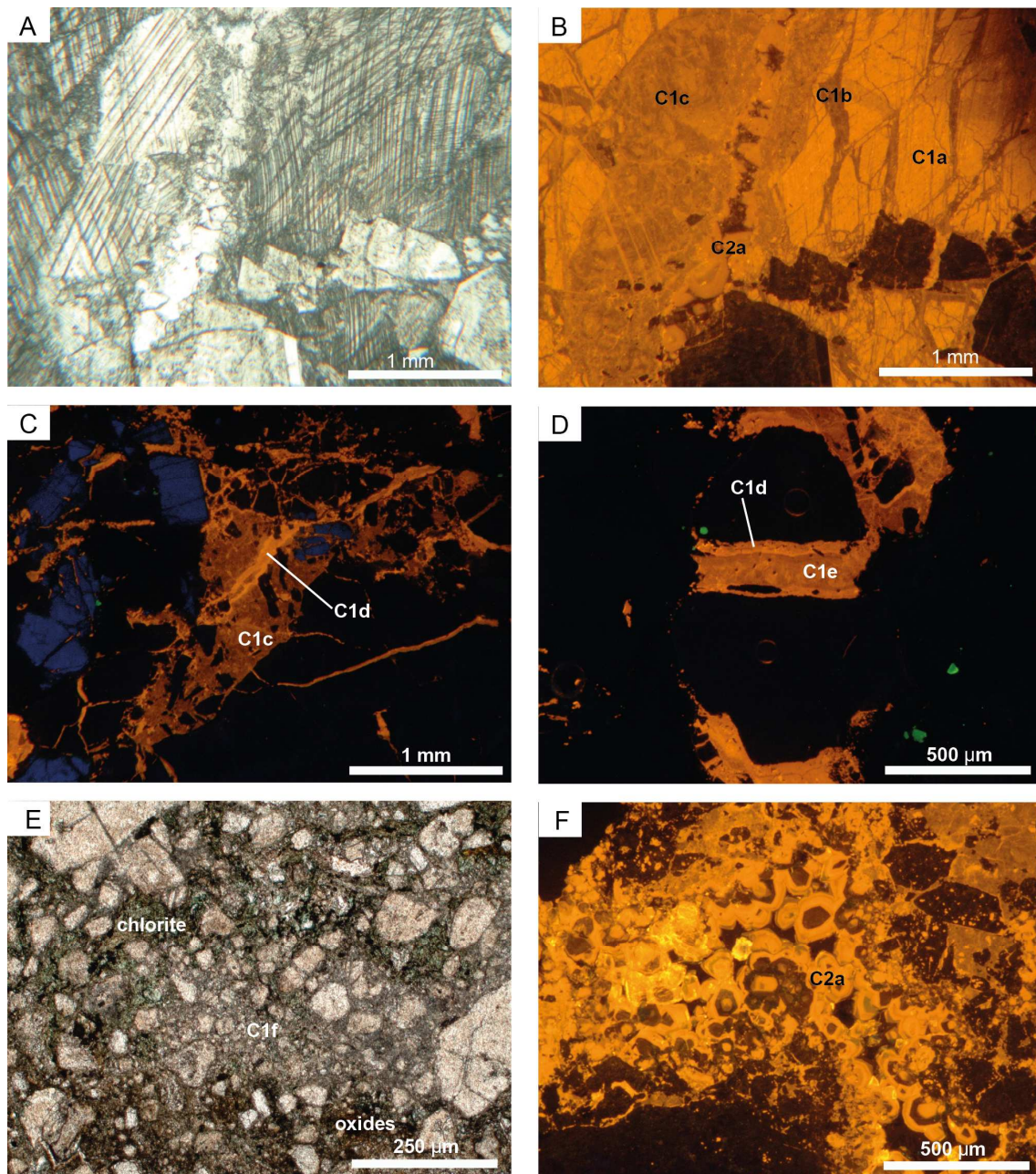


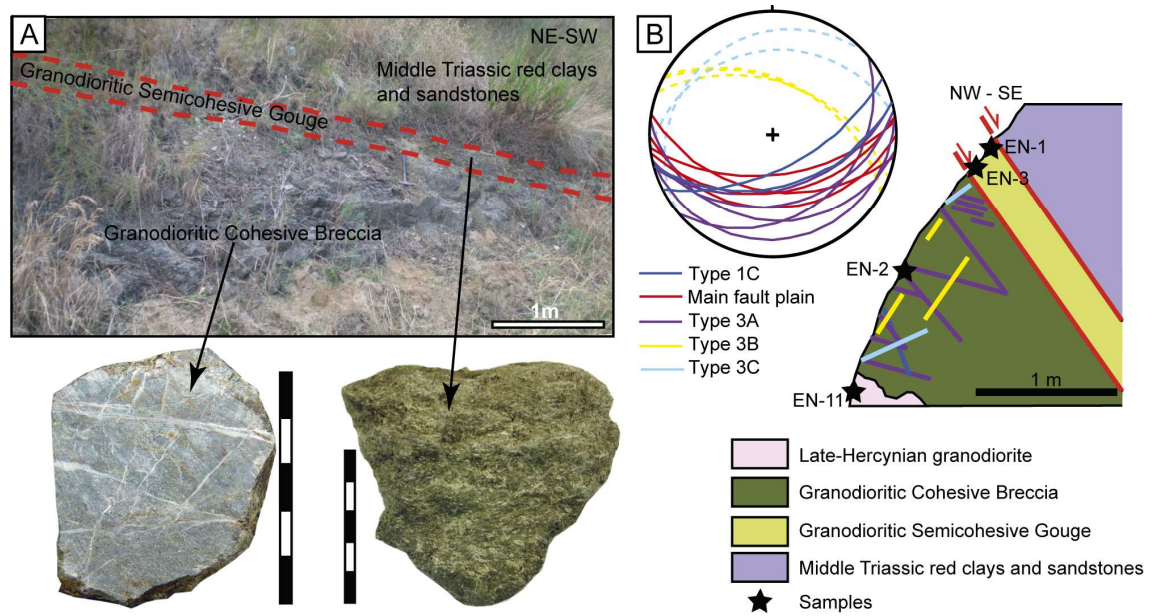
Figure 4



Geofluids



**Figure 5**

**Figure 6**



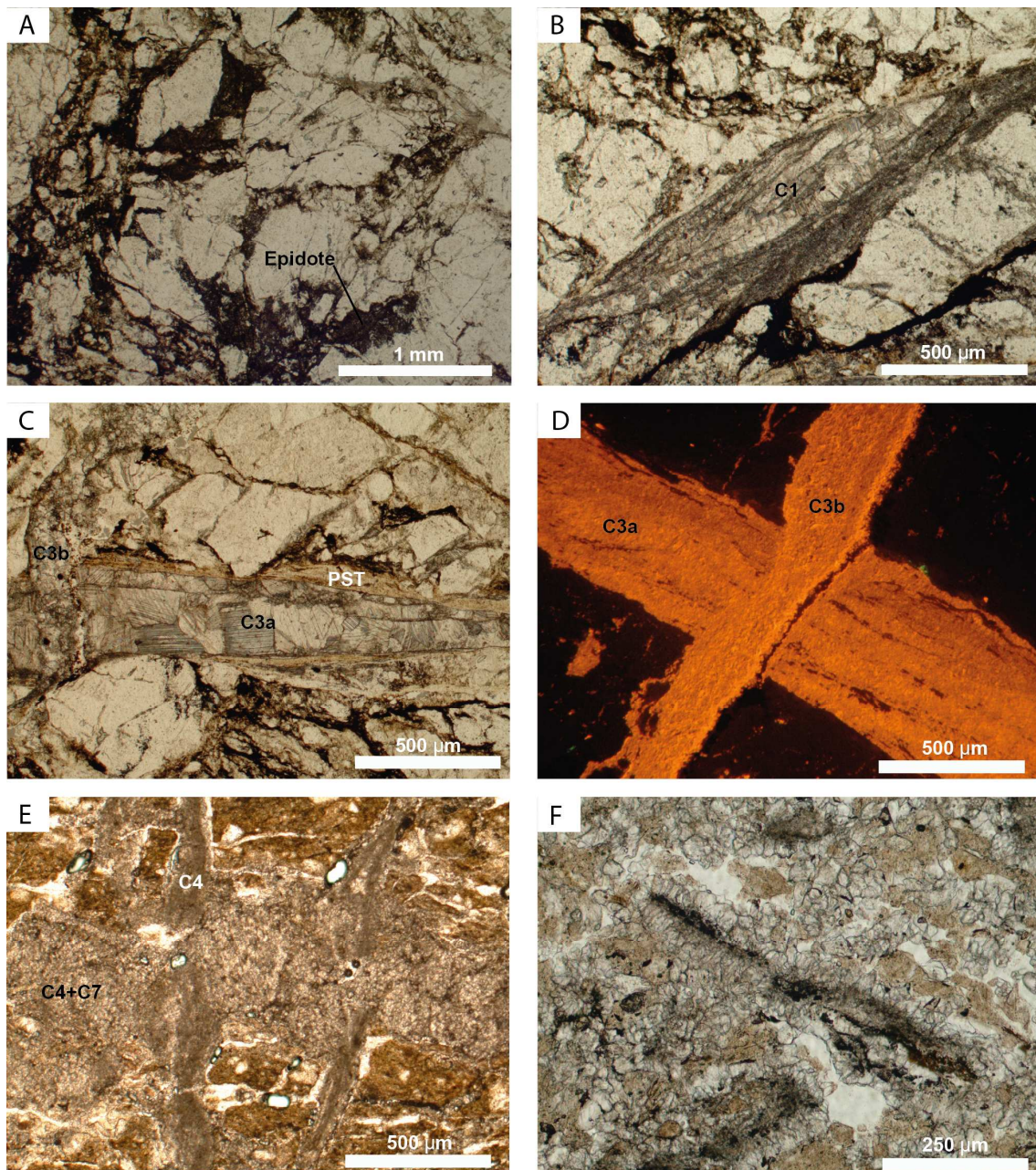
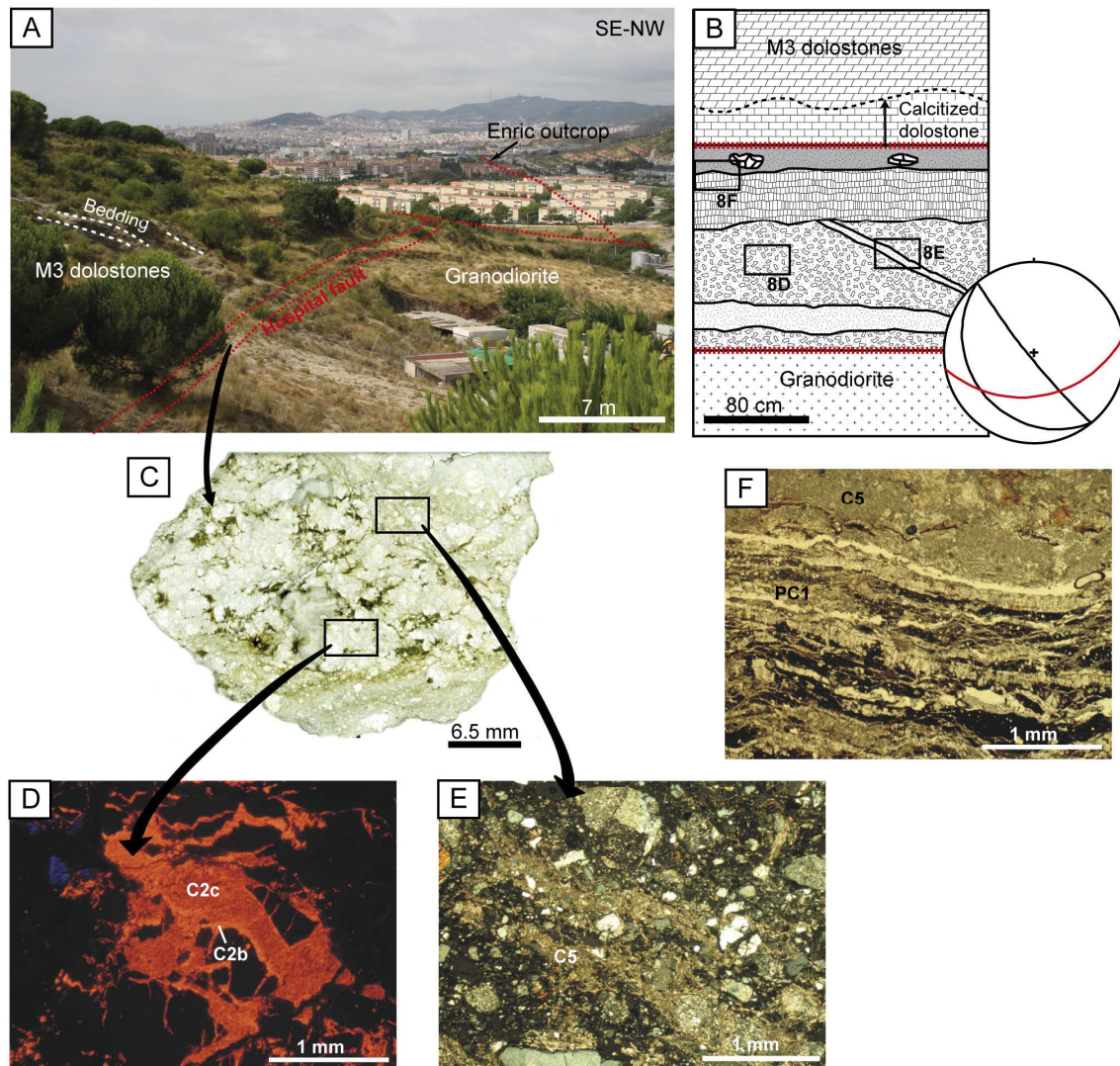
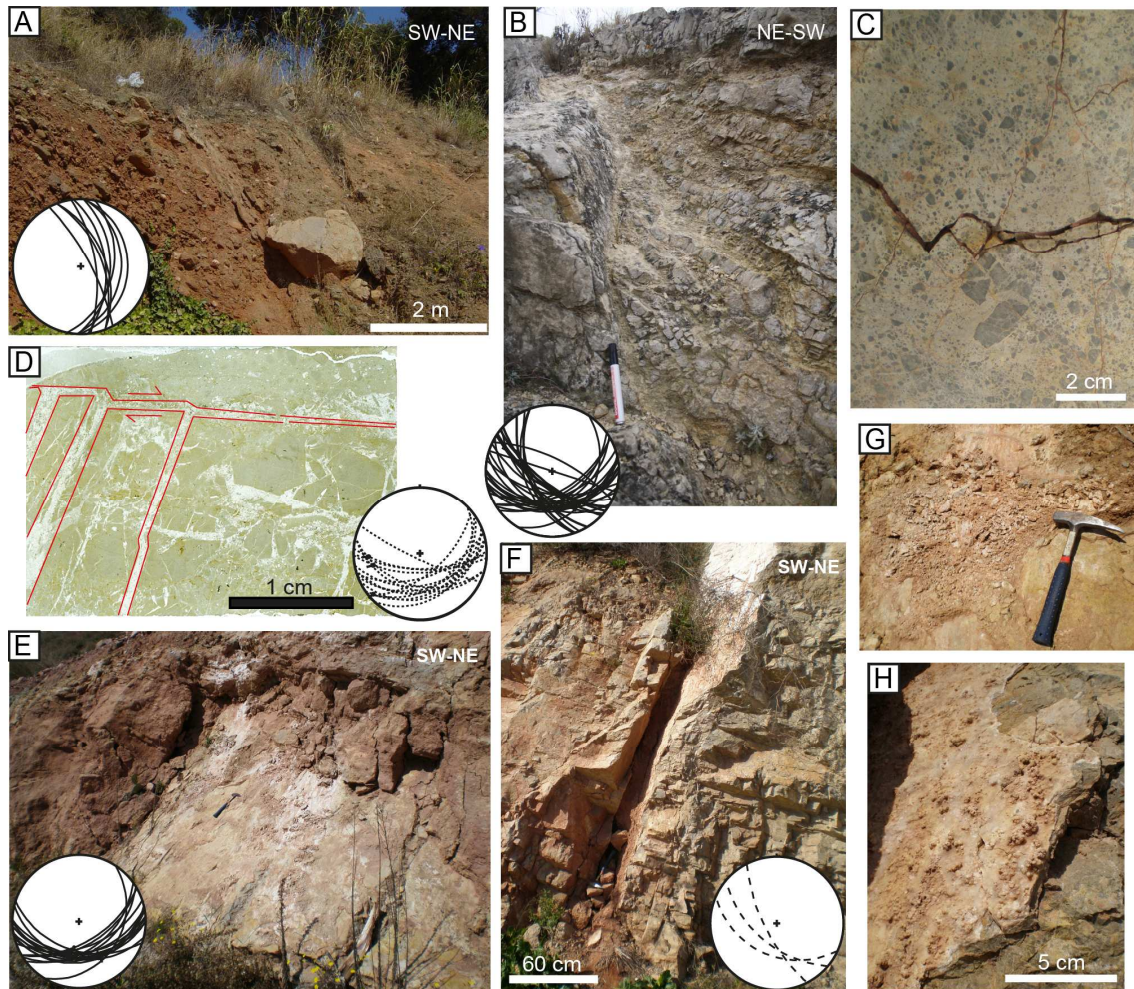
**Figure 7**



Figure 8



**Figure 9**



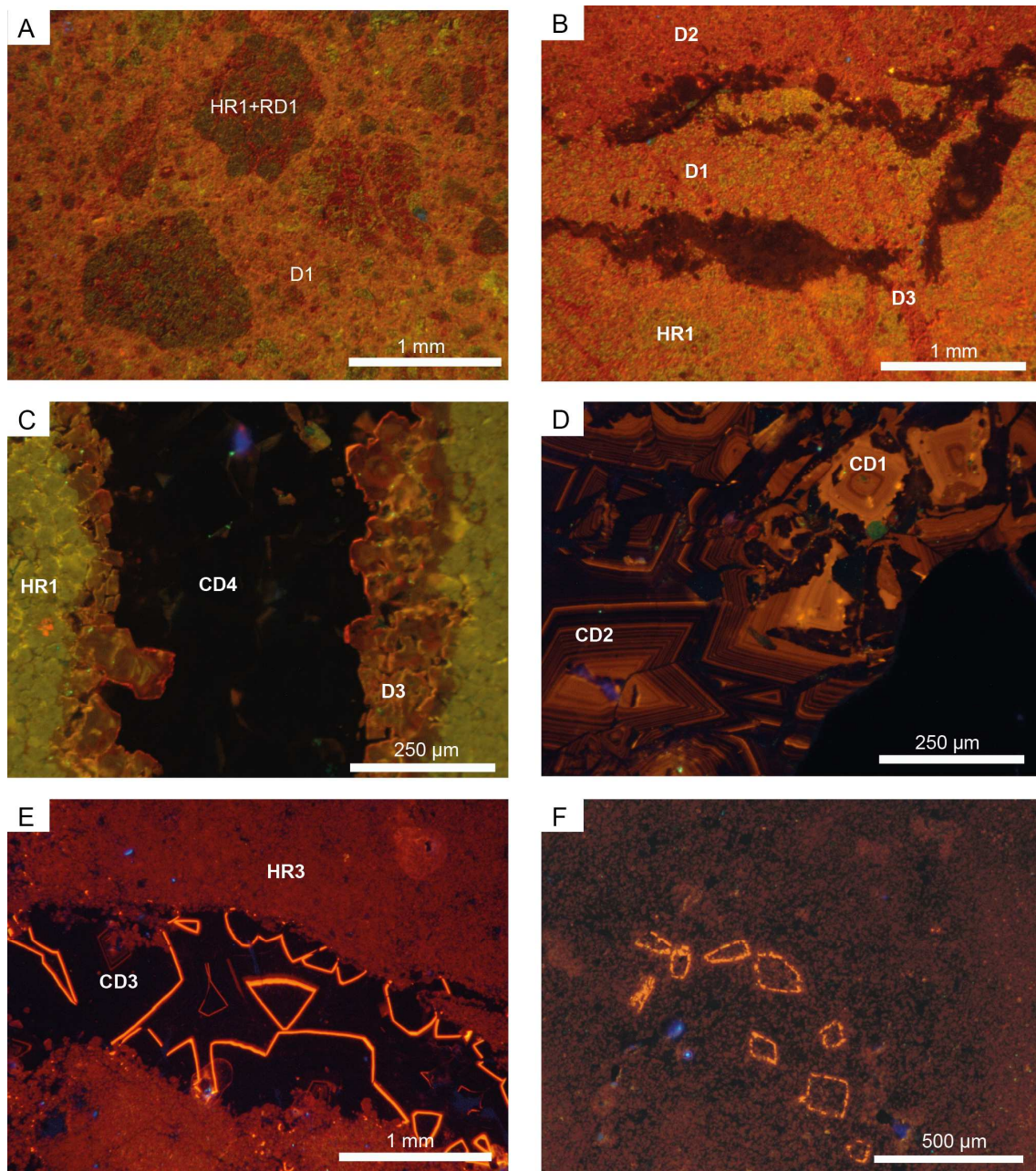
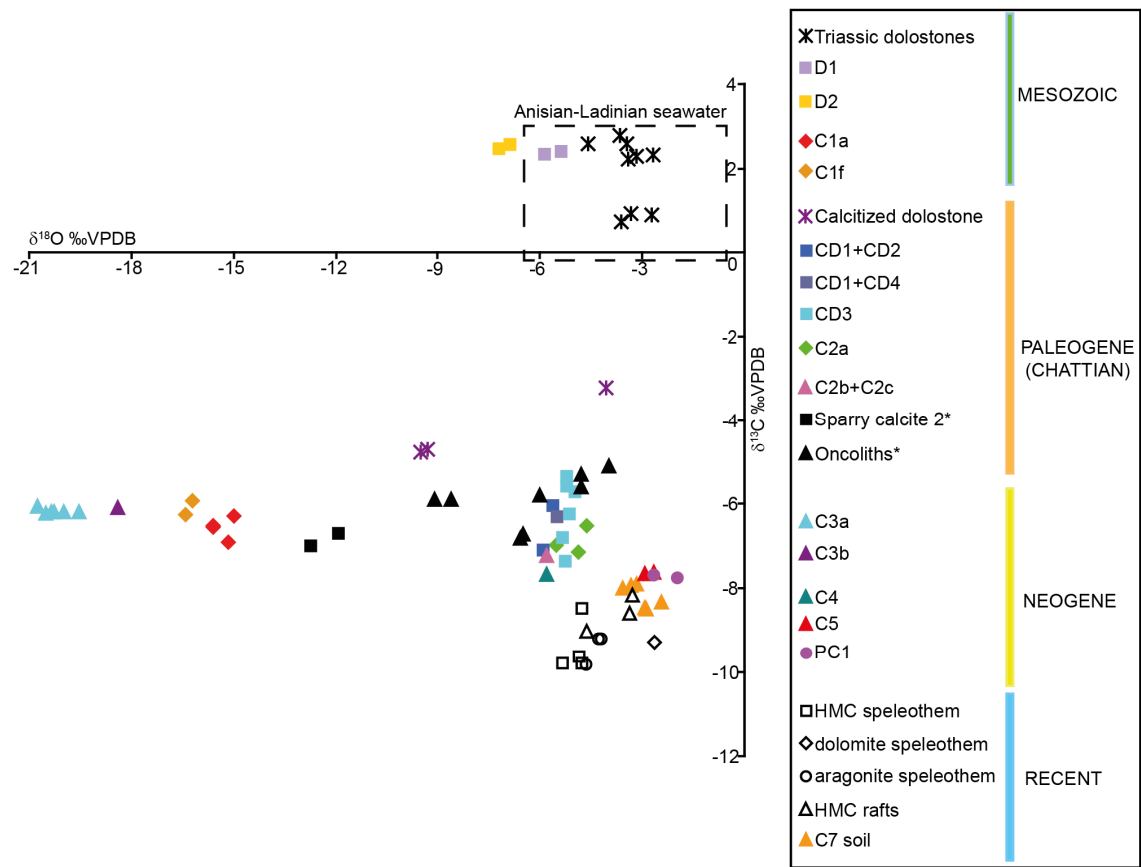
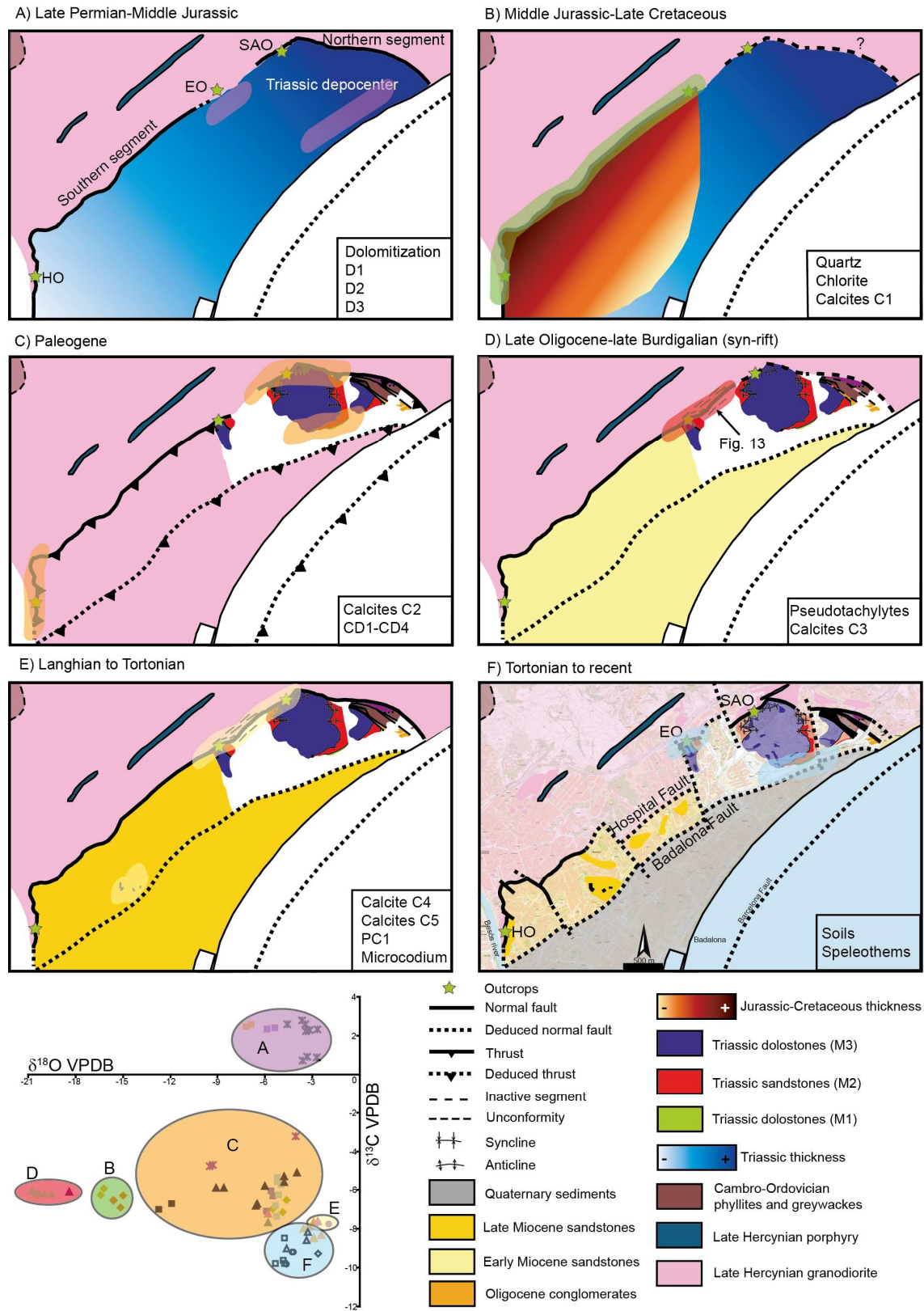
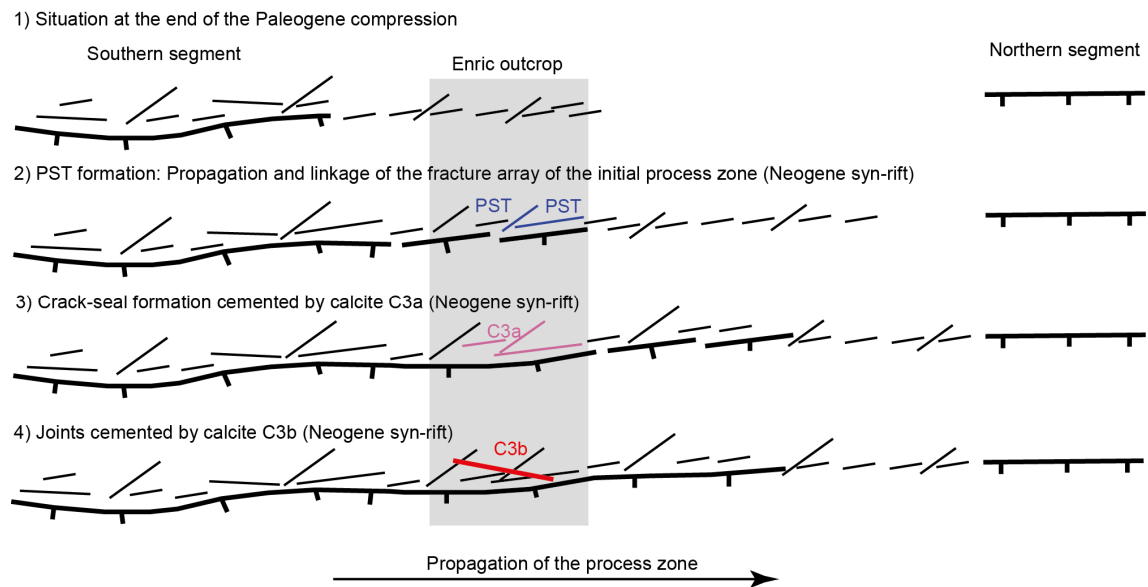
**Figure 10**

Figure 11





**Figure 12**

**Figure 13**

**Table 1**

Hospital fault cements		Ca (ppm)	Mg (ppm)	Na (ppm)	Mn (ppm)	Fe (ppm)	Sr (ppm)	$\delta^{18}\text{O}$ (‰ VPDB)	$\delta^{13}\text{C}$ (‰ VPDB)
C1a (n=10)	min	391591	<d.l.	<d.l.	1681	<d.l.	968	-15.6	-6.5
	max	396633	<d.l.	241	4425	326	1342	-15.0	-6.3
	average	393805	<d.l.	<d.l.	2937	<d.l.	1218	-15.4	-6.4
C1b (n=1)	min	-	-	-	-	-	-	-	-
	max	396148	<d.l.	5302	<d.l.	2983	1044	-	-
	average	-	-	-	-	-	-	-	-
C1c (n=53)	min	387038	<d.l.	<d.l.	190	<d.l.	293	-	-
	max	403308	1049	366	5031	1078	1687	-	-
	average	396219	<d.l.	131	1074	137	1340	-	-
C1d (n=8)	min	386130	<d.l.	<d.l.	<d.l.	<d.l.	1141	-	-
	max	395492	1367	<d.l.	3537	1034	1580	-	-
	average	391541	<d.l.	<d.l.	2305	507	1410	-	-
C1e (n=7)	min	391093	<d.l.	<d.l.	594	<d.l.	1212	-	-
	max	402147	2260	236	2120	734	1867	-	-
	average	394577	<d.l.	<d.l.	1308	387	1437	-	-
C1f (n=11)	min	390100	<d.l.	<d.l.	<d.l.	<d.l.	158	-16.4	-6.2
	max	414500	<d.l.	1906	640	917	480	-16.2	-5.9
	average	403055	<d.l.	419	<d.l.	248	357	-16.3	-6.1
C1 (n=11)	min	385500	<d.l.	<d.l.	<d.l.	<d.l.	251	-	-
	max	411300	4980	216	1160	610	590	-	-
	average	400636	811	107	827	260	467	-15.1	-6.9
C2a (n=47)	min	384720	<d.l.	<d.l.	<d.l.	<d.l.	971	-5.5	-7.1
	max	400837	2990	362	7168	6250	1880	-4.6	-6.5
	average	390998	873	<d.l.	3031	1188	1378	-5.0	-6.9
C2b (n=7)	min	386100	<d.l.	<d.l.	1086	<d.l.	157	-	-
	max	400200	1430	<d.l.	5629	1064	464	-	-
	average	392286	671	<d.l.	3366	633	319	-5.8	-7.2
C2c (n=10)	min	397800	<d.l.	<d.l.	232	<d.l.	198	-	-
	max	405600	<d.l.	<d.l.	770	233	445	-	-
	average	401610	<d.l.	<d.l.	459	<d.l.	309	-	-
C3a (n=38)	min	396200	<d.l.	<d.l.	641	<d.l.	309	-20.8	-6.2
	max	409300	<d.l.	197	2299	313	610	-19.6	-6.1
	average	401982	<d.l.	<d.l.	1102	<d.l.	460	-20.2	-6.2
C3b (n=15)	min	392100	<d.l.	<d.l.	925	<d.l.	<d.l.	-	-
	max	410400	<d.l.	330	6445	6576	879	-	-
	average	402020	<d.l.	123	2161	686	486	-18.4	-6.1
C4 (n=20)	min	378100	<d.l.	<d.l.	<d.l.	<d.l.	195	-	-
	max	407200	9265	230	5421	2475	714	-	-
	average	390495	2981	<d.l.	1766	844	479	-5.8	-7.7
C5 (n=8)	min	209200	761	<d.l.	<d.l.	576	278	-2.9	-7.6
	max	388600	104973	<d.l.	4401	8698	1429	-2.6	-7.6
	average	311650	47549	<d.l.	1510	217	786	-2.8	-7.6
C6 (n=7)	min	340200	<d.l.	<d.l.	<d.l.	<d.l.	<d.l.	-	-
	max	406800	39585	336	2381	593	1599	-	-
	average	373771	18928	139	537	275	925	-	-
C7 (n=22)	min	360100	11294	<d.l.	<d.l.	<d.l.	179	-2.9	-8.5
	max	384800	29628	355	1573	1066	1271	-2.5	-8.3
	average	374086	19127	<d.l.	130	402	750	-2.8	-8.4
PC1a (n=13)	min	225900	<d.l.	<d.l.	<d.l.	<d.l.	<d.l.	-2.7	-7.7
	max	395300	121058	<d.l.	6644	2764	1019	-1.9	-7.7
	average	311385	59794	<d.l.	1043	834	533	-2.3	-7.7
PC1b (n=10)	min	383400	<d.l.	<d.l.	3713	771	<d.l.	-	-
	max	392000	1123	<d.l.	7766	4351	385	-	-
	average	387450	509	<d.l.	5634	1567	262	-	-

&lt;d.l.: below the analytical detection limit

n: number of elemental analysis spots

Hanging-wall cements		Ca (ppm)	Mg (ppm)	Na (ppm)	Mn (ppm)	Fe (ppm)	Sr (ppm)	$\delta^{18}\text{O}$ (‰ VPDB)	$\delta^{13}\text{C}$ (‰ VPDB)
HR1 (n=15)	min	211248	128308	<d.l.	<d.l.	<d.l.	376	-4.6	+0.7
	max	219995	152760	454	160	1269	700	-3.4	+2.6
	average	216260	133803	287	<d.l.	431	556	-3.9	+1.8
HR2 (n=22)	min	202598	121744	107	<d.l.	<d.l.	<d.l.	-3.3	+0.9
	max	222716	132719	354	188	17845	857	-2.7	+2.3
	average	217949	129416	248	<d.l.	1686	532	-3.0	+1.6
HR3 (n=21)	min	213966	104916	<d.l.	<d.l.	597	271	-3.7	+2.6
	max	245753	135569	517	960	3844	564	-3.5	+2.8
	average	219847	126945	191	321	1472	437	-3.6	+2.7
HR4 (n=15)	min	215966	126808	<d.l.	<d.l.	741	<d.l.	-	-
	max	221039	131053	<d.l.	398	3164	<d.l.	-	-
	average	218155	128749	<d.l.	222	1678	<d.l.	-	-
RD1 (n=15)	min	216438	128123	<d.l.	<d.l.	<d.l.	248	-	-
	max	222747	136806	209	205	1466	610	-	-
	average	219484	131651	<d.l.	<d.l.	557	395	-	-
D1 (n=36)	min	213612	127591	<d.l.	<d.l.	<d.l.	<d.l.	-5.9	+2.3
	max	221864	134565	470	201	1800	800	-5.4	+2.4
	average	218295	130251	185	<d.l.	604	563	-5.6	+2.4
D2a (n=18)	min	214197	123803	<d.l.	<d.l.	<d.l.	<d.l.	-7.2	+2.5
	max	223924	131800	351	177	870	681	-6.8	+2.6
	average	218926	128898	181	<d.l.	440	468	-7.0	+2.6
D2b (n=13)	min	216494	121831	<d.l.	<d.l.	424	<d.l.	-	-
	max	221205	132860	230	799	7803	555	-	-
	average	218862	129130	118	187	2813	349	-	-
D3 (n=23)	min	210900	126284	<d.l.	<d.l.	400	448	-	-
	max	224411	132600	200	200	1500	900	-	-
	average	218303	129328	<d.l.	<d.l.	878	640	-	-
CD1 (n=15)	min	389200	<d.l.	<d.l.	<d.l.	<d.l.	1300	-5.9	-7.4
	max	395100	2300	300	400	700	2100	-4.9	-5.4
	average	392793	1053	<d.l.	160	340	1740	-5.3	-6.3
CD2 (n=14)	min	392600	700	<d.l.	<d.l.	<d.l.	700	-	-
	max	404400	2900	300	200	300	2000	-	-
	average	396757	1250	<d.l.	<d.l.	<d.l.	1500	-	-
CD3 (n=88)	min	390000	<d.l.	<d.l.	<d.l.	<d.l.	700	-	-
	max	404800	1900	300	2200	1100	2200	-	-
	average	398092	928	<d.l.	<d.l.	<d.l.	1417	-	-
CD4 (n=18)	min	389800	600	<d.l.	<d.l.	<d.l.	1200	-	-
	max	398500	2700	200	<d.l.	800	1700	-	-
	average	394150	1139	<d.l.	<d.l.	244	1444	-	-
Calcitized dolostone	min	-	-	-	-	-	-	-9.5	-4.8
	max	-	-	-	-	-	-	-4.1	-3.2
	average	-	-	-	-	-	-	-7.6	-4.2
Dolomite speleoth. (n=2)	min	236600	102900	400	<d.l.	<d.l.	2300	-	-
	max	250300	110600	500	<d.l.	<d.l.	3700	-	-
	average	243450	106750	450	<d.l.	<d.l.	3000	-2.6	-9.3
High-Mg calcite sp. (n=17)	min	360400	8800	<d.l.	<d.l.	<d.l.	5300	-5.3	-9.8
	max	385800	24900	600	200	<d.l.	13800	-4.7	-8.5
	average	375176	16976	282	<d.l.	<d.l.	7506	-4.9	-9.4
Calcite speleoth. (n=4)	min	388000	3500	<d.l.	<d.l.	<d.l.	2200	-	-
	max	398700	6700	300	<d.l.	<d.l.	2600	-	-
	average	393800	4400	<d.l.	<d.l.	<d.l.	2425	-	-
Aragonite speleoth. (n=6)	min	389300	<d.l.	<d.l.	<d.l.	<d.l.	4800	-4.6	-9.8
	max	395800	<d.l.	500	<d.l.	<d.l.	8200	-4.2	-9.2
	average	392517	<d.l.	283	<d.l.	<d.l.	6783	-4.4	-9.4
High-Mg rafts (n=8)	min	308600	25800	600	<d.l.	<d.l.	2200	-4.6	-9.0
	max	357400	64300	1400	200	300	3300	-3.3	-8.2
	average	335538	43688	950	<d.l.	<d.l.	2650	-3.8	-8.6

### **Publication 3**

**Cantarero I**, Lanari P, Vidal O, Alías G, Travé A, Baqués V. Long-term fluid circulation in extensional faults in the central Catalan Coastal Ranges: P-T constraints from neoformed chlorite and K-white mica. *Journal of International Earth Sciences* (under review).



# International Journal of Earth Sciences

## Long-term fluid circulation in extensional faults in the central Catalan Coastal Ranges: P-T constraints from neoformed chlorite and K-white mica

--Manuscript Draft--

<b>Manuscript Number:</b>	IJES-D-12-00273
<b>Full Title:</b>	Long-term fluid circulation in extensional faults in the central Catalan Coastal Ranges: P-T constraints from neoformed chlorite and K-white mica
<b>Article Type:</b>	Original Paper
<b>Keywords:</b>	fault rocks; low P-low T estimates; chlorite-mica multi-equilibrium; hydrothermalism; Catalan Coastal Ranges
<b>Corresponding Author:</b>	Irene Cantarero University of Barcelona Barcelona, Barcelona SPAIN
<b>Corresponding Author Secondary Information:</b>	
<b>Corresponding Author's Institution:</b>	University of Barcelona
<b>Corresponding Author's Secondary Institution:</b>	
<b>First Author:</b>	Irene Cantarero
<b>First Author Secondary Information:</b>	
<b>Order of Authors:</b>	Irene Cantarero
	Pierre Lanari
	Olivier Vidal
	Gemma Alías
	Anna Travé
	Vinyet Baqués
<b>Order of Authors Secondary Information:</b>	
<b>Abstract:</b>	<p>The neoformation of chlorite and K-white mica in fault rocks from two main faults of the central Catalan Coastal Ranges, the Vallès and the Hospital faults, has allowed us to constrain the P-T conditions during fault evolution using thermodynamic modelling. Crystallization of M1 and M2 muscovite and microcline occurred as result of deuteritic alteration during the exhumation of the pluton (330°C&gt;T&gt;370°C) in the Permian. After that, three tectonic events have been distinguished. The first tectonic event, attributed to the Mesozoic rifting, is characterized by precipitation of M3 and M4 phengite together with chlorite and calcite C1 at temperatures between 190 and 310°C. The second tectonic event attributed to the Paleogene compression has only been identified in the Hospital fault with precipitation of low-temperature calcite C2. The short-cut produced during inversion of the Vallès fault was probably the responsible of the lack of neoformed minerals within this fault. Finally, the third tectonic event, which is related to the Neogene extension, is characterized in the Vallès fault by a new generation of chlorite, associated to calcite C4 and laumontite, formed at temperatures between 125 and 190°C in the absence of K-white mica. Differently, the Hospital fault was characterized by the precipitation of calcite C3 during the syn-rift stage at temperatures around 150°C and by low-temperature fluids precipitating calcites C5, C6 and PC1 during the post-rift stage.</p> <p>During the two extensional events (Mesozoic and Neogene), faults acted as conduits for hot fluids producing anomalous high geothermal gradients (50°C/km minimum).</p>





**Long-term fluid circulation in extensional faults in the central Catalan Coastal Ranges: P-T constraints from neoformed chlorite and K-white mica**

**I. Cantarero<sup>1</sup>, P. Lanari<sup>2</sup>, O. Vidal<sup>3</sup>, G. Alías<sup>1</sup>, A. Travé<sup>1</sup> and V. Baqués<sup>1</sup>**

<sup>1</sup> Departament de Geoquímica, Petrologia i Prospecció Geològica, Facultat de Geologia, Universitat de Barcelona (UB), Martí i Franqués s/n, 08028 Barcelona, Spain. i\_cantarero@ub.edu, galias@ub.edu, atrave@ub.edu, vbaques@ub.edu

<sup>2</sup> Institute of Geology, University of Bern, Baltzstrasse 1+3 Bern, CH-3012, Switzerland. pierre.lanari@geo.unibe.ch

<sup>3</sup> ISTerre, Université de Grenoble I, CNRS, 1381 rue de la Piscine, 38041 Grenoble, France. olivier.vidal@ujf-grenoble.fr

**Abstract**

The neoformation of chlorite and K-white mica in fault rocks from two main faults of the central Catalan Coastal Ranges, the Vallès and the Hospital faults, has allowed us to constrain the P-T conditions during fault evolution using thermodynamic modelling. Crystallization of M1 and M2 muscovite and microcline occurred as result of deuteritic alteration during the exhumation of the pluton (330°C>T>370°C) in the Permian. After that, three tectonic events have been distinguished. The first tectonic event, attributed to the Mesozoic rifting, is characterized by precipitation of M3 and M4 phengite together with chlorite and calcite C1 at temperatures between 190 and 310°C. The second tectonic event attributed to the Paleogene compression has only been identified in the Hospital fault with precipitation of low-temperature calcite C2. The short-cut produced during inversion of the Vallès fault was probably the responsible of the lack of neoformed minerals within this fault. Finally, the third tectonic event, which is related to the Neogene extension, is characterized in the Vallès fault by a new generation of chlorite, associated to calcite C4 and laumontite, formed at temperatures between 125 and 190°C in the absence of K-white mica. Differently, the Hospital fault was characterized by the precipitation of calcite C3 during the syn-rift stage at temperatures around 150°C and by low-temperature fluids precipitating calcites C5, C6 and PC1 during the post-rift stage.

During the two extensional events (Mesozoic and Neogene), faults acted as conduits for hot fluids producing anomalous high geothermal gradients (50°C/km minimum).

**Keywords:** fault rocks, low P-low T estimates, chlorite-mica multi-equilibrium, hydrothermalism, Catalan Coastal Ranges

## 1. INTRODUCTION

Chemical and isotopic compositions of minerals formed during faulting can record the origin of the fluids and the pressure and temperature (P-T) conditions of deformation regimes, essential parameters to understand fault evolution. Phyllosilicates such as chlorite and K-white mica allow to quantify the P-T conditions as their chemical composition is temperature and pressure dependent. They have been used to constrain P-T equilibrium conditions of crystallization in high-pressure low-temperature (HP-LT) and low-pressure low-temperature (LP-LT) metapelites free of minerals index of metamorphism applying thermodynamic approaches (Vidal and Parra 2000; Parra et al. 2002; Árkai et al. 2003; Vidal et al. 2006; Schwartz et al. 2009; Grosch et al. 2012; Ganne et al. 2012; Dubacq et al. 2010; Lanari et al. 2012 and references therein). Also, the same approach has been successfully used to constrain diagenetic or low-grade metamorphic conditions during fault evolution (Lacroix et al. 2012). In fault zones, phyllosilicates are inherited from the host rock or formed from the alteration of primary minerals due to fluid-rock interaction (e.g. transformation of feldspar to muscovite or biotite to chlorite) (Chen et al. 2007). In granitic systems, where Mg is present (i.e. biotites), phyllosilicates such as K-white mica, chlorite and kaolinite are predicted to precipitate at low temperature (below 350°C) due to water interaction in both rock-dominated and water-dominated systems (Wintsch et al. 1995).

The present work is focused on the study of two faults where deformation is localized in the granodioritic footwall. These two faults belong to the NE-SW trending fault system that controls the Neogene horst and graben structure of the Catalan Coastal Ranges (CCR), at the NE of Spain. Some of the Neogene normal faults are the result of the negative inversion of Paleogene thrusts, which, in turn, inverted previous extensional Mesozoic faults (Santanach et al. 2011). Because of this long fault activity, a detailed study must be done in order to identify the time-relative relationships between the different tectonic events and the P-T conditions of mineral crystallization during the evolution of the fault zones.

Pressure conditions were constrained during the CCR evolution by means of sedimentological, structural and fission-track studies (Anadón et al. 1979; Juez-Larré 2003; Gaspar-Escribano et al. 2004; ter Voorde

et al. 2007). These studies demonstrate that rocks outcropping nowadays were at a maximum of 3.6 km depth previous to the Paleogene compression and 2.2 km previous to the Miocene extension, yielding to maximum pressure conditions around 1 and 0.7 kbar, respectively. Temperature conditions were constrained from fluid inclusion data in fluorite-barite veins (Canals and Cardellach 1997; Cardellach et al. 2002; Tritlla and Cardellach 2003; Piqué et al. 2008). In the Central Catalan Coastal Ranges, i.e. in Berta and Rigròs mines, temperatures recorded in the Mesozoic veins range between 80 and 230°C whereas Miocene veins formed between 100 and 150°C (Cardellach et al. 2002; Piqué et al. 2008). Moreover, fission-track data in the CCR (Juez-Larré 2003) provided constrain on the minimum temperature during the Mesozoic and the Neogene corresponding to the closure temperature of apatites and zircons. Temperature was found to drop from  $T > 200^{\circ}\text{C}$  before Mesozoic to the closure temperature of zircon during Mesozoic, and down to the closure temperature of apatite ( $100^{\circ}\text{C}$ ) during the Miocene. These temperatures mainly occurred in the samples localized close to the graben boundary (Juez-Larré 2003), which is consistent with fluid inclusion data (Piqué et al. 2008).

The above mentioned data provide a general framework, but a more detailed evolution of the P-T conditions linked to fault activities still remains to be done. In the present study, the combination of petrological observations and multi-equilibrium thermodynamic modeling using the compositions of chlorite and K-white mica allows us to reconstruct the P-T path during evolution of the two faults. The aims of this work are: 1) to characterize the different deformation phases associated to each tectonic event along a major and an intermediate fault (the Vallès and the Hospital faults, respectively) affecting the same granodioritic host rock, 2) to propose a detailed interpretation of the relationships between P-T estimates of mineral crystallization and fault evolution, and 3) to establish the factors that control the different associations of neoformed minerals.

## **2. GEOLOGICAL SETTING**

The Catalan Coastal Ranges (CCR), in the NE of Spain, constitute the north-western edge of the Valencia Trough, separating the thin continental crust of this trough from the thickened crust of the Iberian Peninsula. The opening of the Valencia Trough is related to the southwestward propagation of the Western European rift system and the Burdigalian oceanic accretion associated with the southwestward drift of the Corsica-Sardinia block during the Neogene extensional event (Oligocene-middle Miocene)

(Roca et al. 1999). The CCR display a well-developed horst and graben structure limited by listric faults striking NE-SW and NNE-SSW with a detachment level at 12-16 km, acquired during the opening of the Valencia Trough (Roca and Guimerà 1992; Gaspar-Escribano et al. 2004). This structure is also segmented by later faults trending NW-SE to NNW-SSE (Fig. 1). The Neogene extensional event is divided into a syn-rift stage (Aquitania?-late Burdigalian), an early post-rift stage (Langhian-Serravalian) and a late post-rift stage (late Serravalian-Pliocene) (Calvet et al. 1996; Baqués et al. in press).

This extensional structure is superimposed on Paleogene contractional structures formed during the N-S compression caused by the collision between the Iberian and European plates (Late Cretaceous-late Oligocene), which generated the Catalan Intraplate Chain (Guimerà 1984; Bartrina et al. 1992). The formed thick-skinned thrusts had a certain left-lateral component (Ashauer & Teichmüller 1935; Anadón et al. 1985; Roca 1996).

In its turn, Paleogene thrusts inverted major Mesozoic extensional faults. During the Mesozoic, an extensional process related to the opening of the western Tethys and of the North Atlantic took place (Salas and Casas 1993; Rossi et al. 2001). Two rift stages and two related post-rift stages have been described (Salas et al. 2001). The first rift stage is Late Permian-Early Jurassic in age and was related to the westward propagation of the Tethys and southward propagation of the Arctic-North Atlantic rift. This event was followed by an Early to Middle Jurassic post-rift stage characterized by thermal subsidence. The second rift stage lasted from Late Jurassic to Early Cretaceous and was the result of the gradual opening of both the North Atlantic Basin and the Bay of Biscay. A later stage of thermal subsidence was produced during the Late Cretaceous post-rift (late Albian-Maastrichtian).

Nowadays, abundant springs, some of them of hot water (up to 70°C), occur at the intersection between the NW-SE to NNW-SSE faults and the main fault system bounding the grabens (Fernández and Banda 1989). These springs are the result of topographically-driven meteoric fluids (Carmona et al. 2000; Bitzer et al. 2001) and are preferably located in the igneous basement, which constitutes the footwall of the main fault system, i.e. Caldes de Montbui, La Garriga, Caldes d'Estrac (Albert et al. 1979). Two hydrothermal events have been described in the Catalan Coastal Ranges from the study of fault-controlled barite-fluorite-sulphur veins (Canals and Cardellach 1997): one during the Mesozoic (at least Jurassic) and the other during the Neogene (lower Miocene) (Cardellach et al. 2002).

This study is focused on two NE-SW fault zones with dip to the SE, the Vallès and the Hospital faults, which are the northern boundary of the Vallès graben and the Barcelona Plain, respectively, formed during the Neogene extension (Fig.1 and 2). The Vallès graben is up to 65 km long and from 3 to 15 km wide and it is filled by more than 3000 m of sediment next to the fault (Cabrera 1981; Bartrina et al. 1992; Roca et al. 1999) ranging in age from late Oligocene to Present. The Barcelona Plain is a 40 km long and 2-10 km wide basin that is mainly filled by Miocene continental-transitional siliciclastic deposits and Quaternary fluvio-deltaic deposits. In both cases, a Paleozoic basement and a Mesozoic cover mainly constitute the footwalls, although Mesozoic material has been almost eroded in the Montnegre horst (Fig.1). The Paleozoic basement is formed by Cambro-Ordovician shales and phyllites, Silurian black shales and phyllites, Devonian carbonates, Carboniferous Culm facies and late Hercynian leucogranites, tonalites and granodiorites (Julivert and Durán 1990). According to Gil-Ibarguchi and Julivert (1988), the granodiorite was emplaced at 1.5 kbar and 700°C in the Montnegre Horst close to the Barcelona Plain. It shows granular texture and grain size is mostly about 2-3 mm although some feldspars are around 5 mm. It is constituted by quartz, potassic feldspar, plagioclase and biotite (<5%). The studied faults mainly affect the late Hercynian granodiorite, which has recorded all the described tectonic events overprinting the Hercynian deformation.

### **3. METHODOLOGY**

#### **3.1. Petrology and geochemistry**

Thirty samples from the Hospital fault, twenty-two from the Vallès fault and two samples of the unaltered granodiorite obtained from boreholes have been studied. Thin sections were examined under optical and cathodoluminescence microscopes. A Technosyn Cold Cathodoluminescence Model 8200 MkII operating at 16-19 kV and 350 µA gun current was used. Selected thin sections were also examined under ESEM Quanta 200 FEI, XTE 325/D8395 scanning electronic microscope combined with EDS spectroscopy for mineral identification.

X-ray diffraction of bulk rock and oriented aggregates have been performed with a Bragg-Brentano PANalytical X'Pert PRO MPD alpha 1 operating at 1.5406 Å, 45 kV and 40 mA.

After the petrographic study, carbon-coated polished thin sections were analysed for elemental composition of carbonate cements, chlorites and K-white mica with a CAMECA SX-50 electron probe

microanalyser (EPMA). It operated at 15 nA of beam intensity, 20 kV of acceleration voltage and a beam diameter of 10  $\mu\text{m}$ . The detection limits were 428 ppm for Na, 275 ppm for Mg, 272 ppm for Al, 288 ppm for Si, 263 ppm for K, 260 ppm for Ca, 290 ppm for Ti, 672 ppm for Mn, 647 ppm for Fe for silicates. The precision of major elements is 0.64% (at  $2\sigma$  level).

Microsamples of the calcite cements were powdered with a microdrill for carbon and oxygen isotopes. Samples were reacted with 103% phosphoric acid at 70°C for two minutes in an automated Kiel Carbonate Device attached to a Thermal Ionization Mass Spectrometer Thermo Electron (Finnigan) MAT-252. The results are expressed in  $\delta\text{‰}$  VPDB standard. Standard deviation is  $\pm 0.02\text{‰}$  for  $\delta^{13}\text{C}$  and  $\pm 0.05\text{‰}$  for  $\delta^{18}\text{O}$ .

### 3.2. Thermobarometric methods

Chlorite and K-white mica minerals are good candidates for thermobarometric estimates because they present several chemical substitutions (simple and coupled) controlled by the equilibrium conditions (P, T, pH,  $f\text{O}_2$ ...) that can be modelled using a set of different end-members (Vidal et al. 2001, 2005, 2006; Parra et al. 2002; Dubacq et al. 2010). Three main substitutions occur in chlorite ( $\text{FeMg}_{-1}$ , Tschermak and di/trioctahedral substitutions) that can be modelled using the following set of five end-members (e.g. Vidal et al. 2005): Mg-amesite ( $\text{Si}_2\text{Al}_4\text{Mg}_4\text{O}_{10}(\text{OH})_8$ ), Fe-amesite ( $\text{Si}_2\text{Al}_4\text{Fe}_4\text{O}_{10}(\text{OH})_8$ ), daphnite ( $\text{Si}_3\text{Al}_2\text{Fe}_5\text{O}_{10}(\text{OH})_8$ ), clinocllore ( $\text{Si}_3\text{Al}_2\text{Mg}_5\text{O}_{10}(\text{OH})_8$ ), and sudoite ( $\text{Si}_3\text{Al}_4\text{Mg}_2\text{O}_{10}(\text{OH})_8$ ). In K-white mica, three additional substitutions occur ( $\text{NaK}_{-1}$ ,  $\square\text{-(H}_2\text{O)}_{-1}$  and pyrophyllitic substitutions) and can be modelled using the following set of seven end-members (e.g. Dubacq et al. 2010): muscovite ( $\text{Si}_3\text{Al}_3\square_1\text{K}_1\text{O}_{10}(\text{OH})_2$ ), Fe-celadonite ( $\text{Si}_4\text{Al}_1\text{Fe}_1\square_1\text{K}_1\text{O}_{10}(\text{OH})_2$ ), Mg-celadonite ( $\text{Si}_4\text{Al}_1\text{Mg}_1\square_1\text{K}_1\text{O}_{10}(\text{OH})_2$ ), phlogopite ( $\text{Si}_3\text{Al}_1\text{Mg}_3\text{K}_1\text{O}_{10}(\text{OH})_2$ ), pyrophyllite ( $\text{Si}_4\text{Al}_2\square_2\text{O}_{10}(\text{OH})_2$ ), pyrophyllite-1H<sub>2</sub>O ( $\text{Si}_4\text{Al}_2\square_1(\text{H}_2\text{O})_1\text{O}_{10}(\text{OH})_2$ ), and paragonite ( $\text{Si}_3\text{Al}_3\square_1\text{Na}_1\text{O}_{10}(\text{OH})_2$ ).

#### 3.2.1. Chlorite-quartz-water thermometry

Chlorite shows an increase in  $\text{Al}^{\text{IV}}$  and a decrease in vacancy contents with increasing temperature (e.g. Cathelineau et Nieva 1985 and Vidal et al. 2001). The multi-equilibrium approach of Vidal et al. (2005, 2006) proposes a simultaneous estimate of  $\text{Fe}^{3+}$  content in chlorite and equilibrium temperature by the convergence of the following equilibria at a given pressure:



- (1) 5 Mg-amesite + 4 daphnite  $\leftrightarrow$  4 clinochlore + 5 Fe-amesite
- (2) 2 clinochlore + 3 sudoite  $\leftrightarrow$  4 Mg-amesite + 7 quartz + 4 H<sub>2</sub>O
- (3) 16 daphnite + 15 sudoite  $\leftrightarrow$  6 clinochlore + 20 Fe-amesite + 35 quartz + 20 H<sub>2</sub>O
- (4) 4 daphnite + 6 sudoite  $\leftrightarrow$  3 Mg-amesite + 5 Fe-amesite + 14 quartz + 8 H<sub>2</sub>O

The position of these equilibria, (1) to (4), depends on the activities of the chlorite end-members, quartz and water. In this work, temperatures and  $X\text{Fe}^{3+}$  of chlorite were estimated at 1 kbar, which is the maximum pressure according to the regional geology, and with water activity equal to 1. Following the Vidal et al. (2005, 2006) approach, the convergence is achieved with the minimum  $\text{Fe}^{3+}$  proportion and it was considered to be achieved when the temperature difference between the four equilibria was less than 30°C (Lanari et al. 2012 and references therein).

### 3.2.2. Mica-quartz-water thermobarometry

The Si content of K-white mica increases with pressure by Tschermak substitution (Massone and Schreyer 1989). At low temperature, the pyrophyllitic substitution also controls the Si and interlayer contents (e.g. Agard et al. 2001). The mica-quartz-water equilibrium used in this study models the variation of composition with respect to temperature and pressure, taking into account mica hydration of vacancies (Dubacq et al. 2010, Vidal et al. 2010). For a mica in chemical equilibrium with quartz and water, these three equilibria can be written:

- (5) 3 celadonite + 2 pyrophyllite  $\leftrightarrow$  2 muscovite + biotite + 11 quartz + 2 H<sub>2</sub>O
- (6) 3 celadonite + 2 pyrophyllite·1H<sub>2</sub>O  $\leftrightarrow$  2 muscovite + biotite + 11 quartz + 3H<sub>2</sub>O
- (7) pyrophyllite·1H<sub>2</sub>O  $\leftrightarrow$  pyrophyllite + H<sub>2</sub>O

The convergence of these equilibria at various P-T conditions is achieved by varying the  $\text{XH}_2\text{O}_{\text{interlayer}}$  content (i.e. pyrophyllite·1H<sub>2</sub>O proportion). A mica-quartz-H<sub>2</sub>O equilibrium line is then drawn, along which the hydration state varies (Dubacq et al. 2010). The pressure conditions were then estimated at the temperature obtained from the chlorite-quartz-water equilibria (Lanari et al. 2012).

### 3.2.3. Chlorite-mica-quartz-water multi-equilibrium approach

After the application of the previous thermometer and barometer, the equilibrium of chlorite and K-white mica was checked through a full chlorite-mica multi-equilibrium approach involving  $X\text{Fe}^{3+}$  in both

chlorite and mica and  $\text{XH}_2\text{O}_{\text{interlayer}}$  in mica. P-T equilibrium conditions of chlorite-mica-quartz-water assemblage were calculated from the convergence of 159 equilibria obtained from the previous mentioned chlorite and mica end-members. Only those equilibria showing a good convergence were selected, for which the sum of the Gibbs free energy of a selected set of reactions ( $\Delta_r G$ ) of the calculated P and T was less than 7000 J.

#### 4. OUTCROP DESCRIPTION AND STRUCTURAL ANALYSIS

The Vallès fault puts in contact the late Hercynian granodiorite (footwall) within the Miocene materials infilling the Vallès graben (Fig. 2). It generates a fault zone about 60 m thick localized in the footwall that is limited in the northwest by a thrust fault that superposes the granodiorite to the Cambro-Ordovician rocks. Two outcrops separated 600 m have been selected in the footwall of the Vallès fault according to their structural position: the Torrent del Corró and Camí d'En Cisa outcrops. The Torrent del Corró outcrop (TCO) is located at 50 m from the main Neogene fault whereas the Camí d'En Cisa outcrop (CCO) represents the Neogene deformation zone in contact with the Miocene materials.

The Hospital fault puts in contact an equivalent granodiorite with the Triassic and Miocene rocks. The fault zone is also developed in the footwall but it is narrower than in the Vallès fault, ranging from 1 to 3 meters. Three outcrops have been studied: the Hospital, Enric and Sariol outcrops. Each outcrop is located in one of the segments that constitute the Hospital fault and shows the contact with the Triassic rocks (Fig. 2B).

The study of crosscutting relationships of the different sets of fractures at outcrop and thin section scales has allowed us to define seven deformation phases (Fig. 3). The first deformation phase ( $D_1$ ) is formed by type 1 fractures. They consist of NE-SW striking normal faults that dip from 30 to 60° to the SE and NW. The second deformation phase ( $D_2$ ) is defined by type 2A faults in the Vallès fault and type 2B faults in the Hospital fault. Type 2A and 2B faults are NE-SW reverse faults with a limited left-lateral motion and a dip from 22 to 44°SE. The third deformation phase ( $D_3$ ) is related to type 3A fractures, which are E-W to NE-SW striking normal faults with a variable dip (from 15 to 90°) mostly to the E-SE. They show dip-slip slickenlines. Some of these faults are the reactivation of type 1 faults. Deformation phase  $D_4$  is defined by type 3B fractures, which are tension veins of NW-SE trend and dip 55°NE. The fifth

deformation phase (D<sub>5</sub>) is characterized by type 3C fractures that are NE-SW joints with low dip to the NW. Deformation phases D<sub>4</sub> and D<sub>5</sub> have been only identified in the Enric outcrop. Deformation phase D<sub>6</sub> is represented by type 3D fractures, which consist of normal faults of mainly N-S direction dipping from 30 to 80°E and barely to the SW and NE-SW normal faults that are the reactivation of previous 3A and 2A faults (Fig. 3). Finally, the last deformation phase (D<sub>7</sub>) is represented by type 3E dextral strike-slip faults trending NW-SE and dipping 50 to 65 ° to the northeast and southwest. In the Hospital fault, type 3E faults have been deduced by cartographical criteria.

## **5. FLUID/FAULT EVOLUTION: PETROLOGY OF FAULT ROCKS AND CEMENTS**

Deformation in the Vallès and Hospital faults generates cohesive brittle fault rocks, from breccias to ultracataclasites, in the granodiorite constituting the footwall. Petrological and geochemical results show the presence of several neoformed minerals such as calcite, laumontite, iron oxides, white mica and chlorite and also some mineral replacements (orthoclase by microcline, biotite by chlorite and muscovite by K-white mica). All these minerals vary along fault zones and may differ between faults (Fig. 4A) and show different mineral associations depending on the deformation phase (Fig. 4B).

### **5.1. The Vallès fault**

From the seven described deformation phases, four have been identified in the Vallès fault (Fig. 3). Crystallization of coarse, between 0.2 and 1.1 mm long, idiomorphic K-white mica associated to microcline neoformation with tartan-like twin, occurred previously to these phases. Pseudotachylyte veins with corroded quartz clasts and a very fine grained matrix clearly post-dates the K-white mica. However, it is difficult to establish to which tectonic event these pseudotachylytes are related to due to their later reworking and the lack of preferential orientations. The first deformation phase (D<sub>1</sub>) consists of type 1 normal faults, characterized by development of cataclasites and ultracataclasites and microfractures, where small K-white mica flakes (15 and 90 µm in size) and amoeboid chlorite precipitated. Also, during this phase, calcite C1 precipitated in nodules. Calcite C1 is made of dull to bright orange crystals, usually twinned, with  $\delta^{18}\text{O}$  values about -15‰ VPDB and  $\delta^{13}\text{C}$  about -6.5‰ VPDB. The first deformation phase and the previous stages have been only identified in the Torrent del Corró outcrop. The second deformation phase (D<sub>2</sub>), characterized by inverse faults, developed a wide blue gouge band at basin scale.

In the studied outcrops, however, it uniquely forms narrow gouge bands. The third deformation phase ( $D_3$ ) is characterized by successive cataclasite development along 3A normal faults and by the alternating precipitation of laumontite and calcite C4 in these fractures and in vug porosity. Coevally, irregular and ameboid chlorite crystals precipitated along reactivated type 1 and new 3A normal faults. The first generation of laumontite (L1) is made of translucent, anhedral and up to 50  $\mu\text{m}$  in size crystals. L1 precipitation was followed by a third generation of calcite C4, which precipitated in fractures and formed the slickenlines observed in faults 3A. Calcite C4 is formed by bright and dull orange zoned twinned calcite crystals with  $\delta^{18}\text{O}$  values about -23‰ VPDB and  $\delta^{13}\text{C}$  values about -7.5‰ VPDB. Finally, the second generation of laumontite (L2) precipitated and replaced calcite C4 at the wall of some fractures. Laumontite crystals are tabular, brownish under plane light and from cryptocrystalline to 70  $\mu\text{m}$  in size. In this third deformation phase, chlorite, laumontite L1 and calcite C4 are mainly formed in the Torrent del Corró outcrop, whereas laumontite L2 is the main neoformed mineral cementing most of the fractures and breccias in the Camí d'en Cisa outcrop. The strike-slip faults  $D_7$  crosscutting previous fault rocks and filled by iron oxides configure the fourth deformation phase identified in this fault.

The different neoformed minerals within the two outcrops are the responsible of the different colour of fault zones, green in the Torrent del Corró outcrop, due to chlorite crystallization, and white in the Camí d'en Cisa outcrop.

## **5.2. The Hospital fault**

The three studied outcrops are briefly described due to the strong lateral heterogeneities of the Hospital fault. A more detailed description can be found in Cantarero et al. (in press).

In the Hospital outcrop, four deformation phases have been identified. During the first deformation phase ( $D_1$ ), a type 1 fault generated a green cataclastic core zone in the contact between the granodiorite and the Triassic clays and sandstones. This core zone, developed in a zone where previously quartz geodes had formed, is the result of two successive reactivations that produced a dilatant random breccia and a consequent cataclasite. The dilatant random breccia was formed and cemented by five calcite cements, from C1a to C1e, with alternating bright to dull orange luminescence. Due to the small size of these calcite crystals (up to 1 mm) only a bulk isotopic composition could be obtained. The  $\delta^{18}\text{O}$  values range between -15.6 and -15‰ vPDB and the  $\delta^{13}\text{C}$  between -6.5 and -6.3‰ vPDB. This dilatant breccia was

further deformed as a slightly foliated cataclasite cemented by calcite cement C1f, iron oxides and chlorites. Calcite C1f has  $\delta^{18}\text{O}$  values between -16.4 and -16.2‰ vPDB and  $\delta^{13}\text{C}$  values between -6.2 and -5.9‰ vPDB. The second deformation phase ( $D_2$ ) is represented by reverse faults involving Mesozoic and Silurian rocks that develop decimetric-scale duplexes formed by breccias. During this phase, vug porosity was formed within the dilatant breccia ( $D_1$ ) and joints within the Triassic sandstones of the hangingwall were cemented by cement C2a. This cement is constituted by anhedral calcite crystals with a zoned orange and brown luminescence. The  $\delta^{18}\text{O}$  values of C2a range between -5.5 and -4.6‰ vPDB and the  $\delta^{13}\text{C}$  between -7.2 and -6.5‰ vPDB. The third deformation phase,  $D_3$ , generates normal faults where fault rocks or cements have not been observed. The fourth deformation phase recorded in the Hospital outcrop corresponds to  $D_6$ , which generates minor normal faults within the Miocene rocks without a fault core.

In the Enric outcrop, mylonitic bands developed within the ductile regime previous to the four recognized deformation phases. The first deformation phase ( $D_1$ ), settled within the brittle regime, produced the development of a random breccia with chlorite and epidote precipitation in the fractures. Later, multiepisodic pull-aparts developed in type 1 faults of little slip and were cemented by calcite C1. Calcite C1 has a bright orange luminescence and  $\delta^{18}\text{O}$  values about -15.1‰ vPDB and  $\delta^{13}\text{C}$  values about -6.9‰ vPDB. The next deformation phase recognized in this outcrop is  $D_3$  (Fig. 3), which is characterized by the development of pseudotachylytes in type 3A normal faults. This generation of fractures was later reactivated and cemented by calcite C3a forming crack-seals. Simultaneously, a gouge was formed. Consequent type 3B fractures, representing the deformation phase  $D_4$ , were produced and cemented by calcite C3b. Both calcites C3 are formed by bright orange calcite crystals that have  $\delta^{18}\text{O}$  values between -20‰ and -18‰ VPDB and  $\delta^{13}\text{C}$  values about -6‰ VPDB. During deformation phase  $D_5$ , type 3C joints were cemented by iron oxides. Finally, type 3D faults of  $D_6$  were cemented by calcite cement C5, which consists of microsparite calcite crystals with bright orange luminescence that shows a  $\delta^{18}\text{O}$  value of -5.8‰ vPDB and a  $\delta^{13}\text{C}$  value of -7.7‰ vPDB.

Finally, in the Sariol outcrop, no evidence of chloritisation is observed and deformation occurred in both footwall and hanging wall of the Hospital fault, unlike the previous outcrops. Uniquely, two deformation phases have been identified  $D_2$  and  $D_6$ .  $D_2$  is represented by the formation of a random breccia in a type 2B inverse fault affecting the granodiorite. It is cemented by dull to bright orange twinned calcite C2b and C2c crystals with  $\delta^{18}\text{O}$  values about -6‰ VPDB and  $\delta^{13}\text{C}$  values about -7.2‰ VPDB. During  $D_6$ ,

type 3D normal faults were generated producing cataclasites in the previous random breccia and in the Triassic calcitized dolostone of the hanging wall. These cataclasites are cemented by calcite-dolomite cement C6, which has  $\delta^{18}\text{O}$  values about -3‰ VPDB and  $\delta^{13}\text{C}$  values about -7.6‰ VPDB. Finally, the Hospital fault was cemented by calcite PC1 forming a palisade.

### 5.3. Chlorite and white mica petrography

As P-T conditions are estimated from chlorite and mica equilibrium, a brief petrographic description of these minerals is required.

Two types of chlorite were identified. The first one is the result of biotite alteration and it is only identified in the Hospital outcrop. These chlorites are recognised by the alternation with sheets of biotite, their prismatic morphology and/or the marked cleavage of the previous biotite (Fig. 5a). They have a strong pleochroism from yellow to bright or dark green. The second type is constituted by neoformed chlorites that precipitate in type 1 and type 3A faults or as patches in the cataclasite matrix (Fig. 5b). They are larger when precipitate in fractures (200  $\mu\text{m}$ -1mm) than in the cataclastic matrix (7-150  $\mu\text{m}$ ). This chlorite usually shows an irregular and amoeboid morphology and has slight or no pleochroism.

Two groups of K-white mica have been texturally differentiated: a coarse idiomorphic K-white mica between 0.2 and 1.1 mm long in the slightly brecciated granodiorite of the Vallès fault and later small flakes of K-white mica between 15 and 90  $\mu\text{m}$  in size that crystallize along type 1 faults crosscutting or overgrowing detrital flakes of the previous mica (Fig. 5 c-d). The coarse K-white mica is formed by a core with marked cleavage (M1) rimmed by another white mica with poor cleavage (M2). The small flakes crystallize together with chlorite in type 1 faults (Fig. 5e-f). These flakes are named M3 and M4 according to chemical criteria (see section 6.1.1)

## 6. THERMOBAROMETRIC RESULTS

### 6.1. Chemical variations and thermobarometry

#### 6.1.1. K-white mica

The two groups of K-white mica previously described, coarse idiomorphic (M1-M2) and later small flakes (M3-M4), show muscovite/pyrophyllite ratios of 0.9 and 0.8, respectively. M1-M2 mica is muscovite-richer than M3-M4 mica. However, independently from this ratio, both kinds show the same trend, which is marked by an increase of the celadonite proportion associated with a decrease in muscovite and pyrophyllite end-member proportions from M1 to M2 and M3 to M4, respectively (black arrows in Fig. 6). The small flakes that postdate M1-M2 mica are named M3 and M4, where M4 are the celadonite-rich ones. These two trends correspond to two growing events characterized by different mica shapes, P-T conditions and probably bulk rock compositions. The average K-white mica compositions of each group and the corresponding structural formulas are listed in table 1.

A P-T line corresponding to the equilibrium between K-white mica, quartz and water was calculated for each mica composition using the method proposed by Dubacq et al. (2010) (method in § 1.1). At a fixed pressure of 1 kbar, muscovite-rich M1 and M2 K-white mica show higher temperature (360 and 310°C, respectively) than the pyrophyllite-rich M3 and M4 K-white mica (270 and 250°C, respectively) (Fig. 7).

#### 6.1.2. Chlorite

The chlorite compositions were plotted into a (Mg, Fe)-amesite, clinochlore+daphnite and (Mg, Fe)-sudoite ternary diagram, using the structural formulas calculated with the  $\text{Fe}^{3+}$  content predicted by the convergence of R1 to R4 (see below). The chlorite compositions evolve along a trend corresponding to a decrease in amesite, clinochlore and daphnite and an increase in sudoite end-member proportion. Sudoite proportion increases from 0.2 to 0.6 in the Vallès fault and 0.2 to 0.45 in the Hospital fault (Fig. 8). The chlorite compositions and corresponding structural formulas are listed in table 2.

The chlorite-quartz-water equilibria (R1 to R4) are located at temperatures between 125 and 310°C in the Vallès fault and between 240 and 310°C in the Hospital fault at 1 kbar (absolute error about  $\pm 50^\circ\text{C}$ ) (Fig. 9). The temperature histogram allow to differentiate four generations of chlorites within the Vallès fault: CHL1 from 260 to 310°C ( $\text{XFe}^{3+}=0.24$ ), CHL2 from 240 to 260°C ( $\text{XFe}^{3+}=0.28$ ), CHL3 from 190 to 240°C ( $\text{XFe}^{3+}=0.33$ ), and, CHL4 from 125 to 190°C ( $\text{XFe}^{3+}=0.41$ ). The former two groups, CHL1 and CHL2, were also identified in the Hospital fault. The chlorite crystallization temperatures were estimated at 1 kbar, due to regional constraints. Changing the value of pressure within  $\pm 1$  kbar does not change significantly the temperature estimates, because equilibria R1 to R4 are mostly dependent on T over this range of P-T conditions.



The uncertainty on the chlorite temperature stemming from the analytical error was investigated in order to verify that the groups of composition-temperature identified above were not an artifact resulting from the analytical uncertainties of the EMPA measurements. A Monte Carlo method was used: 1000 compositions of chlorites were randomly simulated from the average group compositions using a normal distribution. The simulated distribution was set in order to reproduce the measured precision at  $\pm 1\text{wt}\%$ . The temperature and  $\text{Fe}^{3+}$ -content of each composition was estimated and the results are plotted in the figure 10. The estimated temperatures of the groups of chlorite in the Vallès fault are  $283 \pm 20.4\text{ }^{\circ}\text{C}$ ,  $253 \pm 13.0\text{ }^{\circ}\text{C}$ ,  $228 \pm 11.7\text{ }^{\circ}\text{C}$  and  $142 \pm 13.1\text{ }^{\circ}\text{C}$  (Fig. 10a). The temperatures of the two groups in the Hospital fault are  $307 \pm 17.7\text{ }^{\circ}\text{C}$  and  $245 \pm 7.7\text{ }^{\circ}\text{C}$  (Fig. 10b). These results show that the identified groups of chlorites correspond to true distinct groups of composition and temperature of formation. The above Monte Carlo analysis does not take into account the errors resulting from the uncertainties of the thermodynamic data, which cannot be assessed. However, it is emphasized that such errors have a systematic effect on the absolute temperature, but not on the relative values of the chlorite groups. This is the reason why an absolute uncertainty on the temperature estimates of  $\pm 50^{\circ}\text{C}$  was used.

The generations of chlorites are established by chemical criteria and do not correlate with the types of chlorites differentiate petrographically. The relationships with the structural locations are not easy to identify due to the complexity of the recrystallization of chlorite at low temperature (see example in Lanari et al. 2012). However, some 3A faults are mainly filled by low temperature chlorites (corresponding to the CHL4 group) and most of these chlorites form a rim around high-T chlorites (CHL1 to CHL3 groups), indicating their later formation.

## 6.2. P-T estimates

Chlorite-mica-quartz-water multi-equilibrium approach was applied to chlorite and mica of the Vallès fault. Only equilibrium between chlorite and M3 and M4 mica was obtained, which is coherent with the petrological observations, as only these mica show structural and spatial relationships with chlorite (section 5.3).

The P-T estimates from the chlorite-mica multi-equilibrium show groups of chlorite-mica associations coherent with the previously established chlorite generations (results are plotted with the same colors in

Fig. 11A). The first association is defined by the equilibrium between chlorite and M3 mica and ranges from 260 to 310°C at pressures between 0 and 3.5 kbar  $\pm$  2.5 kbar. The second is defined by the equilibrium between chlorite and M3 and M4 mica. This stage ranges from 240 to 260°C at P between 0 and 1  $\pm$  2.5 kbar with M3 and P between 1 and 3 kbar with M4. Finally, the third group is defined by chlorite in equilibrium with M4 mica. The P-T conditions of this stage ranges from 190 to 240°C at pressures between 0 and 0.6  $\pm$  2 kbar. Although the scatter and the uncertainty on the calculated P-T conditions are significant, the inferred P-T path followed by the fault rocks in the Vallès fault describes general trend of decreasing temperature and pressure.

## 7. DISCUSSION

### 7.1. Origin of K-white mica

M1 mica rimmed by M2 mica conform coarse idiomorphic and muscovite rich K-white micas, resembling result of crystallization from an igneous origin. However, two-mica granodiorites have never been described in the area (Enrique 1990). The formation of this kind of well-developed crystals has been described as resulting from deuteric alteration during cooling (Demange et al. 1996) by igneous water-rich fluids when the igneous mass was already solidified. This alteration affects preferentially the fractured pluton rims (Shelley 1983). Therefore, M1 K-white mica is formed in fractures produced during the exhumation of the granodiorite at temperatures between 330 and 370°C (range established between the minimum temperature estimated with the mica-quartz-water equilibrium lines and the estimated temperature at 1.5 kbar, depth of granodiorite emplacement). Pluton exhumation took place during the Permian and reached the surface as denoted by the unconformity between the granodiorite and Triassic materials of Buntsandstein facies outcropping in the area (Gómez-Gras and Ferrer 1999). M1 mica is in turn partially overgrown by M2 mica at lower temperatures, (between 290 and 330°C), also during the pluton exhumation. Later M3 and M4 phengite crystallize in fractures crosscutting or overgrowing detrital flakes of M1 and M2 mica and have higher pyrophyllite/muscovite ratio than M1 and M2 muscovite. This increase in the pyrophyllite proportion is produced by pyrophyllitic substitution ( $\text{Si} \square \text{K}_{1-2}\text{Al}_1$ ). Taking into account their formation in fractures, the crystallization of pyrophyllite-rich mica is

probably controlled by the circulation of externally derived fluids and a localized increase of pressure due to tectonic stress in the fault core.

Although the granodiorites in the footwalls of the Vallès and the Hospital faults have the same texture and composition, crystallization of M1 and M2 mica has only been observed in the Vallès fault. This location of M1 and M2 mica in the Vallès fault probably indicates that the outcrops of the Vallès fault were near the pluton border whereas the outcrops of the Hospital fault were in an inner position or in a less fractured zone. In the same way, the high density of fractures close to the pluton border would have been the responsible of the thicker fault zone in the Vallès fault (60 m) in front of the narrower Hospital fault zone (1-3 m). As mentioned previously, later M3 and M4 phengite are texturally and spatially related to M1 and M2 muscovite. Therefore the crystallization of M3 and M4 phengite is conditioned by the presence of previous M1 and M2 coarse muscovite, which change the bulk rock composition of the granodiorite that is necessary for the neoformation of the late K-white mica groups.

The coincidence between the localization of Hercynian fractures with M1 and M2 muscovite and the Vallès fault suggests that this fractured zone of the granodiorite was used for the later development of the Vallès fault. In the Enric outcrop (Hospital fault, see Fig. 1), Cenozoic and Mesozoic deformation overprints previous mylonite bands, indicating therefore the reactivation of Hercynian structures, which has not been described previously in the Catalan Coastal Ranges.

## **7.2. Interpretation of P-T estimates linked to main tectonic events**

The petrological study together with P-T estimates show that fault zones followed a continuous retrograde path through time (Fig. 11a). The constraints obtained from fission-track studies allow us to associate the chlorite generations of the Vallès fault with the several tectonic events involved in the formation of the Catalan Coastal Ranges. Fission-track and (U-Th)/He studies with apatites and zircons in this sector of the Catalan Coastal Ranges show that the 190°C isotherm (closure temperature for zircon PAZ) was crossed during Mesozoic extension (Juez-Larré 2003). This observation locates the neoformation of M3 and M4 phengite and related chlorite, and by extension the first deformation phase (D<sub>1</sub>), to this extensional tectonic event (Fig. 11). However, two rift stages followed by their relative post-rift stages occurred during the Mesozoic. In order to delimit the formation of M3-M4 phengite and related chlorites inside one of these rift stages, our data were compared with other works on hydrothermal veins in the

Catalan Coastal Ranges and the Iberian Chain (Fig. 11b). Temperatures between 190 and 230°C in calcites (calcites CI, in Cardellach et al. 2002) have been attributed to the second Mesozoic rifting in the Berta mine (Montnegre Horst, Fig.1). These calcites have the same characteristics as the calcites C1 defined in this work. Temperatures between 120 and 300°C have been also assigned to the second Mesozoic rift stage from illite-kaolinite and illite-pyrophyllite associations within the Permo-Triassic rocks of the Espadán Ranges (Iberian Chain) (Martín-Martín et al. 2008). Both comparisons would point to the formation of chlorite ( $T > 190^{\circ}\text{C}$ ), K-white mica M3 and M4 and calcite C1 to this second Mesozoic rift stage. The  $\delta^{18}\text{O}$  composition of the fluid responsible of the precipitation of these cements was calculated through the modified equation of Craig and Gordon (1965), obtaining values between +7 and +10‰ SMOW. Taking into account that the  $\delta^{18}\text{O}$  composition of granodiorites is about +10‰ SMOW, the origin of these fluids has been interpreted as meteoric waters that have been warmed at depth, previously to their upflow through faults, and that has been completely buffered by the granodioritic host-rock. Moreover due to the submarine conditions in most of the basin during this extensional event, these fluids were mixed with marine waters during their upflow (Cantarero et al. in press) (Fig. 12a).

The timing of low temperature chlorite (125-190°C) growth is more difficult to assess. The temperature conditions of LT chlorite crystallization were achieved both during the Mesozoic and Neogene extension, as denoted by fission-track and fluid inclusion studies. Fission-track studies demonstrated that the 110°C isotherm (closure temperature for apatite PAZ) was crossed at the onset of the Neogene extension. Studies of fluid inclusions in veins of the Catalan Coastal Ranges have shown that temperatures between 110°C and 190°C were reached during both rifting events, i.e. fluorites of the Rigròs veins and calcites of the Berta mine (CII, in Cardellach et al. 2002) (Fig. 11). However, fluid inclusion temperatures between 125 and 190°C belonging to the Mesozoic were measured in fluorites whereas this range of temperatures attributed to the Neogene was obtained from calcites CII. Fluorites are not present in the studied outcrops whereas calcite is a common neoformed mineral. Moreover, these Neogene calcites (CII) show similar geochemical characteristics than the calcites C3 and C4 defined in this paper. Therefore, LT chlorite crystallization (+calcites C3 and C4 and laumontite) and type 3A and 3B fractures, where most of these cements precipitated, took place during the Neogene extensional event. From the  $\delta^{18}\text{O}$  isotopic composition of calcites C3 and C4 (-20 and -24‰ VPDB, respectively) and a medium value of temperature obtained from chlorite (150°C), the origin of the parental fluid of these cements can be inferred applying the modified equation of Craig and Gordon (1965). The results are fluids with  $\delta^{18}\text{O}$

values about 0‰ SMOW for C3 and -4.1‰ SMOW for C4. These fluids have been interpreted as meteoric fluids that have been warmed at depth and later have upflowed through the main faults. During flow, these fluids have suffered a strong interaction with host-rocks, especially the granodiorite, causing the buffering of their isotopic signal. Moreover, in the Hospital fault, due to its position close to the Miocene shoreline, these fluids could have been mixed with marine water yielding to their more positive values (fig. 12).

Nowadays, hot springs along the Vallès fault have superficial temperatures up to 70°C and calculations of the reservoir temperature reach 110-120°C (Trilla 1974; Albert 1975). From reservoir temperature and the  $\delta^{18}\text{O}$  value of these thermal waters, -7‰ SMOW according to Trilla (1974), the  $\delta^{18}\text{O}$  content of the calcites that could precipitate nowadays would be about -23‰ VPDB, value of calcites C4. In turn, calcite C4 is related to the presence of laumontite. The stability of laumontite is constrained at very low carbon dioxide contents in the solution (mole fraction of  $\text{CO}_2$  below 0.1) and neutral to slightly alkaline waters in conditions of low pressure and low temperature (Liou et al. 1985). The present-day thermal waters of Caldes de Montbui have pH values between 7.9 and 8.35 and values of dissolved  $\text{CO}_2$  of 0.88 mg/l, yielding in the laumontite stability field. In fact, the precipitation of calcite C4 or laumontite is caused by very low fluctuations in the  $\text{CO}_2$  content of waters, as laumontite is very sensitive to these variations (Ivanov and Gurevich 1975). Thus hydrothermalism in the Vallès fault has remained active from the onset of the Neogene extension up to nowadays characterized by the precipitation of calcite C4, laumontite and LT chlorite. In contrast, hydrothermalism in the Hospital fault only took place during the Neogene syn-rift stage, as shown by precipitation of calcite C3. The later deformation stages of the Hospital fault associated with the post-rift, from  $\text{D}_5$  to  $\text{D}_7$ , were characterized by low-temperature fluids responsible of precipitation of calcites C5, C6 and PC1 (Cantarero et al. in press).

According to previous works, maximum burial of the studied outcrops reached 3.6 km before the Paleogene compression and 2.2 km before the Miocene extension (e.g. Juez-Larré 2003, ter Voorde et al. 2007). The estimated pressures above 1.5 kbar are not compatible with these results. This inconsistency is possibly due to uncertainties in the P estimates caused by errors in the used thermodynamic models and in the microprobe analyses. However, the uncertainty on P-T estimates is about 50°C and 2.5 kbar, and our results are still in rough agreement with the absolute values of previous studies. The estimated path, which shows a decrease of pressure, is consistent with the tectonic evolution of the Vallès fault. On one hand, deformation is located in the footwall of the fault. During extensional tectonics the footwall is

exhumed due to isostatic rebound and consequent erosion of the shoulder. On the other hand, the traces of the Paleogene thrust and the normal fault are not coincident in surface but the former is displaced to the north (Anadón 1986). Therefore, the previous normal fault was located in the hangingwall of the thrust and was uplifted during thrusting. This divergence between the compressional and extensional structures also explains the lack of microstructures and cements linked to compression overprinting the Mesozoic fractures of the Vallès fault (Fig. 12). Instead, it is produced the blue gouge in 2A thrust faults during the second deformation phase. On the opposite, in the Hospital fault, the Mesozoic fault is inverted during the Paleogene, as registered by the low-temperature calcite cements C2 in 2B thrust faults (fig. 12).

### **7.3. Migration paths of fluids along main faults**

Along both the Vallès and Hospital faults different neoformed mineral associations are evidenced (Fig. 4). This could be due to fault zone architecture changes, inherited structures, independent tectonic activity of fault segments and/or localized migration paths of certain fluids.

In the Hospital fault, these differences in neoformed minerals were mainly interpreted as the result of the different origin of the fault segments during the Mesozoic and their later independent tectonic activity during the Mesozoic, Paleogene and Neogene (Cantarero et al. in press).

In the Vallès fault, these differences are attributed to the different structural position of the outcrops within the footwall. The Camí d'En Cisa outcrop is located in the contact with the Miocene materials and only the formation of laumontite L2 related to the Neogene extension is registered. On the other hand, the Torrent del Corró outcrop, located 50 m from the contact, shows all the deformation stages, mainly chlorite-mica, chlorite and calcite veins. As mentioned above, mica-chlorite veins and calcite C1 have been related to the Mesozoic extension whereas low-T chlorite, laumontite and calcite C4 have been related to the Neogene extension. This means that the TCO outcrop represents the location of a Mesozoic fault zone reactivated during the Neogene deformation. These observations point to an offset between the Mesozoic and the Neogene faults (Fig. 12). Furthermore, most of the low-T chlorites (125 to 190°C group) form a rim around high-T chlorites ( $T > 200^{\circ}\text{C}$ ), indicating the reactivation of the Mesozoic structures with phyllosilicates during the Neogene. This reactivation was possible due to the low friction coefficient of chlorite and K-white mica and their arrangement in localized fracture planes under hydrated conditions (Lacroix 2011; Behnsen and Faulkner 2012; Buatier et al. 2012). Probably, the absence of

Neogene chlorite within the Hospital fault is due to the lack of a strong preferred orientation of chlorite crystals together with the lack connection between them within the foliation.

#### **7.4. Implications on the geothermal gradient**

The calculated high temperature formation of chlorite and K-white mica (125-310°C) together with the formation temperature of laumontite (100- 230°C, Kristmannsdóttir and Tómasson 1976), and linked to depth constraints, imply geothermal gradients higher than the regional gradients during the two extensional tectonics events . According to our data, geothermal gradients during the Mesozoic ranged between 55 and 83°C/km and from 56 to 86°C/km during the Neogene. These values are much larger than the regional gradients estimated on the basis of the thermal boundary conditions and thickness of the lithosphere and the thermal conductivity of materials by Juez-Larré (2003) (27-35°C/km in the Mesozoic and 24±3°C/km in the Neogene). The main hydrothermal processes during Neogene were assumed to take place at the onset of extension as it was marked by fission-track data and therefore the depth previous to the extensional process was taken for calculations. However, evidence of hot fluids associated to faults have been also described during the Neogene post-rift (Calvet et al. 1996, 2001) in the Penedès basin fill and nowadays in the Caldes de Montbui area (López de Azcona 1983). Important exhumation was already achieved at the post-rift stage, which linked with the hydrothermalism, would even cause higher geothermal gradients.

The difference between regional gradients and our data suggests that during both extensional tectonic events faults acted as conduits for ascending hot fluids, which produced anomalous high geothermal gradients along fractures. This fact is also supported by the resetting of fission-tracks mostly near main fault zones limiting the grabens (Juez-Larré 2003).

#### **8. CONCLUSIONS**

The Vallès and Hospital faults are two of the main faults that constitute the central sector of the Catalan Coastal Ranges. In these faults, deformation is localized in the granodiorite that constitutes the footwall where different fault rocks, from breccias to ultracataclasites, were formed.



Seven deformation phases have been related to the three main tectonic events described in the area through structural and petrographic studies, thermodynamic modelling from chlorite and phengite, and fission-track constraints. In the Vallès fault, previously to the first tectonic event, crystallization of muscovite-rich M1 and M2 K-white mica took place as the result of deuteritic alteration during the exhumation of the pluton, which ended in the Permian, at temperatures between 330 and 370°C.

The first tectonic event is attributed to the Mesozoic extension and it is represented by the first deformation phase (D<sub>1</sub>). In the Vallès fault it is characterized by the crystallization of M3 and M4 phengite together with chlorite at temperatures between 190 and 310°C and calcite C1. In the Hospital fault, only chlorite formed at temperatures between 240 and 310°C together with calcite C1.

The second tectonic event is related to the Paleogene compression and it is defined by the second deformation phase (D<sub>2</sub>). Low-temperature calcite cements belonging to the Paleogene compression have been identified in the Hospital fault, whereas in the Vallès fault deformation is concentrated along the short-cut, avoiding the reactivation of the Mesozoic structures.

Finally, the third tectonic event is associated with the Neogene extension. Five deformation phases have been recognised (D<sub>3</sub>-D<sub>7</sub>) from which D<sub>3</sub> and D<sub>4</sub> are related to the syn-rift stage. In the Vallès fault, type 3A normal faults were cemented by chlorite formed at temperatures below 190°C, associated to calcite C4 and laumontite. Later these faults were offset by type 3E strike-slip faults. In the Hospital fault, type 3A and 3B fractures were cemented by calcite C3. During the post-rift, calcites C5, C6 and PC1 precipitated. Both faults have registered two hydrothermal events, one during the Mesozoic and one during the Neogene. However, hydrothermalism has remained active up to recent times in the Vallès fault only. Hydrothermalism in the Hospital fault was restricted to the syn-rift stage, and the post-rift stage was dominated by low-temperature fluids.

The different association of neoformed minerals along the two main faults is conditioned by: 1) *Tectonic processes*: the various origin and later tectonic activity of the segments that form the Hospital fault, and the offset between the Mesozoic and the Neogene faults that constitute the Vallès fault both control the temporal and spatial distribution of fluids and cements. 2) *The rheologic properties of minerals*: the presence of preferentially oriented chlorites concentrated along plains generates a microfabric that weakens the fault. The drop of friction coefficient favours stable sliding, and therefore the formation of successive generations of chlorite. 3) *Previous mineralogic compositions*: the existence of previous mineral phases only in certain areas can cause the necessary change in the bulk rock composition to

generate a new neoformed mineral (i.e. only where M1-M2 muscovite exist, M3-M4 phengite are formed). Also small oscillations on the chemical conditions of the fluid can control the precipitating phase (i.e. the calcite-laumontite relationship).

The structural and temporal relationships between M3-M4 phengite and M1-M2 muscovite indicates that hercynian fractures were reactivated and overprinted by the Mesozoic and Cenozoic development of the Vallès fault. During Mesozoic and Neogene tectonic events, faults acted as conduits for hot fluids producing localized anomalous high geothermal gradients (50°C/km minimum) along the faults.

The estimated decrease of pressure is consistent with exhumation produced during Alpine compression and Mesozoic and Neogene extensions. During the Neogene extension, exhumation of the granodiorite followed a nearly isobaric cooling path.

## 9. ACKNOWLEDGEMENTS

We thank Anne-Marie Boullier for discussion and useful comments during thin section description. We are grateful with Jordi Illa for sample preparations and with the Thin Section Service of the Universitat de Barcelona. The stable isotopy, the electron microprobe and the SEM analyses were carried out at “Serveis Científic-Tècnics” of the Universitat de Barcelona. This research was performed within the framework of DGICYT Spanish Project CGL2010-18260, *Grup Consolidat de Recerca "Geologia Sedimentària"* (2009SGR-1451) and the grants 2010BE1 00708 and 2010FI\_B2 00179 supported by the Comissionat per a Universitats i Recerca del Departament d'Innovació, Universitats i Empresa de la Generalitat de Catalunya i el Fons Social Europeu.

## 10. REFERENCES

- Agard P, Vidal O, Goffé B (2001) Interlayer and Si content of phengite in HP–LT carpholite-bearing metapelites. *J Metamorph Geol* 19(5):479–496
- Albert JF (1975) El equilibrio albita-anortita como termómetro hidrogeotérmico en zonas graníticas. *Acta Geol Hisp X* (5):170-174

655 Albert JF, Corominas J, París C (1979) El estudio hidrogeológico de los manantiales y su aplicación  
 656 geológica: caso de las aguas termales, carbónicas y sulfhídricas de Cataluña. *Acta Geol Hisp. Homenatge*  
 657 a Lluís Solé i Sabarís 14:391-394  
 658 Anadón P, Colombo F, Esteban M, Marzo M, Robles MS, Santanach P, Solé-Sugrañes LI (1979)  
 659 Evolución tectonoestratigráfica de los Catalánides. *Acta Geol Hisp* 14:242-270  
 660 Anadón P, Cabrera L, Guimerà J, Santanach P (1985) Paleogene strike-slip deformation and  
 661 sedimentation along the southeastern margin of the Ebro Basin. In: *Strike-slip Deformation, Basin*  
 662 *Formation Sedimentation* (eds. K.T. Biddle & N. Christie-Blick) Special Publication of the Society of  
 663 Economic Paleontologists and Mineralogists 37:303-318  
 664 Anadón P (1986) Las facies lacustres del Oligoceno de Campins (Vallès Oriental, Provincia de  
 665 Barcelona). *Cuadernos de Geología Ibérica* 10:271-294  
 666 Árkai P, Faryad SW, Vidal O, Balogh K (2003) Very low-grade metamorphism of sedimentary rocks of  
 667 the Meliata unit, Western Carpathians, Slovakia: implications of phyllosilicate characteristics. *Int J Earth*  
 668 *Sci* 92:68-85  
 669 Ashauer H, Teichmüller R (1935) Die variszische und alpidische Gebirgsbildung Kataloniens.  
 670 *Abhandlungen Gesellschaft Wissenschaften Göttingen, Math Phys K1, 3F, 16.*  
 671 Baqués V, Travé A, Cantarero I (in press) Development of successive karstic systems within the Baix  
 672 Penedès Fault zone (onshore of the Valencia Trough, NW Mediterranean). *Geofluids*.  
 673 Bartrina MT, Cabrera L, Jurado MJ, Guimerà J, Roca E (1992) Evolution of the central Catalan margin of  
 674 the Valencia trough (western Mediterranean). *Tectonophys* 203:219-247  
 675 Behnsen J, Faulkner DR (2012) The effect of mineralogy and effective normal stress on frictional  
 676 strength of sheet silicates. *J Struct Geol* 42:49-61.  
 677 Bitzer K, Travé A, Carmona JM (2001) Fluid flow processes at basin scale. *Acta Geol Hisp* 36(1-2):1-20  
 678 Buatier M, Lacroix B, Labaume P, Moutarlier V, Charpentier D, Sizun JP, Travé A (2012) Microtextural  
 679 investigation (SEM and TEM study) of phyllosilicates in a major thrust fault zone (Monte Perdido,  
 680 southern Pyrenees): impact on fault reactivation. *Swiss J Geosci.* 105: 313-324. doi: 10.1007/s00015-  
 681 012-0098-0  
 682 Cabrera LI (1981) Influencia de la tectónica en la sedimentación continental de la cuenca del Vallès-  
 683 Penedès (provincia de Barcelona, España) durante el Mioceno inferior. *Acta Geol Hisp* 16(3):165-171

684 Calvet F, Travé A, Roca E, Soler A, Labaume P (1996) Fracturación y migración de fluidos durante la  
685 evolución tectónica neógena en el Sector Central de las Cadenas Costero Catalanas. *Geogaceta*  
686 20(7):1715-1718

687 Calvet F, Travé A, Bitzer K, Roca E, Tritlla J, Baker J (2001) Dolomitization of detrital deposits related  
688 to Neogene extensional faults, Catalan Coastal Ranges (Spain). *Geotemas* 3(1):109-111

689 Canals À, Cardellach E, Rye DM, Ayora C (1992) Origin of the Atrevida vein (Catalan Coastal Ranges,  
690 Spain): mineralogic, fluid inclusion and stable isotopy study. *Econ Geol* 87:142-153

691 Canals À, Cardellach E (1997) Ore lead and sulphur isotope pattern from the low-temperature veins of the  
692 Catalanian Coastal Ranges (NE Spain). *Miner Deposita* 32:243-249

693 Cantarero I, Travé A, Alías G, Baqués V (in press) From hydrothermal to meteoric fluid regimes in a  
694 segmented fault affecting crystalline and carbonate rocks: case study of the Barcelona Plain (NE Spain).  
695 *Geofluids*

696 Cardellach E, Canals À, Grandia F (2002) Recurrent hydrothermal activity induced by successive  
697 extensional episodes: the case of the Berta F-(Pb-Zn) vein system (NE Spain). *Ore Geol Rev* 22:133-141

698 Carmona JM, Bitzer K, López E, Bouazza M (2000) Isotopic composition and origin of geothermal  
699 waters at Caldetes (Maresme-Barcelona). *J Geochem Explor* 69-70:441-447

700 Cathelineau M, Nieva D (1985) A chlorite solid solution geothermometer the Los Azufres (Mexico)  
701 geothermal system. *Contrib Mineral Petrol* 91(3):235-244

702 Chen WD, Tanaka H, Huang H, Lu C, Lee C, Wang C (2007) Fluid infiltration associated with seismic  
703 faulting: Examining chemical and mineralogical compositions of fault rocks from the active Chelungpu  
704 fault. *Tectonophys* 443:243-254

705 Craig H, Gordon I (1965) Deuterium and oxygen-18 variations in the ocean and marine atmosphere. In:  
706 Tongiorgi E (ed) *Stable Isotopes in Oceanographic Studies and Paleotemperatures*. Consiglio Nazionale  
707 delle Ricerche, Laboratorio di Geologia Nucleare, Pisa, pp 9-130

708 Demange M, Alvarez JO, López L, Zarco JJ (1996) The Achala Batholith (Cordoba, Argentina): a  
709 composite intrusion made of five independent magmatic suites. Magmatic evolution and deuterium  
710 alteration. *J S Am Earth Sci* 9(1-2):11-25

711 Dubacq B, Vidal O, de Andrade V (2010) Dehydration of dioctahedral aluminous phyllosilicates:  
712 thermodynamic modelling and implication for thermobarometric estimates. *Contrib Mineral Petrol*  
713 159:159-174

714 Enrique P (1990) The Hercynian intrusive rocks of the Catalan Coastal Ranges (NE Spain). *Acta Geol*  
 715 *Hisp* 25(1-2):39-64  
 716 Fernández M, Banda E (1989) An approach to the thermal field in northeastern Spain. *Tectonophys*  
 717 164:259-266  
 718 Ganne J, De Andrade V, Weinberg R, Vidal O, Allibon J, Dubacq B, Baratoux L, Chardon D, Jessell M,  
 719 Kagambega N, Naba S (2012) The Dawn of Modern Earth Plate Subduction in the Paleoproterozoic West  
 720 African Craton (2.2-2.0 Ga). *Nat Geosci* doi:10.1038/ngeo1321  
 721 Gaspar-Escribano JM, Garcia-Castellanos D, Roca E, Cloetingh S (2004) Cenozoic vertical motions of  
 722 the Catalan Coastal Ranges (NE Spain): The role of tectonics, isostasy, and surface transport. *Tectonics*  
 723 23, TC1004. doi: 10.1029/2003TC001511  
 724 Gil-Ibarguchi JI (1988) Petrología de la aureola metamórfica de la granodiorita de Barcelona en la Sierra  
 725 de Collserola (Tibidabo) *Est Geol* 44(5-6):353–374  
 726 Gómez-Gras D, Ferrer C (1999) Caracterización petrológica de perfiles de meteorización antiguos  
 727 desarrollados en granitos tardihercínicos de la Cordillera Costero Catalana. *Rev Soc Geol España*  
 728 12(2):281-299  
 729 Grosch EG, Vidal O, Abu-Alam T, McLoughlin N (2012) *PT*-Constraints on the metamorphic evolution  
 730 of the Paleoproterozoic Kromberg type-section, Barberton Greenstone Belt, South Africa. *J Petrol* 53(3):513-  
 731 545  
 732 Guimerà J (1984) Palaeogene evolution of deformation in the northeastern Iberian Peninsula. *Geol Mag*  
 733 121(5):413-420  
 734 Ivanov IP, Gurevich LP (1975) Experimental Study of T-X<sub>CO2</sub> Boundaries of Metamorphic Zeolite  
 735 Facies. *Contrib Mineral Petrol* 53:55-60  
 736 Juez-Larré J (2003) Post Late Paleozoic tectonothermal evolution of the northeastern margin of Iberia,  
 737 assessed by fission-track and (U-Th)/He analyses. A case history from the Catalan Coastal Ranges.  
 738 Dissertation, Vrije Universiteit.  
 739 Julivert M, Durán H (1990) Paleozoic stratigraphy of the Central and Northern part of the Catalanian  
 740 Coastal Ranges (NE Spain). *Acta Geol Hisp* 25(1-2):3-12  
 741 Kristmannsdóttir H, Tómasson J (1978) Zeolite zones in geothermal areas in Iceland. In: Sand LB and  
 742 Mumpton FA (eds.) *Natural Zeolites: Occurrence, Properties, Use*. Pergamon Press, Elmsford, New York,  
 743 pp 277-284

744 Lacroix B (2011) Interaction fluide-roche et comportement des phyllosilicates à basses températures en  
 745 contexte sédimentaire: exemple du prisme orogénique sud-pyrénéen. Dissertation, Université de Franche  
 746 Comté.  
 747 Lacroix B, Charpentier D, Buatier M, Vennemann T, Labaume P, Adatte T, Travé A, Dubois M (2012)  
 748 Formation of chlorite during thrust fault reactivation. Record of fluid origin and P-T conditions in the  
 749 Monte Perdido thrust fault (southern Pyrenees). *Contrib Mineral Petrol* 163(6):1083-1102  
 750 Lanari P, Guillot S, Schwartz S, Vidal O, Tricart P, Riel N, Beyssac O (2012) Diachronous evolution of  
 751 the alpine continental subduction wedge: Evidence from P-T estimates in the Briançonnais Zone houillère  
 752 (France-Western Alps). *J Geodyn* 56-57:39-54  
 753 Liou JG, Seki Y, Guillemette RN, Sakai H (1985) Compositions and parageneses of secondary minerals  
 754 in the Onikobe geothermal system, Japan. *Chem Geol* 49:1-20  
 755 López de Azcona JM (1983) Consideraciones sobre el grupo de manatiales de aguas mineromedicinales  
 756 de Caldas de Montbui. In: *Monografía X Caldas de Montbui. Monografías de aguas mineromedicinales*,  
 757 pp 5-21  
 758 Martín-Martín JD, Tritlla J, Cardellach E, Gómez-Gras D (2006) Tectonically driven fluid flow and  
 759 associated low-grade metamorphism during the Alpine compression in the eastern Iberian Chain (Spain).  
 760 *J Geochem Explor* 89:267-270  
 761 Martín-Martín JD, Salas R, Gómez-Gras D (2008) Datación por K-Ar de la diagénesis y el metamorfismo  
 762 de muy bajo grado en red-beds permo-triásicos de la Cadena Ibérica oriental (Castellón y Valencia):  
 763 resultados preliminares. *Geo-Temas* 10:257-260  
 764 Martín-Martín J, Salas R, Gómez-Gras D, Zwingmann H (2009) K/Ar isotopic dating of very low-grade  
 765 metamorphic and diagenetic conditions during the Mesozoic rifting evolution of the Iberian Chain, Spain.  
 766 XIV International Clay Conference, Italia.  
 767 Massone HJ, Schreyer W (1989) Stability field of the high-pressure assemblages talc-phengite and two  
 768 new phengite barometers. *Eur J Mineral* 1:391-410  
 769 Parra T, Vidal O, Agard P (2002) A thermodynamic model for Fe-Mg dioctahedral K White micas using  
 770 data from phase-equilibrium experiments and natural pelitic assemblages. *Contrib Mineral Petrol*  
 771 143:706-732

772 Piqué À, Canals À, Grandia F, Banks DA (2008) Mesozoic fluorite veins in NE Spain record regional  
 773 base metal-rich brine circulation through basin and basement during extensional events. *Chem Geol*  
 774 257:139-152  
 775 Roca E and Guimerà J (1992) The Neogene structure of the eastern Iberian margin: structural constraints  
 776 on the crustal evolution of the València trough (Western Mediterranean). *Tectonophysics* 203:203-218  
 777 Roca E (1996) La evolución geodinámica de la Cuenca Catalano-Balear y áreas adyacentes desde el  
 778 Mesozoico hasta la actualidad. *Acta Geol Hisp* 29:3-25  
 779 Roca E, Sans M, Cabrera L, Marzo M (1999) Oligocene to Middle Miocene evolution of the central  
 780 Catalan margin (Northwestern Mediterranean). *Tectonophysics* 315:209-233  
 781 Rossi C, Goldstein RH, Marfil R, Salas R, Benito MI, Permanyer A, de la Peña JA, Caja MA (2001)  
 782 Diagenetic and oil migration history of the Kimmeridgian Ascla Formation, Maestrat Basin, Spain. *Mar*  
 783 *Petrol Geol* 18:287- 306  
 784 Salas R, Casas A (1993) Mesozoic extensional tectonics, stratigraphy and crustal evolution during the  
 785 Alpine cycle of the eastern Iberian basin. *Tectonophysics* 228(1-2):33-55  
 786 Salas R, Guimerà J, Mas R, Martín-Closas C, Meléndez A, Alonso A (2001) Evolution of the Mesozoic  
 787 central Iberian Rift System and its Cainozoic inversion (Iberian Chain). In: Ziegler PA, Cavazza W,  
 788 Robertson AHF and Crasquin-Soleau S (eds) *Peri-Tethys Memoir 6: Peri-Tethyan Rift/Wrench Basins*  
 789 *and Passive Margins. Mem Mus natn Hist Nat* 186:145-185  
 790 Santanach P, Casas JM, Gratacós O, Liesa M, Muñoz JA, Sàbat F (2011) Variscan and Alpine structure  
 791 of the hills of Barcelona: geology in an urban area. *J Iber Geol* 37(2):121-136  
 792 Schwartz S, Tricart P, Guillot S, Lardeau JM, Vidal O (2009) Late tectonic and metamorphic evolution of  
 793 the Piedmont accretionary wedge (Queyras Schistes lustrés, western Alps: Evidences for tilting during  
 794 Alpine collision. *Geol Soc Am Bull* 121:502-518  
 795 Shelley D (1983) *Igneous and metamorphic rocks under the microscope: classification, textures,*  
 796 *microstructures and mineral preferred orientations.* Chapman and Hall, London  
 797 ter Voorde M, Gaspar-Escribano JM, Juez-Larré J, Roca E, Cloetingh S (2007) Thermal effects of linked  
 798 lithospheric and upper crustal-scale processes: Insights from numerical modeling of the Cenozoic Central  
 799 Catalan Coastal Ranges (NE Spain). *Tectonics* 26: TC5018.  
 800 Trilla J (1974) Sobre el origen de las aguas termales de Caldes de Montbui. *Acta Geol Hisp* IX (4):144-  
 801 148



Vidal O, Parra T (2000) Exhumation of high pressure metapelites obtained from local equilibria for chlorite phengite assemblage. *Geol Mag* 35:139–161

Vidal O, Parra T, Trotet F (2001) A thermodynamic model for Fe-Mg aluminous chlorite using data from phase equilibrium experiments and natural pelitic assemblages in the 100-600°C 1-25 kbar range. *Am J Sci* 63:557-592

Vidal O, Parra T, Vieillard P (2005) Thermodynamic properties of the Tschermak solid solution in Fe-chlorite: Application to natural examples and possible role of oxidation. *Am Mineral* 90:347-358

Vidal O, De Andrade V, Lewin E, Munoz M, Parra T, Pascarelli S (2006) P-T-deformation-Fe<sup>3+</sup>/Fe<sup>2+</sup> mapping at the thin section scale and comparison with XANES mapping. Application to a garnet-bearing metapelite from the Sambagawa metamorphic belt (Japan). *J Metamorph Geol* 24:669-683

Vidal O, Dubacq B, Lanari P (2010) Comment on "The role of H<sub>3</sub>O<sup>+</sup> in the crystal structure of illite" by F. Nieto, M. Melini, and I. Abad. *Clay Clay Miner* 58: 717-720

Wintsch RP, Christoffersen R, Kronenberg AK (1995) Fluid-rock reaction weakening of fault zones. *J Geophys Res* 100 (B7):13021-13032

TABLE CAPTIONS

Table 1. K-white mica analysis and atom site distribution for each mica groups.

Table 2. Chlorite composition, atom site distribution and temperature estimate for the different chlorite generations of both faults.

FIGURE CAPTIONS

**Fig. 1** Simplified geological map of the central Catalan Coastal Ranges (modified from Santanach et al. 2011). Squares indicate study areas that are enlarged in figure 2. T: Tagamanent; MT: Martorell; BT: Berta Mine; CM: Caldes de Montbui; LG: La Garriga; CE: Caldes d'Estrac.

**Fig. 2** Simplified geological maps of the studied areas. A) Vallès fault in the vicinity of Caldes de Montbui village and outcrop situation. A1) Enlarged area of the Torrent del Corró outcrop with sample location. B) Northern sector of Barcelona Plain.

**Fig. 3** Stereoplots in Schmidt lower hemisphere projections of the different generations of fractures according to crosscutting relationships. Legend: FS: fracture set; DF: deformation phase; r: reactivated fracture; Continuous line: normal fault; dotted line: inverse fault; dashed line: joint; and, dashed-dotted line: strike-slip fault.

**Fig. 4** Neoformed minerals. A) Neoformed minerals constituting fault rocks in the outcrops of the Vallès fault and Hospital fault. X marks the outcrops where the mineral is present and (X) when it is almost inexistent. B) Temporal relationships between them.

**Fig. 5** Microphotographs of chlorite and mica from Hospital and Vallès faults. A) Chlorite resulting from biotite alteration. B) Neoformed chlorite between cataclasite clasts. C) Coarse white mica M1 rimmed by M2. D) Small white mica flakes overgrowing and crosscutting big detrital flakes of M1 and M2 mica. E-F) Plane and cross-polarised light photographs of chlorite and mica association in a type 1 fracture.

**Fig. 6** Ternary plot muscovite (mus)-celadonite (cel)- pyrophyllite (pyr) of mica in fault rocks of the Vallès fault.

**Fig. 7** P-T diagram showing the results of mica-quartz-water thermometer for the four groups of mica

**Fig. 8** Ternary plot amesite (am)-clinochlore+daphnite (clin+daph)- sudoite (sud) of chlorite in fault rocks. A) Vallès fault. B) Hospital fault. Colours indicates temperature according to figure 9.

**Fig. 9** Histograms of chlorite temperatures. A) Vallès fault. B) Hospital fault.

**Fig. 10** Histogram of chlorite temperature for each group of chlorite calculated with the compositions from the Monte Carlo simulation (see text). The colors are the same as in figure 9.

**Fig. 11** A) P-T path of fault rocks in the Vallès fault and interpretation of the age through fission-track constraints. Squares represent chlorite in equilibrium with M3 mica and diamonds represents chlorite in equilibrium with M4 mica. The different colours represents the four chlorite generations. The blue square indicates the location of chlorites under 190°C, which are not in equilibrium with mica. B) Temperature and age comparison with other mineralizations of the Catalan Coastal Ranges (Berta, Rigròs and Atrevida) and the Iberian Chain (Espadán Ranges). The asterisk marks our data. 1) Cardellach et al. (2002); 2) Piqué et al. (2008); 3) Martín-Martín et al. (2006, 2008, 2009 ); 4) Canals et al. (1992).

**Fig. 12** Evolution of the Vallès and Hospital faults from Mesozoic to Neogene. A) Mesozoic extensional event. Topographically driven meteoric fluids, percolating in emerged areas, are warmed at depth and upflow through faults. Due to the submarine conditions of the major part of the basin, these fluids are mixed with marine waters at surface. B) Paleogene compressional event. In the Vallès fault a thrust system uplifts the previous normal fault. Deformation is localized in the thrust faults generating a blue gouge. In the Hospital fault, the previous Mesozoic fault is inverted and percolation of low-T meteoric waters occurs. C) Neogene extensional event. During this event, the Neogene normal Vallès fault is

890 formed (CCO) and the reactivation of some of the Mesozoic structures occurs (TCO). Hydrothermal  
891 fluids are topographically driven meteoric fluids warmed at depth. In the hospital fault, syn-rift and post-  
892 rift stages differ. During the syn-rift, meteoric hot fluids are mixed with marine waters, as occurred during  
893 the Mesozoic. On the opposite, the post-rift is dominated by low-T meteoric fluids. TCO, Torrent del  
894 Corró outcrop; CCO: Camí d'en Cisa outcrop; FPT, Frontal Paleogene thrust.

**Figure 1**

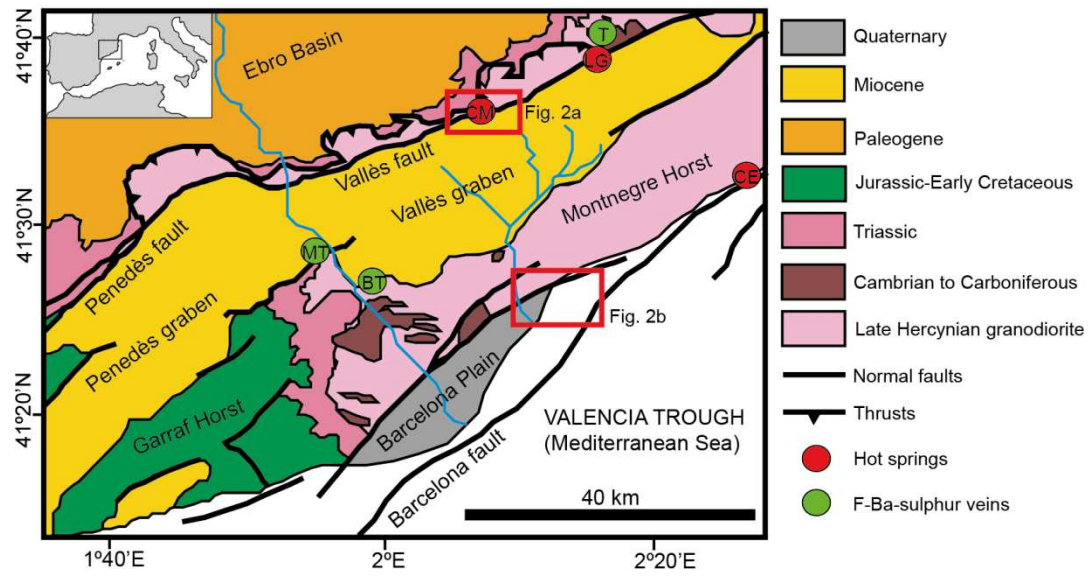


Figure 2

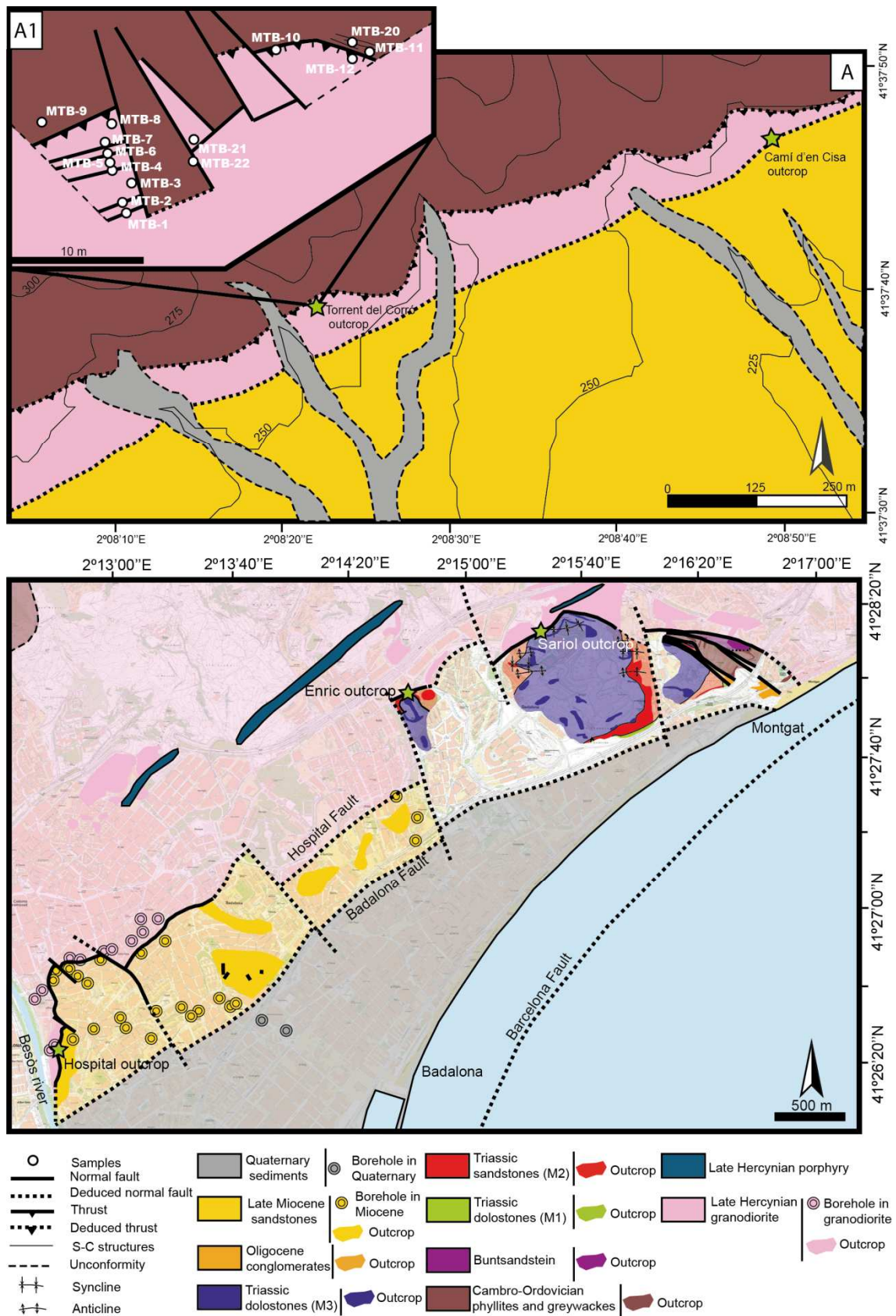
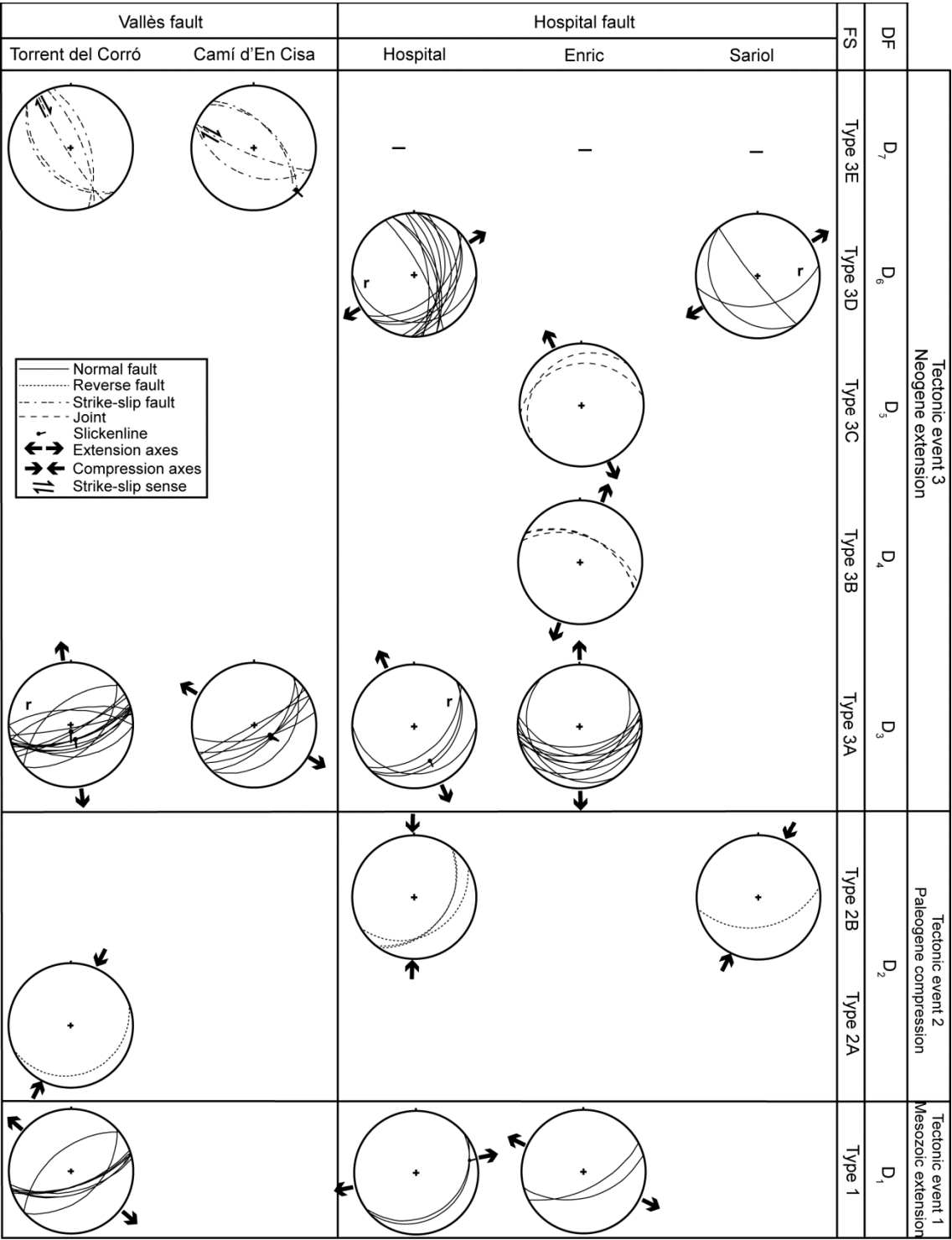


Figure 3





**Figure 4**

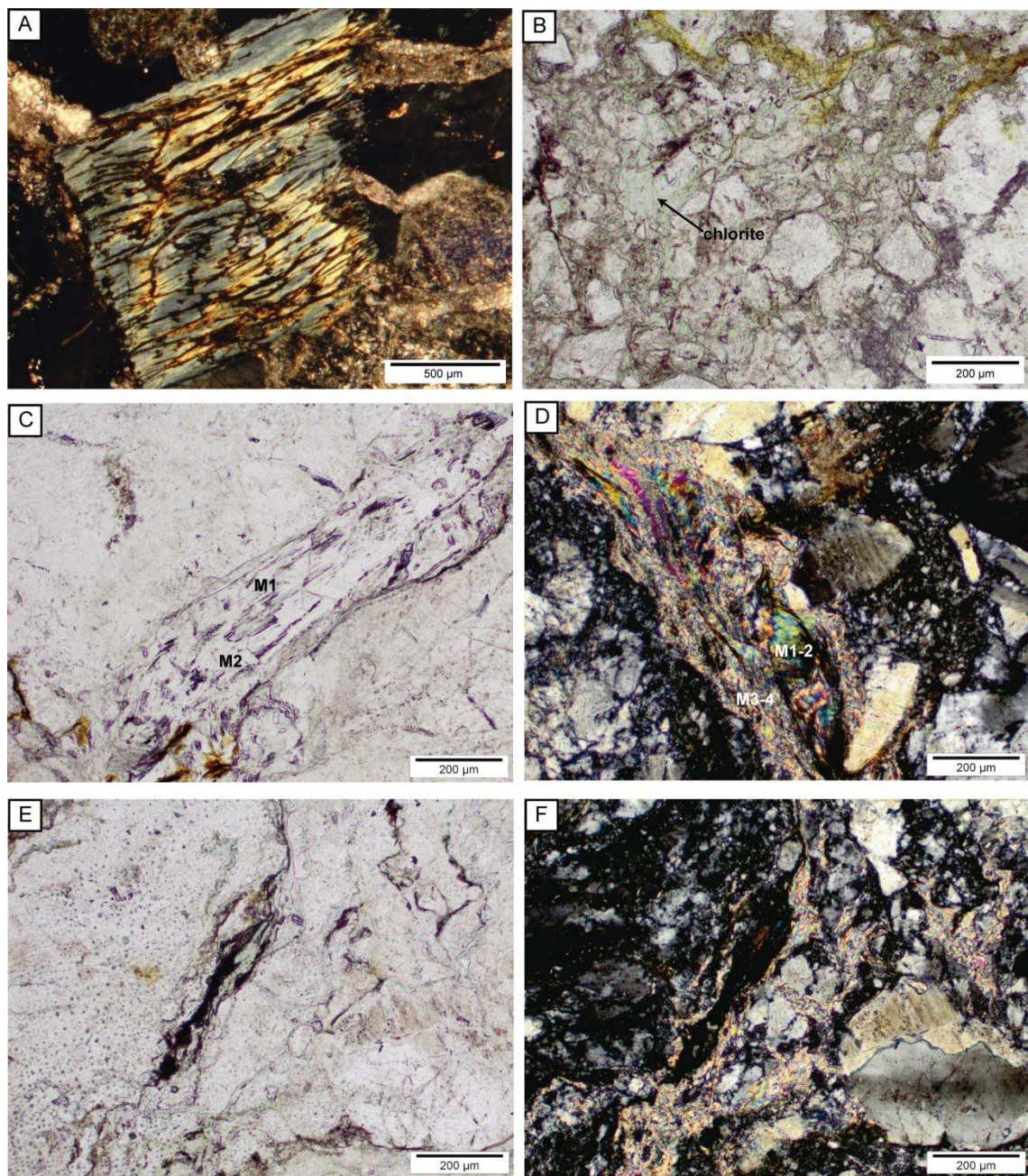
A)

Minerals	outcrops	Vallès fault		Hospital fault		
		Torrent del Corró	Camí d'En Cisa	Hospital	Enric	Sariol
Microcline		X	X			
Coarse white mica M1-M2		X	X			
Small white mica M3-M4		X	(X)			
Chlorite		X	(X)	X	X	
Epidote					X	
Quartz					X	
Calcite C1 (a-f)		X		X	X	
Iron oxides		X		X	X	
Calcite C2 (a-c)				X		X
Calcite C3 (a,b)					X	
Laumontite L1		X	(X)			
Calcite C4		X	(X)			
Laumontite L2			X			
Calcite C5					X	
Calcite C6						X
Calcite PC1						X

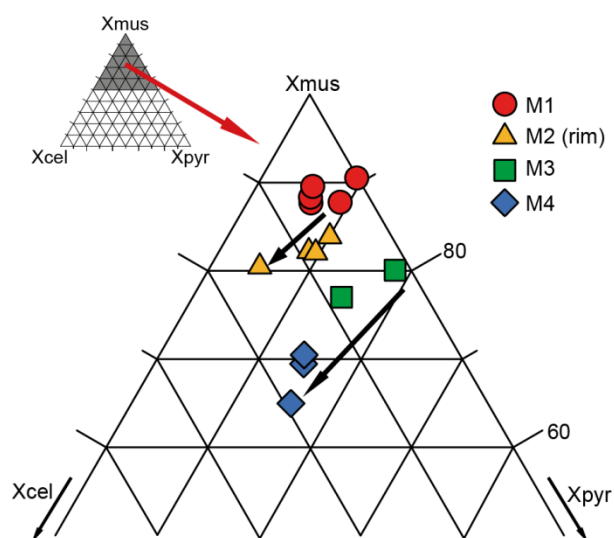
B)

	Host-rock	D <sub>1</sub>	D <sub>2</sub>	D <sub>3</sub> -D <sub>4</sub>	D <sub>5</sub>	D <sub>6</sub>	D <sub>7</sub>
Microcline							
Coarse white mica M1-M2							
Small white mica M3-M4							
Chlorite							
Epidote							
Quartz							
Calcite C1 (a-f)							
Iron oxides							
Calcite C2 (a-c)							
Calcite C3 (a,b)							
Laumontite L1							
Calcite C4							
Laumontite L2							
Calcite C5							
Calcite C6							
Calcite PC1							

**Figure 5**



**Figure 6**



**Figure 7**

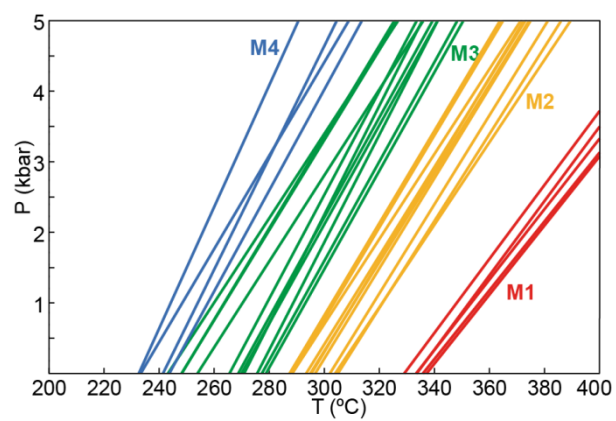


Figure 8

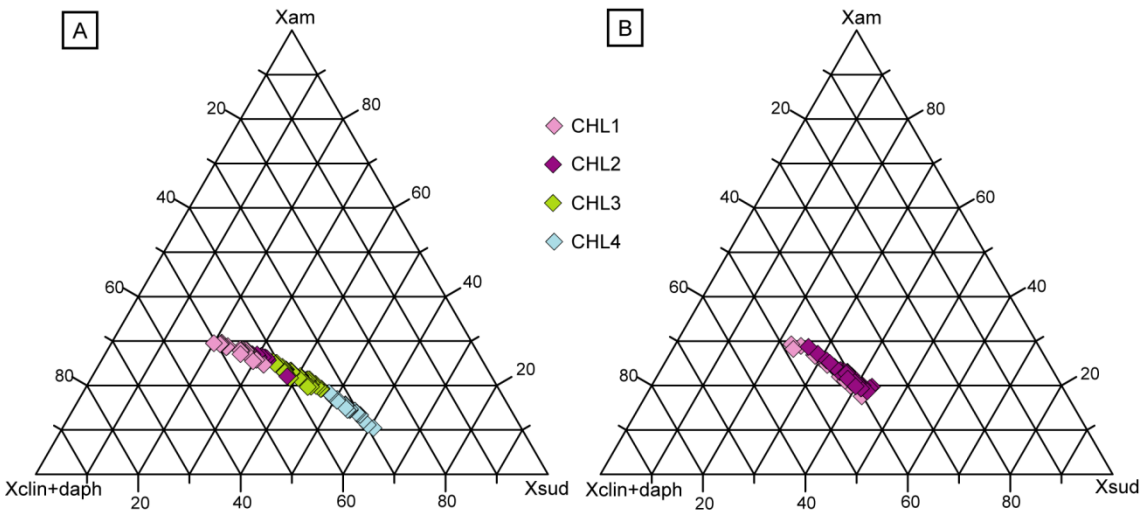


Figure 9

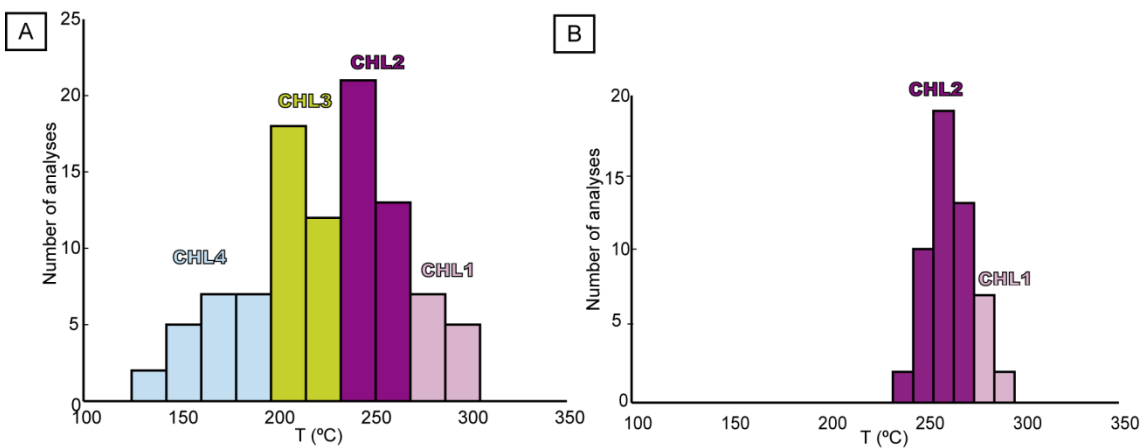


Figure 10

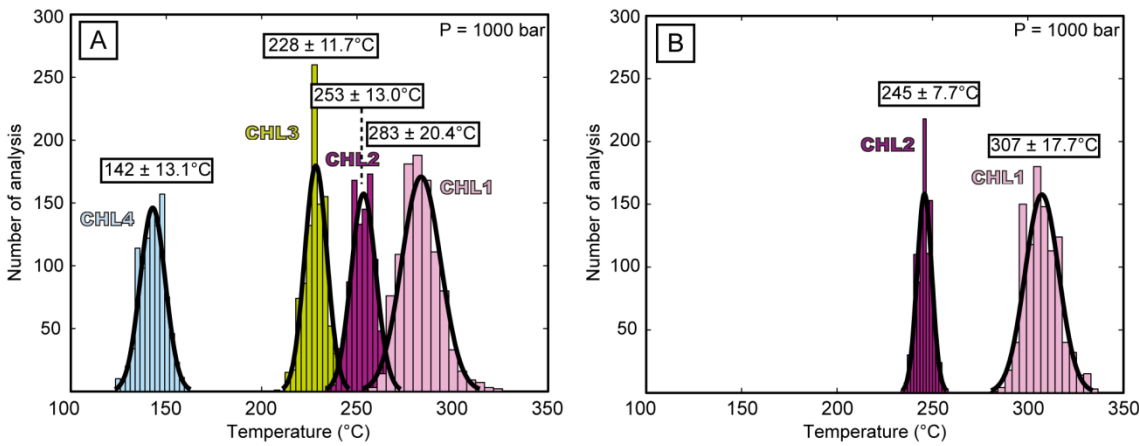


Figure 11

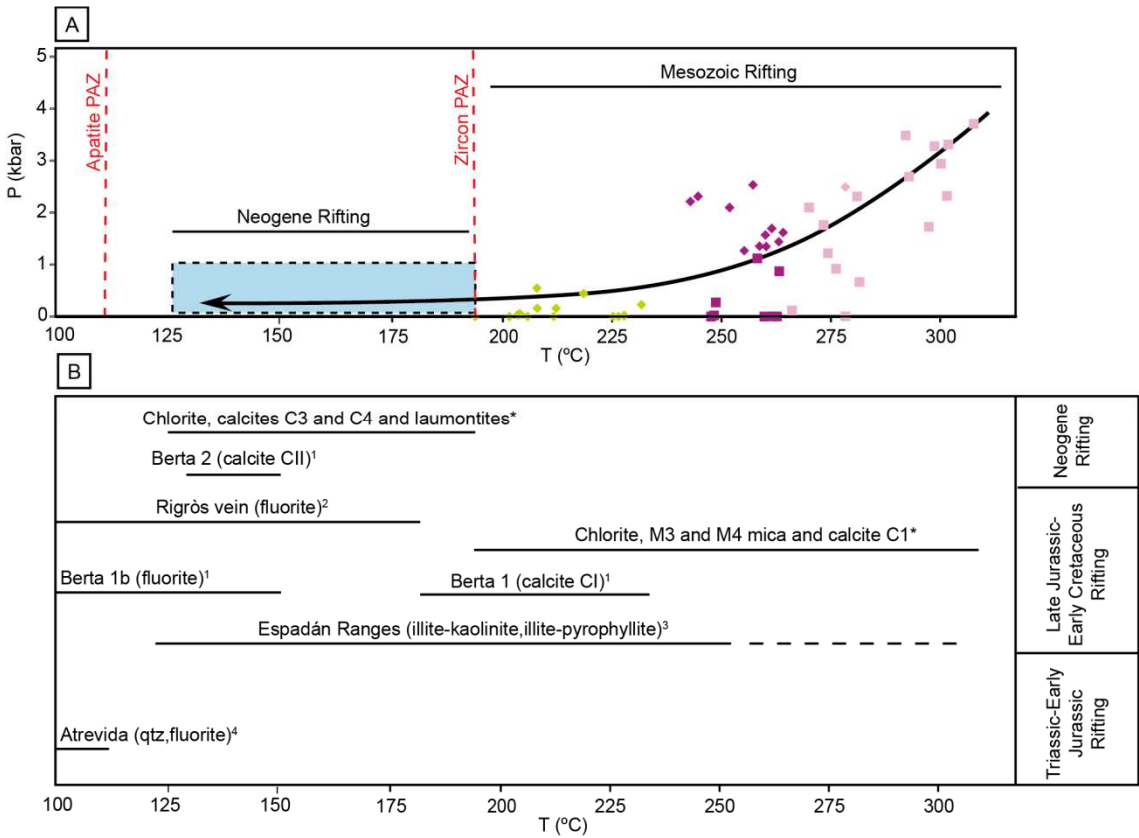
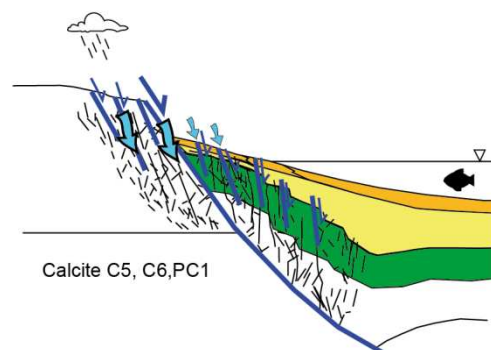
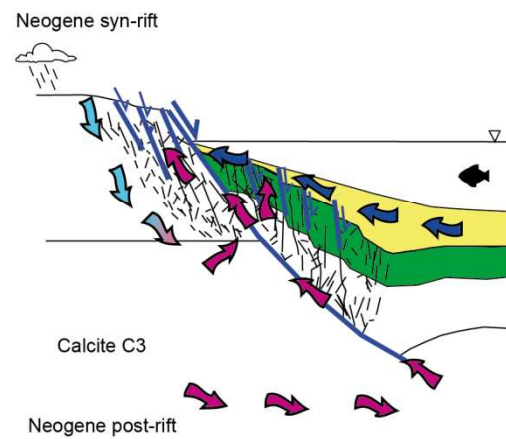
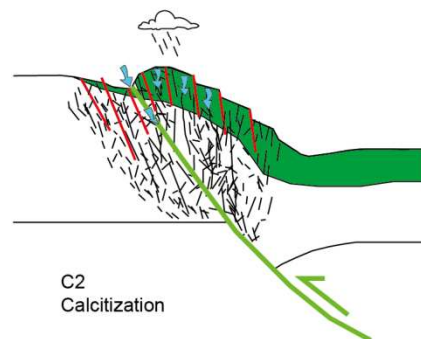
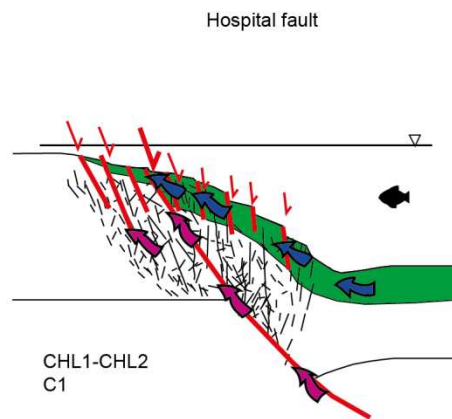
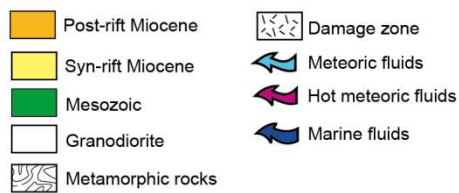
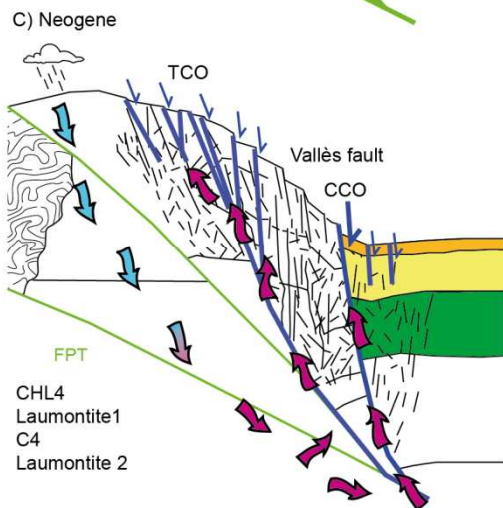
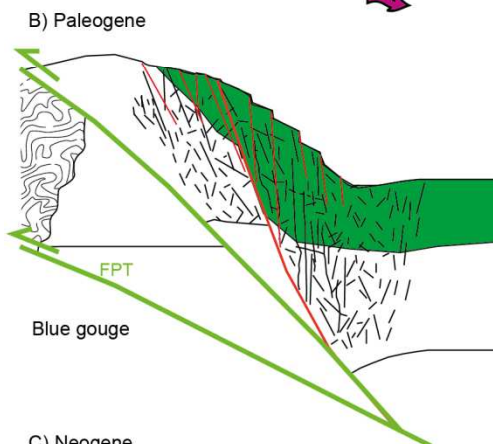
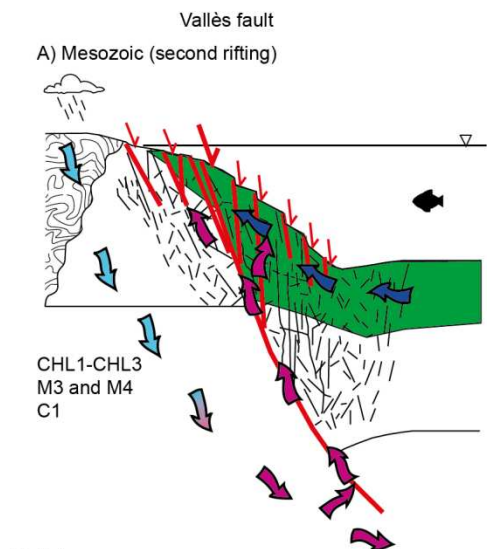


Figure 12





**Table 1**

	M1 (n=5)	M2 (n=12)	M3 (n=11)	M4 (n=4)
SiO <sub>2</sub>	46.85	43.58	48.34	50.69
Al <sub>2</sub> O <sub>3</sub>	35.01	29.98	31.45	29.99
FeO	2.18	2.7	2.76	2.2
MnO	0.03	0.06	0.06	0.01
MgO	0.52	1.21	1.72	2.12
CaO	0.04	0.08	0.07	0.12
Na <sub>2</sub> O	0.86	0.39	0.47	0.2
K <sub>2</sub> O	9.87	9.14	9.39	9.67
Atom site distribution (11 anhydrous-oxygen basis including Fe <sup>3+</sup> )				
Si(T1+T2)	3.11	3.17	3.22	3.35
Al(T2)	0.89	0.83	0.78	0.65
V(M1)	0.98	0.98	1.00	0.98
Mg(M1)	0.01	0.01	0.00	0.01
Fe <sup>2+</sup> (M1)	0.02	0.01	0.00	0.01
Al(M2+M3)	1.85	1.73	1.68	1.69
Mg(M2+M3)	0.04	0.12	0.17	0.2
Fe(M2+M3)	0.1	0.15	0.07	0.12
K(A)	0.84	0.85	0.8	0.82
Na(A)	0.11	0.05	0.06	0.03
V(A)	0.05	0.09	0.14	0.15

n: number of analysis



**Table 2**

	Neoformed						From biotite	
Chlorite generation	CHL1 (n=19)	CHL2 (n=17)	CHL3 (n=42)	CHL4 (n=19)	CHL1 (n=15)	CHL2 (n=7)	CHL1 (n=17)	CHL2 (n=13)
SiO <sub>2</sub>	26.3	26.62	27.03	28.47	26.39	27.99	26.81	27.26
Al <sub>2</sub> O <sub>3</sub>	21.8	21.42	21.62	21.68	17.6	19.09	17.73	18.44
FeO	26.92	25.84	25.36	25.8	27.53	24.26	24.83	27.41
MnO	0.46	0.52	0.59	0.55	0.78	0.42	0.73	0.64
MgO	13.18	13.55	13.31	11.11	13.44	16.76	15.41	13.56
CaO	0.15	0.1	0.1	0.55	0.06	0.00	0.04	0.06
Na <sub>2</sub> O	0.00	0.02	0.00	0.06	0.03	0.05	0.00	0.00
K <sub>2</sub> O	0.04	0.08	0.02	0.18	0.12	0.00	0.00	0.05
Atom site distribution (14 anhydrous-oxygen basis including Fe <sup>3+</sup> )								
Si(T1+T2)	2.71	2.73	2.76	2.86	2.79	2.79	2.8	2.81
Al(T2)	1.29	1.26	1.24	1.12	1.21	1.21	1.2	1.19
Al(M1)	0.29	0.26	0.24	0.12	0.21	0.2	0.2	0.19
Mg(M1)	0.25	0.24	0.22	0.17	0.25	0.28	0.28	0.23
Fe <sup>2+</sup> (M1)	0.23	0.19	0.17	0.13	0.17	0.12	0.14	0.15
V(M1)	0.23	0.3	0.37	0.58	0.37	0.4	0.39	0.43
Mg(M2+M3)	1.78	1.84	1.81	1.5	1.87	2.22	2.12	1.85
Fe(M2+M3)	1.69	1.47	1.39	1.17	1.27	0.94	1.03	1.22
Al(M2+M3)	0.47	0.62	0.74	1.19	0.77	0.8	0.78	0.86
Al(M4)	0.61	0.44	0.39	0.13	0.00	0.03	0.00	0.01
Fe <sup>3+</sup> (M4)	0.39	0.56	0.61	0.87	1.00	0.97	1.00	0.99
XFe <sup>2+</sup>	0.48	0.44	0.44	0.43	0.33	0.3	0.33	0.4
Temperature (°C)*	286	256	230	144	286	254	285	256

n: number of analyses

\* Vidal et al. (2005, 2006), see text

